Atomistic Simulations of Room Temperature Ionic Liquids: Biomass Dissolution, Interfaces and Mixtures

A Thesis submitted in partial fulfillment

for the degree of

DOCTOR OF PHILOSOPHY

in the Faculty of Science

by

Rajdeep Singh Payal

CHEMISTRY AND PHYSICS OF MATERIALS UNIT
JAWAHARLAL NEHRU CENTRE FOR ADVANCED SCIENTIFIC RESEARCH
Bangalore – 560 064, India

JANUARY 2015

DECLARATION

I hereby declare that the matter embodied in the thesis entitled "**Atomistic Simulations of Room Temperature Ionic Liquids: Biomass Dissolution, Interfaces and Mixtures**" is the result of investigations carried out by me at the Chemistry and Physics of Materials Unit, Jawaharlal Nehru Centre for Advanced Scientific Research, Bangalore, India under the supervision of Prof. S. Balasubramanian and that it has not been submitted elsewhere for the award of any degree or diploma.

In keeping with the general practice in reporting scientific observations, due acknowledgement has been made whenever the work described is based on the findings of other investigators. Any omission that might have occurred by oversight or error of judgement is regretted.

Rajdeep Singh Payal

CERTIFICATE

I hereby certify that the matter embodied in this thesis entitled "**Atomistic Simulations of Room Temperature Ionic Liquids: Biomass Dissolution, Interfaces and Mixtures**" has been carried out by Mr. Rajdeep Singh Payal at the Chemistry and Physics of Materials Unit, Jawaharlal Nehru Centre for Advanced Scientific Research, Bangalore, India under my supervision and that it has not been submitted elsewhere for the award of any degree or diploma.

Prof. S. Balasubramanian
(Research Supervisor)

Acknowledgements

This thesis would not have been possible without the guidance of my research supervisor **Prof. S. Balasubramanian**. *His support, encouragement and efforts made this thesis possible. I will always be grateful to him, for introducing me to this exciting world of computer simulations (where I was a complete stranger).*

I would also like to especially thank Dr. Sandeep Kumar Reddy for his help and support.

I would like to thank all the present (Satya, Anirban, Tarak, Karteek, Anurag, Chidambar, Promit, Chaitanya, Sudip and Dr. Anant) and past (Dr. Raju, Dr. Saswati, Dr. Kanchan and Dr. Ganga) lab members for the various moments of joy I shared with them.

I express my sincerity towards all my course instructors Prof. N. S. Vidhyadhiraja, Prof. A. Chakrabarty, Prof. S. Narasimhan and Prof. S. Balasubramanian. I also express my sincerity towards all other faculty members of CPMU and other units in JNCASR.

I thank JNCASR and CCMS (Vijay, Anand and Bharti) for the computational facilities and various resources. I also thank CSIR for the fellowship and DST for the funding. I would like to express my gratitude towards the academic and non-academic staff of JNCASR.

I also thank my collaborators Dr. I. Rudra, Dr. K. Tandon, Dr. F. Thakkar, Dr. A. Verma and Dr. R. Cracknell.

I thank my all other friends from JNCASR and elsewhere.

Preface

The thesis presents results of investigations of room temperature ionic liquids (RTILs) in three different contexts: (i) as a solvent for the dissolution of biomass, on which topic three chapters are devoted (ii) its organization on a charged solid surface, an aspect that is vital to understanding the role of RTILs in supercapacitors and (iii) the molecular level mixing of binary RTILs. These problems are studied using a variety of computational methods which include quantum chemical cluster calculations, atomistic molecular dynamics (MD) simulations using empirical potentials as well as density functional theory (DFT) based ab initio MD simulations.

The first chapter of the thesis provides a basic introduction to RTILs and various simulation methods used in the course of research.

In the second chapter, the dissolution of lignocellulosic biomass represented by monomers cellobiose and xylan in the RTIL, [emim][OAc] was studied using quantum chemical cluster calculations. Gas phase, implicit and explicit solvent calculations were carried out to examine intermolecular interactions between the ions and solvents such as water, methanol and RTILs. The complete disruption of intra-molecular hydrogen bonds of cellobiose and xylan by the anions of RTILs and the consequent formation of intermolecular hydrogen bonds is key to the effectiveness of RTILs over other solvents in biomass dissolution.

In Chapter 3, the results from these gas phase calculations are confirmed through ab initio MD simulations of cellobiose in bulk [emim][OAc], at ambient conditions.

The anion plays the primary role in solvating cellobiose; however, the cation too is found to form weak hydrogen bonds with the solute through its acidic proton located on the imidazolium ring. The presence of a small amount of co-solvent, water, is seen not to affect this mechanism of solvation.

The dependence of biomass dissolution on the anion of the RTIL is investigated through atomistic MD simulations in the forth chapter of the thesis. The conformational free energy of cellobiose in seven different RTILs composed of the same cation, [bmim], but with different anions has been calculated using the Adaptive Biasing Force (ABF) method and the anti-anti conformer is found to be the most stable. The solvation free energy of cellobiose in each of these RTILs has been calculated and the contributions of potential energy and entropy to it have been elucidated. Results are compared to experimental observations on cellulose dissolution in various RTILs.

Chapters 5 and 6 examine the ordering of ions of [NTf_2] [bis(trifluoromethylsulfonyl)-imide] based RTILs on a charged mica surface. In particular, the effect of the length of the alkyl tail of the cation on its organization in the first adsorbed layer has been examined. In Chapter 6, the simulations are extended to consider the symmetry of alkyl tails present on the imidazolium ring on the structure of the RTIL at the liquid-solid interface. In the first adsorbed layer, the ring plane of cations with shorter alkyl groups (less than four carbon atoms) are observed to be oriented either parallel or perpendicular to the surface. However, cations with longer alkyl tails are seen to have their ring planes parallel to mica surface. The alkyl groups too show a similar dependence of their orientation on the tail length. Further, symmetric cations with alkyl groups of intermediate length are highly structured at the interface than their asymmetric counterparts.

The extent of mixing in binary mixtures of RTILs containing the same cation but two different anions, has been examined at various mole fractions using atomistic

MD simulations in Chapter 7. Both $[PF_6]/[BF_4]$ and $[PF_6]/[Cl]$ mixtures have been investigated. The coordination environment of an anion around the cation is altered in the presence of another type of anion. The extent of change is larger for anions with much different radii. Atomistic MD and coarse grain MD simulations do not show any evidence for the clustering of like anions at any concentration. The binary liquids are well mixed at the molecular level.

Contents

List of Figures

List of Tables

Chapter 1

Introduction

Room temperature ionic liquids (RTILs) have gained a lot of attention owing to their attractive physiochemical properties. Low vapor pressure [1–3], inflammability [4, 5], high chemical and thermal stability [6, 7], wide electrochemical window [8–12] and tunable solubility [13] make RTILs a better choice over conventional solvents. The environmentally benign nature of RTILs is one of the major force driving the boost in RTILs research and its applications. Initially, the use of RTILs was limited as green solvents [14–17]. Most of the initial work in RTILs was focused on the ability of RTILs to dissolve biomass [18–26]. Later, with the synthesis of new RTILs, their applications have also increased. In recent years, RTILs have been used in the variety of applications e.g. electrolytes for batteries and supercapacitors [27–35], for gas adsorption [36–41], as lubricants [42–44] and in catalysis [45–48], *etc.*

Many aspects of RTILs has been reviewed in the literature [24, 49–65]. RTILs have been investigated from experimental as well as computational points of view for pure and mixed systems [66–93]. Hence only a mini summary of relevant background material needed for the thesis is present.

1.1 Room temperature ionic liquids

Room temperature ionic liquids are salts that are liquid below 100 ^{o}C [1, 94, 95]. These consist solely of ions. Unlike other conventional ionic compounds that we see in our daily life e.g. NaCl or common salt, where both Na^+ ion and Cl^- ion are held together by strong Coulomb interactions, the electrostatic interactions in RTILs are much a weak. RTILs are constituted of both organic and inorganic moieties. They contain bulky cations (e.g. alkylimidazolium) and anions (e.g. hexafluorophosphate) where charge is delocalized, resulting in weaker Coulomb interaction and hence, RTILs are liquid at or near ambient conditions [45]. Figure 1.1 shows some common cation and anions of RTILs. Cations of RTILs are mostly organic and asymmetric moieties. Anions of RTILs can either be inorganic or organic. Generally, anions have higher symmetry as compared to cations. Structural properties of both cation and anion greatly influence physical and chemical properties [96–99]. A suitable choice of cation and anion can be used to tune physical and chemical properties of RTILs [6, 40, 100–103]. RTILs can also be made task specific by appropriate choice of cation and anion. With an appropriate choice of cation and anion, RTILs can be made to function like acids, bases or ligands [104–106]. For these reasons RTILs are also known as designer solvents [107–109].

1.1.1 Properties of room temperature ionic liquids

Density: RTILs in general are denser than common organic solvents and water [1, 6, 110, 111]. RTIL densities decrease linearly with increasing temperature. Density of RTIL also depends on the size and symmetry of cation. Cation with longer tail length and the higher asymmetry lead to lower densities. For example, in the case of $[NTf_2]^-$ anion, density of RTILs varies as $[emim]^+ > [bmim]^+ > [hmim]^+ > [omim]^+$ [1, 94, 95]. In the case of anion, the density of RTILs decreases with the size of anion. For example, within the $[bmim]^+$ cation family, density of RTIL varies as

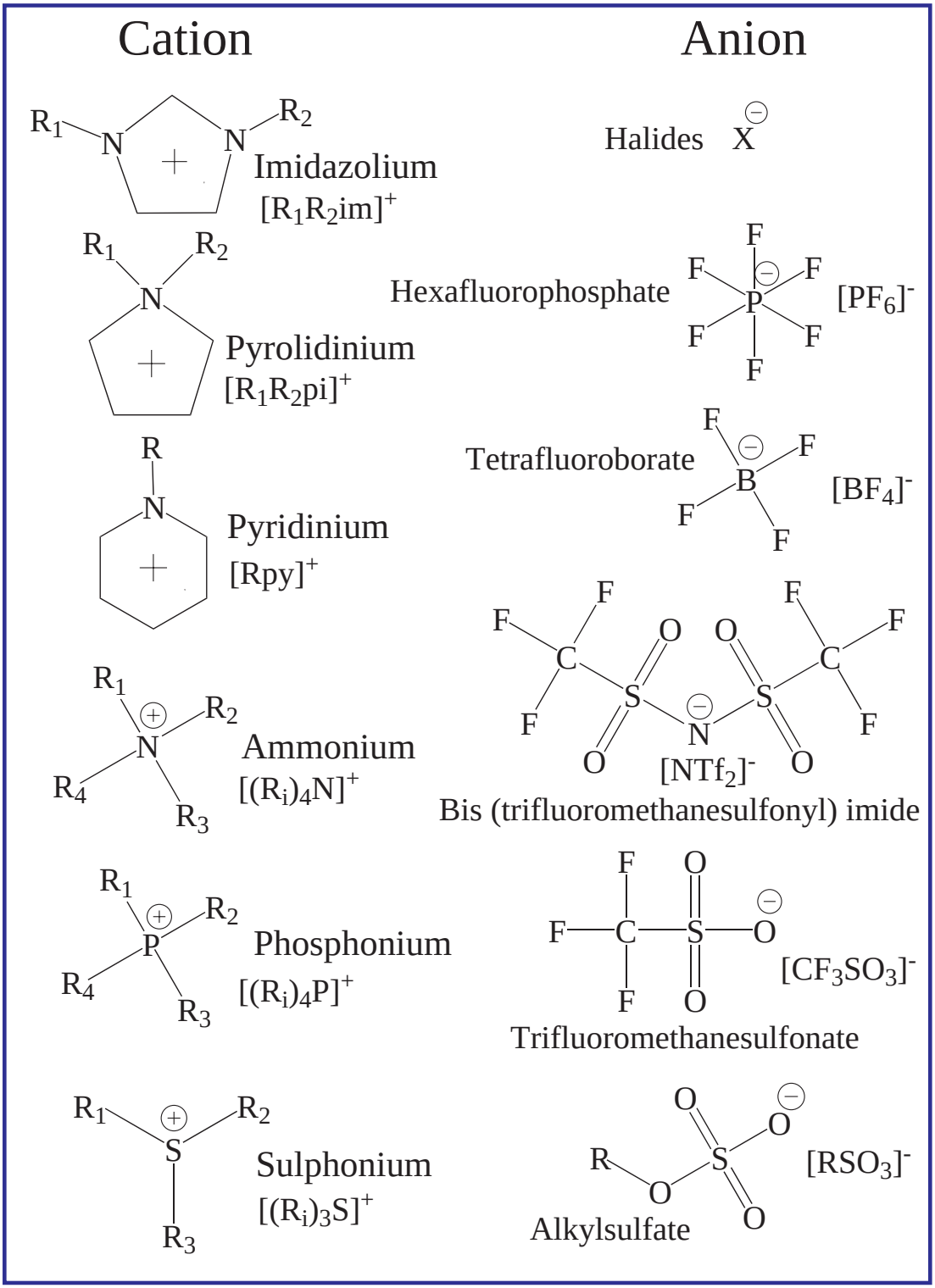

Figure 1.1: Schematic of some cations and anions constituting RTILs.

$[Cl]^- > [BF_4]^- > [PF_6]^- > [NTf_2]^-$ [1, 94, 95].

Viscosity: RTILs have viscosities higher by at least an order of magnitude as compared to water [1, 110–112]. At ambient conditions, water has viscosity 1 mPa. s, whereas for RTILs, viscosity typically varies between 10 to 500 mPa. s. Viscosity of RTIL increases with an increase in size of cation. For $[PF_6]^-$ anion, viscosity varies as $[emim]^+ > [bmim]^+ > [hmim]^+ > [omim]^+$ [1, 94, 95]. In the case of anion, viscosity increases with coordinating strength of anion with cation. For example for $[bmim]^+$ cation, viscosity varies as $[Cl]^- > [PF_6]^- > [NTf_2]^-$ [1, 94, 95]. Viscosities of RTILs decrease with increasing temperature [113, 114]. Addition of impurities (water, solvent molecules) changes the viscosity of RTILs drastically [115, 116].

Melting point: Melting point of RTILs decreases with the increase in the size of cation and anion [110, 111]. A small variation in alkyl tail length of cation can lead to a significant difference in melting point. For example the melting point of $[Cl]^-$ containing RTIL varies as $[emim]^+ > [bmim]^+ > [hmim]^+ > [omim]$ [1, 94, 95]. In case of $[bmim]^+$, melting point varies as $[Cl]^- > [PF_6]^- > [NTf_2]^-$ [109]. Apart from the size of cation, its symmetry is also an important factor in determining the melting point of the RTILs. With the increase in symmetry, melting point increases [1].

1.1.2 Applications

Solvent: One of the most important application of RTILs is their use as solvent [15, 45]. RTILs can be used as solvents for a large number of organic and inorganic compounds. Also, since RTILs are non-volatile, they are the preferred choice for high vacuum conditions. However, one of the most important application of RTILs is the ability to dissolve biomass [18, 100, 117]. RTILs can dissolve cellulose, which is difficult to dissolve in conventional solvents or otherwise require harsh conditions. Also, RTILs can be used to stabilize biomolecules like DNA [118–120].

Electrolytes: High thermal and chemical stability and wide electrochemical window of RTILs make them an apt choice for use in electrochemical processes [27]. RTILs are used as electrolytes in solar cells, Li^+ ion batteries, supercapacitors, *etc* [121, 122]. Wide electrochemical window of RTILs provides them stability against redox reactions. Recently, binary and ternary mixtures of RTILs for electrochemical applications [123]. Mixtures provide better control over charge diffusion which can be regulated by varying the ratio of ions in it [124].

Gas adsorption: RTILs can be designed for some particular tasks [125–127]. Many research groups across the globe have used RTILs to adsorb selectively CO_2 from a mixture of gases [41]. Apart from CO_2, adsorption of other gases like H_2S, SO_2 *etc* in RTILs have also been studied [39, 40, 128]. Advantage with RTILs is the simple recovery process that involves heating of RTILs under reduced pressure condition. Once gas molecules are removed, the same RTILs can be reused for the next cycle of gas adsorption.

Purification and waste treatment: RTILs are used as electrolytic media for recovery of Uranium and heavy metals from nuclear waste [129, 130]. In petroleum industry, RTILs are used to separate heavy metals from the crude oil. [49] Also, they can be used to separate aromatic and aliphatic hydrocarbons [131, 132]. RTILs have also been employed to extract various organic and inorganic compounds from aqueous solutions [133].

Catalysis: Ability of RTILs to dissolve a large number of organic and inorganic compounds makes them a suitable choice for monophasic and multiphasic catalysis. Also, they can act as reaction media for homogeneous catalysis [45–47, 134]. Selectivity of RTILs can be tuned by the choice of cation and anion. This makes them extremely useful in catalysis. This enhances the reaction rate and hence makes the

process less energy intensive.

1.2 Previous studies on ionic liquids

RTILs have unique physiochemical properties as they are both Coulombic as well as molecular fluids. Their intermoleculr structure plays a major role in the determination of these properties. Unlike other molecular liquids, RTILs exhibit charge ordering [135]. Since it was difficult to evaporate RTILs (due to their negligible vapor pressure), electrospray ionization mass spectroscopy was employed to understand the stability of ion clusters in RTILs [136, 137]. Presence of different size of charged and uncharged clusters was observed during these studies. Charge ordering in RTILs was also evident in molecular dynamics simulations [138, 139]. RTILs were also found to show lamellar [140–142], bicontinuous [77, 143] and liquid-crystalline [143, 144] phases.

Structure of RTILs has also been probed using X-ray diffraction [67, 68, 145], X-ray scattering [146, 147] and nuclear magnetic resonance (NMR) [148] studies. Mesoscopic structure and nanostructural inhomogeneity in RTILs were revealed by these studies. This nanoscale heterogeneity of the RTILs was shown to be dependent on the alkyl tail length. It was so argued that RTILs cannot be considered as conventional liquids, but as a mesophase [149, 150]. It was proposed that this mesophase was driven by three dimensional hydrogen bonding network. Computational efforts were also carried out to understand the nanoscale heterogeneity of RTILs [61, 77, 151]. These studies showed the existence of stationary phase composed of polar and non-polar domains [55, 61]. Further, the dependence of nanoscale heterogeneity on the alkyl tail length was also demonstrated [55, 61, 152, 153]. Another important aspect of RTILs, Hydrogen bonding network between cation and anion was also elucidated using computer simulations [154, 155]. Both ab-initio

molecular dynamics and quantum chemical calculations were employed to understand the molecular and electronic structure of RTILs [70, 74]. These studies show an important aspect that Coulombic stabilization drove hydrogen bonding network in RTILs. Hydrogen bonding interactions were dominated by a large positive charge at most acidic carbon and π-electron cloud formation above and below the ring plane [70].

Other experimental methods such as differential scanning calorimetry (DSC) [156, 157], optical Kerr effect (OKE) spectroscopy [158–160], quasi-elastic neutron scattering spectroscopy [161, 162] and far infrared spectroscopy [163, 164] etc have been carried out to understand the molecular motions in RTILs. Vibrational spectra of RTILs was also calculated using ab-initio computational methods. Computational methods were employed to identify the various different conformers contributing to characteristic Raman lines in RTILs [71, 165].

Transport properties, such as viscosity [110, 114, 116, 166, 167], transport coefficients [168, 169] and electrical conductivity [170–172] etc of RTILs and their dependence on temperature, density and pressure etc were also measured. Calculating the transport property is a challenging task from the simulation point of view as it requires large time scales. Most of the earlier efforts were unable to reproduce correct estimate of the viscosity. Generally, computer simulations would overestimate the viscosity and underpredict the transport coefficients [62, 173]. In the recent past, development of better force fields have led to a better estimate of dynamical properties of RTILs [174, 175]. One of the important finding of computer simulations in this field was to show that despite being bulkier, cations were able to diffuse faster as compared to the anions. However, the underlying cause for this observation is still a matter of research.

1.3 Simulation methodologies

1.3.1 Density functional theory

Density functional theory (DFT) is one the most celebrated method to calculate ground state properties of a system e.g. electronic structure, interaction *etc* [176, 177]. Importance of DFT lies in the fact that it provides a solution for N-particle system with certain approximations. As the analytical solution of N-body problem is difficult to find, one needs simplified models. Let us consider a system with N electrons and M nuclei. The non-relativistic Schrödinger equation for this system may be written as

$$\mathcal{H}\Psi(r_1,..,r_N,R_1,..R_M) = \mathcal{E}\Psi(r_1,..,r_N,R_1,..R_M) \tag{1.1}$$

where r_i represent electronic coordinates and R_I are nuclear coordinates. Hamiltonian of eq (1.1) can be decomposed into electronic, nuclear and cross terms.

$$\mathcal{H} = -\sum_{i=1}^{N}\frac{{\nabla_i}^2}{2m_{ele}} + \sum_{i=1}^{N}\sum_{j>1}^{N}\frac{e^2}{r_{ij}} - \sum_{I=1}^{M}\frac{\nabla_I^2}{2m_{nu}} + \sum_{I=1}^{M}\sum_{J>1}^{M}\frac{Z_I Z_J e^2}{R_{IJ}} - \sum_{i=1}^{N}\sum_{I=1}^{M}\frac{Z_I e^2}{r_{iI}} \tag{1.2}$$
$$\mathcal{H} = \mathcal{H}_{ele} + \mathcal{H}_{nu} + \mathcal{H}_{ele-nu}$$

Now, using Born-Oppenheimer approximation, we can approximate the kinetic energy of nucleus to be zero and potential energy of nucleus to be constant. Hence total Hamiltonian becomes

$$\mathcal{H} = \mathcal{H}_{ele} + const + \mathcal{H}_{ele-nu} \tag{1.3}$$

This states that there are N electrons moving in the field of M nuclei. Hartree-Fock approximated that this ground state wavefunction for N electron system may

be expanded in terms of spin and spatial components of individual electrons. This in tern may be written as a Slater determinant

$$\Psi_0 \approx \Psi_{HF} = \frac{1}{\sqrt{N}} \begin{vmatrix} \psi_1(\mathbf{r}_1)\ \psi_2(\mathbf{r}_1)\ .\ .\ .\ .\ .\ .\psi_N(\mathbf{r}_1) \\ \psi_1(\mathbf{r}_2)\ \psi_2(\mathbf{r}_2)\ .\ .\ .\ .\ .\ .\ \psi_N(\mathbf{r}_2) \\ .\ .\ .\ .\ .\ .\ .\ .\ . \\ .\ .\ .\ .\ .\ .\ .\ .\ . \\ \psi_1(\mathbf{r}_N)\ \psi_2(\mathbf{r}_N)\ .\ .\ .\ .\ .\ .\ \psi_N(\mathbf{r}_N) \end{vmatrix} \tag{1.4}$$

Every $\psi_i(\mathbf{r}_j)$ is product of its spin function and spatial orbital. Now the energy of the system may be approximated as

$$\mathcal{E}_{HF} = \langle \Psi_{HF} | \mathcal{H} | \Psi_{HF} \rangle = \sum_{i=1}^{N} \mathcal{H}_i + \frac{1}{2} \sum_{i,j=1}^{N} (\mathcal{J}_{ij}\ \mathcal{K}_{ij}) \tag{1.5}$$

Here $\mathcal{H}_i$ is the Hamiltonian of individual electron in presence of field of nuclei. $\mathcal{J}_{ij}$ *and* $\mathcal{K}_{ij}$ are Coulomb and Exchange integrals respectively and can be written as

$$\begin{aligned} \mathcal{J}_{ij} &= \int\int \psi_i(\mathbf{r}_i)\psi_i^*(\mathbf{r}_i)\frac{1}{r_{ij}}\psi_j^*(\mathbf{r}_j)\psi_j(\mathbf{r}_j) \\ \mathcal{K}_{ij} &= \int\int \psi_i^*(\mathbf{r}_i)\psi_j(\mathbf{r}_j)\frac{1}{r_{ij}}\psi_i(\mathbf{r}_i)\psi_j^*(\mathbf{r}_j) \end{aligned} \tag{1.6}$$

In 1964, Hohenberg and Kohn [178] showed that ground state energy of the system can be uniquely be determined from probability density of electron ($\rho(\mathbf{r})$).

$$\rho(\mathbf{r}) = N \int ... \int |\Psi(\mathbf{r}_1, \mathbf{r}_2, ..., \mathbf{r}_N)| d\mathbf{r}_1 d\mathbf{r}_2 ... d\mathbf{r}_N$$

$$\rho(\mathbf{r} \longrightarrow \infty) = 0$$

$$\int \rho(\mathbf{r}) d\mathbf{r} = N \tag{1.7}$$

$$\mathcal{E}_0 = -\frac{1}{2} \sum_{i=1}^{N} \langle \psi_i | \nabla^2 | \psi_i \rangle + \sum_I \int \frac{Z_I \rho}{r_I} dv + \frac{1}{2} \int \int \frac{\rho(i)\rho(j)}{r_{ij}} dv_1 dv_2 + E_{xc}[\rho]$$

Where $\mathcal{E}_0$ is ground state energy of the system, described by Kohn-Sham. E_{xc} is the exchange-correlation energy and a function of ρ [179]. Accurate determination of E_{xc} is very important for Kohn-Sham formalism to yield correct energy. There are different methods to calculate E_{xc}, like local density approximation (LDA), generalized gradient approach (GGA) *etc.*

Since these calculations are computationally expensive, they are limited to only few atoms or molecules.

1.3.2 Molecular dynamics simulations

Molecular dynamics (MD) simulations generate configurations in the phase space as a function of time; such configurations obey the probability distribution function of the specific ensemble. System sizes in MD simulations typically vary between few atoms or particles to million of atoms or particles. Using MD simulations, one can study all three states of matter: solid, liquid and gas. One can try to mimic both gas phase properties using a few atom cluster calculations or bulk system having reasonably large number of atoms by applying periodic boundary conditions. MD integration utilizes numerical techniques to solve classical equations of motion

$$\begin{aligned} \mathcal{H} &= \mathcal{K} + \mathcal{U} \\ \dot{\mathbf{q}} = \frac{\partial \mathcal{H}}{\partial p},\ \dot{\mathbf{p}} &= -\frac{\partial \mathcal{H}}{\partial q} \end{aligned} \tag{1.8}$$

where $\mathbf{p}$ and $\mathbf{q}$ are position and momentum vector of an atom. $\mathcal{H}, \mathcal{K}$ and $\mathcal{U}$ are Hamiltonian, kinetic energy and potential energy of the system respectively.

Solving these equations of motion, one generates the trajectory over a certain amount of time. Then, any physical quantity is calculated as time average of that quantity of interest. In experiment, any physical quantity is ensemble average as number of atoms are large. Ergodic hypothesis states that time average and ensemble average are equal if both time and number of atoms are sufficiently large.

$$\begin{aligned} \langle \mathcal{A} \rangle_{time} &= \lim_{t \to \infty} \frac{1}{t} \int_0^t \mathcal{A}(\mathbf{p}, \mathbf{q}) \\ \langle \mathcal{A} \rangle_{ensemble} &= \int \int d\mathbf{p}\ d\mathbf{q}\ \mathcal{A}(\mathbf{p}, \mathbf{q})\ \rho(\mathbf{p}, \mathbf{q}) \\ \rho(\mathbf{p}, \mathbf{q}) &= \frac{1}{Z}\ exp\left(-\frac{\mathcal{H}(\mathbf{p}, \mathbf{q})}{k_B T}\right) \\ Z &= \int \int d\mathbf{p}\ d\mathbf{q}\ exp\left(-\frac{\mathcal{H}(\mathbf{p}, \mathbf{q})}{k_B T}\right) \\ \langle \mathcal{A} \rangle_{time} &= \langle \mathcal{A} \rangle_{ensemble} \end{aligned} \tag{1.9}$$

Here $\mathcal{A}$ and ρ are the quantity of interest and probability density respectively. Z, k_B and T are the canonical partition function, Boltzmann constant and simulation temperature respectively.

The equations of motion are solved using various numerical integration methods e.g. Leap-Frog algorithm, Gear predictor-corrector algorithm, velocity Verlet algorithm *etc.* One of the most common integration method is velocity Verlet algorithm [180]. This algorithm can be described as follows

$$\begin{aligned} \mathbf{p_i}(t+\frac{\delta t}{2}) &= \mathbf{p_i} + \frac{\delta t \mathbf{F}_i(t)}{2} \\ \mathbf{q_i}(t+\delta t) &= \mathbf{q_i} + \frac{\delta t \mathbf{p_i}(t+\frac{\delta t}{2})}{m_i} \\ \mathbf{p_i}(t+\delta t) &= \mathbf{p_i}(t+\frac{\delta t}{2}) + \frac{\delta t \mathbf{F}_i(t+\delta t)}{2} \end{aligned} \tag{1.10}$$

where $\mathbf{F_i}$ is the force experienced by atom i. δt is the integration time step. Choice of the integration time step depends on fastest vibrational mode present in the system (In current thesis fastest vibrational mode was C-H vibrational mode and hence the integration time step was chosen to be 0.5 fs). While generating the analysis trajectory, one should keep in mind that trajectory run length (t_{run}) should be large as compared to the correlation length (t_A)of the desired property i.e. $t_A << t_{run}$.

Classical molecular dynamics simulations

Classical MD is an empirical force field based technique. It uses a predefined potential to calculate the energy of the system. These predefined potential parameters or force field parameters are standardized against various physical properties of the system. Interaction between atoms is divided into two parts: Non-bonded and bonded interactions. Non-bonded interactions involve electrostatic and a weak dispersion interactions. Bonded interactions consist of bond, angle, dihedral and improper torsion terms. Some of the most common forms are listed below:

Non-bonded interactions

$$\begin{aligned} \mathcal{U}_{ij}^{dispersion}(r_{ij}) &= 4\varepsilon_{ij}\left[\left(\frac{\sigma_{ij}}{r_{ij}}\right)^{12} - \left(\frac{\sigma_{ij}}{r_{ij}}\right)^{6}\right] \\ \mathcal{U}_{ij}^{electrostatic}(r_{ij}) &= \frac{1}{4\pi\epsilon_0}\frac{q_i q_j}{r_{ij}} \end{aligned} \tag{1.11}$$

Here q_i and q_j are charges on atoms i and j. ε, σ and ϵ_0 are depth of potential well, distance of minimum approach between two atoms and dielectric permittivity of vacuum respectively. r_{ij} is the distance between atom i and j.

Bonded interactions

$$\begin{aligned} \mathcal{U}_{ij}^{bond}(r_{ij}) &= \frac{k_{ij}}{2}(r_{ij} - r_0)^2 \\ \mathcal{U}_{ijk}^{angle}(\theta_{ijk}) &= \frac{k_{ijk}}{2}(\theta_{ijk} - \theta_0)^2 \\ \mathcal{U}_{ijkl}^{torsion}(\phi_{ijkl}) &= \sum_{n=1}^{4} k_n(1 + (-1)^n cos(n\phi)) \end{aligned} \tag{1.12}$$

Here r_0 and θ_0 are equilibrium bond length and angle between respective atoms. ϕ is the angle between planes formed by ijk and jkl atoms.

A force field defines all the parameters required to employ these equations. These parameters are calculated either using high level quantum chemical calculations or through experiments. In classical MD simulations, interactions between atoms are calculated in two parts:

Within cutoff radius r_c: Here interaction is calculated directly using the equations (1.11) and (1.12). Beyond the cutoff radius, the interaction energy of individual pair has insignificant contributions to total energy, but contribution of all the pairs may still be significant for long range interactions. Cutoff radius (r_c) is generally defined as $r_c \leq L/2$ (where L is the box length).

Long range interactions: Generally if an interaction does not decay faster than r^{-d}, where d is dimensionality of the system, interaction is said to be long range. In equation (1.11), electrostatic interaction decays as r^{-1} and hence falls under the category of long range interactions. These interactions do not decay to zero at the cutoff radius. Further, the total electrostatic energy is conditionally convergent.

Calculation of these interactions in real space is computationally expensive. To address this problem, Ewald summation method was developed to treat long range interactions.

Ewald summation method

Ewald summation method calculate long range interaction for periodic systems [181]. This is done by splitting the electrostatic interaction into two parts. Let us assume cubic box of volume V (V=L^3). Now the total electrostatic interaction may be given as

$$\mathcal{U}_{tot}^{electrostatic} = \frac{1}{2}\sum_{i=1}^{N}\sum_{j=1}^{N}\sum_{n}^{N'}\frac{q_i q_j}{4\pi\epsilon|\mathbf{r}_{ij}+\mathbf{n}|} \tag{1.13}$$

Here $\mathbf{n}$=$(n_x L, n_y L, n_z L)$ (n_x, n_y, n_z being integers). Now the 1/r dependence is split in two parts each of which converges faster as compared to 1/r itself.

$$\frac{1}{r} = \frac{f(r)}{r} + \frac{1-f(r)}{r} \tag{1.14}$$

$f(r) = erfc(\alpha r)$ is the most common choice for $f(r)$ and α is known as Ewald splitting parameter. Now total electrostatic energy can be divided into four components

$$\begin{aligned}
\mathcal{U}_{r}^{electrostatic} &= \frac{1}{2}\sum_{i=1}^{N}\sum_{j=1}^{N}\sum_{n} q_i q_j \frac{erf(\alpha|\mathbf{r}_{ij}+\mathbf{n}|)}{4\pi\epsilon(|\mathbf{r}_{ij}+\mathbf{n}|)} \\
\mathcal{U}_{k}^{electrostatic} &= \frac{1}{2L^3}\sum_{k>0}\frac{4\pi}{k^2}exp(\frac{-k^2}{4\alpha^2})\sum_{i=1}^{N}\sum_{j=1}^{N} q_i q_j exp(-\imath\mathbf{k}.\mathbf{r}_{ij}) \\
\mathcal{U}_{self}^{electrostatic} &= -\frac{\alpha}{\sqrt{\pi}}\sum_{i=1}^{N} q_i^2 \\
\mathcal{U}_{dipolar}^{electrostatic} &= \frac{2\pi}{(1+2\epsilon)L^3}\left(\sum_{i=1}^{N} q_i r_i\right)^2
\end{aligned} \tag{1.15}$$

where $U_r^{electrostatic}$ and $U_k^{electrostatic}$ are real space and Fourier space contributions.

Ab initio molecular dynamics simulations

Classical MD simulation provides key insight into a wide variety of systems. It is very efficient in determining the structure and dynamics of systems. But one of the major limitations of classical MD is its predefined potentials. These predefined potentials are generally determined by pairwise potentials and higher order interactions are neglected. Hence the results will be dependent on the model force field. Only a good model force field can yield good results. Transferability of these model potential is another issue. Also, in general, empirical force fields do not account for the chemical reactions.

Ab initio MD simulation is the combination of molecular dynamics and density functional theory [182]. Here, *ab initio* part deals with electronic degrees of freedom that are not involved in traditional MD simulations. *Ab inito* simulation basically relies on Born-Oppenheimer approximation. The ground state wave function for the system is calculated using Kohn-Sham formalism [179] and plane wave basis set. According to the Blöch theorem, electronic wave function can be represented as linear combination of basis functions.

$$\phi_i = \sum_{\mathbf{k}} C_{\mathbf{k}}^i \psi(\mathbf{k}) \tag{1.16}$$

In *ab initio* MD simulations, these basis functions are plane wave basis functions. So the electronic wave function in terms of plane wave basis can be written as

$$\begin{aligned} \varphi^{\mathbf{k}}(\mathbf{r}) &= \frac{1}{\sqrt{\Omega}} exp(\imath \mathbf{G}.\mathbf{r}) \\ \phi_i &= \frac{1}{\sqrt{\Omega}} \sum_{\mathbf{G}} c_\imath(\mathbf{G}) exp(\imath \mathbf{G}.\mathbf{r}) \end{aligned} \tag{1.17}$$

where **G** is the reciprocal lattice vector.

Ehrenfest was the first person to show that classical Newtonian dynamics can be achieved by solving time dependent Schrödinger equations for point particles. In *ab initio* methods, one solves Newtons equations of motion for nuclei and Schrödinger's equations for electrons simultaneously. Car and Parrinello in 1985 suggested that for reducing the computational cost, one can consider electrons as active degrees of freedom. Hence, they mapped the quantum-classical system to a purely classical system.

Car-Parrinello molecular dynamics: Car and Parrinello defined a Lagrangian such that the force on the nuclei can be calculated through derivatives of Lagrangian with respect to nuclear positions [182].

$$\mathcal{L}_{cp} = \sum_I \frac{1}{2} M_I \dot{\mathbf{R}}_I^2 + \sum_i \mu \langle \dot{\psi}_i | \dot{\psi}_i \rangle - \langle \phi_0 | \mathcal{H}_e | \phi_0 \rangle + constraints \tag{1.18}$$

Here $M_I, R_i, \mathcal{H}_e$ and μ are mass of nuclei, nuclear coordinates, electronic Hamiltonian and fictitious mass respectively. The equation of motions for this system can be obtained by solving the Euler-Lagrange equations for both nuclear coordinates and electronic orbitals.

$$\begin{aligned} \frac{d}{dt}\frac{\partial \mathcal{L}}{\partial \dot{\mathbf{R}}_I} &= \frac{\partial \mathcal{L}}{\partial \mathbf{R}_I} \\ \frac{d}{dt}\frac{\delta \mathcal{L}}{\delta \dot{\psi}_i^*} &= \frac{\delta \mathcal{L}}{\delta \psi_i^*} \end{aligned} \tag{1.19}$$

Hence Car-Parrinello equations of motions can be written as

$$
\begin{aligned}
M_i\ddot{\mathbf{R}}_I(t) &= -\frac{\partial}{\partial \mathbf{R}_I}\langle\phi_0|\mathcal{H}_e|\phi_0\rangle + \frac{\partial}{\partial \mathbf{R}_I}(constraints) \\
\mu\ddot{\psi}_i(t) &= -\frac{\delta}{\delta\psi_i^*}\langle\phi_0|\mathcal{H}_e|\phi_0\rangle + \frac{\delta}{\delta\psi_i*}(constraints)
\end{aligned}
\tag{1.20}
$$

1.4 Software and hardware used

All the classical MD simulations were carried out using software package LAMMPS [183]. Trajectory visualization, snapshot of the simulation box at any instant and snapshot of spatial density maps were taken through software package VMD [184, 185]. *Ab initio* MD simulations were done using software package CP2K [186]. All the analysis was done using home grown code written in FORTRAN 90 programming language. All the graphs were plotted using Xmgrace software package. DFT calculations were done using software packages Gaussian 09 and 03 [187, 188]. All computations were carried out using the various computational resources in our group, JNCASR central computational facility and at CDAC computational facility. Most of the codes were written on the desktop PC.

1.5 Scope of thesis

Work presented in the thesis is devoted to understanding the interaction of RTILs with various matter. These complex interactions were examined using computer simulations. Different techniques like DFT, AIMD and classical MD simulations were employed to understand these problems. Work presented in the thesis can be divided into three parts. In the first part, we have tried to understand the interaction of RTILs with lignocellulosic biomass, chiefly cellulose. We have attempted to quantify the role of cation and anion in the dissolution of lignocellulosic biomass in RTILs. In the second part of the thesis, we have sought to understand the behavior

of RTILs near charged surfaces. Here, we tried to elaborate the effect of cation structure and symmetry on the solid-liquid interface. The third part of the thesis elucidates behavior of the mixture of two RTILs. Intermolecular structure of the binary mixture of RTILs was studied.

Bibliography

[1] Wasserscheid, P.; Welton, T. *Ionic liquids in synthesis*; Wiley Online Library, 2008; Vol. 1.

[2] Aschenbrenner, O.; Supasitmongkol, S.; Taylor, M.; Styring, P. *Green Chem.* **2009**, *11*, 1217–1221.

[3] Rebelo, L. P.; Canongia Lopes, J. N.; Esperança, J. M.; Filipe, E. *J. Phys. Chem. B* **2005**, *109*, 6040–6043.

[4] Fox, D. M.; Gilman, J. W.; Morgan, A. B.; Shields, J. R.; Maupin, P. H.; Lyon, R. E.; De Long, H. C.; Trulove, P. C. *Ind. Eng. Chem. Res.* **2008**, *47*, 6327–6332.

[5] Smiglak, M.; Reichert, W. M.; Holbrey, J. D.; Wilkes, J. S.; Sun, L.; Thrasher, J. S.; Kirichenko, K.; Singh, S.; Katritzky, A. R.; Rogers, R. D. *Chem. Comm.* **2006**, 2554–2556.

[6] Wasserscheid, P.; Keim, W. *Angew. Chem. Int. Ed.* **2000**, *39*, 3772–3789.

[7] Valkenburg, M. E. V.; Vaughn, R. L.; Williams, M.; Wilkes, J. S. *Thermochim. Acta* **2005**, *425*, 181–188.

[8] MacFarlane, D.; Meakin, P.; Sun, J.; Amini, N.; Forsyth, M. *J. Phys. Chem. B* **1999**, *103*, 4164–4170.

[9] Hultgren, V. M.; Mariotti, A. W.; Bond, A. M.; Wedd, A. G. *Anal. Chem.* **2002**, *74*, 3151–3156.

[10] Evans, R. G.; Klymenko, O. V.; Hardacre, C.; Seddon, K. R.; Compton, R. G. *J. Electroanal. Chem.* **2003**, *556*, 179–188.

[11] Boxall, D. L.; ODea, J. J.; Osteryoung, R. A. *J. Electrochem. Soc.* **2002**, *149*, E468–E471.

[12] Boxall, D. L.; Osteryoung, R. A. *J. Electrochem. Soc.* **2002**, *149*, E185–E188.

[13] Huang, J.; Riisager, A.; Berg, R. W.; Fehrmann, R. *J. Mol. Catal. A* **2008**, *279*, 170–176.

[14] Earle, M. J.; Seddon, K. R. *Pure Appl. Chem.* **2000**, *72*, 1391–1398.

[15] Rogers, R. D.; Seddon, K. R. *Science* **2003**, *302*, 792–793.

[16] Wilkes, J. S. *Green Chem.* **2002**, *4*, 73–80.

[17] Seddon, K. R. *J. Chem. Tech. Biotech.* **1997**, *68*, 351–356.

[18] Swatloski, R. P.; Spear, S. K.; Holbrey, J. D.; Rogers, R. D. *J. Am. Chem. Soc.* **2002**, *124*, 4974–4975.

[19] Turner, M. B.; Spear, S. K.; Holbrey, J. D.; Rogers, R. D. *Biomacromolecules* **2004**, *5*, 1379–1384.

[20] Remsing, R. C.; Swatloski, R. P.; Rogers, R. D.; Moyna, G. *Chem. Comm.* **2006**, 1271–1273.

[21] Sun, N.; Rahman, M.; Qin, Y.; Maxim, M. L.; Rodríguez, H.; Rogers, R. D. *Green Chem.* **2009**, *11*, 646–655.

[22] Sun, N.; Rodríguez, H.; Rahman, M.; Rogers, R. D. *Chem. Commun.* **2011**, *47*, 1405–1421.

[23] Vancov, T.; Alston, A.-S.; Brown, T.; McIntosh, S. *Renewable Ener.* **2012**, *45*, 1–6.

[24] Wang, H.; Gurau, G.; Rogers, R. D. *Chem. Soc. Rev.* **2012**, *41*, 1519–1537.

[25] Fort, D. A.; Remsing, R. C.; Swatloski, R. P.; Moyna, P.; Moyna, G.; Rogers, R. D. *Green Chem.* **2007**, *9*, 63–69.

[26] Brandt, A.; Gräsvik, J.; Hallett, J. P.; Welton, T. *Green Chem.* **2013**, *15*, 550–583.

[27] Galiński, M.; Lewandowski, A.; Stepniak, I. *Electrochim. Acta* **2006**, *51*, 5567–5580.

[28] Buzzeo, M. C.; Evans, R. G.; Compton, R. G. *ChemPhysChem* **2004**, *5*, 1106–1120.

[29] Ohno, H. *Electrochemical aspects of ionic liquids*; John Wiley & Sons, 2011.

[30] Wang, P.; Zakeeruddin, S. M.; Comte, P.; Exnar, I.; Grätzel, M. *J. Am. Chem. Soc.* **2003**, *125*, 1166–1167.

[31] Fabregat-Santiago, F.; Bisquert, J.; Palomares, E.; Otero, L.; Kuang, D.; Zakeeruddin, S. M.; Grätzel, M. *J. Phys. Chem. C* **2007**, *111*, 6550–6560.

[32] Wang, P.; Zakeeruddin, S. M.; Exnar, I.; Grätzel, M. *Chem. Comm.* **2002**, 2972–2973.

[33] Wang, P.; Zakeeruddin, S. M.; Moser, J.-E.; Grätzel, M. *J. Phys. Chem. B* **2003**, *107*, 13280–13285.

[34] Ito, S.; Zakeeruddin, S. M.; Comte, P.; Liska, P.; Kuang, D.; Grätzel, M. *Nat. Photonics* **2008**, *2*, 693–698.

[35] Fei, Z.; Kuang, D.; Zhao, D.; Klein, C.; Ang, W. H.; Zakeeruddin, S. M.; Grätzel, M.; Dyson, P. J. *Inorg. Chem.* **2006**, *45*, 10407–10409.

[36] Karadas, F.; Atilhan, M.; Aparicio, S. *Ener. Fuels* **2010**, *24*, 5817–5828.

[37] Anthony, J. L.; Anderson, J. L.; Maginn, E. J.; Brennecke, J. F. *J. Phys. Chem. B* **2005**, *109*, 6366–6374.

[38] Cadena, C.; Anthony, J. L.; Shah, J. K.; Morrow, T. I.; Brennecke, J. F.; Maginn, E. J. *J. Am. Chem. Soc.* **2004**, *126*, 5300–5308.

[39] Wu, W.; Han, B.; Gao, H.; Liu, Z.; Jiang, T.; Huang, J. *Angew. Chem. Int. Ed.* **2004**, *43*, 2415–2417.

[40] Anthony, J. L.; Maginn, E. J.; Brennecke, J. F. *J. Phys. Chem. B* **2002**, *106*, 7315–7320.

[41] Bates, E. D.; Mayton, R. D.; Ntai, I.; Davis, J. H. *J. Am. Chem. Soc.* **2002**, *124*, 926–927.

[42] Zhou, F.; Liang, Y.; Liu, W. *Chem. Soc. Rev.* **2009**, *38*, 2590–2599.

[43] Ye, C.; Liu, W.; Chen, Y.; Yu, L. *Chem. Comm.* **2001**, 2244–2245.

[44] Bermúdez, M.-D.; Jiménez, A.-E.; Sanes, J.; Carrión, F.-J. *Molecules* **2009**, *14*, 2888–2908.

[45] Welton, T. *Chem. Rev.* **1999**, *99*, 2071–2084.

[46] Welton, T. *Coord. Chem. Rev.* **2004**, *248*, 2459–2477.

[47] Gordon, C. M. *Appl. Catal. A* **2001**, *222*, 101–117.

[48] Olivier-Bourbigou, H.; Magna, L. *J. Mol. Catal. A* **2002**, *182*, 419–437.

[49] Han, X.; Armstrong, D. W. *Acc. Chem. Res.* **2007**, *40*, 1079–1086.

[50] Pádua, A. A.; Costa Gomes, M. F.; Canongia Lopes, J. N. *Acc. Chem. Res.* **2007**, *40*, 1087–1096.

[51] Abedin, S. Z. E.; Endres, F. *Acc. Chem. Res.* **2007**, *40*, 1106–1113.

[52] Rebelo, L. P. N.; Lopes, J. N. C.; Esperanca, J. M.; Guedes, H. J.; Łachwa, J.; Najdanovic-Visak, V.; Visak, Z. P. *Acc. Chem. Res.* **2007**, *40*, 1114–1121.

[53] Ohno, H.; Fukumoto, K. *Acc. Chem. Res.* **2007**, *40*, 1122–1129.

[54] Shim, Y.; Jeong, D.; Manjari, S.; Choi, M. Y.; Kim, H. J. *Acc. Chem. Res.* **2007**, *40*, 1130–1137.

[55] Lynden-Bell, R. M.; Del Popolo, M. G.; Youngs, T. G.; Kohanoff, J.; Hanke, C. G.; Harper, J. B.; Pinilla, C. C. *Acc. Chem. Res.* **2007**, *40*, 1138–1145.

[56] Hardacre, C.; Holbrey, J. D.; Nieuwenhuyzen, M.; Youngs, T. G. *Acc. Chem. Res.* **2007**, *40*, 1146–1155.

[57] Del Popolo, M. G.; Kohanoff, J.; Lynden-Bell, R. M.; Pinilla, C. *Acc. Chem. Res.* **2007**, *40*, 1156–1164.

[58] MacFarlane, D. R.; Forsyth, M.; Howlett, P. C.; Pringle, J. M.; Sun, J.; Annat, G.; Neil, W.; Izgorodina, E. I. *Acc. Chem. Res.* **2007**, *40*, 1165–1173.

[59] Iwata, K.; Okajima, H.; Saha, S.; Hamaguchi, H.-o. *Acc. Chem. Res.* **2007**, *40*, 1174–1181.

[60] Smiglak, M.; Metlen, A.; Rogers, R. D. *Acc. Chem. Res.* **2007**, *40*, 1182–1192.

[61] Wang, Y.; Jiang, W.; Yan, T.; Voth, G. A. *Acc. Chem. Res.* **2007**, *40*, 1193–1199.

[62] Maginn, E. J. *Acc. Chem. Res.* **2007**, *40*, 1200–1207.

[63] Anderson, J. L.; Dixon, J. K.; Brennecke, J. F. *Acc. Chem. Res.* **2007**, *40*, 1208–1216.

[64] Castner Jr, E. W.; Wishart, J. F.; Shirota, H. *Acc. Chem. Res.* **2007**, *40*, 1217–1227.

[65] Angell, C. A.; Byrne, N.; Belieres, J.-P. *Acc. Chem. Res.* **2007**, *40*, 1228–1236.

[66] Triolo, A.; Russina, O.; Hardacre, C.; Nieuwenhuyzen, M.; Gonzalez, M. A.; Grimm, H. *J. Phys. Chem. B* **2005**, *109*, 22061–22066.

[67] Triolo, A.; Russina, O.; Bleif, H.-J.; Di Cola, E. *J. Phys. Chem. B* **2007**, *111*, 4641–4644.

[68] Triolo, A.; Russina, O.; Fazio, B.; Triolo, R.; Di Cola, E. *Chem. Phys. Lett.* **2008**, *457*, 362–365.

[69] Russina, O.; Triolo, A.; Gontrani, L.; Caminiti, R. *J. Phys. Chem. Lett.* **2011**, *3*, 27–33.

[70] Hunt, P. A.; Kirchner, B.; Welton, T. *Chem. Eur. J.* **2006**, *12*, 6762–6775.

[71] Nockemann, P.; Thijs, B.; Pittois, S.; Thoen, J.; Glorieux, C.; Van Hecke, K.; Van Meervelt, L.; Kirchner, B.; Binnemans, K. *J. Phys. Chem. B* **2006**, *110*, 20978–20992.

[72] Zhao, W.; Leroy, F.; Heggen, B.; Zahn, S.; Kirchner, B.; Balasubramanian, S.; Muller-Plathe, F. *J. Am. Chem. Soc.* **2009**, *131*, 15825–15833.

[73] Thar, J.; Brehm, M.; Seitsonen, A. P.; Kirchner, B. *J. Phys. Chem. B* **2009**, *113*, 15129–15132.

[74] Hunt, P. A.; Gould, I. R.; Kirchner, B. *Aus. J. Chem.* **2007**, *60*, 9–14.

[75] Bhargava, B. L.; Balasubramanian, S.; Klein, M. L. *Chem. Comm.* **2008**, 3339–3351.

[76] Bhargava, B.; Balasubramanian, S. *J. Chem. Phys.* **2007**, *127*, 114510_1–114510_6.

[77] Bhargava, B. L.; Devane, R.; Klein, M. L.; Balasubramanian, S. *Soft Matter* **2007**, *3*, 1395–1400.

[78] Bhargava, B.; Balasubramanian, S. *J. Chem. Phys.* **2005**, *123*, 144505.

[79] Chandran, A.; Prakash, K.; Senapati, S. *Chem. Phys.* **2010**, *374*, 46–54.

[80] Annapureddy, H. V.; Kashyap, H. K.; De Biase, P. M.; Margulis, C. J. *J. Phys. Chem. B* **2010**, *114*, 16838–16846.

[81] Kashyap, H. K.; Biswas, R. *J. Phys. Chem. B* **2009**, *114*, 254–268.

[82] Kashyap, H. K.; Biswas, R. *J. Phys. Chem. B* **2008**, *112*, 12431–12438.

[83] Kashyap, H. K.; Biswas, R. *J. Phys. Chem. B* **2010**, *114*, 16811–16823.

[84] Kashyap, H. K.; Annapureddy, H. V.; Raineri, F. O.; Margulis, C. J. *J. Phys. Chem. B* **2011**, *115*, 13212–13221.

[85] Kashyap, H. K.; Hettige, J. J.; Annapureddy, H. V.; Margulis, C. J. *Chem. Comm.* **2012**, *48*, 5103–5105.

[86] Anil, K. *Pure Appl. Chem.* **2008**, *80*, 1267–1279.

[87] Cammarata, L.; Kazarian, S.; Salter, P.; Welton, T. *Phys. Chem. Chem. Phys.* **2001**, *3*, 5192–5200.

[88] Bhargava, B.; Klein, M. L. *J. Phys. Chem. A* **2008**, *113*, 1898–1904.

[89] Palchowdhury, S.; Bhargava, B. *J. Phys. Chem. B 118*, 6241–6249.

[90] Kumar, M.; Venkatnathan, A. *J. Phys. Chem. B* **2013**, *117*, 14449–14456.

[91] Shukla, S. K.; Kumar, A. *Chem. Phys. Lett.* **2013**, *566*, 12–16.

[92] Sunda, A. P.; Dhavale, V. M.; Kurungot, S.; Venkatnathan, A. *J. Phys. Chem. B* **2014**, *118*, 1831–1838.

[93] Rai, G.; Kumar, A. *J. Phys. Chem. B* **2014**, *118*, 4160–4168.

[94] Kirchner, B. *Ionic liquids*; Springer, 2009; Vol. 290.

[95] Freemantle, M. *An introduction to ionic liquids*; Royal Society of Chemistry, 2010.

[96] Seki, S.; Kobayashi, T.; Kobayashi, Y.; Takei, K.; Miyashiro, H.; Hayamizu, K.; Tsuzuki, S.; Mitsugi, T.; Umebayashi, Y. *J. Mol. Liq.* **2010**, *152*, 9 – 13.

[97] Tokuda, H.; Hayamizu, K.; Ishii, K.; Susan, M. A. B. H.; Watanabe, M. *J. Phys. Chem. B* **2004**, *108*, 16593–16600.

[98] Tokuda, H.; Hayamizu, K.; Ishii, K.; Susan, M. A. B. H.; Watanabe, M. *J. Phys. Chem. B* **2005**, *109*, 6103–6110.

[99] Tokuda, H.; Ishii, K.; Susan, M. A. B. H.; Tsuzuki, S.; Hayamizu, K.; Watanabe, M. *J. Phys. Chem. B* **2006**, *110*, 2833–2839.

[100] Rogers, R. D.; Seddon, K. R.; Volkov, S. *Green industrial applications of ionic liquids*; Springer, 2002; Vol. 92.

[101] Holbrey, J. D.; Reichert, W. M.; Nieuwenhuyzen, M.; Sheppard, O.; Hardacre, C.; Rogers, R. D. *Chem. Comm.* **2003**, 476–477.

[102] Hussey, C. L. *Pure Appl. Chem.* **1988**, *60*, 1763.

[103] Zhou, T.; Chen, L.; Ye, Y.; Chen, L.; Qi, Z.; Freund, H.; Sundmacher, K. *Ind. Eng. Chem. Res.* **2012**, *51*, 6256–6264.

[104] Cole, A. C.; Jensen, J. L.; Ntai, I.; Tran, K. L. T.; Weaver, K. J.; Forbes, D. C.; Davis, J. H. *J. Amer. Chem. Soc.* **2002**, *124*, 5962–5963.

[105] MacFarlane, D. R.; Pringle, J. M.; Johansson, K. M.; Forsyth, S. A.; Forsyth, M. *Chem. Comm.* **2006**, 1905–1917.

[106] Vicente, J. A.; Mlonka, A.; Gunaratne, H. Q. N.; Swadzba-Kwasny, M.; Nockemann, P. *Chem. Comm.* **2012**, *48*, 6115–6117.

[107] H. Davis, J., Jr *Chem. lett.* **2004**, *33*, 1072–1077.

[108] Giernoth, R. *Angew. Chem. Int. Ed.* **2010**, *49*, 2834–2839.

[109] Fredlake, C. P.; Crosthwaite, J. M.; Hert, D. G.; Aki, S. N. V. K.; Brennecke, J. F. *J. Chem. Eng. Data* **2004**, *49*, 954–964.

[110] Bonhote, P.; Dias, A.-P.; Papageorgiou, N.; Kalyanasundaram, K.; Grätzel, M. *Inorg. Chem.* **1996**, *35*, 1168–1178.

[111] G. Huddleston, J.; D. Rogers, R. *Chem. Comm.* **1998**, 1765–1766.

[112] Marsh, K.; Boxall, J.; Lichtenthaler, R. *Fluid Phase Equilib.* **2004**, *219*, 93–98.

[113] Okoturo, O. O.; VanderNoot, T. J. *J. Electroanal. Chem.* **2004**, *568*, 167–181.

[114] Harris, K. R.; Woolf, L. A.; Kanakubo, M. *J. Chem. & Eng. Data* **2005**, *50*, 1777–1782.

[115] Perry, R. L.; Jones, K. M.; Scott, W. D.; Liao, Q.; Hussey, C. L. *J. Chem. & Eng. Data* **1995**, *40*, 615–619.

[116] Seddon, K. R.; Stark, A.; Torres, M.-J. *Pure and Appl. Chem.* **2000**, *72*, 2275–2287.

[117] Mora-Pale, M.; Meli, L.; Doherty, T. V.; Linhardt, R. J.; Dordick, J. S. *Biotech. bioeng.* **2011**, *108*, 1229–1245.

[118] Fujita, K.; MacFarlane, D. R.; Forsyth, M. *Chem. Comm.* **2005**, 4804–4806.

[119] Chandran, A.; Ghoshdastidar, D.; Senapati, S. *J. Am. Chem. Soc.* **2012**, *134*, 20330–20339.

[120] Vijayaraghavan, R.; Izgorodin, A.; Ganesh, V.; Surianarayanan, M.; MacFarlane, D. R. *Angew. Chem. Int. Ed.* **2010**, *49*, 1631–1633.

[121] Lewandowski, A.; Świderska-Mocek, A. *J. Power Sources* **2009**, *194*, 601–609.

[122] Balducci, A.; Bardi, U.; Caporali, S.; Mastragostino, M.; Soavi, F. *Electrochem. Comm.* **2004**, *6*, 566–570.

[123] Wang, P.; Zakeeruddin, S. M.; Humphry-Baker, R.; Grätzel, M. *Chem. Mater.* **2004**, *16*, 2694–2696.

[124] Niedermeyer, H.; Hallett, J. P.; Villar-Garcia, I. J.; Hunt, P. A.; Welton, T. *Chem. Soc. Rev.* **2012**, *41*, 7780–7802.

[125] H. Davis, J., Jr *Chem. lett.* **2004**, *33*, 1072–1077.

[126] Giernoth, R. *Angew. Chem. Int. Ed.* **2010**, *49*, 2834–2839.

[127] Bates, E. D.; Mayton, R. D.; Ntai, I.; Davis, J. H. *J. Am. Chem. Soc.* **2002**, *124*, 926–927.

[128] Camper, D.; Scovazzo, P.; Koval, C.; Noble, R. *Ind. Eng. Chem. Res.* **2004**, *43*, 3049–3054.

[129] Ha, S. H.; Menchavez, R. N.; Koo, Y.-M. *Kor. J. Chem. Eng.* **2010**, *27*, 1360–1365.

[130] Giridhar, P.; Venkatesan, K.; Srinivasan, T.; Rao, P. V. *Electrochimica Acta* **2007**, *52*, 3006 – 3012.

[131] Wytze Meindersma, G.; Podt, A. J.; de Haan, A. B. *Fuel Process. Technol.* **2005**, *87*, 59–70.

[132] Zhang, J.; Huang, C.; Chen, B.; Ren, P.; Lei, Z. *Ener. fuels* **2007**, *21*, 1724–1730.

[133] Visser, A. E.; Swatloski, R. P.; Reichert, W. M.; Mayton, R.; Sheff, S.; Wierzbicki, A.; Davis Jr, J. H.; Rogers, R. D. *Chem. Comm.* **2001**, 135–136.

[134] Sheldon, R. *Chem. Comm.* **2001**, 2399–2407.

[135] Bhargava, B. L.; Klein, M. L.; Balasubramanian, S. *ChemPhysChem* **2008**, *9*, 67–70.

[136] Gozzo, F. C.; Santos, L. S.; Augusti, R.; Consorti, C. S.; Dupont, J.; Eberlin, M. N. *Chem. Eur. J.* **2004**, *10*, 6187–6193.

[137] DaSilveira Neto, B. A.; Santos, L. S.; Nachtigall, F. M.; Eberlin, M. N.; Dupont, J. *Angew. Chem.* **2006**, *118*, 7409–7412.

[138] Canongia Lopes, J. N.; Pádua, A. A. *J. Phys. Chem. B* **2006**, *110*, 3330–3335.

[139] Del Pópolo, M. G.; Voth, G. A. *J. Phys. Chem. B* **2004**, *108*, 1744–1752.

[140] Hao, J.; Zemb, T. *Curr. Opin. Coll. Interface Sci.* **2007**, *12*, 129–137.

[141] Atkin, R.; Warr, G. G. *J. Phys. Chem. B* **2008**, *112*, 4164–4166.

[142] Raju, S. G.; Balasubramanian, S. *J. Mater. Chem.* **2009**, *19*, 4343–4347.

[143] Ichikawa, T.; Yoshio, M.; Hamasaki, A.; Mukai, T.; Ohno, H.; Kato, T. *J. Am. Chem. Soc.* **2007**, *129*, 10662–10663.

[144] Holbrey, J. D.; Seddon, K. R. *Dalton Trans.* **1999**, 2133–2140.

[145] Bodo, E.; Gontrani, L.; Caminiti, R.; Plechkova, N. V.; Seddon, K. R.; Triolo, A. *J. Phys. Chem. B* **2010**, *114*, 16398–16407.

[146] Russina, O.; Triolo, A.; Gontrani, L.; Caminiti, R.; Xiao, D.; Hines Jr, L. G.; Bartsch, R. A.; Quitevis, E. L.; Plechkova, N.; Seddon, K. R. *J. Phys. Condens. Matter* **2009**, *21*, 424121.

[147] Triolo, A.; Russina, O.; Fazio, B.; Appetecchi, G. B.; Carewska, M.; Passerini, S. *J. Chem. Phys.* **2009**, *130*, 164521–164521.

[148] Ott, L. S.; Cline, M. L.; Deetlefs, M.; Seddon, K. R.; Finke, R. G. *J. Am. Chem. Soc.* **2005**, *127*, 5758–5759.

[149] Schröder, U.; Wadhawan, J. D.; Compton, R. G.; Marken, F.; Suarez, P. A.; Consorti, C. S.; de Souza, R. F.; Dupont, J. *New J. Chem.* **2000**, *24*, 1009–1015.

[150] Dupont, J. *J. Braz. Chem. Soc.* **2004**, *15*, 341–350.

[151] Aoun, B.; Goldbach, A.; González, M. A.; Kohara, S.; Price, D. L.; Saboungi, M.-L. *J. Chem. Phys.* **2011**, *134*, 104509.

[152] Wang, Y.; Voth, G. A. *J. Am. Chem. Soc.* **2005**, *127*, 12192–12193.

[153] Wang, Y.; Voth, G. A. *J. Phys. Chem. B* **2006**, *110*, 18601–18608.

[154] Del Pópolo, M. G.; Lynden-Bell, R. M.; Kohanoff, J. *J. Phys. Chem. B* **2005**, *109*, 5895–5902.

[155] Dong, K.; Zhang, S.; Wang, D.; Yao, X. *J. Phys. Chem. A* **2006**, *110*, 9775–9782.

[156] Diedrichs, A.; Gmehling, J. *Fluid Phase Equilib.* **2006**, *244*, 68–77.

[157] Fredlake, C. P.; Crosthwaite, J. M.; Hert, D. G.; Aki, S. N.; Brennecke, J. F. *J. Chem. Eng. Data* **2004**, *49*, 954–964.

[158] Xiao, D.; Rajian, J. R.; Cady, A.; Li, S.; Bartsch, R. A.; Quitevis, E. L. *J. Phys. Chem. B* **2007**, *111*, 4669–4677.

[159] Hyun, B.-R.; Dzyuba, S. V.; Bartsch, R. A.; Quitevis, E. L. *J. Phys. Chem. A* **2002**, *106*, 7579–7585.

[160] Turton, D. A.; Hunger, J.; Stoppa, A.; Hefter, G.; Thoman, A.; Walther, M.; Buchner, R.; Wynne, K. *J. Am. Chem. Soc.* **2009**, *131*, 11140–11146.

[161] Triolo, A.; Mandanici, A.; Russina, O.; Rodriguez-Mora, V.; Cutroni, M.; Hardacre, C.; Nieuwenhuyzen, M.; Bleif, H.-J.; Keller, L.; Ramos, M. A. *The Journal of Physical Chemistry B* **2006**, *110*, 21357–21364.

[162] Laage, D. *J. Phys. Chem. B* **2009**, *113*, 2684–2687.

[163] Fumino, K.; Wulf, A.; Ludwig, R. *Angew. Chem. Int. Ed.* **2008**, *47*, 3830–3834.

[164] Dominguez-Vidal, A.; Kaun, N.; Ayora-Cañada, M. J.; Lendl, B. *J. Phys. Chem. B* **2007**, *111*, 4446–4452.

[165] Lassegues, J.; Grondin, J.; Holomb, R.; Johansson, P. *J. Raman Spectrosc.* **2007**, *38*, 551–558.

[166] Crosthwaite, J. M.; Muldoon, M. J.; Dixon, J. K.; Anderson, J. L.; Brennecke, J. F. *J. Chem. Thermodyn.* **2005**, *37*, 559–568.

[167] Tokuda, H.; Hayamizu, K.; Ishii, K.; Susan, M. A. B. H.; Watanabe, M. *J. Phys. Chem. B* **2005**, *109*, 6103–6110.

[168] Shobukawa, H.; Tokuda, H.; Tabata, S.-I.; Watanabe, M. *Electrochim. Acta* **2004**, *50*, 305–309.

[169] Every, H. A.; Bishop, A. G.; MacFarlane, D. R.; Orädd, G.; Forsyth, M. *Phys. Chem. Chem. Phys.* **2004**, *6*, 1758–1765.

[170] Fannin Jr, A. A.; Floreani, D. A.; King, L. A.; Landers, J. S.; Piersma, B. J.; Stech, D. J.; Vaughn, R. L.; Wilkes, J. S.; Williams John, L. *J. Phys. Chem.* **1984**, *88*, 2614–2621.

[171] Vila, J.; Gines, P.; Pico, J.; Franjo, C.; Jimenez, E.; Varela, L.; Cabeza, O. *Fluid Phase Equilib.* **2006**, *242*, 141–146.

[172] Leys, J.; Wübbenhorst, M.; Menon, C. P.; Rajesh, R.; Thoen, J.; Glorieux, C.; Nockemann, P.; Thijs, B.; Binnemans, K.; Longuemart, S. *J. Chem. Phys.* **2008**, *128*, 064509.

[173] Kelkar, M. S.; Maginn, E. J. *The Journal of Physical Chemistry B* **2007**, *111*, 4867–4876.

[174] Köddermann, T.; Paschek, D.; Ludwig, R. *ChemPhysChem* **2007**, *8*, 2464–2470.

[175] Mondal, A.; Balasubramanian, S. *J. Chem. Eng. Data* **2014**, 3061–3068.

[176] Kohanoff, J. *Electronic structure calculations for solids and molecules*; Cambridge University Press, 2006.

[177] Szabo, A.; Ostlund, N. S. *Modern quantum chemistry: introduction to advanced electronic structure theory*; Courier Dover Publications, 2012.

[178] Hohenberg, P.; Kohn, W. *Phys. Rev.* **1964**, *136*, B864–B871.

[179] Kohn, W.; Sham, L. J. *Phys. Rev.* **1965**, *140*, A1133–A1138.

[180] Verlet, L. *Phys. Rev.* **1967**, *159*, 98–103.

[181] Ewald, P. P. *Annalen der Physik* **1921**, *369*, 253–287.

[182] Car, R.; Parrinello, M. *Phys. Rev. lett.* **1985**, *55*, 2471.

[183] Plimpton, S. *J. Comput. Phys.* **1995**, *117*, 1 – 19.

[184] Humphrey, W.; Dalke, A.; Schulten, K. *J. Mol. Graph.* **1996**, *14*, 33–38.

[185] Stone, J. *An Efficient Library for Parallel Ray Tracing and Animation*. M.Sc. thesis, Computer Science Department, University of Missouri-Rolla, 1998.

[186] Hutter, J.; Iannuzzi, M.; Schiffmann, F.; VandeVondele, J. *Wiley Interdisciplinary Reviews: Computat. Mol. Sci.* **2014**, *4*, 15–25.

[187] Frisch, M. J. et al. Gaussian 03, Revision C.02. Gaussian, Inc., Wallingford, CT, 2004.

[188] Frisch, M. J. et al. Gaussian 09, Revision D.01. Gaussian Inc. Wallingford CT 2009.

Chapter 2

Dissolution of lignocellulosic biomass in room temperature ionic liquids: cluster calculations*

2.1 Introduction

With increase in the human population, the consumption of energy has increased enormously. Most of our energy requirement is dependent on the use of fossil fuels. Non-renewability of these fossil fuels in near future will lead to an energy crisis. This is one of the most important challenges that our society is facing today. In order to overcome this situation, we should focus on alternate sources of energy that can reduce the use of fossil fuels. Some of the most important alternatives are solar energy, wind energy, hydrothermal energy *etc.* Apart from these, lignocellulosic biomass may also be used as an alternate source of energy [1–3]. Lignocellulosic biomass is abundant in form of plant waste. This biomass chiefly consist of three main componenets, cellulose (40-50 %), hemicellulose (20-30 %) and lignin (20-30

*Work reported in this chapter is published in: R. S. Payal, R. Bharath, G, Periyasamy and S. Balasubramanian, J. Phys. Chem. B **116**, 833-840 (2012). Reproduced by permission of The American Chemical Society (ACS). Copyright 2012, American Chemical Society.

%) [4–6]. Among these three, cellulose is crystalline in nature, while hemicellulose and lignin are amorphous. Chemical processing of biomass involves various steps. One of the most important and difficult task is to dissolve this lignocellulosic biomass. Lignocellulosic biomass is insoluble in conventional solvents like water or ethanol *etc.* Dissolving it requires harsh conditions e.g. acid pretreatment, high temperature *etc.* These methods and solvent used in these processes are not environment friendly.

Cellulose and hemicellulose are polysaccharides, present in plant cell wall with β(1-4) linked backbones in an equatorial configuration [7–9]. Although both are polysaccharides, cellulose is a crystalline polymer with a highly ordered structure whereas hemicellulose is amorphous with a random structure, and many of them contains xylan backbone. In cellulose, cellobiose units are connected to one another via strong inter- and intramolecular hydrogen bonding networks (Figure 2.1(a)), thus providing it and the cell wall, high chemical and mechanical stability. However, amorphous hemicellulose (Figures 2.1(b)) stabilizes the cell wall by interacting with neighboring hemicellulose, cellulose, or lignin units.

Many research groups have attempted to dissolve lignocellulosic materials in common organic solvents at various physical conditions [9–16]. Some of the solvents such as N-methylmorpholine-N-oxide monohydrate, N,N-dimethylacetate/LiCl and $LiClO_4.3H_2O$ have been shown to dissolve cellulose upto 15-20 % of weight of lignocellulosic biomass. However these solvents have disadvantages like toxicity, instability or high cost *etc* [9–17]. To overcome these issues, Rogers and coworkers [18] for the first time, demonstrated that room temperature ionic liquids (RTILs) can dissolve cellulose under mild conditions. Also the fact that these RTILs are environmental friendly make them a better choice over conventional solvents. They were able to regenerate the dissolved cellulose by addition of water. In some of the recent studies people, have reported that RTILs can dissolve wood directly, without any pretreatment [19]. It has been reported that RTILs belonging to dialkylimidazolium family

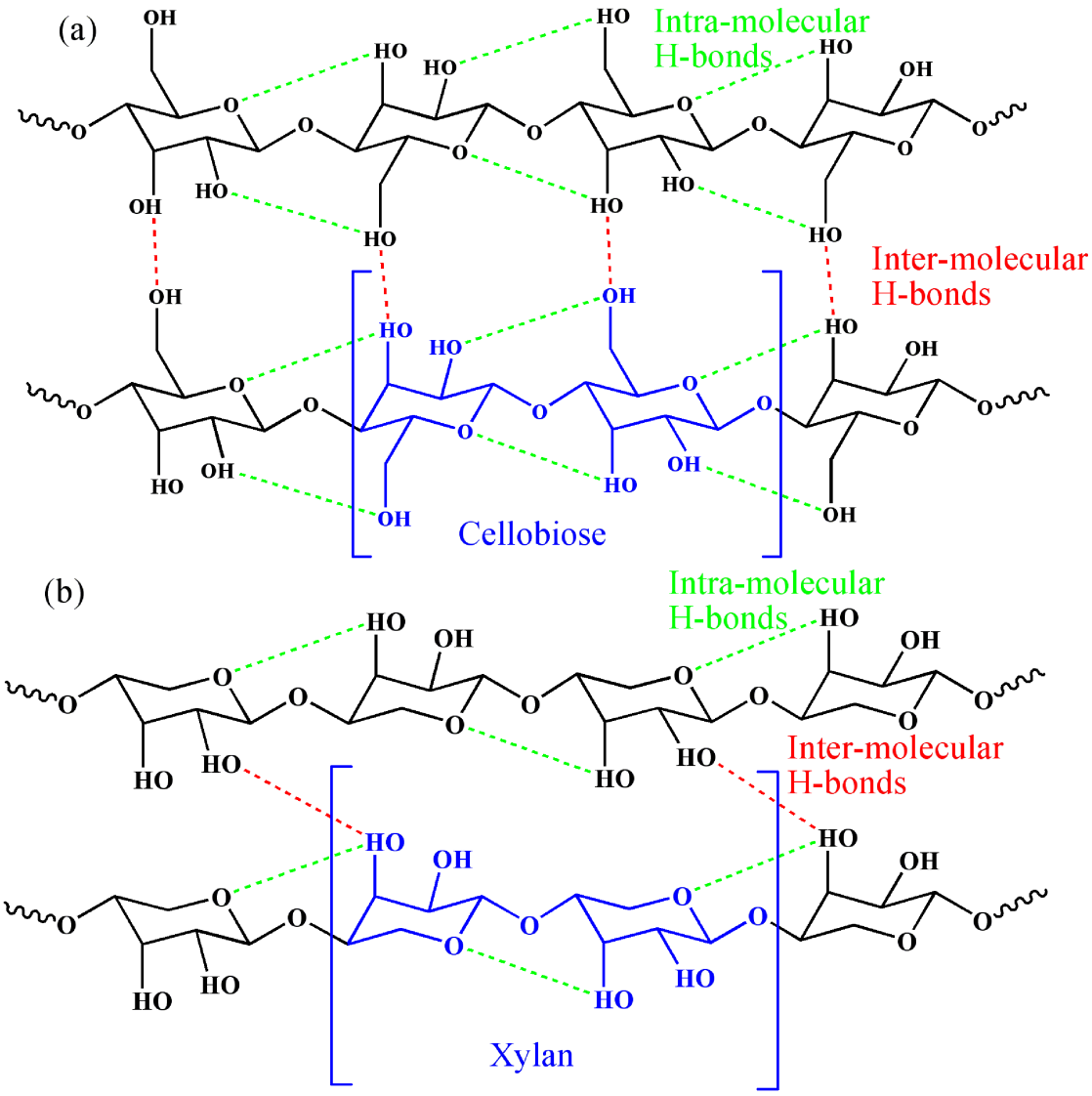

Figure 2.1: Schematic representation of (a) cellulose and (b) hemicellulose. Monomer units of cellulose and hemicellulose, cellobiose and xylan are shown in blue color. Inter- and intramolecular hydrogen bonds are also shown.

(see Table 2.1) such as 1-*n*-butyl-3-methylimidazolium chloride ([C_4mim][Cl]) can dissolve cellulose and other polysaccharide in high concentration with no derivization at high temperature [19]. In addition, hemicellulose has also been dissolved in RTILs. The solubility of cellulose and hemicellulose in various RTILs at ambient conditions is reported in Table 2.1

RTILs with imidazolium cation and acetate anion has shown good wood solubility at room temperature [25–27]. Although it is known that RTILs are best solvents

Table 2.1: Various RTILs and their corresponding cellulose and hemicellulose solubility.

RTIL	Celluose solubility (wt %)	Hemicellulose solubility (wt %)
$[C_4mim][CH_3COO]$	15.5-20.5 [20, 21]	10.0 [17]
$[C_4mim][HSCH_2COO]$	13.5 [22, 23]	-
$[C_4mim][HCOO]$	12.5 [24]	-
$[C_4mim][C_6H_3COO]$	12.0 [23]	-
$[C_4mim][H_2NCH_2COO]$	10.5 [23]	-
$[C_4mim][CH_3CHOHCOO]$	9.5 [23]	-

for biomass, the mechanism of dissolution continues to be a matter of study [1, 28–34]. Computational efforts are certainly poised to offer deep insight into the process of dissolution. The nature of solvent-solute interactions can be probed at the moleculat level using computer simulations. Such a fundamental understanding of the solute-slvent interaction will help in designing better solvents. The specific role of individual ions of RTILs can also be understood through computer simulations.

Gas phase, quantum chemical calculations on cellobiose [35] interacting with one ion pair [36, 37] or only with cation or anion [38, 39] have been reported. Studies revealed that the binding affinity of cellobiose with the anion was 6-10 kcal/mol larger as compared to that with the cation [37]. Also, classical MD simulations of cellulose soaked in RTILs have also been previously reported [40, 41]. However, there is no report on implicit and explicit solvation of cellobiose with RTILs. This is one of the major objective of this study. Also, there are no reports on computational study of dissolution of hemicellulose in RTILs. It is believed that comparison between cellulose and hemicellulose can shed light on various parameters that effect dissolution mechanism. This kind of approach is not only feasible but can also provide an understanding on polarization and H-bonding interactions between solute and RTILs. Insight obtained thus on structural and electronic factors contributing to the dissolution mechanism can be helpful to further increase the solubility of cellobiose and xylan in RTILs. Since cellulose and hemicellulose exhibit polymorphism [42], understanding the effect of structure on dissolution becomes more important. The

relative stability of the conformers can influence the dissolution process.

The current chapter focuses on obtaining various ground state conformers (and configurations) of monomeric units of cellulose and hemicellulose in gas phase, implicit solvent and explicit RTIL media. The lowest energy structures were validated by comparing the computed ^{1}H and ^{13}C NMR chemical shielding values with corresponding experimental data [43, 44].

2.2 Computational details

Cellobiose (Figure 2.2(a)) and xylan (Figure 2.2(b)) are considered as models for cellulose and hemicellulose, respectively. There are many chiral centers in cellobiose and xylan, which leads to many conformers. Herein, the conformers of cellobiose were considered based on three important dihedral angles, which are: ω(O6-C6-C6′-O6′), ϕ(C5-C1-O4′-C4′) and ψ(C1-O4′-C4′-C5′). Similarly, the dihedral angles Ω (C1-O4′-C4′-C5′) and Φ(O5-C1-O4′-C4′) were considered for xylan. All the dihedral angles were varied from 0° to 180° in steps of 10° to identify the minimum energy structures.

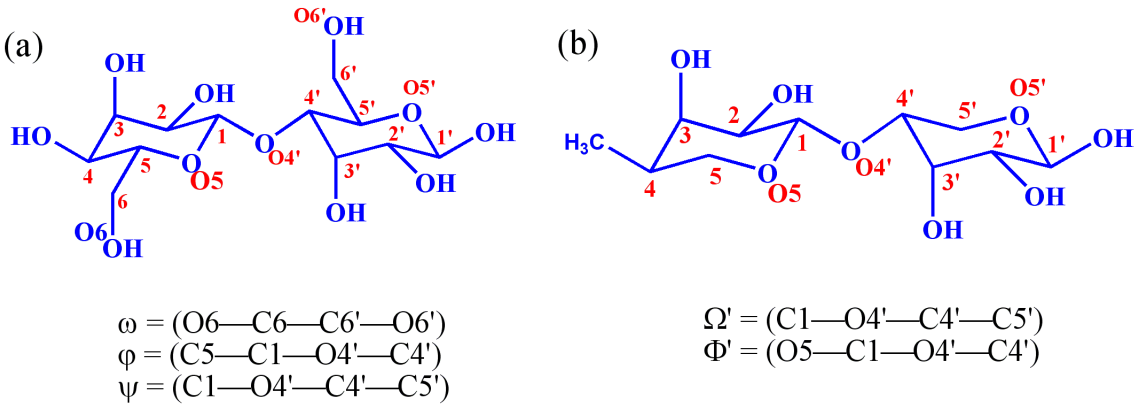

Figure 2.2: Schematic representation of (a) cellobiose and (b) xylan structures are shown. The numbering scheme and the dihedrals considered for the work are also shown.

The use of atom centered basis functions together with diffused and polarized basis sets for all atoms and hybrid functional has been well established for these

kinds of systems [45–49]. However, this approach becomes increasingly expensive because of the computation of the multicenter electron integrals. It was found to be computationally more efficient to resort to a plane wave expansion combined with pseudopotentials, as implemented in, for example, the ab initio molecular dynamics package, CPMD [50]. Hence, some of the initial geometry optimizations were carried out using this code. Thus, the plane wave code was used to screen structures and the final optimizations were carried out using the Gaussian code [51]. In the former calculations, the PerdewBurkeErnzerhof [52] (PBE) exchange-correlation functional was employed with an energy cutoff for the wave function of 85 Ry. The effect of core electrons and the nuclei on the valence electrons were treated using Troullier-Martins pseudopotentials [53]. The optimizations were performed with tight energy convergence criterion and the maximum magnitude of the force on any ion was demanded to be less than 10^{-5} a. u. The optimizations were carried out in a cubic box of edge length 16.0 Å. Cluster boundary conditions and the Hockney-Poisson solver consistent with calculations for an isolated system were employed [54]. The four lowest energy conformers found in the plane wave approach were further optimized using B3LYP hybrid exchange and correlation functional [55–57] with 6-31++G(d,p) atomic center basis set as implemented in the Gaussian 03 program [51]. It is noteworthy that the energy ranking of these structures as obtained from the PBE/85 Ry and the B3LYP/6-31++G(d,p) calculations matched. Similar methods have been adopted by other workers in the quantum modeling of ion pairs of RTILs and systems similar to those studied here [58–61]. Local properties of the system, such as NMR chemical shielding values and local atomic charges were calculated using the Gaussian code. The optimized structures in gas phase and implicit solvation media were characterized as minima on the basis of calculation of their harmonic vibrational frequencies and no imaginary frequencies were observed. All the results reported here were obtained from the B3LYP/6-31++G(d,p) set of calculations.

Although both implicit and explicit solvation media were considered for cellobiose in order to understand the effect of three solvents-water, methanol, and RTIL the calculations for xylan under explicit solvent conditions were carried out only with the RTIL. Implicit solvent calculations were carried out using the polarized continuum model (PCM) approach as implemented in the Gaussian 03 program. This provides the effect of electrostatic interactions alone on the solubility of molecules. In these calculations, the dielectric constants of water, methanol, and the RTIL were taken as 80, 33, and 11, respectively. The effect due to hydrogen bonding (and any other specific) interaction between the solvent molecules and the cellobiose unit was also studied by explicitly surrounding the cellobiose unit with layer(s) of solvent molecules. Initially, various configurations of solvent molecules around the lowest energy gas phase conformers of cellobiose and xylan were studied using plane wave approach as the CPMD code scaled well. Four low energy configurations were further optimized in the atom centered basis set approach. Although in the case of water and methanol 19 molecules were considered to form the solvent layer, for the case of the RTIL, seven molecules of ([C_1mim][OAc]) were explicitly considered to surround the cellobiose unit. As mentioned earlier, calculations with explicit solvent molecules for xylan were carried out only with the RTIL. Here again, seven ion pairs were included. The number of ion pairs was chosen based on the reported experimental NMR studies [43]. Since water and methanol molecules are smaller in size as compared to a RTIL ion pair, more number of solvent molecules are required to solvate cellobiose completely (cation>anion$\sim$methanol>water). However, smaller size can be an advantage, as solvent molecules can approach cellobose closer; other factors such as the binding strength of a molecule with cellobiose also play a vital role in the dissolution mechanism. Such cluster calculations, mimicking the effect of the solvent have been carried out for other systems [62]. All the molecular properties were calculated at the same level of theory and using the Gaussian 03 program

package. ^{1}H and ^{13}C NMR chemical shielding values were calculated using the gauge including atomic orbital (GIAO) method [63–67]. The molecular structure of ion pair is shown in Figure 2.3.

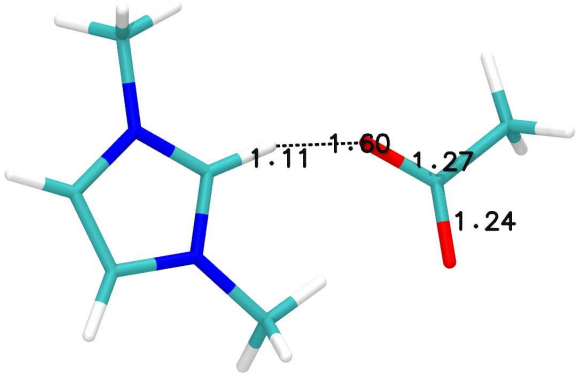

Figure 2.3: Optimized structure of [C_1mim][OAc] ion pair with important bond distances (Å) shown. Color Carbon : Cyan, Nitrogen : Blue, Oxygen : Red and Hydrogen : White.

2.3 Results and discussion

2.3.1 Low energy conformers of cellobiose in the gas phase

Density functional theory based computations have been carried out to identify low energy conformers of cellobiose in the gas phase. Among the various structures, the anti-anti and anti-syn conformers are highly stable with the maximum number of intramolecular H-bonds (see Figure 2.4). The presence of an additional H-bond stabilizes the anti-anti conformer by 4.53 kcal/mol(table 2.2) relative to the anti-syn one.

The presence and the strength of H-bonds red shifts the -OH (covalent bond) stretching frequency when compared with that for free -OH (i.e., -OH without the H-bonding interaction) in the same molecule. For example, in the anti-anti conformer, three different -OH stretching frequencies were observed: 3721 cm^{-1} (for O3′-H3′), 3785-3826 cm^{-1} (for O2-H2, O2′-H2′, O3-H3, O1′-H1′) and 3845-3850 cm^{-1} (O6-H6, O6′-H6′, O4-H4) (table 2.3). These are consistent with the magnitude of the H-bond

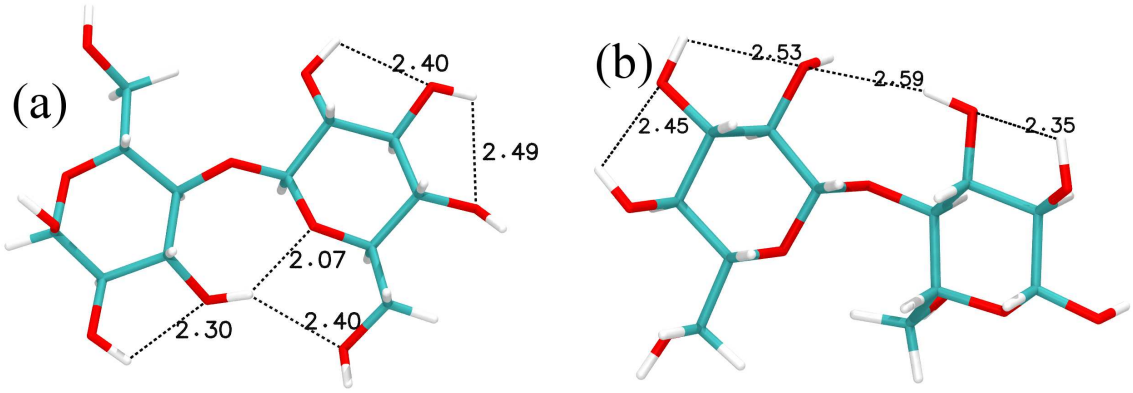

Figure 2.4: Computed two lowest energy conformers of cellobiose in gas phase. H-bonds are shown as dotted lines and their lengths (Å) are indicated. Color scheme same as previous figure.

strength of the OH donors, which are O3′-H3′ > O2-H2 ≈ O2′-H2′ ≈ O3-H3 ≈ O1′-H1′ > O6-H6 ≈ O6′-H6′ ≈ O4-H4 and also reflected in the bond distances as shown in Figure 2.4. Similarly, two types of -OH stretching modes were observed for the anti-syn conformer with respect to their H-bond formation ability.

Room temperature ^{1}H and ^{13}C NMR data of synthetic cellobiose analogues and of [C_2mim][OAc] have been reported in DMSO-d6 solvent at different mole fractions [43, 44]. However, chemical shift values were discussed only for specific atoms due to experimental difficulties. It would thus be useful for us to validate our computational work against these experimental data. The calculated ^{1}H NMR chemical shift values of 2-5 ppm for the H-bonded -OH and ^{13}C NMR values 55-95 ppm for the anti-anti conformer are comparable to the experimental ^{1}H (3-5 ppm) and ^{13}C NMR values (49-91 ppm) of cellobiose synthetic analogues. In contrast, the corresponding values for the anti-syn conformer are ^{1}H, 1.5-2.5 ppm and ^{13}C, 52-90 ppm (table 2.5) [68, 69]. Minor differences in the chemical shift value are likely due to differences in the functional groups between the synthetic analogues and cellobiose and also due to the absence of a solvent environment in these calculations. The presence of one extra H-bond in anti-anti conformer (O3′-H3′—O6) shifted the H3′ ^{1}H NMR value to the downfield (4.65 ppm) than in the anti-syn conformer (2.07 ppm). Furthermore,

the computed energy difference of 4.53 kcal/mol between the anti-anti and anti-syn conformers at the B3LYP/6-31++G(d, p) level is in good agreement with the value of 5 kcal/mol as reported through MP2/6-31G(d) calculations in the gas phase [38]. These data further validate the methods adopted here.

2.3.2 Gas phase structure of xylan

The lowest energy conformers for xylan are analyzed based on the Ω and Φ dihedral angles. In contrast to cellobiose, the two hexose rings in xylan are oriented at 70^o to each other. This prevents the formation of a large number of intramolecular H bonds as in cellobiose. The anti-syn conformers **1** and **2** (shown in Figure 2.5) are lower in energy than the others (anti-anti and syn-syn). The anti-syn conformers differ from each other in the orientation of the -OH groups, which leads to different number of intramolecular H bonds. The larger number of intramolecular H bonds in the anti-syn conformer **2** (panel b of Figure 2.5) stabilizes it by 3.22 kcal/mol (table 2.2) than conformer **1** (panel a of Figure 2.5). Similar to the case of cellobiose, the presence of H-bonding interactions is reflected in the -OH stretching frequencies and ^{1}H NMR values. The presence of both free (i.e., -OH group without any H bonding interaction) as well as H-bonded OH groups in the conformers leads to a large spread of OH stretching frequency ranging from 3770 cm^{-1} to 3820 cm^{-1} (table 2.3). This is also observed in the values of ^{1}H NMR chemical shift which is in the range of 1.87-2.28 ppm for the H-bonded OH group. Extra H-bond in anti-syn conformer **2** shifts the ^{1}H NMR value of the H2$'$ (1.27) atom to downfield more than the anti-syn conformer **1** H2$'$ (0.79). Compared to the values for free OH, these are shifted downfield by 1.0-1.6 ppm (table 2.5).

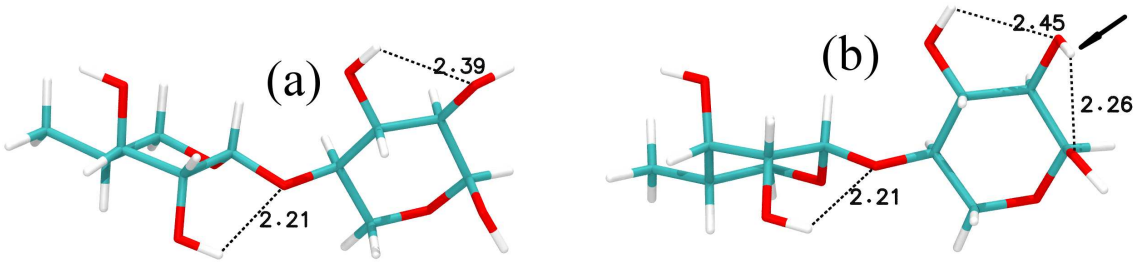

Figure 2.5: Computed two lowest energy conformers of xylan in the gas phase. Hydrogen bonds are shown as dotted lines and their lengths (Å) are indicated. Arrow in the figure marks the difference between two conformers. Color scheme same as previous figures.

Table 2.2: Computed energy differences ΔE between the most stable conformers in gas and implict solvent media

Molecules	Medium	ΔE (kcal/mol)	
		anti-anti	anti-syn
Cellobiose	Gas phase	0.0	4.53
	Implicit solvent RTIL	0.0	1.97
	Water	0.0	1.60
	Methanol	0.0	1.27
		conformer **1**	conformer **2**
Xylan	Gas phase	0.0	3.22
	Implicit solvent RTIL	0.0	2.53
	Water	0.0	1.40
	Methanol	0.0	2.68

2.3.3 Implicit solvation

While gas phase calculations provide details of the structure and hydrogen bonding in the cellulosic units, it will be more appropriate to compare experimental data to a system in which such units are solvated at the same thermodynamic conditions as in experiments. With advancements in simulation methods and computing environments, this is an achievable aim to a large extent through the method of ab initio molecular dynamics simulations. Pending such simulations, in the current work the effect of solvation of cellulosic units through two gas phase quantum techniques: (i) using a dielectric continuum model and (ii) cluster calculations of cellulosic units surrounded by layer(s) of solvent molecules have been studied. In this section, results from the former are discussed.

Table 2.3: Computed OH IR stretching frequency (cm^{-1}) for two lowest energy conformers of cellobiose (Figure 2.4) and xylan (Figure 2.5)

Molecule	Media	conformer	IR frequencuey(cm^{-1})	
			Free OH	H-bonded
Cellobiose	Gas phase	anti-anti	3845-3850	3721-3826
		anti-syn	3746-3818	3691-3712
	Implicit RTIL	anti-anti	3495-3630	3414-3478
		anti-syn	3557-3581	3537-3555
Xylan	Gas phase	conformer **1**	3810-3840	3790-3807
		conformer **2**	3835-3850	3770-3830
	Implicit RTIL	conformer **1**	3810-3840	3780-3820
		conformer **2**	3810-3860	3760-3800

Implicit solvation effects on cellobiose

Four lowest energy conformers of cellobiose obtained from plane wave calculations in the gas phase were further optimized within dielectric media using the atom centered basis set approach (Gaussian 03). The inclusion of the dielectric medium did not affect the order of the stability of the conformers. However, it reduced the energy difference between the stable conformers (see Figures 2.4 and 2.5 for the gas phase structures) by 2.56 kcal/mol (RTIL), 2.93 kcal/mol (water), and 3.02 kcal/mol (methanol) (see Table 2.2). Increasing the dielectric constant decreases the energy difference between the anti-anti and anti-syn conformer by the following amounts: for RTIL (1.97 kcal/mol), methanol (1.60 kcal/mol), and for water (1.27 kcal/mol). The hydrogen bond length is seen to correspondingly increase by 0.01-0.03 Å. The subtle change in the interaction strength is also reflected in the -OH stretching mode and in the ^{1}H NMR chemical shielding values (see Tables 2.3 and 2.5). The -OH stretching mode of anti-anti cellobiose in RTIL is red-shifted by about 200 cm^{-1} relative to the gas phase value. Implicit solvation also changes the ^{1}H NMR chemical shift values of the hydroxyl group upfield by 0.2-0.4 ppm than in the gas phase due to the weakening of H bonds. The computed ^{1}H and ^{13}C NMR chemical shift values for the anti-anti conformer in the implicit solvation media are

in good agreement with experimental values. This provides further evidence for the stability of the anti-anti conformer of cellobiose molecule.

Implicit solvation effects on xylan

Similar to cellobiose, implicit solvation did not affect the conformer stability order of xylan. However, the energy difference between the two conformers was reduced by 0.69 kcal/mol in the implicit presence of the RTIL. For both conformers of xylan, the H-bonded -OH stretching frequencies were red-shifted (3780-3830 cm^{-1} for conformer **1** and 3760-3800 cm^{-1} for conformer **2**) than for the free -OH group (3810-3840 cm^{-1} for conformer **1** and 3810-3860 cm^{-1} for conformer **2**) (see Table 2.3). The polarization effects due to intramolecular H bonds are also clearly reflected in the ^{1}H NMR (2.91-3.74 ppm) and ^{13}C NMR (41.93-105.04 ppm) chemical shielding values, which is shifted upfield by 0.8-2.9 ppm compared with their gas phase values (see Table 2.5).

The implicit solvations studies suggest that a solvent with high polarization could dilute intermolecular H bonds of cellobiose and xylan. To verify this, calculations with explicit solvent molecules need to be carried out. This is the object of the next section.

2.3.4 Explicit solvation effects

An understanding of explicit solvent effects on the energetics and structure of cellobiose and xylan units requires an appreciation of the electrostatics of the molecules involved. Compared with water (oxygen: -0.720 e; hydrogen: 0.36 e) and methanol (oxygen: -0.541 e, hydrogen: 0.340 e), the acetate oxygen (-0.751 e) and the acidic hydrogen of the imidazolium cation (0.527 e) have high negative and positive Mulliken atomic charges respectively. This suggests the higher ability of RTIL to donate or accept H bonds relative to water or methanol. The difference in charge density

Table 2.4: Computed energy differences ΔE between the most stable configurations in explicit RTIL solvent medium

Molecule	RTIL cluster	ΔE (kcal/mol)	Binding energy (kcal/mol)
Cellobiose	configuration **1** (anti-syn conformer)	0.0	-21.10
	configuration **2** (anti-anti conformer)	6.02	-11.05
	configuration **3** (anti-syn conformer)	11.22	-9.98
	configuration **4** (anti-syn conformer)	13.13	-8.07
Xylan	configuration **1** (anti-syn conformer **1**)	0.0	-55.39
	configuration **2** (anti-syn conformer **2**)	16.52	-35.26

between the three solvents is clearly seen in the molecular electrostatic potential maps too (Figure 2.6).

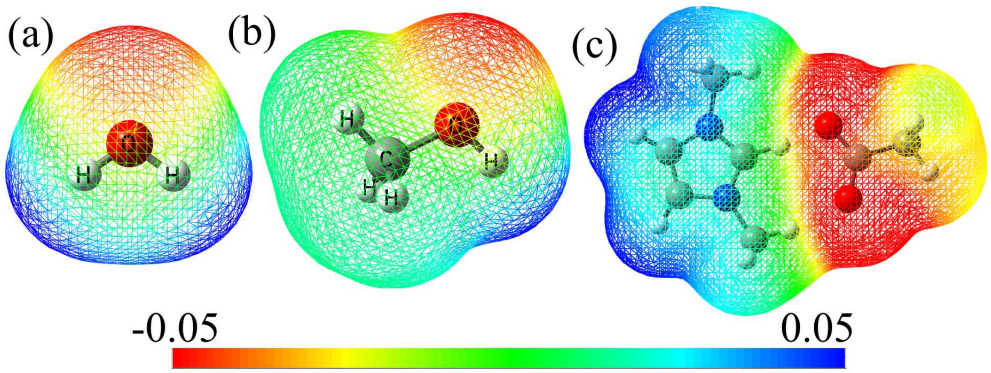

Figure 2.6: Mapping of the molecular electrostatic potential (MEP) on an isocontour of the electron density taken to be 0.04 e bohr^{-1} for (a) water, (b) methanol and (c) [C_1mim][OAc].

Explicit solvation effects: cellobiose

The computed lowest energy conformers in the gas phase for cellobiose were also optimized in the presence of explicit solvent environment. A layer of solvent molecules were added at arbitrary locations around the cellobiose molecule, as an initial configuration for geometry optimization runs. In the optimized configuration, water

and methanol molecules form intermolecular H bonds with cellobiose as shown in Figure 2.7. However, this solvation does not completely break the intramolecular H-bonding between cellobiose moieties. The calculated negative BE values ranging between -10 and -20 kcal/mol reflect the stability of water/methanol solvated cellobiose cluster. The anti-anti conformer is highly stable in both water and methanol media than the anti-syn conformer, similar to its stability in the gas and implicit solvent phases. It was noticed that the small size of the water/methanol molecules allows for all the nineteen solvent molecules to be present in the first coordination shell of cellobiose. Further, intermolecular H-bonding is seen to weaken the intramolecular H bonds, which can decrease the energy difference between the anti-anti and anti-syn conformers by 0.2-0.3 kcal/mol.

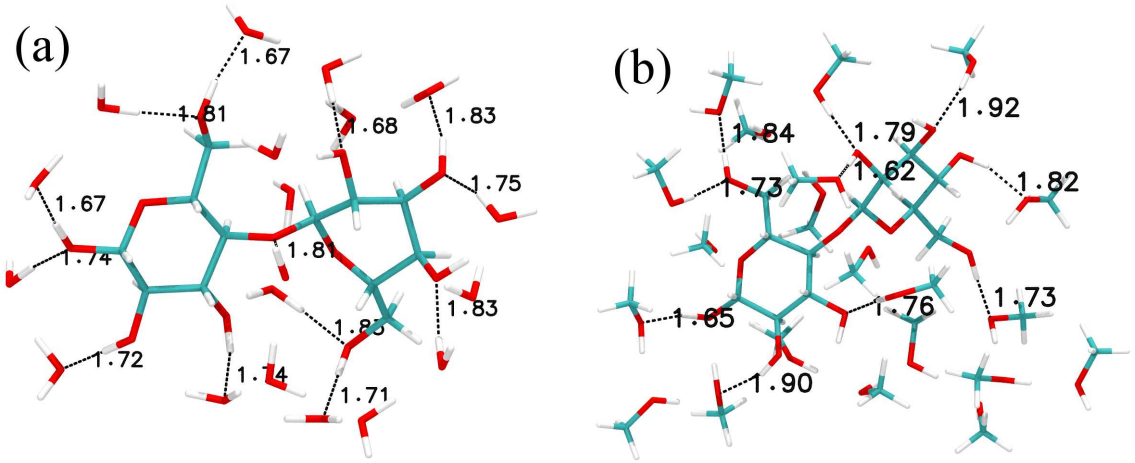

Figure 2.7: Computed lowest energy configuration of cellobiose in (a) water and (b) methanol clusters. Color scheme same as previous figures.

However, the effect on cellobiose due to the explicit solvation by ion pairs of an RTIL is vastly different. In particular, the larger size of the cation and the anion prevents the direct, proximal interaction between every ion and the -OH group of cellobiose. This is clearly reflected in the computed minimum energy geometries of cellobiose which are shown in Figure 2.8. Optimization of cellobiose solvated by ion pairs of $[C_1mim][OAc]$ leads to four low energy configurations, where the cellobiose unit is present in anti-syn configuration **1** (Figure 2.8(a)), anti-anti configuration **2**

(Figure 2.8(b)), anti-syn configuration **3** (Figure 2.8(c)), and anti-syn configuration **4** (Figure 2.8(d)). All four configurations have negative binding energies ranging from -8.07 to -21 kcal/mol (see Table 2.4), which indicates the strong interaction between the ions and cellobiose. The computed BE values in RTIL medium are larger than the corresponding values for water and methanol media. The high H-donating and accepting nature of ion pairs results in the formation of inter-molecular H-bonds and also breaks all the intra-molecular H bonds of cellobiose.

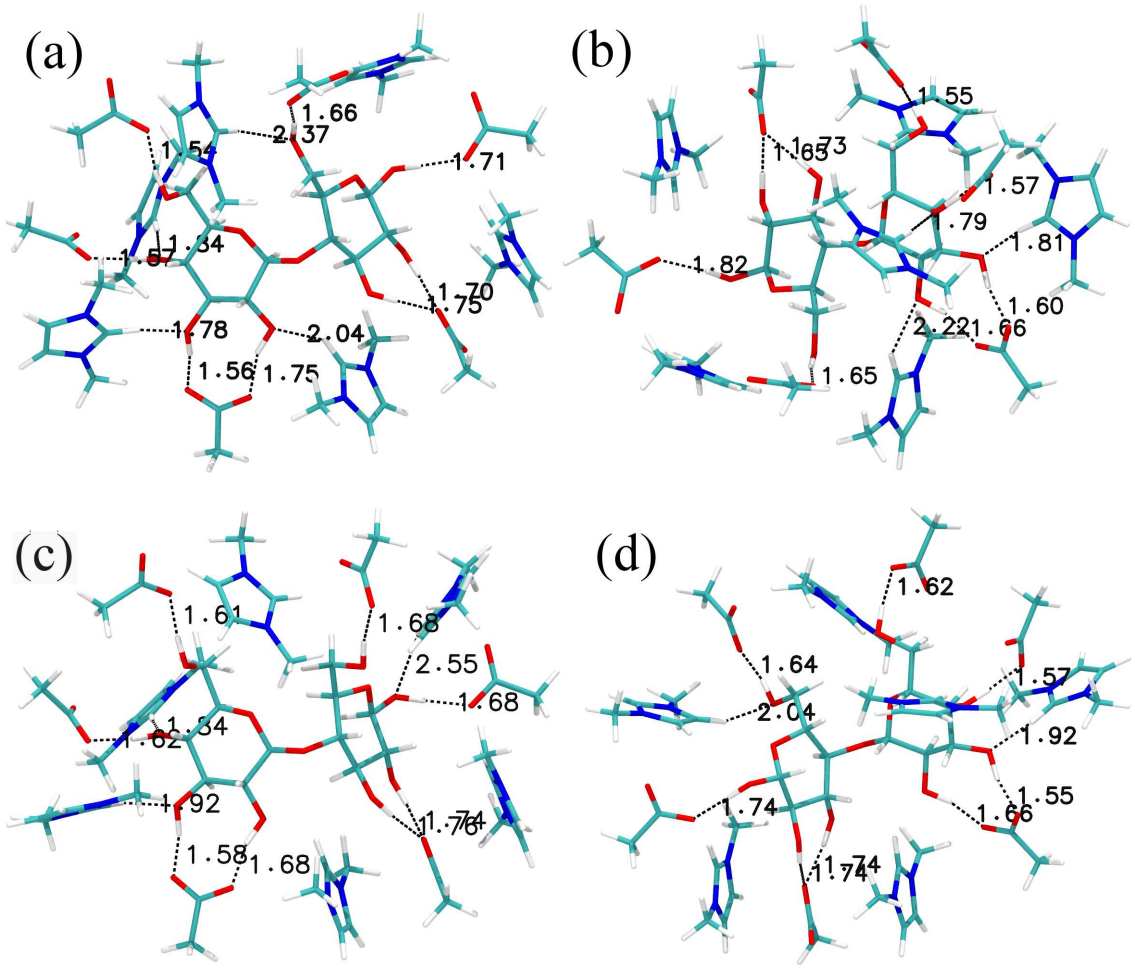

Figure 2.8: Computed lowest energy configurations of cellobiose surrounded by RTIL ion pairs. Intramolecular H-bonds are also shown. Color scheme same as previous figures.

Dramatically, these effects swap the order of conformer stability. In the presence

of [C_1mim][OAc], the anti-syn configuration becomes more stable than the anti-anti conformer by 6 kcal/mol (see Tables 2.2 and 2.4). This is in contrast to the observations on conformer stability found in the gas, implicit solvent, explicit water, and methanol media. Reversal of the conformer stability in explicit RTIL media can be associated to the relative stability of conformer in gas phase. Since the anti-anti conformer forms more intra-molecular hydrogen bonds in gas phase, it is difficult for it to dissolve in RTILs as compared to the anti-syn conformer which forms fewer intra-molecular hydrogen bonds. Since all the hydroxyl hydrogens are not involved in intra-molecular hydrogen bonding, it is easy for them to form hydrogen bond with ion pairs. However, in the case of anti-anti conformer, the breaking of additional intra-molecular hydrogen bonds involves a energy penalty. Furthermore, in agreement with NMR studies [43, 44], both the cation and the anion of the RTIL are seen to interact with the cellobiose unit. All the seven anions form strong H-bonds with the cellobiose solute. However among the seven cations, only four form H-bonds with cellobiose. The remaining cations form H-bonds with the anions alone. Values of dihedral angles for the four lowest energy conformers studied here are in good agreement with those seen in molecular dynamics simulations. The values seen in MD simulations were (ϕ = -125°, ψ = 50°), (ϕ = -50°, ψ = 100°), and (ϕ = -120°, ψ = -50°) [41]. The changes from intra- to intermolecular H-bonding network are also clearly reflected in the ^{1}H NMR values of the hydroxyl group as shown in table 2.5. Strong intermolecular H-bonding interactions are the reason for larger downfield movement of ^{1}H and ^{13}C chemical shifts by 3.5-4.6 ppm and 66.5-80.1 ppm compared to the values observed in gas and implicit solvent media calculations. The computed chemical shift values are comparable with experimental ^{1}H (3.0-6.0 ppm) and ^{13}C (68.0-103.0 ppm) NMR chemical shift values [43, 44]. Minor differences could be due to the lack of more solvent layers in the calculations. Similar calculations were carried out with the inclusion of a second solvent shell. In these calculations, a

total 19 ion pairs of RTIL were placed around the cellobiose conformers and then geometry optimization was carried out. Binding energy calculations exhibited the same trend as that in the case of 7 ion pairs. In the next section, the stability of conformers of xylan in explicit RTIL medium is examined.

Explicit solvation effects: xylan

Similar to cellobiose, xylan forms intermolecular H-bonding with ions which leads to negative binding energy values of -33 to -51 kcal/mol. The computed binding energy for xylan is higher by -29 kcal/mol than that for the cellobiose molecule, which is a likely reason for the high solubility of hemicellulose in RTIL media over that of cellulose [17]. Figure 2.9 shows two of the low energy configurations of xylan solvated by ions of the RTIL. Again, conformer **2** (Figure 2.9 (b)) differs from conformer **1** (Figure 2.9(a)) in the orientation of the OH group indicated by an arrow in Figure 2.5. Similar to cellobiose, the xylan molecule also interacts with four cations. This shows that the fewer number of hydroxyl groups on xylan does not affect its interactions with the cation. However the number of anions forming hydrogen bonds with xylan is reduced to a value of six from the value of seven that was observed for cellobiose. This difference could be a minor one and its importance (or otherwise) can be checked only by doing simulations of the solute in explicit bulk solvent. Further, six out of seven anions of the RTIL form H bonds with xylan. The intermolecular H bonds between the ions and xylan are shorter by 0.1-0.3 Å than the corresponding distances between the ions and cellobiose., There are no intramolecular hydrogen bonds in both the configurations of solvated xylan. Configuration **1** contains ten intermolecular hydrogen bonds (i.e., xylan forming H bonds either with the cation or the anion) stabilizing it over configuration 2 in which only seven intermolecular H bonds are observed. The reduction in the number of H-bonds in conformer **2** is due to the orientation of the -OH group indicated by

an arrow in Figure 2.5. These results suggest that the cation in the RTIL could also be involved in the solvation by the formation of intermolecular H-bonds with the cellulosic units, similar to those formed by the anion. In addition, the xylan molecules maintain the 60° orientation between the hexose rings as in gas phase, which might be the reason for its amorphous nature.

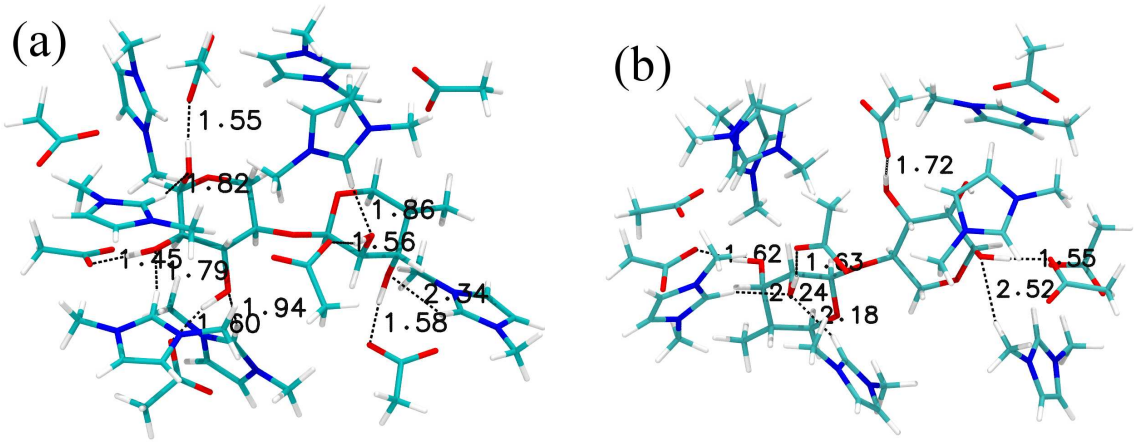

Figure 2.9: Computed lowest energy configuration of xylan surrounded by RTIL ion pairs. Intramolecular H-bonds are also shown. Colour scheme same as previous figures.

Table 2.5: ^{1}H and ^{13}C NMR cehmical shift value (in ppm, relative to TMS) of cellobiose and xylan in gas phase, implicit solvent RTIL and explicit RTIL media.

Molecule	Medium			NMR chemical shift (ppm)									
				1	2	3	4	6	1′	2′	3′	4′	6′
Cellobiose	Gas phase	C1	^{1}H	1.75	2.56	4.65	-	0.32	-	2.36	2.63	2.63	0.78
			^{13}C	85.42	64.9	65.5	77.9	56.1	95.1	65.9	69.2	65.3	55.1
		C2	^{1}H	2.37	2.43	2.07	-	0.42	-	2.49	2.5	1.58	0.33
			^{13}C	59.8	68.8	67.57	88.1	52.6	67.7	63.4	69.3	89.5	53.57
	Implicit solvent	C1	^{1}H	4.12	3.72	5.33	-	2.64	-	3.87	4.18	3.59	2.81
			^{13}C	86.04	64.93	66.41	77.89	56.56	96.12	66.51	70.29	64.62	55.77
		C2	^{1}H	3.72	3.93	4.37	-	2.43	-	5.69	3.72	3.77	2.43
			^{13}C	89.12	71.8	69.3	87.6	53.43	68.81	64.4	69.1	89.7	53.61
	Exp [68, 69]		^{13}C	85.9	63.4	84.4	70.4	49.1	91.1	68.4	81.1	73.0	-
	Exlicit solvent	C1	^{1}H	4.61	4.21	5.63	-	2.71	-	3.94	4.78	3.73	3.22
			^{13}C	87.25	66.23	70.02	79.94	57.23	97.21	68.21	71.23	66.23	57.27
		C2	^{1}H	3.92	4.01	4.53	-	2.76	-	5.81	3.84	3.91	2.66
			^{13}C	90.01	72.02	70.43	87.92	54.34	70.02	66.78	71.23	91.89	54.43
	Exp [43]		^{1}H	4.42	3,05	3.42	-	3.28	-	-	-	3.63	-
			^{13}C	103.00	73.9	75.2	-	75.2	-	-	-	79.3	60.8
Xylan	Gas phase	C1	^{1}H	5.26	1.87	0.69	2.55	-	1.28	0.79	2.28	3.98	-
			^{13}C	100.21	72.46	76.25	33.97	-	96.24	77.12	75.61	75.42	-
		C2	^{1}H	5.25	1.83	0.71	2.24	-	1.46	1.27	2.26	3.98	-
			^{13}C	99.47	75.52	76.1	33.97	-	95.41	75.93	78.16	75.01	-
	Implicit solvent	C1	^{1}H	4.96	1.65	1.92	2.26	-	2.45	2.05	2.69	3.74	-
			^{13}C	101.85	73.82	78.18	43.95	-	97.66	77.24	75.87	79.63	-
		C2	^{1}H	4.78	2.19	2.08	2.13	-	2.76	1.7	1.68	3.66	-
			^{13}C	102.98	74.62	75.65	34.81	-	96.7	77.38	77.17	81.51	-
	Explicit solvent	C1	^{1}H	1.66	9.65	10.05	2.21	-	11.31	14.19	11.01	3.24	-
			^{13}C	104.67	72.78	77.69	93.66	-	96.29	73.77	77.65	89.89	-
		C2	^{1}H	4.81	10.72	10.47	1.69	-	11.37	0.08	8.7	2.97	-
			^{13}C	104.59	73.77	72.96	36.82	-	94.98	78.16	73.2	88.35	-

2.4 Conclusions

Quantum chemical calculations of cellobiose and xylan were carried out in order to obtain a microscopic understanding of their solubility in RTIL. The calculations, using density functional theory, have been performed in (a) gas phase, (b) under implicit solvent conditions, and (c) with a layer of explicit solvent molecules. The solvent molecules considered were water, methanol, and 1,3-dimethylimidazolium acetate, [C_1mim][OAc].

Our study shows that the conformational stability of cellobiose and xylan are highly dependent upon the number of inter- and intramolecular H bonds. In the gas phase, the moiety with large number of intramolecular H bonds (the anti-anti conformer of cellobiose and the anti-syn conformer **2** of xylan) is most stable. The structural features were reflected in the calculated NMR chemical shifts and vibrational frequencies. The energy differences between the conformers are within 5-6 kcal/mol which is within the capability of the solvent to induce a conformational change. The polarization effect due to the dielectric constant of the solvent, captured through continuum calculations, is seen to further reduce the energy difference. The primary cause appears to be the reduction of the H-bond strength; however the conformers follow the same trend in energy as in the gas phase.

In addition, our quantum calculations on a cluster of solvent molecules solvating the cellulosic units yield rich information on solute-solvent hydrogen bonding [70, 71]. While the explicit presence of water and methanol around cellobiose (or xylan) does not change the order of conformational stability, it is seen to partially remove the intramolecular H-bonds. Strikingly, all intramolecular H-bonds are removed in the explicit RTIL medium, due to solute-solvent H-bonding interaction. As a result, the anti-syn conformer of cellobiose and the anti-syn conformer **1** of xylan (wherein the glucose units are rotated by about 60°) become more stable than other conformers. Nearly all the anions coat (forming hydrogen bonds) cellobiose exclusively, while only

a fraction of the cations do so. This result is in good agreement with experimental NMR studies [43, 44]. The remaining cations form H bonds with their corresponding anions. The same trend was observed in xylan, where out of the seven ion pairs present in the calculation, four cations and six anions form solute-solvent hydrogen bonds. However, the two rings in xylan are oriented at 60° to each other, while in cellobiose they are coplanar.

The computed structural parameters of cellobiose-RTIL cluster, especially dihedral values are in good agreement with those seen in earlier molecular dynamics simulations. Our studies suggest that both the cation and the anion are responsible for the dissolution of cellobiose and xylan in RTILs, which is in good agreement with previous experimental studies. In addition, our results confirm that the H-bonding interactions between anion and cation with the cellobiose or xylan units contribute significantly in their dissolution. The work also points out the necessity of considering explicit solvent molecules to capture these subtle effects that are so crucial to cellulose solubility in RTILs.

Bibliography

[1] Simmons, B. A.; Loque, D.; Blanch, H. W. *Genome Biol.* **2008**, *9*, 242–242.

[2] Wyman, C. E. *Trends in Biotech.* **2007**, *25*, 153 – 157.

[3] Richard, T. L. *Science* **2010**, *329*, 793–796.

[4] Saha, B. C. *J. Ind. Microbiol. Biotech.* **2003**, *30*, 279–291.

[5] Ohno, H.; Fukaya, Y. *Chem. Lett.* **2009**, *38*, 2–7.

[6] Kennedy, J. F.; Phillips, G. O.; Williams, P. A. *Ellis Horwood series in polymer science and technology (USA)* **1990**,

[7] Scheller, H. V.; Ulvskov, P. *Annu. Rev. Plant Biol.* **2010**, *61*, 263–289.

[8] Pinkert, A.; Marsh, K. N.; Pang, S.; Staiger, M. P. *Chem. Rev.* **2009**, *109*, 6712–6728.

[9] Nishino, T.; Matsuda, I.; Hirao, K. *Macromolecules* **2004**, *37*, 7683–7687.

[10] Terbojevich, M.; Cosani, A.; Conio, G.; Ciferri, A.; Bianchi, E. *Macromolecules* **1985**, *18*, 640–646.

[11] Nishio, Y.; Manley, R. J. *Macromolecules* **1988**, *21*, 1270–1277.

[12] McCormick, C. L.; Dawsey, T. R. *Macromolecules* **1990**, *23*, 3606–3610.

[13] Williamson, S. L.; Armentrout, R. S.; Porter, R. S.; McCormick, C. L. *Macromolecules* **1998**, *31*, 8134–8141.

[14] Edgar, K. J.; Buchanan, C. M.; Debenham, J. S.; Rundquist, P. A.; Seiler, B. D.; Shelton, M. C.; Tindall, D. *Prog. Polym. Sci.* **2001**, *26*, 1605–1688.

[15] Kuang, Q.-L.; Zhao, J.-C.; Niu, Y.-H.; Zhang, J.; Wang, Z.-G. *J. Phys. Chem. B* **2008**, *112*, 10234–10240.

[16] Kubisa, P. *Prog. Polym. Sci.* **2009**, *34*, 1333–1347.

[17] Zhao, H.; Baker, G. A.; Cowins, J. V. *Biotech. Prog.* **2010**, *26*, 127–133.

[18] Swatloski, R. P.; Spear, S. K.; Holbrey, J. D.; Rogers, R. D. *J. Am. Chem. Soc.* **2002**, *124*, 4974–4975.

[19] Fort, D. A.; Swatloski, R. P.; Moyna, P.; Rogers, R. D.; Moyna, G. *Chem. Commun.* **2006**, 714–716.

[20] Zavrel, M.; Bross, D.; Funke, M.; Büchs, J.; Spiess, A. C. *Biores. Tech.* **2009**, *100*, 2580–2587.

[21] Singh, S.; Simmons, B. A.; Vogel, K. P. *Biotech. Bioeng.* **2009**, *104*, 68–75.

[22] Fukaya, Y.; Sugimoto, A.; Ohno, H. *Biomacromolecules* **2006**, *7*, 3295–3297.

[23] Xu, A.; Wang, J.; Wang, H. *Green Chem.* **2010**, *12*, 268–275.

[24] Fukaya, Y.; Hayashi, K.; Wada, M.; Ohno, H. *Green Chem.* **2008**, *10*, 44–46.

[25] Samayam, I. P.; Hanson, B. L.; Langan, P.; Schall, C. A. *Biomacromolecules* **2011**, *12*, 3091–3098.

[26] Lovell, C. S.; Walker, A.; Damion, R. A.; Radhi, A.; Tanner, S. F.; Budtova, T.; Ries, M. E. *Biomacromolecules* **2010**, *11*, 2927–2935.

[27] Sun, N.; Rahman, M.; Qin, Y.; Maxim, M. L.; Rodríguez, H.; Rogers, R. D. *Green Chem.* **2009**, *11*, 646–655.

[28] Mason, P. E.; Neilson, G. W.; Enderby, J. E.; Saboungi, M.-L.; Brady, J. W. *J. Am. Chem. Soc.* **2005**, *127*, 10991–10998.

[29] Mason, P.; Neilson, G.; Enderby, J.; Saboungi, M.-L.; Brady, J. *J. Phys. Chem. B* **2005**, *109*, 13104–13111.

[30] Youngs, T.; Hardacre, C.; Holbrey, J. *J. Phys. Chem. B* **2007**, *111*, 13765–13774.

[31] Remsing, R. C.; Hernandez, G.; Swatloski, R. P.; Massefski, W. W.; Rogers, R. D.; Moyna, G. *J. Phys. Chem. B* **2008**, *112*, 11071–11078.

[32] da Costa Sousa, L.; Chundawat, S. P.; Balan, V.; Dale, B. E. *Curr. Opin. Biotech.* **2009**, *20*, 339–347.

[33] Peng, X.-w.; Ren, J.-l.; Sun, R.-c. *Biomacromolecules* **2010**, *11*, 3519–3524.

[34] Remsing, R. C.; Swatloski, R. P.; Rogers, R. D.; Moyna, G. *Chem. Commun.* **2006**, 1271–1273.

[35] Bergenstråhle, M.; Wohlert, J.; Himmel, M. E.; Brady, J. W. *Carbohydr. Res.* **2010**, *345*, 2060–2066.

[36] Guo, J.; Zhang, D.; Duan, C.; Liu, C. *Carbohydr. Res.* **2010**, *345*, 2201–2205.

[37] Janesko, B. G. *Phys. Chem. Chem. Phys.* **2011**, *13*, 11393–11401.

[38] Mohamed, M. N. A.; Watts, H. D.; Guo, J.; Catchmark, J. M.; Kubicki, J. D. *Carbohydr. Res.* **2010**, *345*, 1741–1751.

[39] Guo, J.; Zhang, D.; Liu, C. *J. Theor. Comput. Chem.* **2010**, *9*, 611–624.

[40] Derecskei, B.; Derecskei-Kovacs, A. *Mol. Sim.* **2006**, *32*, 109–115.

[41] Liu, H.; Sale, K. L.; Holmes, B. M.; Simmons, B. A.; Singh, S. *J. Phys. Chem. B* **2010**, *114*, 4293–4301.

[42] Wada, M.; Heux, L.; Sugiyama, J. *Biomacromolecules* **2004**, *5*, 1385–1391.

[43] Zhang, J.; Zhang, H.; Wu, J.; Zhang, J.; He, J.; Xiang, J. *Phys. Chem. Chem. Phys.* **2010**, *12*, 1941–1947.

[44] Hesse-Ertelt, S.; Heinze, T.; Kosan, B.; Schwikal, K.; Meister, F. Solvent Effects on the NMR Chemical Shifts of Imidazolium-Based Ionic Liquids and Cellulose Therein. Macromolecular Symposia. 2010; pp 75–89.

[45] Appell, M.; Strati, G.; Willett, J.; Momany, F. *Carbohydr. Res.* **2004**, *339*, 537 – 551.

[46] Csonka, G. I.; French, A. D.; Johnson, G. P.; Stortz, C. A. *J. Chem. Theor. and Comput.* **2009**, *5*, 679–692.

[47] Jockusch, R. A.; Talbot, F. O.; Rogers, P. S.; Simone, M. I.; Fleet, G. W.; Simons, J. P. *J. Am. Chem. Soc.* **2006**, *128*, 16771–16777.

[48] Kozmon, S.; Tvaroška, I. *Collect. Czech. Chem. Commun.* **2006**, *71*, 1453–1469.

[49] Momany, F. A.; Appell, M.; Willett, J.; Bosma, W. B. *Carbohydr. Res.* **2005**, *340*, 1638–1655.

[50] Hutter, J.; Ballone, P.; Bernasconi, M.; Focher, P.; Fois, E.; Goedecker, S.; Parrinello, M.; Tuckerman, M. *Max-Planck Institut f ur Festk orperforschung and IBM Zurich Research Laboratory* **1995**, *1999*.

[51] Frisch, M. J. et al. Gaussian 03, Revision C.02. Gaussian, Inc., Wallingford, CT, 2004.

[52] Perdew, J. P.; Burke, K.; Ernzerhof, M. *Phys. Rev. lett.* **1996**, *77*, 3865.

[53] Troullier, N.; Martins, J. L. *Phys. Rev. B* **1991**, *43*, 1993.

[54] Barnett, R. N.; Landman, U. *Phys. Rev. B* **1993**, *48*, 2081.

[55] Becke, A. D. *J. Chem. Phys.* **1993**, *98*, 5648–5652.

[56] Lee, C.; Yang, W.; Parr, R. *Phys. Rev. A* **1988**, *38*, 3098.

[57] Parr, R. G.; Yang, W. *Density-functional theory of atoms and molecules*; Oxford university press, 1989; Vol. 16.

[58] Zahn, S.; Bruns, G.; Thar, J.; Kirchner, B. *Phys. Chem. Chem. Phys.* **2008**, *10*, 6921–6924.

[59] Tsuzuki, S.; Uchimaru, T.; Mikami, M. *J. Phys. Chem. B* **2009**, *113*, 5617–5621.

[60] Bhargava, B.; Balasubramanian, S.; Klein, M. L. *Chem. Commun.* **2008**, 3339–3351.

[61] Hunt, P. A.; Gould, I. R. *J. Phys. Chem. A* **2006**, *110*, 2269–2282.

[62] Thar, J.; Zahn, S.; Kirchner, B. *J. Phys. Chem. B* **2008**, *112*, 1456–1464.

[63] London, F. *J. Phys. Radium* **1937**, *8*, 397–409.

[64] McWeeny, R. *Phys. Rev.* **1962**, *126*, 1028.

[65] Ditchfield, R. *Mol. Phys.* **1974**, *27*, 789–807.

[66] Wolinski, K.; Hinton, J. F.; Pulay, P. *J. Am. Chem. Soc.* **1990**, *112*, 8251–8260.

[67] Cheeseman, J. R.; Trucks, G. W.; Keith, T. A.; Frisch, M. J. *J. Chem. Phys.* **1996**, *104*, 5497–5509.

[68] Novoselov, N.; Sashina, E.; Petrenko, V.; Zaborsky, M. *Fibre Chem.* **2007**, *39*, 153–158.

[69] Pépin, M.; Hubert-Roux, M.; Martin, C.; Guillen, F.; Lange, C.; Gouhier, G. *Eur. J. Org. Chem.* **2010**, *2010*, 6366–6371.

[70] Shen, T.; Langan, P.; French, A. D.; Johnson, G. P.; Gnanakaran, S. *J. Am. Chem. Soc.* **2009**, *131*, 14786–14794.

[71] others,, et al. *J. Am. Chem. Soc.* **2011**, *133*, 11163–11174.

Chapter 3

Dissolution of cellobiose in room temperature ionic liquids: *ab-initio* molecular dynamics simulations study*

3.1 Introduction

The depletion of fossil fuels and the increasing need for energy sources is an issue of paramount importance. Among many alternatives, biomass is a promising candidate. It is most abundant in the form of lignocellulosic matter present in wood or plant biomass. Major components of lignocellulosic biomass are cellulose (40-50%), hemicellulose (20-30%) and lignin (20-30%) [1]. Notwithstanding its abundance and utility, the conversion of biomass to biofuel is a rather difficult process. One of the main hurdles in this conversion is its dissolution. Biomass is reluctant to dissolve in

*Work reported in this chapter is published in: R. S. Payal and S. Balasubramanian, Phys. Chem. Chem. Phys. **16**, 17458-17465 (2014). Reproduced by permission of The Royal Society of Chemistry (RSC).

conventional organic solvents and requires harsh conditions of pressure and temperature [2]. Furthermore, traditional solvents for biomass have been associated with issues such as toxicity, volatility *etc.*

Rogers and coworkers [3] pioneered the dissolution of cellulose in room temperature ionic liquids (RTILs) under mild conditions, without any pretreatment and overcame these challenges. They were also able to regenerate cellulose with addition of water and other common solvents. RTILs are salts that are liquid at room temperature [4, 5]. Since their early work, significant progress has been made in the dissolution of biomass in RTILs. Some of the recent studies show that even wood can be directly dissolved in RTILs without any pretreatment [6–8]. Researchers have employed a variety of experimental techniques to investigate the dissolution mechanism of cellulose in RTILs. Nuclear magnetic resonance (NMR) studies performed by Moyna and coworkers [9] revealed that hydrogen-bonding interaction between the hydroxyl group of cellulose and the anion of RTILs was responsible for the dissolution of cellulose in RTILs and that the cation plays a negligible role. Ludwig and coworkers did a systematic study of dissolution of polyols in different salt solution and RTILs [10]. Shift in the OH frequency was used to determine the ability of any solvent to dissolve the polyols. Molecular dynamics (MD) simulations carried out by Youngs *et al* [11, 12] suggested a similar mechanism. Seddon and coworkers [13] used RTILs to assist the acid-catalysed hydrolysis of lignocellulosic biomass. Motivated by the work of Rogers and coworkers [3], many researchers have employed RTILs to dissolve other biomolecules. Silk fibroin [14], starch and Zein protein [15], hemicellulose [16], lignin [17], chitin and chitosan [18] *etc.* have also been dissolved in RTILs.

Over time, newer RTILs to improve the dissolution of cellulose have been identified [19–23]. Experimental studies suggest that RTILs with imidazolium cation and acetate anion are the best solvents for cellulose. $[C_4mim][CH_3COO]$ can dissolve 15

- 20 % of biomass [19, 21]. Although it is now well known that RTILs currently serve as the best solvents for cellulose dissolution, yet the role of cation in this process is under debate. A recent NMR study by Zhang *et al* [24] suggests that both cation and anion form hydrogen bonds with cellulose. Role of anion as primary factor for the dissolution of biomass in RTILs has been widely accepted [3, 7]. Experimentally it was observed that glucose, sucrose or other polysaccharides' solubility is the same for [emim][dca] and [bmim][dca] [25]. But the solubility changes rapidly when the anion is changed [3, 7, 25].

The mechanism of dissolution has been investigated by many researchers using various computational techniques. Bergenstråhle *et al* [26] carried out force field based MD simulations to understand the insolubility of cellulose in aqueous solutions. Singh and coworkers [27] used MD simulations to study the dissolution mechanism of cellulose in [C_2mim][OAc]. They reported that the strong hydrogen bonding between the anion and cellobiose was a major factor in dissolution. They also reported the interaction of a few cations with cellobiose. In particular, they observed a change in the conformation of cellulose with respect to the β(1-4) linkage when it was dissolved in the RTIL. Zhao et al [28, 29] carried out systematic MD simulations to understand the effect of the structure of cation and anion on the dissolution of cellobiose in RTILs. Cations with less steric hindrance showed a better dissolution capability. In the case of anions, apart from steric hindrance, a high electronegativity and absence of electron withdrawing groups were shown to aid cellulose dissolution. Recently, Rabideau *et al* [30] carried out atomistic MD simulations to study the dissolution of cellulose bundles in RTILs. They too observed that RTILs weaken the intra- and intermolecular hydrogen bonding between the cellobiose units, resulting in their dissolution. Quantum chemical calculations have also been employed to understand the interaction of cations and anions with cellulose. Janesko [31] employed dispersion corrected density functional theory (DFT) to understand the interaction between one

ion pair of RTIL and cellulose. They found that the cellulose unit mainly interacts with the anion (Cl^- in their case). Guo *et al* [32, 33] employed DFT calculations to probe the effect of cation and anion structure on interaction with cellulose. They too reported that the dissolution of cellulose in RTILs will have contributions from both cation and anion. Pincu and Gerber have recently carried out *ab-initio* molecular dynamics (AIMD) simulations of β-cellobiose conformer in pure water and examined differences in the solvation of the two conformers [34].

In the previous chapter, dissolution mechanism of cellulose and hemicellulose in RTILs was explained using density functional theory applied to clusters. It was shown that cations can indeed form weak hydrogen bonds with the hydroxyl groups of cellulose and hemicellulose. While both gas phase quantum chemical studies as well as force field based MD simulations have been employed to understand the dissolution mechanism of cellobiose in RTIL, to our knowledge no AIMD simulations have been carried out so far. AIMD simulations have the advantage of both configurational sampling intrinsic to a liquid phase and a quantum chemical framework within which it is realized [35–40]. Results of such simulations are reported here. RTILs, particularly in conditions employed to dissolve biomass are rarely devoid of water. Thus, the effect of water concentration in the RTIL on the solvation of the cellulosic unit have also been examined.

3.2 Details of simulation

In order to examine the microscopic interactions between cellulose and RTILs, one monomer unit of cellulose, i.e., cellobiose was considered as the solute. Initial geometries of the structural unit and of the cation and anion were constructed using GaussView [41]. These were later optimized independently in gas phase at B3LYP/6-311++(g,d) level of theory using the Gaussian 09 software package [41]. Two lowest energy conformers for cellobiose and the lowest energy structure of the ions were

taken for further calculations. The conformers of cellobiose were either anti-anti or anti-syn, as determined by the torsional state of the two CH_2OH groups (Figure 3.1). For each of these conformers, two different sets of simulation were carried out. In the first, cellobiose was solvated in pure RTIL (with 30 ion pairs of RTIL only). In addition, a simulation containing cellobiose dissolved in 30 ion pairs of RTIL along with 5 water molecules was also carried out. While the former system consisted of 825 atoms and 2176 valence electrons, the latter involved 840 atoms and 2216 valence electrons, making these simulations rather computationally challenging. Prior experimental studies have suggested the first and second solvation shells of cellobiose to contain 7 and 19 ion pairs respectively [24] and thus these system sizes, although small, are not unreasonable.

The system was initially equilibrated using classical MD simulations during which the RTIL was described using the force field of Senapati et al [42]. Water was described using the SPC/E model [43]. Gas phase ESP charges for atoms on cellobiose were calculated through Gaussian-09 [41] and the same were used in these classical MD simulations. The initial configuration of solvent molecules in each system was generated using Packmol [44]. The system was energy minimized prior to a short MD run under constant NVT conditions of 500 ps. Subsequently, the systems were studied under constant NPT conditions for 15 ns. This was followed by a constant NVT run for 16 ns whose final configuration constituted the initial configuration for the AIMD run. Box lengths for the systems containing anti-anti or anti-syn conformer soaked in pure RTIL were 19.8802 Å and 19.8806 Å respectively. For the RTIL+$5H_2O$ systems, it was 19.9796 Å for the anti-anti conformer and 20.1040 Å for the anti-syn one. All classical MD simulations were carried out using the LAMMPS [45] software package.

AIMD simulations were performed using the CP2K/Quickstep code [46]. Double zeta valence polarization (DZVP) basis with Goedecker, Teter and Hutter (GTH)

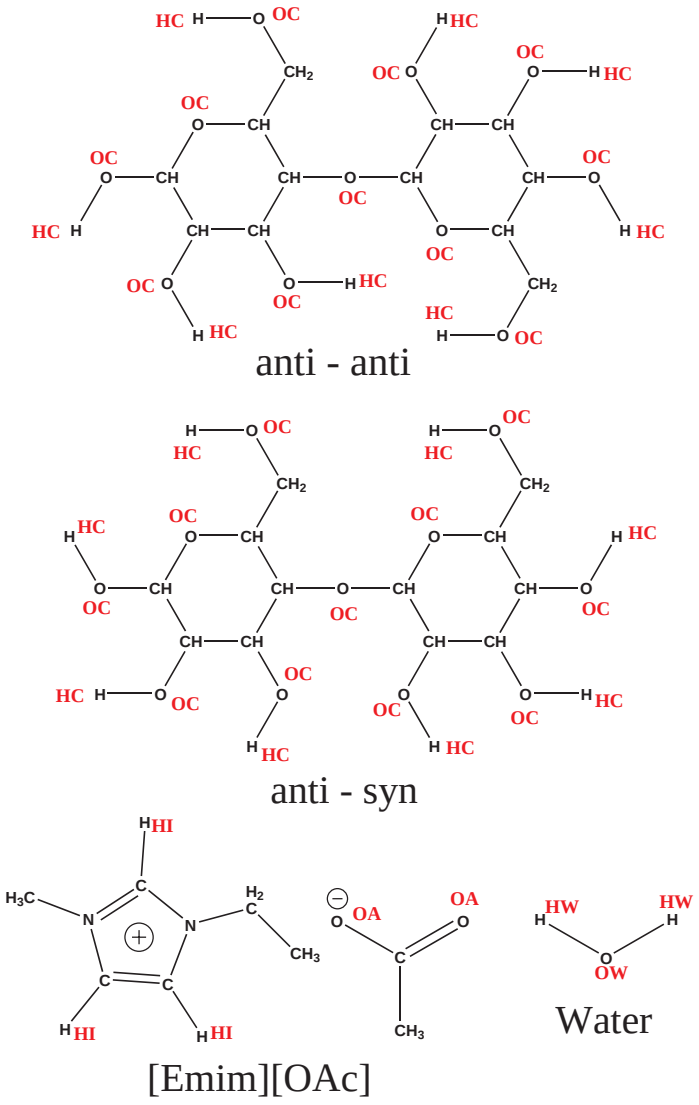

Figure 3.1: Schematic of the two cellobiose conformers, ions of RTIL and water molecule, showing different atom types used in the discussion.

pseudopotentials were used. The BLYP [47] exchange-correlation functional was employed. Dispersion corrections at the D2 level [48] were also included. Simulations were carried out in the NVT ensemble at 300 K using a Nosé-Hoover chain thermostat [49]. Equations of motion were integrated with 0.5 fs timestep. Three dimensional periodic boundary conditions were employed in order to mimic a bulk system. Electronic orbitals were expanded in a Gaussian basis set. The electron density was expanded in plane wave basis set with energy cut off of 280 Ry. All the

systems were studied for 35 ps. All the analyses were carried out on the last 25 ps of the AIMD trajectory using home grown codes written in FORTRAN 90.

MD trajectories were visualized and spatial density maps were created using VMD [50].

3.3 Results and discussion

3.3.1 Radial distribution functions

The structural properties of a liquid system can be well studied through the radial distribution function, g(r). Figure 3.2(a) shows the g(r) between the three ring hydrogen atoms of the cation (HIs) and the oxygen (OC) atom of cellobiose. All these pair correlation functions exhibit a first peak at around 2.7 Å; on rare occasions, the ring hydrogen of the cation approaches cellobiose to distances less than 2 Å indicating the likely formation of a weak cation-cellobiose hydrogen bond. Addition of water decreases the height of the first peak in the anti-anti case; thus, water could partially displace the cations in the first coordination shell of cellobiose. The difference in the intensities of the g(r)s between the anti-anti and anti-syn cases is likely due to poor statistics. Figure 3.2(b) shows the g(r) between oxygen (OA) of anion and hydroxyl hydrogen (HC) of cellobiose. The sharp peak at 1.6 Å in all the g(r)s indicates the formation of strong hydrogen bonds. Also the peak height changes negligibly upon addition of water, implying that anions surrounding the cellobiose unit are more or less unaffected by the presence of water molecules.

This behavior is evident from the running coordination number (Figure 3.3). The running coordination number of cation HIs around OC of cellobiose is insignificant till 2 Å. However, in the corresponding distance range, that of anion OAs around HC of cellobiose varies between 0.70 to 0.85. Thus, each of the hydroxyl hydrogen of cellobiose is surrounded by 0.75 anion oxygens. Given that there are eight HC atoms

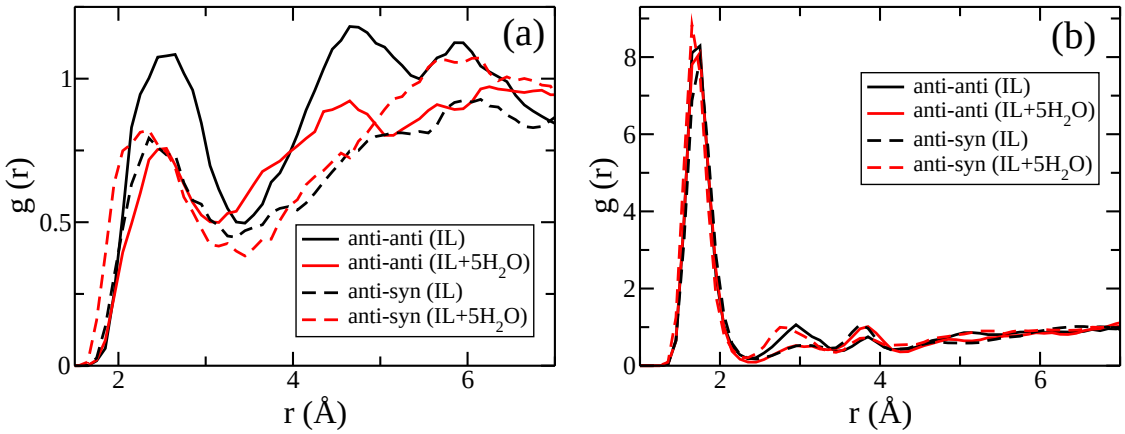

Figure 3.2: Radial distribution function between (a) OC of cellobiose and HI of cation and (b) HC of cellobiose and OA of anion.

in cellobiose, presence of around six to seven anions hydrogen bonded to cellobiose, in its first coordination shell can be concluded. This observation can be further supported by the radial distribution function between the HC of cellobiose and carboxylate carbon of anion (Figure 3.4). At the first coordination minimum (3.5 Å), the coordination number is around 0.85. As there are 8 HCs in cellobiose, one can say that nearly 7 anions are hydrogen bonded to it. The acetate anion possesses two carboxylate oxygen atoms (OA). Either of them can form hydrogen bond with hydroxyl hydrogen (HC) of cellobiose. However, it was observed that only one of the two OAs hydrogen bonds with HC. The other OA atom is hydrogen bonded with the acidic proton of the cation (see Figure 3.5). For the case of cellobiose-cation, the first coordination shell extends up to 3.25 Å and the number of cations varies between 0.50 to 1.0; however, the coordination number at 2.5 Å is only 0.4. Thus, within this distance from cellobiose, nearly six to seven anions are hydrogen bonded and around three to four cations are present. This observation is in reasonable agreement with the earlier NMR study of Zhang *et al* [24], where they suggested the first coordination shell of cellobiose to consist of 7 ion pairs. Since anions are seen to be closer to the cellobiose units, it can be concluded that they form stronger hydrogen bonds and play the primary role in its dissolution which is in agreement

with earlier experimental [9, 11] and simulation studies [27].

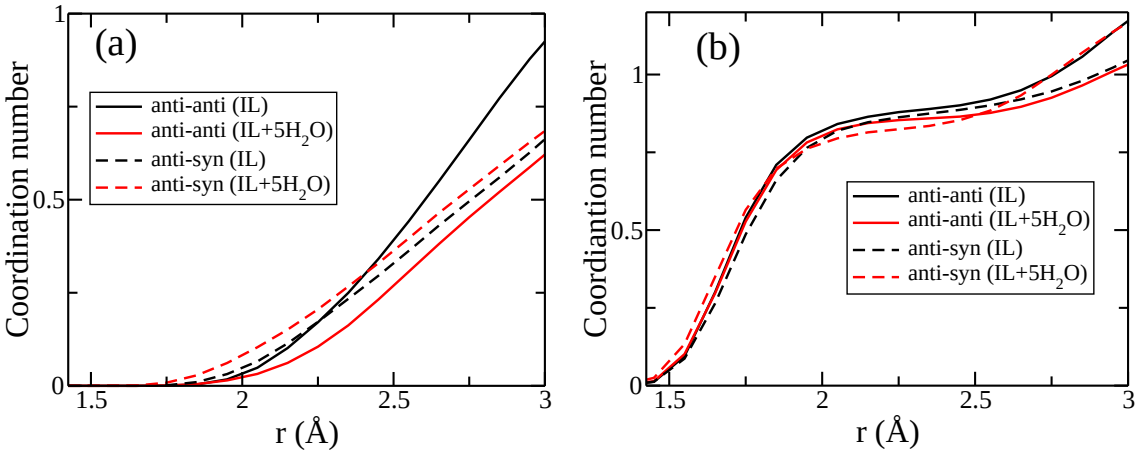

Figure 3.3: Running coordination number between (a) OC atom of cellobiose and HI of cation and (b) HC of cellobiose and OA of anion.

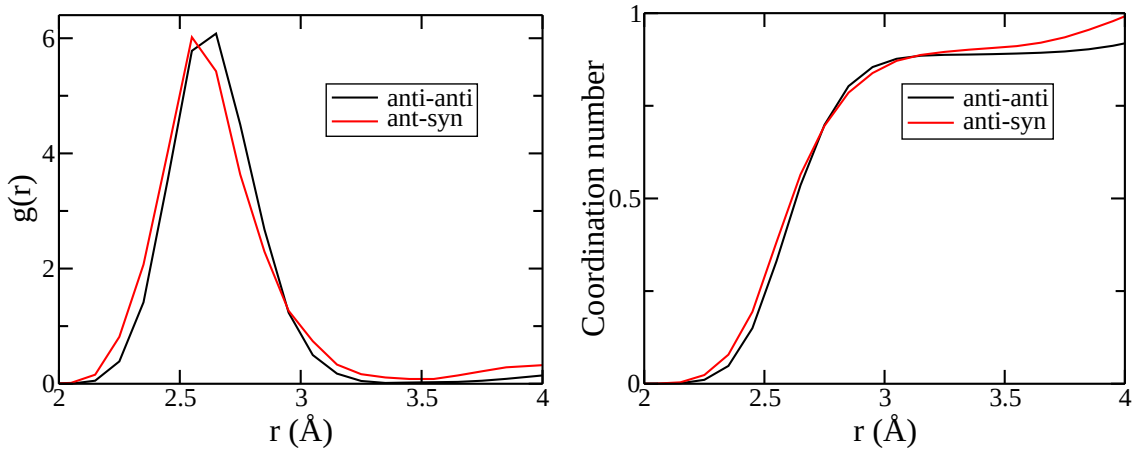

Figure 3.4: (a) Radial distribution function and (b) running coordination number between HC of cellobiose and carboxylate carbon of anion.

While the role of anions in the dissolution mechanism is widely accepted, that of the cations needs to be understood better. Plots of both radial distribution function and running coordination number suggest that cations can approach cellobiose close enough such that their HIs can form weak hydrogen bonds with the OC atoms of cellobiose. The cation-cellobiose hydrogen bonds are considerably weaker as compared to those formed by the anions. These results are in agreement with our previous

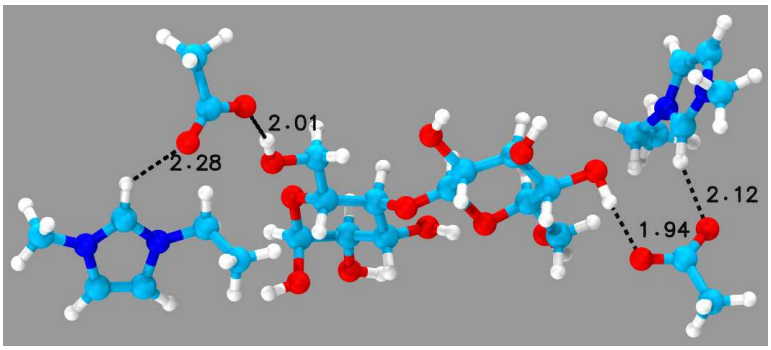

Figure 3.5: Snapshot from simulation displaying the neighborhood of cellobiose in RTIL. Only one of the OA atom of acetate anion is hydrogen bonded with HC of cellobiose. The other OA atom is hydrogen bonded to HI of the cation. Only two anions present around cellobiose are shown for the sake of clarity.

cluster calculations [51], in the sense that both cation and anion are found to interact favorably with cellobiose. Further, these observations are in agreement with the NMR spectroscopic studies of Zhang *et al* [24]. Thus, although the cation has only a secondary role to play in the dissolution mechanism, its effect cannot be neglected, a conclusion drawn through MD simulations recently reported by Zhao *et al* [28]. Further, the shortest distance of approach for both the cation and the anion to cellobiose is independent of the amount of water present, although the peak height of the cellobiose-ion g(r) decreases with increasing water concentration. Similar effect of cation on dissolution of CO_2 in RTILs was observed by Kirchner and coworkers [52], although the anion plays the major role [53, 54]. Examination of the first solvation shell for the anti-anti conformer of cellobiose shows that all but one of its intramolecular hydrogen bonds are replaced by intermolecular hydrogen bonds between cellobiose and ions of RTIL (Figure 3.6). Interestingly, the unbroken intramolecular hydrogen bond present in the anti-anti conformer is found to be broken in the anti-syn case (Figure 3.7). Through DFT calculations of clusters in the previous chapter. It was found that that the anti-anti conformer, which is the most stable in gas phase, becomes less stable than the anti-syn one in the presence of explicit ions of RTIL. The results reported here on the absence of an intramolecular

hydrogen bond in the anti-syn conformer confirms the earlier observations. This structural detail is observed in the systems studied with water as well.

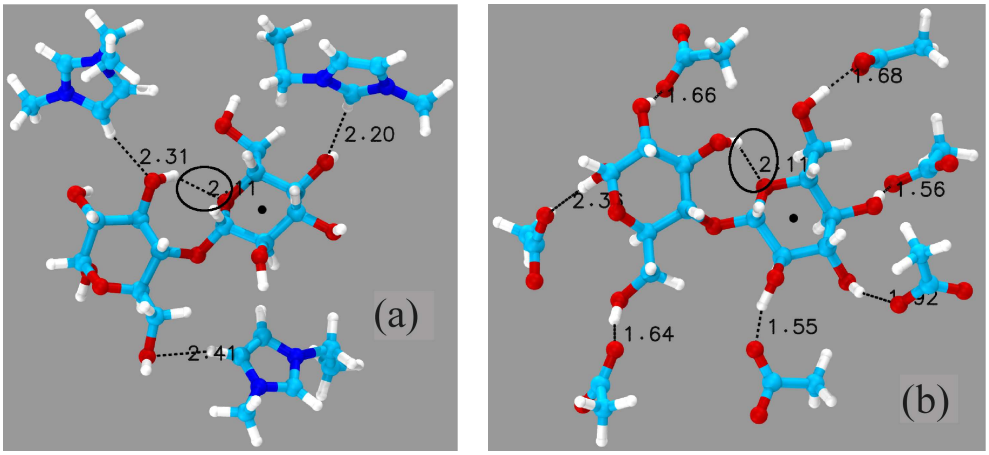

Figure 3.6: Snapshot of environment around anti-anti conformer of cellobise showing the formation of hydrogen bonds with (a) cation and (b) anion. Intramolecular hydrogen bond of the cellobiose unit is also shown. Color scheme Nitrogen : Blue, Carbon : Cyan, Oxygen : Red and Hydrogen : White. Black dot can be used to identify the specific hexose ring of the cellobiose across the two panels.

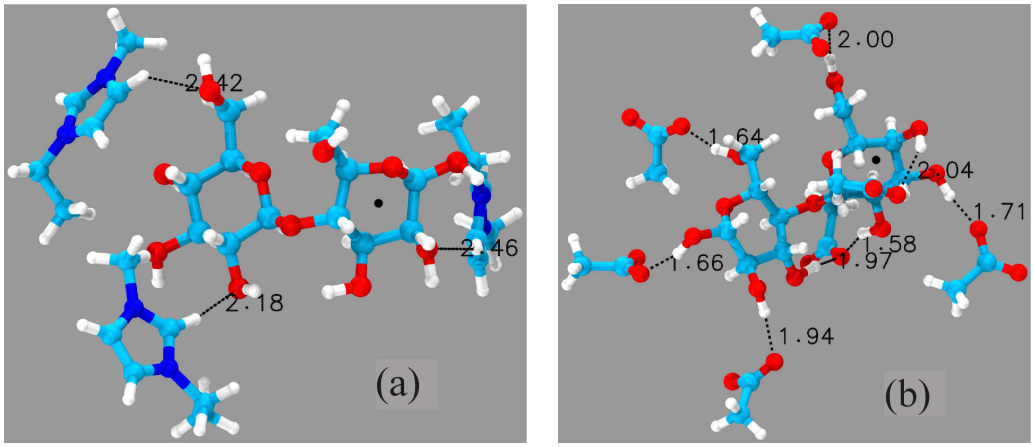

Figure 3.7: Snapshot of environment around anti-syn conformer of cellobise showing the formation of hydrogen bonds with (a) cation and (b) anion. Color scheme is the same as in earlier figures. Black dot can be used to identify the specific hexose ring of the cellobiose across the two panels.

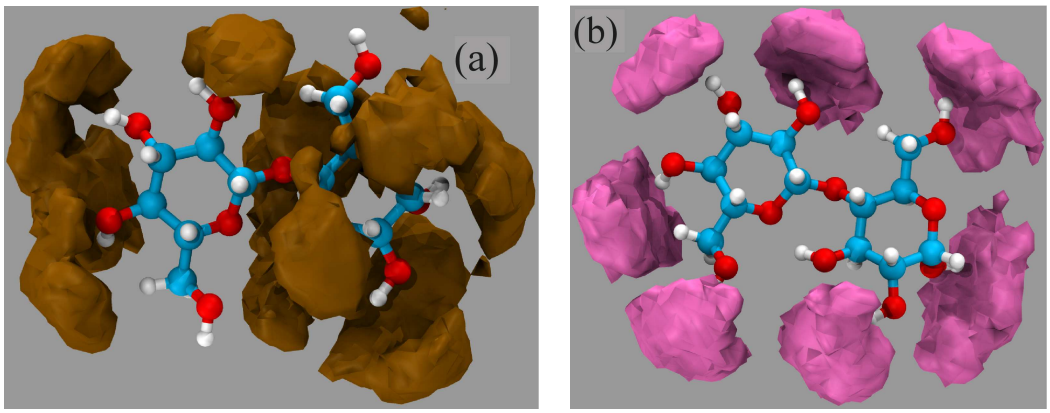

Figure 3.8: Spatial distribution of (a) cation's ring hydrogen and of (b) anion's oxygen around cellobiose in anti-anti conformation. Isosurface values are 0.01 $Å^{-3}$ and 0.001 $Å^{-3}$ respectively. Carbon : Cyan, Oxygen : Red and Hydrogen : White.

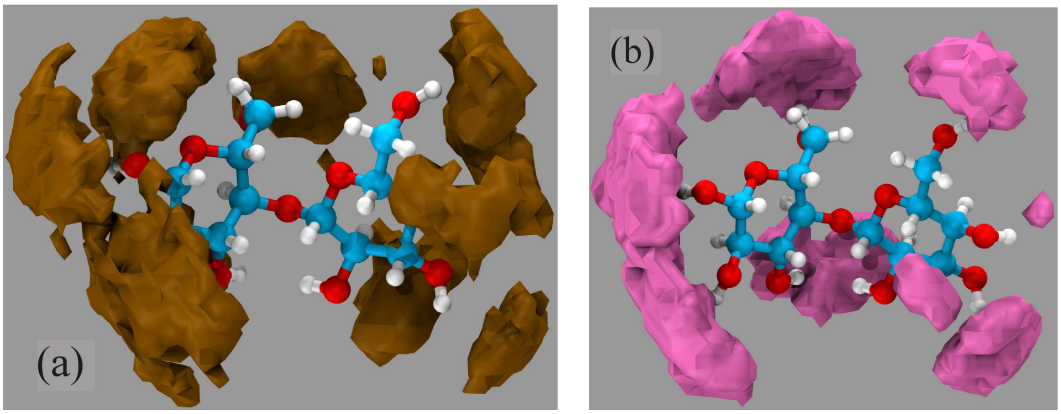

Figure 3.9: Spatial distribution of (a) cation's ring hydrogen and of (b) anion's oxygen around cellobiose in anti-syn conformation. Isosurface values and color scheme are same as in Figure 3.8.

3.3.2 Distribution of cations and anions around cellobiose

Figures 3.8 and 3.9 show the spatial density map of the three ring hydrogens of cation (HI) and of oxygens of the anion (OA) around the two cellobiose conformers. Both anion and the cation are present in the first coordination shell of cellobiose. The isosurface value used for the cation in the figures is an order of magnitude larger than that for the anion. Despite its higher isosurface value, the cation map is much more dispersed than the corresponding one for the anion. Anions exhibit

very specific binding as seen from their relatively narrow spatial distribution. The bulky nature of the cations may impose steric hindrance and does not permit them to approach closer to the hydroxyl sites of cellobiose. In addition, the larger volume over which the positive charge is distributed on the cation could also be a reason for its weaker binding to cellobiose. In the case of the anti-anti conformer, anions are absent near one of the hydroxyl hydrogen as the latter forms an intramolecular hydrogen bond which is intact over the entire duration of the simulation (Figure 3.6). In fact, the hydrogen bond that this hydrogen atom participates in, exhibits an interesting behavior. As shown in Figure 3.10(a), it can form a hydrogen bond with either O1 (ring oxygen) or with O2 (CH_2OH). Shown in Figure 3.10(b) is the distance of this hydrogen from these two sites as a function of time in the case of cellobiose dissolved in pure RTIL. Over the duration of the AIMD trajectory, this hydrogen was found to forms a hydrogen bond between these two sites in the ratio of approximately 4:1, i.e., the ring oxygen site (O1) is more preferred than the CH_2OH oxygen (O2). There also exists a transient state where the intramolecular hydrogen bond is replaced by the intermolecular hydrogen bond (3.10(c)). In the anti-syn conformer, this intramolecular hydrogen bond was never observed and is replaced by an intermolecular one – the hydrogen atom h-bonds with OA of the anion (Figure 3.7).

Figure 3.11 is a snapshot from the AIMD simulation displaying the cations and anions in the vicinity of the cellobiose unit. Most of the HC atoms of cellobiose form hydrogen bonds with one of the OA atoms. The other OA atoms of the anion are seen to form a hydrogen bond with the HI of cation. In most cases of hydrogen bond between the anion and the cation, the most acidic ring hydrogen is the atom which is involved. In the vicinity of cellobiose, some cations are seen not to form hydrogen bond with it. However, they are involved in hydrogen bonds with anions.

Figure 3.12 compare the pair correlation functions between anions and cellobiose

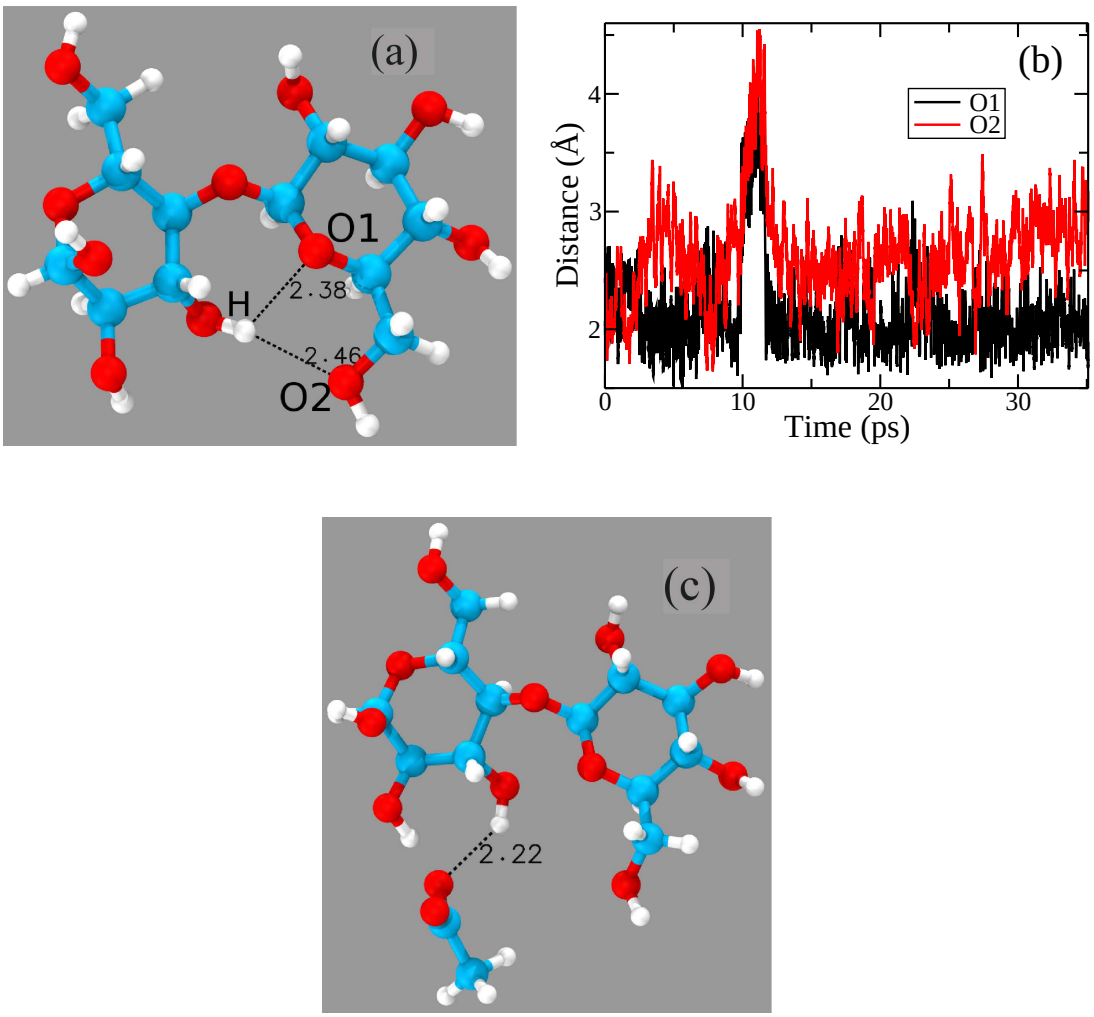

Figure 3.10: (a) Snapshot of cellobiose taken from the AIMD trajectory. O1 and O2 are two possible hydrogen bonding sites for H atom of cellobiose in its anti-anti conformation. (b) distance of H from O1 and O2 during the AIMD trajectory and (c) a transient state, where such intramolecular hydrogen bond(s) are replaced by one intermolecular hydrogen bond with the anion. Color scheme is the same as in earlier figures. Distances are in Å units.

obtained from force field based MD (with empirical potentials) and AIMD simulations. The g(r)s between the anion's oxygen and cellobiose's hydroxyl hydrogen are nearly identical as obtained from the two methods. Since this hydrogen bonding is the most dominant interaction between cellobiose and the ions, the current results can also be seen as a validation of the classical force field. However in both the cases, the anion-cellobiose g(r) is shifted to higher distances in AIMD simulations.

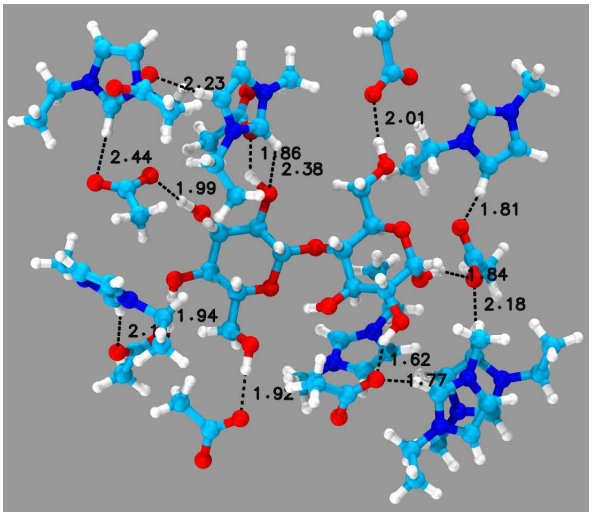

Figure 3.11: Environment around cellobiose solvated in RTIL. Color scheme same as in earlier figures, Nitrogen : Blue.

This observation suggests that the anion may be overbound in classical force field based simulations. Typical force fields of RTILs employ a unit charge on the ions although many researchers [55–58] advocate a sub-unit charge to account for charge transfer and polarization effects present in the condensed phase. The force field employed herein treats the ions with unit charge and this is likely to have led to the overbinding of anions to cellobiose within the force field description.

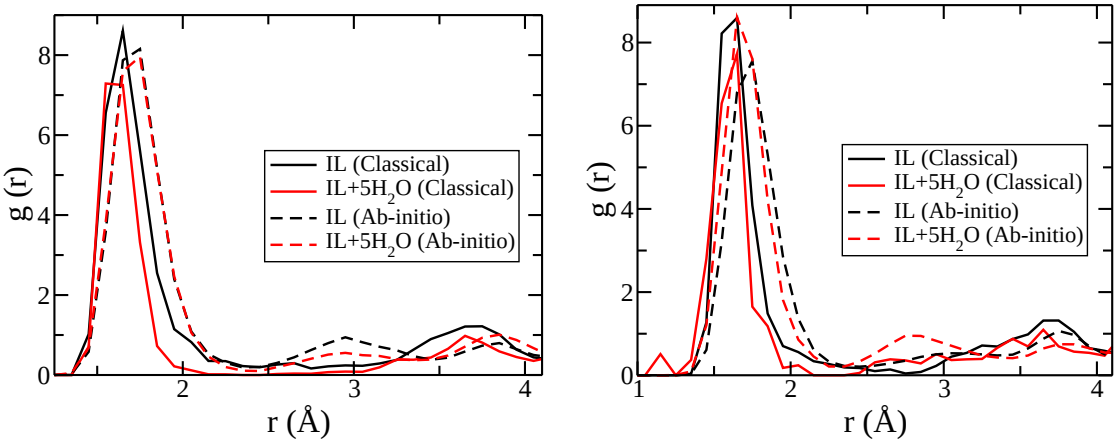

Figure 3.12: Comparison of OA-HC RDFs obtained from classical and *ab-initio* MD simulations for (a) anti-anti and (b) anti-syn conformers of cellobiose.

Figure 3.13 compares various g(r)s of RTIL-cellobiose and water-cellobiose. The ions approach the cellobiose unit closer than water does. Furthermore, within water,

its oxygen atom (OW) is closer to cellobiose than its hydrogen (HW). Thus, water chiefly acts as a hydrogen bond acceptor with cellobiose. However, the effect of water on the two conformers is different. A comparison between the running coordination number of (HI-HW) and (OA-OW) pairs (Figure 3.13) captures the difference in the nature of interaction of water molecules with the two cellobiose conformers rather well. For both the conformers, the running coordination number of HW around OC is insignificant for distances less than 2.5 Å, while OW approaches HC up to a distance of 2.0 Å. The latter suggests the occasional formation of a OW-HC hydrogen bond. Figure 3.13 also demonstrates that water molecules interact differently with each conformer. Water molecules are able to approach closer to the anti-anti conformer as compared to the anti-syn conformer. The effect of cellobiose geometry on its interaction with pure water has already been studied by Pincu and Gerber [34] using AIMD simulations. They too observed the two conformers of cellobiose to interact differently with water and concluded that water molecules are able to better solvate the anti-anti conformer than the anti-syn one. The presence of water was not able to alter the nature of the solvation shell of cellobiose significantly. This may be due to the small concentration of water studied here.

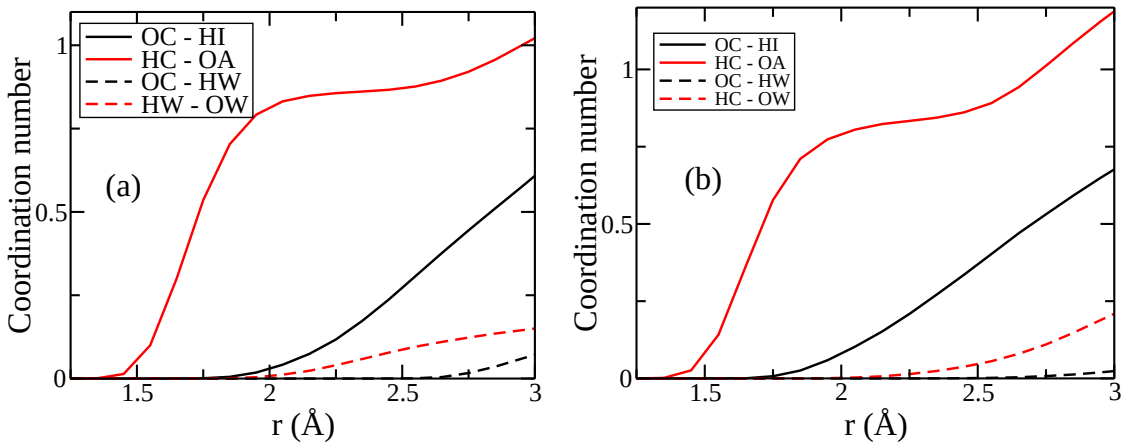

Figure 3.13: Running coordination number for (a) anti-anti and (b) anti-syn conformers of cellobiose solvated in RTIL+5H_2O.

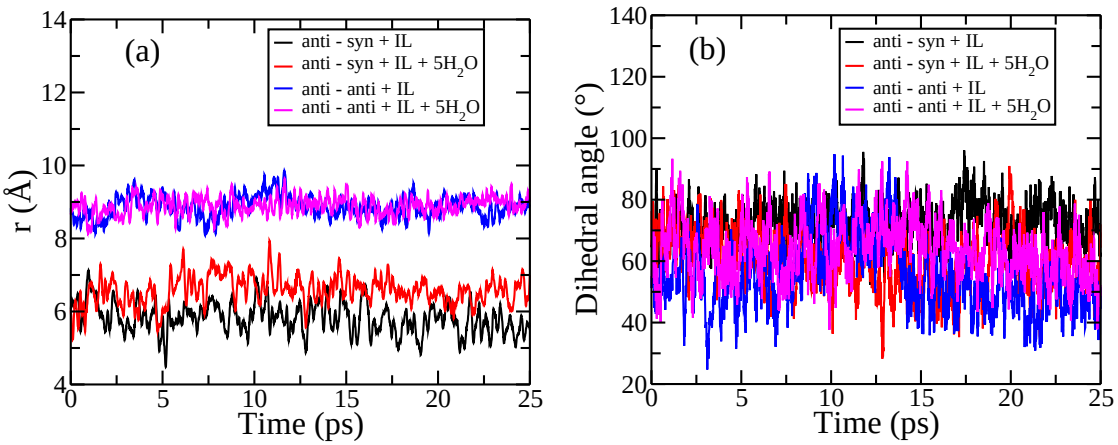

Figure 3.14: Distribution of (a) distance between oxygen atoms of two CH_2OH in cellobiose conformers (b) dihedral angle between two hexose rings of cellobiose conformers as function of time.

During the AIMD run, no conformational transition was observed in the cellobiose; the anti-anti and anti-syn conformers retained their respective torsional angles for the bond between the two hexose rings (Figure 3.14). The torsional angle about the β(1-4) linkage varied between 40 and 80^o, in agreement with an earlier MD simulations of Singh *et al* [27]. Furthermore, it was observed that the hydrogen bonds formed by cellobiose with the cation, anion or any water molecule were intact during the entire duration of the AIMD simulation.

3.4 Conclusions

The dissolution of cellulose in RTILs depends on the breaking of the strong, inter and intra-molecular hydrogen bonding network present in cellulose. RTILs are able to disrupt this hydrogen bonding network more efficiently. The anions of RTIL play the major role in the dissolution mechanism. They form strong hydrogen bonds with hydroxyl hydrogens of cellobiose, in either of its conformers (anti-anti or anti-syn). However, the role of cation in the solvation of cellobiose cannot be completely ignored. Strong electrostatic interactions between the cation and the

anion necessitate that the cation be proximal to the anion. Thus, a few cations are indeed present in the first coordination shell of cellobiose. They too form hydrogen bonds with the cellobiose unit, albeit weaker ones than what the anions do. The coordination offered by the ions of RTIL to the anti-anti and anti-syn conformer of cellobiose are different. Thus the conformation of cellobiose will play a crucial role in its dissolution in the RTIL. The addition of a small quantity of water does not significantly alter the local environment of the cellobiose which continues to be coordinated primarily by the ions.

Bibliography

[1] Saha, B. C. *J. Ind. Microbiol. Biotech.* **2003**, *30*, 279–291.

[2] Nishino, T.; Matsuda, I.; Hirao, K. *Macromolecules* **2004**, *37*, 7683–7687.

[3] Swatloski, R. P.; Spear, S. K.; Holbrey, J. D.; Rogers, R. D. *J. Am. Chem. Soc.* **2002**, *124*, 4974–4975.

[4] Rogers, R. D.; Seddon, K. R. *Science* **2003**, *302*, 792–793.

[5] Hunt, P. *Mol. Sim.* **2006**, *32*, 1–10.

[6] Fort, D. A.; Remsing, R. C.; Swatloski, R. P.; Moyna, P.; Moyna, G.; Rogers, R. D. *Green Chem.* **2007**, *9*, 63–69.

[7] Sun, N.; Rahman, M.; Qin, Y.; Maxim, M. L.; Rodriguez, H.; Rogers, R. D. *Green Chem.* **2009**, *11*, 646–655.

[8] Brandt, A.; Hallett, J. P.; Leak, D. J.; Murphy, R. J.; Welton, T. *Green. Chem.* **2010**, *12*, 672–679.

[9] Remsing, R. C.; Swatloski, R. P.; Rogers, R. D.; Moyna, G. *Chem. Commun.* **2006**, 1271–1273.

[10] Papanyan, Z.; Roth, C.; Wittler, K.; Reimann, S.; Ludwig, R. *ChemPhysChem* **2013**, *14*, 3667–3671.

[11] Youngs, T. G. A.; Hardacre, C.; Holbrey, J. D. *J. Phys. Chem.* **2007**, *111*, 13765–13774.

[12] Youngs, T. G.; Holbrey, J. D.; Deetlefs, M.; Nieuwenhuyzen, M.; Costa Gomes, M. F.; Hardacre, C. *ChemPhysChem* **2006**, *7*, 2279–2281.

[13] Vanoye, L.; Fanselow, M.; Holbrey, J. D.; Atkins, M. P.; Seddon, K. R. *Green Chem.* **2009**, *11*, 390–396.

[14] Phillips, D. M.; Drummy, L. F.; Conrady, D. G.; Fox, D. M.; Naik, R. R.; Stone, M. O.; Trulove, P. C.; De Long, H. C.; Mantz, R. A. *J. Am. Chem. Soc.* **2004**, *126*, 14350–14351.

[15] Biswas, A.; Shogren, R.; Stevenson, D.; Willett, J.; Bhowmik, P. K. *Carbohydr. Polym.* **2006**, *66*, 546–550.

[16] Zhao, H.; Baker, G. A.; Cowins, J. V. *Biotech. Prog.* **2010**, *26*, 127–133.

[17] Pu, Y.; Jiang, N.; Ragauskas, A. J. *J. Wood Chem. Tech.* **2007**, *27*, 23–33.

[18] Xie, H.; Zhang, S.; Li, S. *Green Chem.* **2006**, *8*, 630–633.

[19] Singh, S.; Simmons, B. A.; Vogel, K. P. *Biotech. Bioeng.* **2009**, *104*, 68–75.

[20] Fukaya, Y.; Hayashi, K.; Wada, M.; Ohno, H. *Green Chem.* **2008**, *10*, 44–46.

[21] Zavrel, M.; Bross, D.; Funke, M.; Bchs, J.; Spiess, A. C. *Biores. Tech.* **2009**, *100*, 2580–2587.

[22] Fukaya, Y.; Sugimoto, A.; Ohno, H. *Biomacromolecules* **2006**, *7*, 3295–3297.

[23] Xu, A.; Wang, J.; Wang, H. *Green Chem.* **2010**, *12*, 268–275.

[24] Zhang, J.; Zhang, H.; Wu, J.; Zhang, J.; He, J.; Xiang, J. *Phys. Chem. Chem. Phys.* **2010**, *12*, 1941–1947.

[25] others,, et al. *Chem. Comm.* **2002**, 714–715.

[26] Bergenstråhle, M.; Wohlert, J.; Himmel, M. E.; Brady, J. W. *Carbohydr. Res.* **2010**, *345*, 2060–2066.

[27] Liu, H.; Sale, K. L.; Holmes, B. M.; Simmons, B. A.; Singh, S. *J. Phys. Chem. B* **2010**, *114*, 4293–4301.

[28] Zhao, Y.; Liu, X.; Wang, J.; Zhang, S. *ChemPhysChem* **2012**, *13*, 3126–3133.

[29] Zhao, Y.; Liu, X.; Wang, J.; Zhang, S. *Carbohydr. Poly.* **2013**, *94*, 723–730.

[30] Rabideau, B. D.; Agarwal, A.; Ismail, A. E. *J. Phys. Chem. B* **2013**, *117*, 3469–3479.

[31] Janesko, B. G. *Phys. Chem. Chem. Phys.* **2011**, *13*, 11393–11401.

[32] Liu, C.; Guo, J.; Zhang, D. *J. Theor. Comput. Chem.* **2010**, *09*, 611–624.

[33] Guo, J.; Zhang, D.; Duan, C.; Liu, C. *Carbohydr. Res.* **2010**, *345*, 2201–2205.

[34] Pincu, M.; Gerber, R. B. *Chem. Phys. Lett.* **2012**, *531*, 52–58.

[35] Iftimie, R.; Minary, P.; Tuckerman, M. E. *Proc. Natl. Acad. Sci. USA* **2005**, *102*, 6654–6659.

[36] Marx, D.; Hutter, J. *Modern methods and algorithms of quantum chemistry* **2000**, *1*, 301–449.

[37] Thomas, M.; Brehm, M.; Fligg, R.; Vöhringer, P.; Kirchner, B. *Phys. Chem. Chem. Phys.* **2013**, *15*, 6608–6622.

[38] Spickermann, C.; Thar, J.; Lehmann, S.; Zahn, S.; Hunger, J.; Buchner, R.; Hunt, P.; Welton, T.; Kirchner, B. *J. Chem. Phys.* **2008**, *129*, 104505.

[39] Boese, A. D.; Chandra, A.; Martin, J. M.; Marx, D. *J. Chem. Phys.* **2003**, *119*, 5965–5980.

[40] Chakraborty, D.; Chandra, A. *J. Chem. Phys.* **2011**, *135*, 114510.

[41] Frisch, M. J. et al. Gaussian 09 Revision D.01. Gaussian Inc. Wallingford CT 2009.

[42] Chandran, A.; Prakash, K.; Senapati, S. *Chem. Phys.* **2010**, *374*, 46 – 54.

[43] Berendsen, H. J. C.; Grigera, J. R.; Straatsma, T. P. *J. Phys. Chem.* **1987**, *91*, 6269–6271.

[44] Martínez, L.; Andrade, R.; Birgin, E. G.; Martínez, J. M. *J. Comput. Chem.* **2009**, *30*, 2157–2164.

[45] Plimpton, S. *J. Comput. Phys.* **1995**, *117*, 1 – 19.

[46] Hutter, J.; Iannuzzi, M.; Schiffmann, F.; VandeVondele, J. *Wiley Interdisciplinary Reviews: Computational Molecular Science* **2013**, 15–25.

[47] Becke, A. D. *Phys. Rev. A* **1988**, *38*, 3098–3100.

[48] Grimme, S. *J. Comput. Chem.* **2006**, *27*, 1787–1799.

[49] Martyna, G. J.; Klein, M. L.; Tuckerman, M. *J. Chem. Phys.* **1992**, *97*, 2635–2643.

[50] Humphrey, W.; Dalke, A.; Schulten, K. *J. of Mol. Graph.* **1996**, *14*, 33–38.

[51] Payal, R. S.; Bharath, R.; Periyasamy, G.; Balasubramanian, S. *J. Phys. Chem. B* **2012**, *116*, 833–840.

[52] Hollóczki, O.; Kelemen, Z.; Könczöl, L.; Szieberth, D.; Nyulászi, L.; Stark, A.; Kirchner, B. *ChemPhysChem* **2013**, *14*, 315–320.

[53] Bhargava, B.; Balasubramanian, S. *Chem. Phys. Lett.* **2006**, *417*, 486–491.

[54] Bhargava, B.; Balasubramanian, S. *J. Phys. Chem. B* **2007**, *111*, 4477–4487.

[55] Dommert, F.; Wendler, K.; Berger, R.; Delle Site, L.; Holm, C. *ChemPhysChem* **2012**, *13*, 1625–1637.

[56] Mondal, A.; Balasubramanian, S. *J. Phys. Chem. B* **2014**, *118*, 3409–3422.

[57] Leontyev, I. V.; Stuchebrukhov, A. A. *J. Chem. Phys.* **2009**, *130*, 085102.

[58] Bhargava, B. L.; Balasubramanian, S. *J. Chem. Phys.* **2007**, *127*, 114510.

Chapter 4

Dissolution of cellulose in room temperature ionic liquids: anion dependence

4.1 Introduction

Lignocellulosic biomass is a potential source of biofuel which can be converted into ethanol. However, one of the challenging task in this process is its dissolution. While cellulose is a crystalline polymer, other components of wood, i.e., hemicellulose and lignin are amorphous [1]. The crystalline nature of the former arises from strong inter- and intra-molecular hydrogen bonding between its monomers, i.e., cellobiose. These are covalently bonded to one another by β(1-4) linkages to form long polymeric units. Conventional solvents such as water or benzene are unable to dissolve cellulose and the process requires harsh conditions such as acid pretreatment and high temperature [2].

This issue was addressed by Rogers and coworkers in 2002, who successfully

dissolved cellulose in room temperature ionic liquids (RTIL) at relatively mild conditions [3]. They were also able to regenerate cellulose by addition of water or simple solvents. This discipline has seen a large amount of activity since then [1, 4–28].

NMR spectroscopy has been effectively employed to understand the dissolution mechanism of cellulose in RTILs [29]. The disruption of inter- and intra-molecular hydrogen bonding network of cellulose polymer in RTILs was identified as key to its dissolution and the anion was shown to be chiefly responsible. In most RTILs, the cation is bulkier and acts only as a weak hydrogen bond (H-bond) donor and thus its role is not as significant as that of the anion. A recent NMR study by Zhang *et al* [30] showed that cations too can form H-bonds with cellulose, albeit a weaker one.

There have been many attempts to understand the dissolution mechanism of lignocellulosic biomass in RTILs through theoretical methods [31–33]. Both empirical force field and ab-initio based methods have been employed [34–37]. These studies also showed the weakening/disruption of the inter- and intra-molecular hydrogen bond network in polymeric cellulose in various RTILs. Examining the specific role of the ions, Zhao *et al* [38, 39] suggested the following attributes for better dissolution: (i) ions with less steric hindrance (ii) anions with high electronegativity and without any electron withdrawing group.

Quantum cluster calculations [40] and density functional theory (DFT) based ab initio MD simulations [41] presented in previous chapters investigated the disruption of intra-molecular H-bonds and the dependence of the conformation of cellobiose on solvation.

Future development towards the choice of novel anions demand a comprehensive rationalization of experimental observations. Crucial solute-solvent interactions responsible for the dissolution of the polymer can be understood by carrying out studies on the solvation environment of the monomer. Thus far, the free energy of

solvation of model cellulose has not been examined in the literature. The current work is aimed at calculating the solvation free energy of a monomer of cellulose, i.e., cellobiose and its dependence on the anion of the RTILs. It is carried out to obtain a microscopic understanding of the experimental observation that the acetate anion is the most suited for this process. The calculations have been performed in thermodynamically most stable conformational state of the cellobiose, anti-anti, an observation which too has been established here. Anticipating the results, it was found that the RTIL with the acetate anion is the most suited for cellobiose solvation in terms of the magnitude of change in its free energy from gas phase, upon solvation. A possible choice of anion which could potentially enhance cellulose solubility is also suggested.

4.2 Simulation details

RTILs containing the [bmim] cation and any of the following anions were studied: $[OAc]^-$, $[NO_3]^-$, $[Cl]^-$, $[BF_4]^-$, $[PF_6]^-$, $[CF_3SO_3]^-$, and $[NTf_2]^-$. The conformational free energy profile of cellobiose in these RTILs was studied in a system containing 100 ion pairs, while its solvation free energy was studied in systems containing 256 ion pairs. Cellobiose was modeled using the OPLS force field for carbohydrates [42] while RTILs were modeled using the all-atom force field developed by Mondal and Balasubramanian [43].

Three-dimensional periodic boundary conditions were employed. Tail corrections to energy and pressure were applied. Long range electrostatic interactions were evaluated using the particle-particle particle-mesh (PPPM) solver [44]. All the simulations were done at 353 K. The higher than ambient temperature was necessitated to include results from liquid [bmim][Cl] [m. pt. 343 K]. Furthermore, such temperatures are routinely employed in experiments (see Table 3 of Ref. [1].) Temperature and pressure were maintained using Nosé-Hoover thermostat and barostat

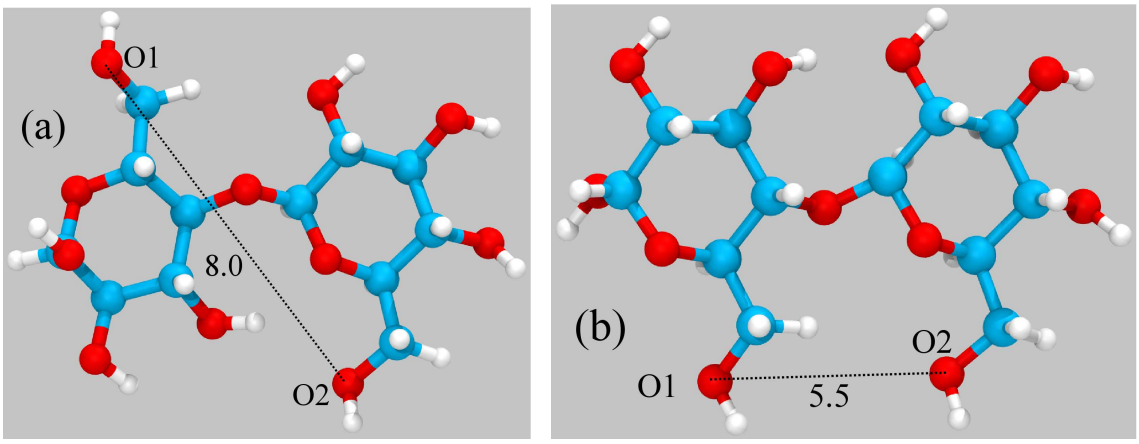

Figure 4.1: (a) Anti-anti and (b) anti-syn conformers of cellobiose. Color scheme C: Cyan, O: Red and H: Blue. Distance (in Å) between hydroxyl oxygens atoms (O1, O2) in the two hexose rings marked. The same can be used to distinguish the two conformational states.

respectively. Simulation trajectories were visualized and snapshots were rendered using VMD [45].

The two stable conformers of cellobiose are anti-anti and anti-syn (Figure 4.1) which can be distinguished by the torsional state of the two CH_2OH groups in the cellobiose.

Free energy calculations: All the FE simulations were carried out using the collective variables (colvars) module [46] embedded in LAMMPS [47]. The Adaptive Biasing Force (ABF) [48] method was used to determine the FE profiles. The span of the reaction coordinate (RC) was divided into bins in which accumulation of force takes place.

Adaptive Biasing Force: ABF method calculates the mean force along the RC ζ. Calculated mean force is then cancelled by equal and opposite biasing force. This allows the system to overcome the energy barriers and diffuse freely in energy landscape.

Free energy of the system with respect to RC can be written as

$$\mathcal{A}(\zeta) = -\frac{1}{\beta} ln\mathcal{P}(\zeta) + A_0 \tag{4.1}$$

Mean force can be calculated in terms of the free energy

$$\nabla_\zeta \mathcal{A}(\zeta) = \langle -\mathcal{F}_\zeta \rangle_\zeta \tag{4.2}$$

ABF applied to the system is

$$\mathcal{F}^{ABF} = \nabla_x \mathcal{A} = -\langle \mathcal{F}_\zeta \rangle_\zeta \nabla_x \zeta \tag{4.3}$$

In the ABF scheme, RC ζ is unconstrained. During the simulations, RC is divided into small bins, with bin width $\delta\zeta$, allowing RC to be explored in a continuous manner.

Collective variable method: COLVARS can be defined as the set of parameters that are used to alter the dynamics of the system with an application of biasing potential. Dynamics of the system is altered in a controlled fashion.

$$\xi(\mathcal{X}) = \xi(x_1, x_2, ..., x_n) \tag{4.4}$$

Generally, ξ is differential function of atomic coordinates. Choice of $\xi(\mathcal{H})$ is system dependent and mostly a function of few arguments.

COLVARS module applies biasing potential to the system and calculates the potential of mean force.

Conformational Free Energy: Cellobiose was solvated in a cubic box containing 100 RTIL molecules and equilibrated in the isothermal-isobaric (NPT) ensemble. The FE barrier across the C-C-C-O (see Figure 4.2(a)) torsion was determined using the ABF method. RC was spanned from -180^o to 180^o with a bin width of 5 degree. FE calculations using the dihedral angle as the reaction coordinate were carried out for 100 ns in the NPT ensemble. ABF forces were applied every 500 steps.

Solvation Free Energy (SFE): SFE is the energy required to bring one cellobiose molecule from gas phase into the bulk RTIL. 256 ion pairs were equilibrated in the NPT ensemble (P=1 atm, T=353K). Later, simulations were carried out in the canonical ensemble (NVT), after increasing the box-length along the Z direction to a value of 150 Å, to create two liquid-vapor interfaces, which was followed by FE calculations in the NVT ensemble. Colvar style 'distance Z' was used in determining the SFE profiles. RC was defined as the distance between the center of mass of RTIL molecules to the center of mass of cellobiose. It was divided into five non-overlapping windows spanning from 7 Å to 50 Å along the Z direction such that cellobiose is completely immersed at 7 Å and completely in gas-phase at 50 Å. Force samples were collected for 500 steps with bin width of 0.2 Å. Each window was run for at least 30 ns so as to achieve a sampling ratio, between the highest and lowest point, of around 5.

SFE could have also been calculated using the Bennet acceptance ratio (BAR) [49] or expanded ensemble [50, 51] methods. But, the equally facile ABF method was adopted here.

4.3 Results and discussion

4.3.1 Conformational free energy

Figure 4.2(b) displays the molecule in its anti-anti conformation and illustrates two categories of intra-molecular H-bonds: (i) Longer and bent (ii) Shorter and linear. The conformational free energy profile of cellobiose across ϕ in gas phase is shown in Figure 4.3(a). A minimum in the free energy occurs at -25°, corresponding to its anti-anti state. This conformer is nearly planar and contains five intra-molecular H-bonds, two of which are stronger than the other three. Two other minima are seen at 160° and -165° which correspond to the anti-syn state of cellobiose. This conformer possesses four intra-molecular H-bonds, of which two are stronger than the rest. The non-planar conformer is thus less stable than the anti-anti one. The two maxima at 110° and -120° correspond to states where the hexose rings are nearly perpendicular to each other.

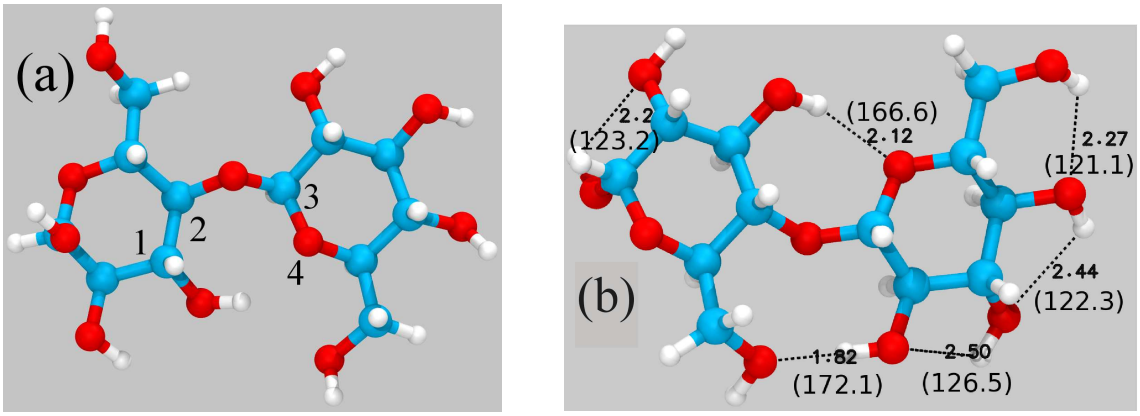

Figure 4.2: Cellobiose molecule (a) atoms (labeled 1 thorough 4) involved in the definition of the torsion angle, ϕ (b) intra-molecular H-bonds in the anti-anti conformer of cellobiose. Bond lengths and angles are in Å and ° respectively. Color scheme C: Cyan, O: Red and H: White.

Figure 4.3(b) shows the conformational free energy (FE) profiles of cellobiose soaked in RTIL. The anti-anti configuration of cellobiose is more stable than the anti-syn one even when it is solvated in any RTIL. However the torsional angle at

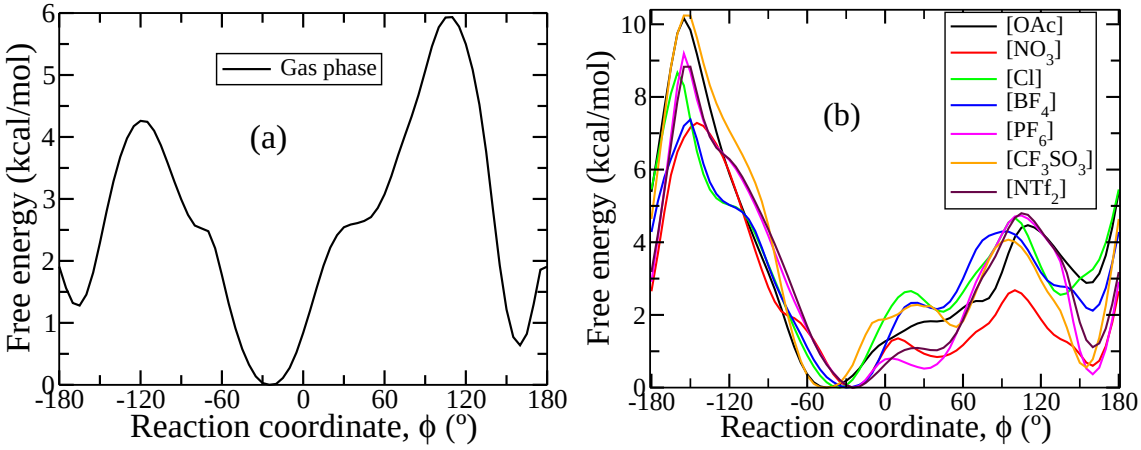

Figure 4.3: Conformational free energy of cellobiose (a) in gas phase and (b) solvated in RTILs. Anions are shown in the legend, while the cation is [bmim]. T=353 K.

which the free energy is a minimum, shifts to a lower value (more negative) than what it was in the gas phase. In fact, the extent of shift in a specific RTIL is correlated with the potential energy change (ΔU) associated with solvation (see later). The shift is caused due to the breaking of intra-molecular H-bonds of cellobiose and consequent formation of inter-molecular H-bonds with solvent ions. In fact, the anti-syn conformational state too gets shifted in solution. In most RTILs, it is found at 140°-160°. Two maxima are seen in the conformational FE profiles of solvated cellobiose. One of them is around 100° (shorter) and another at around -150° (taller). As compared to the gas phase data [Figure 4.3(a)], the relative intensities of these maxima are observed to be swapped in the presence of RTIL. The change can be explained thus: The FE maximum at 100° occurs when the two hexose rings are almost perpendicular to each other. In this situation, most of the hydroxyl hydrogen atoms are exposed to the solvent and can form H-bonds with solvent ions which decreases the free energy of this state relative to its value in gas phase. When ϕ=-145°, none of the hydroxyl hydrogens are able to form either intra- or inter-molecular H-bonds, leading to a high FE barrier.

Again, two kinds of H-bonds can be formed between cellobiose and RTIL viz.

one between the anion of RTIL and hydroxyl hydrogen of cellobiose (stronger) and second between the cation of RTIL and oxygen of cellobiose (relatively weaker). In general, the former are more in number than the latter. These results are in good agreement with results from the previuos chapters [40, 41]. In [emim][OAc], all intra-molecular H-bonds of cellobiose in its anti-syn state were found to be broken, while the anti-anti state retains one or two such H-bonds [41]. Figures 4.4 and 4.5 display snapshots of the H-bonds formed between cellobiose and the ions in [bmim][OAc] and [bmim][NTf_2].

4.3.2 Solvation free energy

Conformational free energy profiles of cellobiose solvated in various RTILs have unambiguously shown the greater stability of the anti-anti conformer over the anti-syn one. Thus, the question of relative stability and consequently the solubility of cellobiose in different RTILs can be addressed now. The free energy profiles for bringing the solute, cellobiose, from its vapor phase into the RTIL have thus been calculated using its anti-anti conformer. Needless to state, cellobiose was not constrained to be present in this conformation during the free energy simulations. However, once initiated from this torsional state, the same remained invariant (withn fluctuations) during the simulations Figure 4.6). Figure 4.7 displays solvation free energy profiles in various RTILs containing the same cation but different anions. The difference in the free energies between the vapor (gas phase) and the solvated state is the solvation free energy (SFE) of cellobiose in that particular RTIL. SFE is highest for [bmim][OAc] and lowest for [bmim][PF_6].

Enthalpic contributions to this relative stability can be interpreted in terms of the strength of the inter-molecular H-bonds. $[OAc]^-$, $[NO_3]^-$ and $[Cl]^-$ anions form strong H-bonds with cellobiose. Solvation free energies in [bmim][NTf_2], [bmim][CF_3SO_3] and [bmim][PF_6] are comparable as the H-bonding strength of their

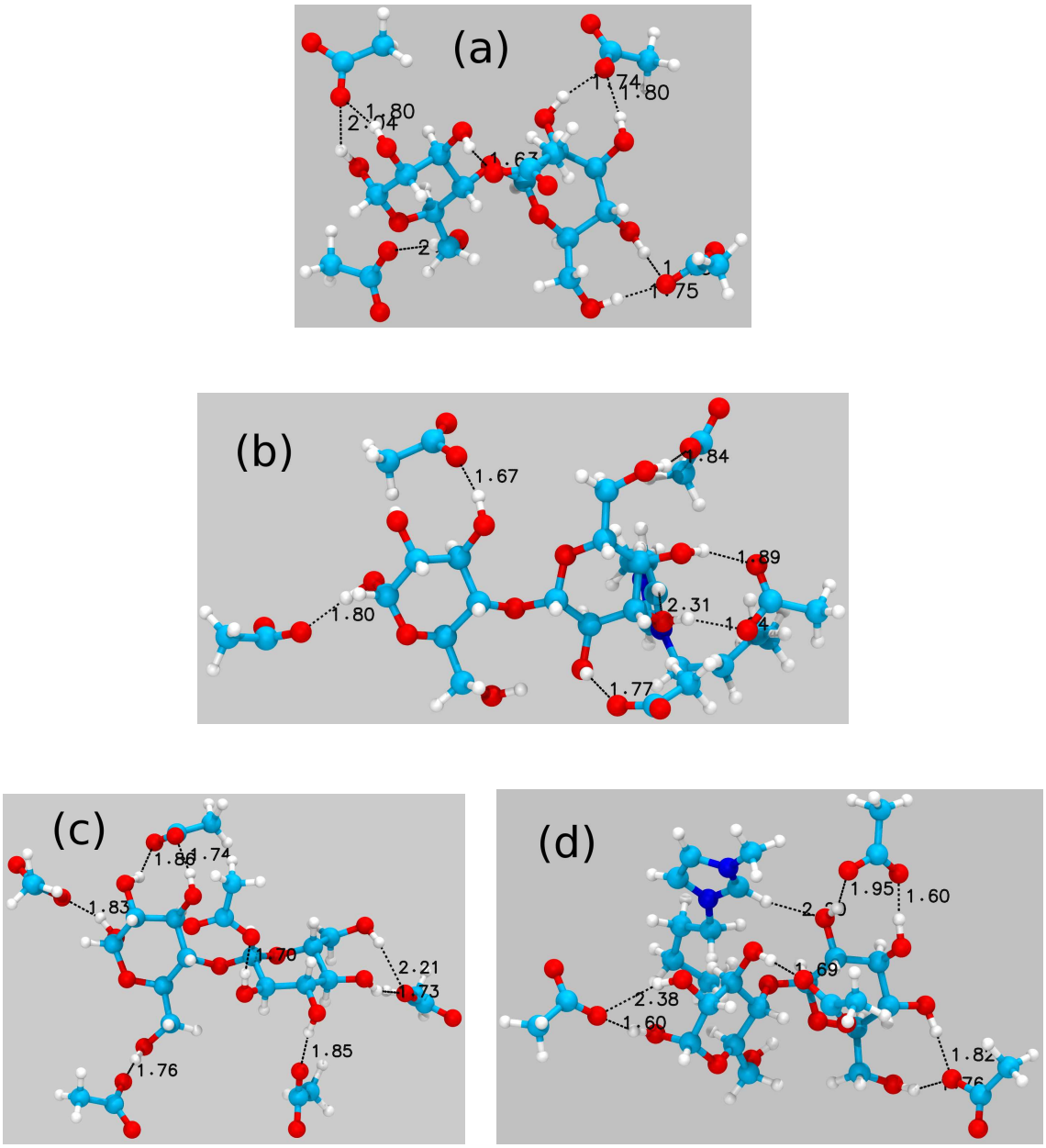

Figure 4.4: Hydrogen bonded ions around cellobiose in [bmim][OAc] at ϕ values (a) -160°, (b) -45°, (c) 120° and (d) 170°. Color scheme same as previous figures.

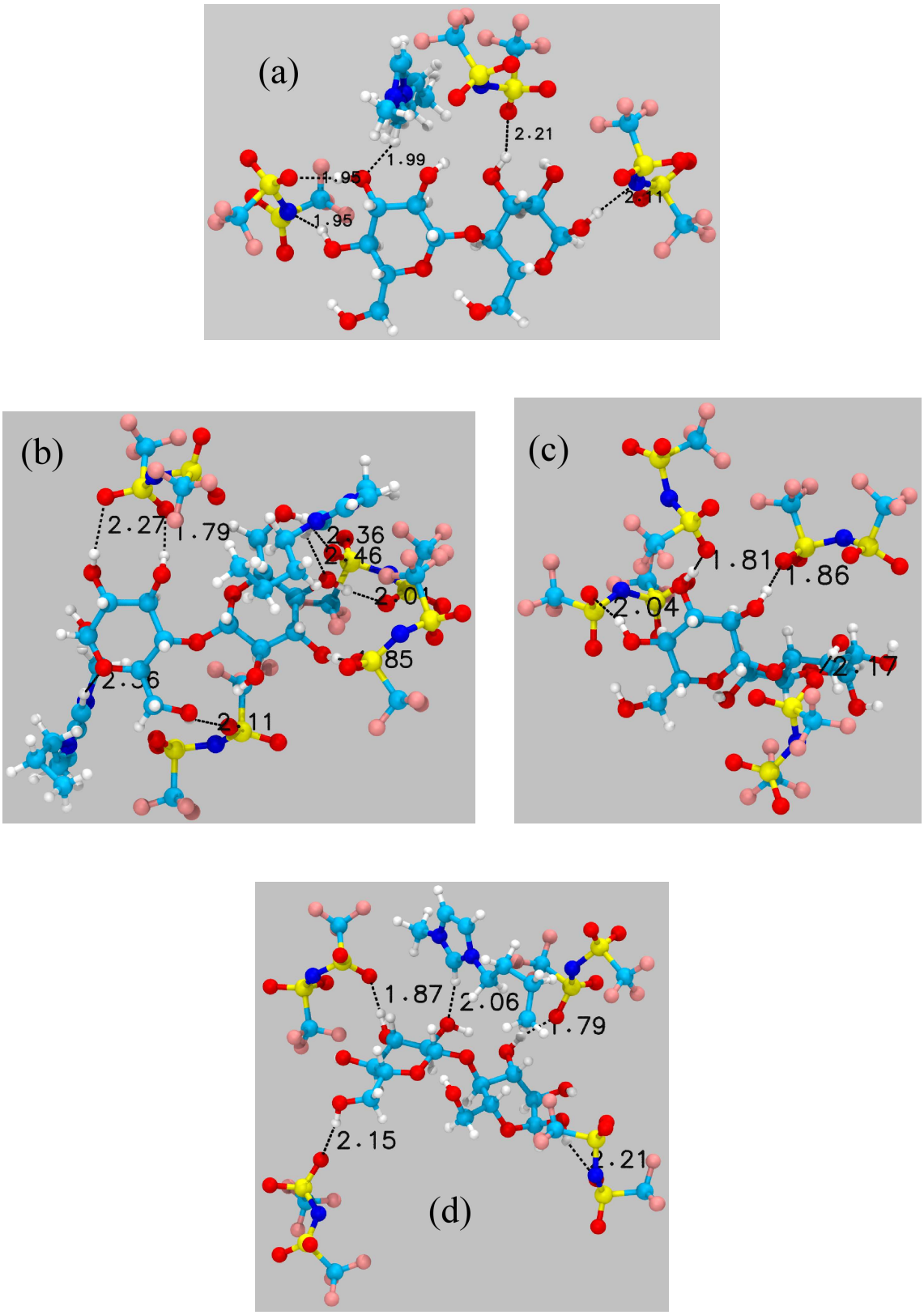

Figure 4.5: Hydrogen bonded ions around cellobiose in [bmim][NTf_2] at ϕ values (a) -160°, (b) -25°, (c) 120° and (d) 170°. Color scheme same as previous figures, S: Yellow and F: Pink.

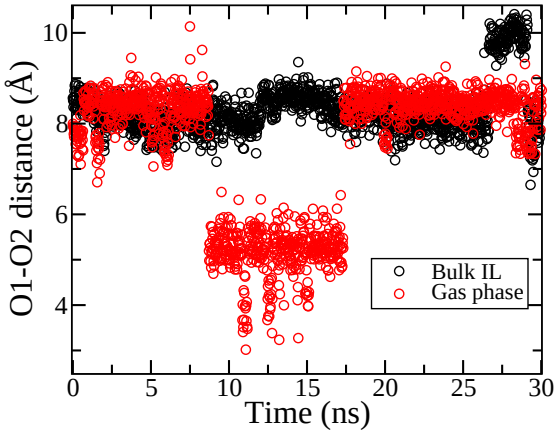

Figure 4.6: Distance between O1 and O2 atoms of cellobiose in gas phase and in bulk [bmim][OAc] during the free energy simulations. Cellobiose is found to be largely in the anti-anti conformation. Refer Figure 4.1 for the definitions of O1 and O2.

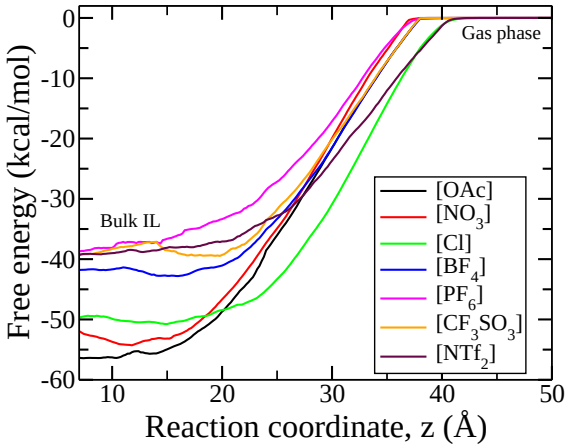

Figure 4.7: Solvation free energy of cellobiose in various RTILs, at 353 K.

Table 4.1: Binding energy of RTIL with cellobiose.

RTIL	Binding Energy (kcal/mol)	Solvation free energy (kcal/mol)
[OAc]	-31.8	-56.4
[NO_3]	-31.4	-53.7
[Cl]	-29.7	-49.9
[BF_4]	-25.6	-41.7
[PF_6]	-26.8	-36.5
[CF_3SO_3]	-26.0	-38.2
[NTf_2]	-27.9	-38.8

anions are nearly the same. [bmim][BF_4] exhibits an intermediate behavior. This behavior is also observed in the radial distribution function between hydroxyl hydrogen of cellobiose and the H-bonding site of anion(Figure 4.8). The first peak for $[OAc]^-$, $[NO_3]^-$ and $[Cl]^-$ occurs at 1.8 Å whereas for $[NTf_2]^-$, $[CF_3SO_3]^-$ and $[PF_6]^-$ it is at 2.10 Å. In the case of $[BF_4]^-$, the peak position is 2.0 Å. The trend in the SFE is similar to that exhibited by the binding energy of one ion pair of any RTIL with cellobiose. Table 4.1 provides BE of cellobiose with ion pairs in gas phase. A correlation between the BE in gas phase and SFE can be established, which is displayed in Figure 4.9, which suggests an enthalpic basis for cellulose dissolution.

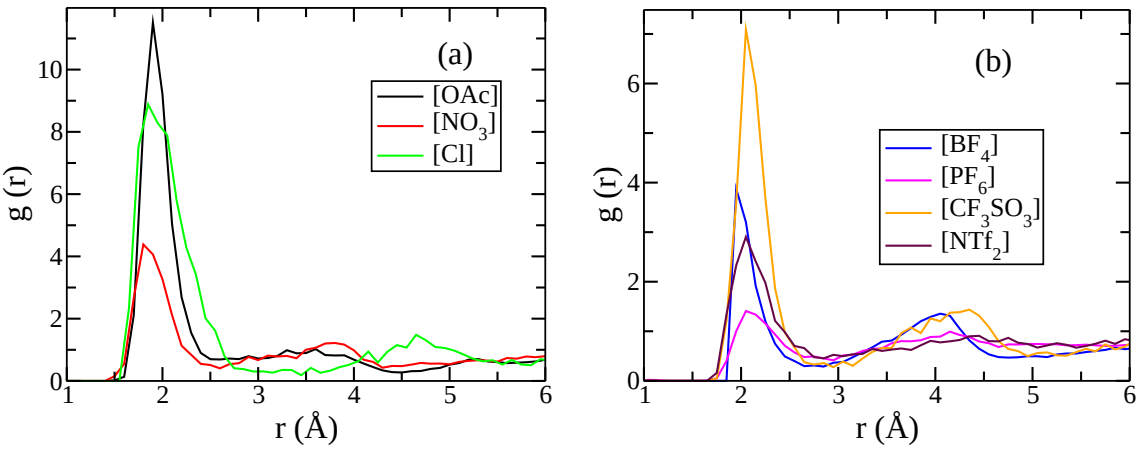

Figure 4.8: Radial distribution function between hydroxyl hydrogen of cellobiose and hydrogen bonding sites of anions.

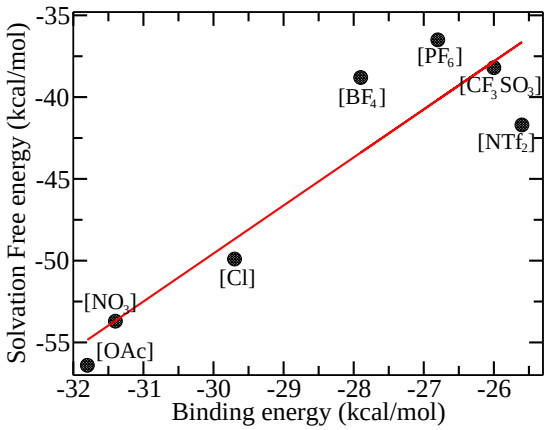

Figure 4.9: Binding energy of cellobiose with the ion pair where [bmim] is the cation versus the solvation free energy of cellobiose in bulk RTIL. The line is best fit for the data and positive slope indicates that the dissolution is determined by enthalpic contribution.

In Figure 4.7, moving in from the gas phase, the SFE profiles in most RTILs become non-zero at around 38 Å. However, in the cases of [bmim][Cl] and [bmim][NTf_2], such changes start at 41 Å itself. This observation can be explained by examining the density profile of the ions which is shown in Figure 4.10(a). The mean density in the bulk liquid region of the profile closely matches the values obtained from bulk-NPT simulations [52], as expected. Due to the larger molecular volume of [NTf_2] anion, the profile for [bmim][NTf_2] extends up to 40 Å on either side of the centre of mass. The thicker liquid slab thus leads to a wider SFE profile. Although the liquid-vapor interface of [bmim][Cl] is sharp (in terms of density profiles), its SFE profile at the interface is wide; during the ABF-MD simulations, the displacement of a few chloride ions from the liquid phase towards cellobiose (which was in gas phase) was observed. This is the underlying cause for the width in its SFE profile (see Figure 4.11).

As an illustrative case, Figure 4.10(b) shows the number density profile of cation ring center, anion center of mass and butyl terminal carbon atom of cation for [bmim][NTf_2]. As with many other RTILs [53], the interface is enriched with the butyl tail which is oriented nearly normal to the interface plane. An ultra-thin dielectric layer exists at the interface wherein the anion is present closer to the

vapor phase and the cation lies closer to the liquid phase.

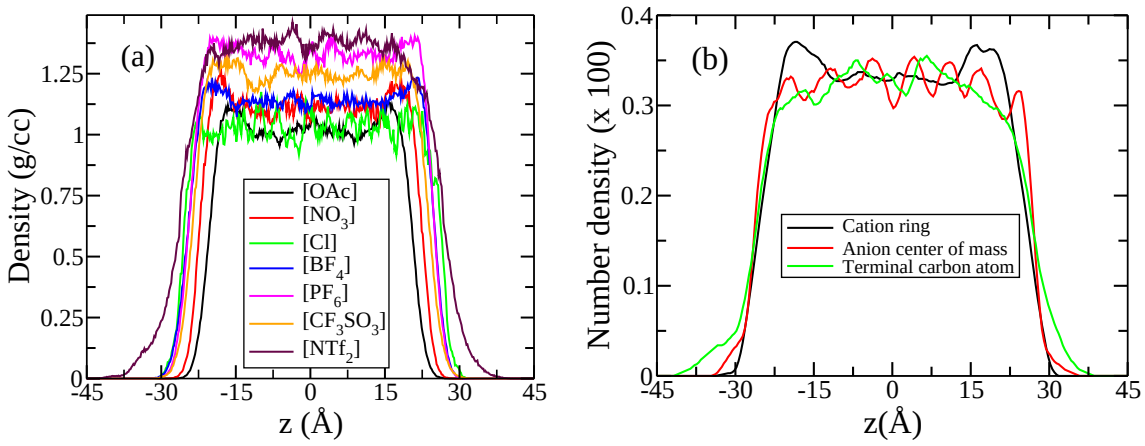

Figure 4.10: (a) Mass density profile of RTILs (b) number density profile of cation ring center, anion center of mass and terminal carbon atom of butyl tail in [bmim][NTf_2].

A break-up of the solvation free energy into its energetic and entropic contributions is vital to understand its anion dependence. Figure 4.12 provides the solvation free energy and potential energy profiles for cellobiose in [bmim][Cl]. The latter was calculated as the interaction energy of cellobiose with every other atom in the system. Similar profiles were calculated for all the liquids. Interestingly, the potential energy profile shows a small barrier at the liquid-vapor interface, which likely arises from the repulsive interaction between cellobiose and the butyl tails of the cation preferentially present at the interface. Similar barrier was present in the potential energy vs RC profiles in all RTILs. In bulk RTIL, the cellobiose is well solvated by the ions which leads to a large, negative potential energy. The difference between the solvation free energy and the potential energy equals the entropy change (times the temperature) upon solvation. The same has been calculated for cellobiose dissolution in different RTILs and is presented in Table 4.2.

In the case of [bmim][OAc], [bmim][NO_3] and [bmim][Cl], the energy differences are relatively high whereas the entropic contribution is moderate. Hence, the solvation free energy of cellobiose is higher in these liquids than in others. In

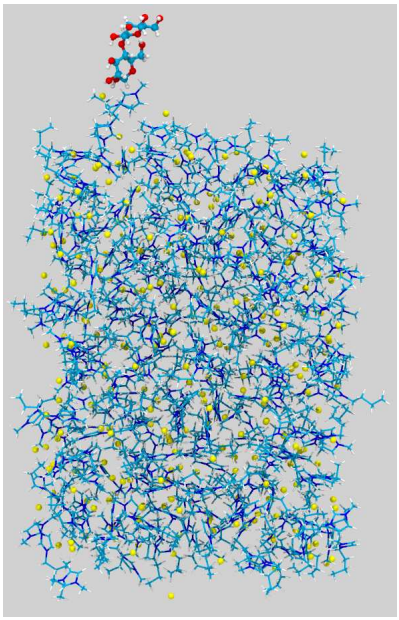

Figure 4.11: Snapshot of the simulation showing cellobiose present in gas phase disrupting the liquid-vapor interface for [bmim][Cl]. Color scheme Cl: Yellow, O: Red, C: Cyan, N: Blue and H: White.

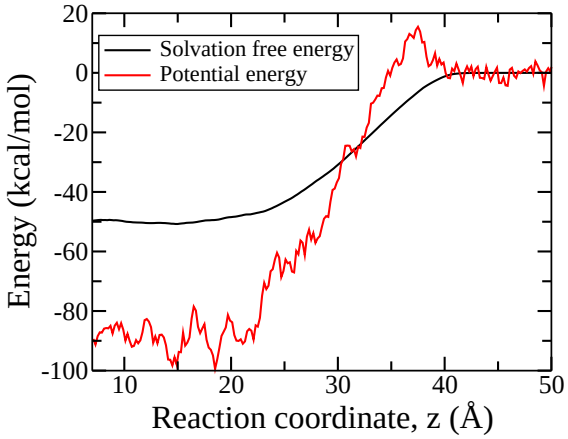

Figure 4.12: Solvation free energy and potential energy profiles of cellobiose in [bmim][Cl]. The two curves have been plotted by considering the respective gas phase values as reference.

[bmim][CF_3SO_3], both energy and entropy differences are high, and as a result, the net solvation free energy is low. In other RTILs, both energy and entropy contributions are moderate, causing the poor solubility of cellobiose in these RTILs. Among the RTILs studied here, the dissolution of cellulose is most facile in [bmim][OAc] as determined experimentally. The calculated SFE for cellobiose in [bmim][OAc] being

Table 4.2: Change in the free energy (ΔA= A_{liq}-A_{gas}), potential energy (ΔU= U_{liq}-U_{gas}) and entropy contribution ($T\Delta S$= U_{liq}-U_{gas}) for the dissolution of cellobiose in various RTILs relative to its gas phase. [bmim] is the cation and T= 353 K.

RTIL	ΔA (kcal/mol)	ΔU (kcal/mol)	TΔS (kcal/mol)	T$\Delta S/\Delta U$
[OAc]	-56.4	-113.8	-57.4	0.5
[NO_3]	-53.7	-84.1	-30.3	0.3
[Cl]	-49.9	-87.4	-37.4	0.4
[BF_4]	-41.7	-78.5	-36.7	0.4
[PF_6]	-36.5	-64.7	-28.1	0.4
[CF_3SO_3]	-38.2	-127.0	-88.7	0.7
[NTf_2]	-38.8	-71.1	-32.3	0.4

the most negative (among RTILs studied here) is consistent with the experimental observation and offers a microscopic understanding of its dissolution.

Figure 4.13 shows the distribution of the angle between the normal vector of the hexose rings of cellobiose. The distributions in [bmim][OAc] and [bmim][CF_3SO_3] are much broader than in other RTILs. They are also compared against the distributions in gas phase cellobiose in Figure 4.14. The larger width in these two RTILs indicates the facile deviation from planar geometry of cellobiose; it is also consistent with the high entropy difference (TΔS) in these two RTILs. The non-planar geometry is also responsible for the high enthalpy values as it allows for the formation of inter-molecular hydrogen bonds at the expense of intra-molecular ones.

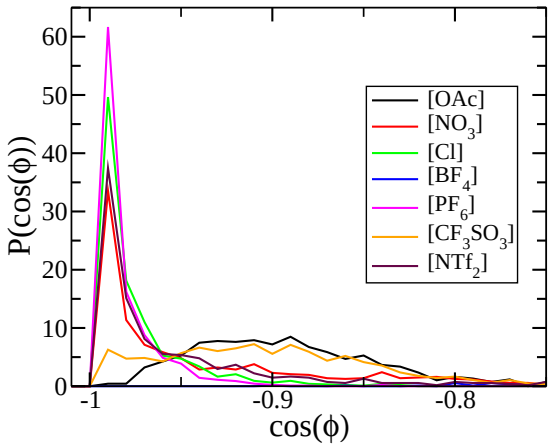

Figure 4.13: Distribution of the angle between the two hexose ring planes of cellobiose in various RTILs.

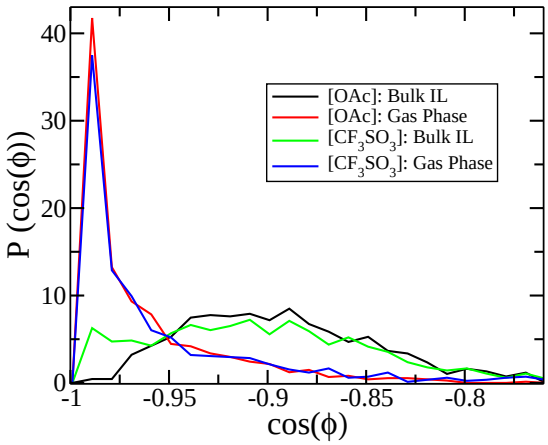

Figure 4.14: Distribution of angle between ring normals of cellobiose in gas phase and bulk RTIL.

4.4 Conclusions

In summary, these simulations show that a high enthalpy difference with a moderate entropic contribution appears to be vital in determining the solubility of cellulosic biomass in RTILs. A good solvent is one which contains a strong H-bond acceptor and a moderate H-bond donor. Anions have earlier been implicated to play an crucial role in cellulose dissolution and the same has been examined here. The experimental solubility of cellulose in RTILs varies as $[OAc]^-$>$[Cl]^-$>$[BF_4]^-$∼$[PF_6]^-$ [1, 3]. The SFE calculated here are consistent with the experimental observations.

The disruption of inter- and intra-molecular hydrogen bonding network of cellulose is the key to its dissolution mechanism. Fluorine in $[CF_3SO_3]$ makes it less basic due to its electron withdrawing nature. Replacing fluorine atoms with hydrogen can make it a better hydrogen bond acceptor. Methylsulfonate anion could also be explored as anion. Also, the reduction in the size of anion will result in less steric hindrance. This may also improve the solubility of cellulose in RTILs.

Bibliography

[1] Sun, N.; Rodríguez, H.; Rahman, M.; Rogers, R. D. *Chem. Commun.* **2011**, *47*, 1405–1421.

[2] Nishino, T.; Matsuda, I.; Hirao, K. *Macromolecules* **2004**, *37*, 7683–7687.

[3] Swatloski, R. P.; Spear, S. K.; Holbrey, J. D.; Rogers, R. D. *J. Am. Chem. Soc.* **2002**, *124*, 4974–4975.

[4] Zhu, S.; Wu, Y.; Chen, Q.; Yu, Z.; Wang, C.; Jin, S.; Ding, Y.; Wu, G. *Green Chem.* **2006**, *8*, 325–327.

[5] Zhao, B.; Greiner, L.; Leitner, W. *RSC Advances* **2012**, *2*, 2476–2479.

[6] Hummel, M.; Froschauer, C.; Laus, G.; Röder, T.; Kopacka, H.; Hauru, L. K.; Weber, H. K.; Sixta, H.; Schottenberger, H. *Green Chem.* **2011**, *13*, 2507–2517.

[7] Zhao, H.; Jones, C. L.; Baker, G. A.; Xia, S.; Olubajo, O.; Person, V. N. *J. Biotech.* **2009**, *139*, 47–54.

[8] Moulthrop, J. S.; Swatloski, R. P.; Moyna, G.; Rogers, R. D. *Chem. Commun.* **2005**, 1557–1559.

[9] Li, W.; Sun, N.; Stoner, B.; Jiang, X.; Lu, X.; Rogers, R. D. *Green Chem.* **2011**, *13*, 2038–2047.

[10] Freire, M. G.; Teles, A. R. R.; Rocha, M. A.; Schroder, B.; Neves, C. M.; Carvalho, P. J.; Evtuguin, D. V.; Santos, L. M.; Coutinho, J. A. *J. Chem Eng. Data* **2011**, *56*, 4813–4822.

[11] Binder, J. B.; Raines, R. T. *Proc. Nat. Acad. Sci.* **2010**, *107*, 4516–4521.

[12] Brandt, A.; Hallett, J. P.; Leak, D. J.; Murphy, R. J.; Welton, T. *Green Chem.* **2010**, *12*, 672–679.

[13] Zhang, H.; Wu, J.; Zhang, J.; He, J. *Macromolecules* **2005**, *38*, 8272–8277.

[14] Kosan, B.; Michels, C.; Meister, F. *Cellulose* **2008**, *15*, 59–66.

[15] Zakrzewska, M. E.; Bogel-Łukasik, E.; Bogel-Łukasik, R. *Energy & Fuels* **2010**, *24*, 737–745.

[16] Wishart, J. F. *Ener. & Environ. Sci.* **2009**, *2*, 956–961.

[17] Xie, H.; King, A.; Kilpelainen, I.; Granstrom, M.; Argyropoulos, D. S. *Biomacromolecules* **2007**, *8*, 3740–3748.

[18] Samayam, I. P.; Hanson, B. L.; Langan, P.; Schall, C. A. *Biomacromolecules* **2011**, *12*, 3091–3098.

[19] Li, B.; Asikkala, J.; Filpponen, I.; Argyropoulos, D. S. *Ind. Eng. Chem. Res.* **2010**, *49*, 2477–2484.

[20] Gao, D.; Chundawat, S. P.; Sethi, A.; Balan, V.; Gnanakaran, S.; Dale, B. E. *Proc. Nat. Acad. Sci.* **2013**, *110*, 10922–10927.

[21] Pinkert, A.; Marsh, K. N.; Pang, S.; Staiger, M. P. *Chem. Rev.* **2009**, *109*, 6712–6728.

[22] Wang, H.; Gurau, G.; Rogers, R. D. *Chem. Soc. Rev.* **2012**, *41*, 1519–1537.

[23] Sun, N.; Rahman, M.; Qin, Y.; Maxim, M. L.; Rodriguez, H.; Rogers, R. D. *Green Chem.* **2009**, *11*, 646–655.

[24] Brandt, A.; Hallett, J. P.; Leak, D. J.; Murphy, R. J.; Welton, T. *Green. Chem.* **2010**, *12*, 672–679.

[25] Fort, D. A.; Remsing, R. C.; Swatloski, R. P.; Moyna, P.; Moyna, G.; Rogers, R. D. *Green Chem.* **2007**, *9*, 63–69.

[26] Ohno, H.; Fukaya, Y. *Chem. Lett.* **2009**, *38*, 2–7.

[27] Vancov, T.; Alston, A.-S.; Brown, T.; McIntosh, S. *Renewable Ener.* **2012**, *45*, 1–6.

[28] Shen, T.; Langan, P.; French, A. D.; Johnson, G. P.; Gnanakaran, S. *J. Am. Chem. Soc.* **2009**, *131*, 14786–14794.

[29] Remsing, R. C.; Swatloski, R. P.; Rogers, R. D.; Moyna, G. *Chem. Commun.* **2006**, 1271–1273.

[30] Zhang, J.; Zhang, H.; Wu, J.; Zhang, J.; He, J.; Xiang, J. *Phys. Chem. Chem. Phys.* **2010**, *12*, 1941–1947.

[31] Youngs, T. G. A.; Hardacre, C.; Holbrey, J. D. *J. Phys. Chem.* **2007**, *111*, 13765–13774.

[32] Youngs, T. G.; Holbrey, J. D.; Deetlefs, M.; Nieuwenhuyzen, M.; Costa Gomes, M. F.; Hardacre, C. *ChemPhysChem* **2006**, *7*, 2279–2281.

[33] Liu, H.; Sale, K. L.; Holmes, B. M.; Simmons, B. A.; Singh, S. *J. Phys. Chem. B* **2010**, *114*, 4293–4301.

[34] Rabideau, B. D.; Agarwal, A.; Ismail, A. E. *J. Phys. Chem. B* **2013**, *117*, 3469–3479.

[35] Janesko, B. G. *Phys. Chem. Chem. Phys.* **2011**, *13*, 11393–11401.

[36] Guo, J.; Zhang, D.; Duan, C.; Liu, C. *Carbohydr. Res.* **2010**, *345*, 2201–2205.

[37] Liu, C.; Guo, J.; Zhang, D. *J. Theor. Comput. Chem.* **2010**, *09*, 611–624.

[38] Zhao, Y.; Liu, X.; Wang, J.; Zhang, S. *ChemPhysChem* **2012**, *13*, 3126–3133.

[39] Zhao, Y.; Liu, X.; Wang, J.; Zhang, S. *Carbohydr. Poly.* **2013**, *94*, 723–730.

[40] Payal, R. S.; Bharath, R.; Periyasamy, G.; Balasubramanian, S. *J. Phys. Chem. B* **2012**, *116*, 833–840.

[41] Payal, R. S.; Balasubramanian, S. *Phys. Chem. Chem. Phys.* **2014**, *16*, 17458–17465.

[42] Damm, W.; Frontera, A.; Tirado-Rives, J.; Jorgensen, W. L. *J. Comput. Chem.* **1997**, *18*, 1955–1970.

[43] Mondal, A.; Balasubramanian, S. *J. Phys. Chem. B* **2014**, *118*, 3409–3422.

[44] Hockney, R. W.; Eastwood, J. W. *Computer Simulation Using Particles*; Adam Hilger, 1988.

[45] Humphrey, W.; Dalke, A.; Schulten, K. *J. of Mol. Graph.* **1996**, *14*, 33–38.

[46] Fiorin, G.; Klein, M. L.; Hénin, J. *Mol. Phys.* **2013**, *111*, 3345–3362.

[47] Plimpton, S. *J. Comput. Phys.* **1995**, *117*, 1 – 19.

[48] Darve, E.; Rodríguez-Gómez, D.; Pohorille, A. *J. Chem. Phys.* **2008**, *128*, 144120.

[49] Bennett, C. H. *J. Comput. Phys.* **1976**, *22*, 245–268.

[50] Paluch, A. S.; Shah, J. K.; Maginn, E. J. *J. Chem. Theor. Comput.* **2011**, *7*, 1394–1403.

[51] Paluch, A. S.; Mobley, D. L.; Maginn, E. J. *J. Chem. Theor. Comput.* **2011**, *7*, 2910–2918.

[52] Mondal, A.; Balasubramanian, S. *J. Phys. Chem. B* **2014**, *118*, 3409–3422.

[53] Bhargava, B.; Balasubramanian, S. *J. Am. Chem. Soc.* **2006**, *128*, 10073–10078.

Chapter 5

Orientational ordering of room temperature ionic liquids near a charged mica surface*

5.1 Introduction

Room temperature ionic liquids (RTILs) exhibit rich intrinsic characteristics such as charge ordering, and nanoscale heterogeneity [1]. The length of the alkyl group is one of the many parameters which can be used to tune their phase behavior, viscosity and polarity. The presence of an interface (either near a vapor or near a solid) introduces another dimension to the problem. Charge ordering at the RTIL-vapor interface manifests itself as out-of-phase density oscillations [2]. The surface of the liquid in equilibrium with its vapor is found to be largely hydrophobic, with the alkyl groups protruding out into the vapor phase. Various workers have evinced keen interest in studying the interface between RTILs and a solid [3, 4]. The structure of RTILs adsorbed on substrates such as mica, graphite and metals have been studied

*Work reported in this chapter is published in: R. S. Payal and S. Balasubramanian, ChemPhysChem **13**, 1764-1771 (2012). Reproduced by permission of John Wiley and Sons. Copyright 2012 WILEY-VCH Verlag GmbH & Co. KGaA, Weinheim.

using a variety of techniques, including atomic force microscopy, sum frequency vibrational spectroscopy [5, 6] and atomistic computer simulations [7–9]. The solid-liquid interface of RTILs is important in electrochemistry and nano-lubrication. In particular, an understanding of this interface is crucial in the application of RTILs in solar cells and supercapacitors [10–13].

Atomic force microscopy (AFM) experiments by Liu *et al* have shown the formation of a crystalline phase of $[C_4mim][PF_6]$ (where $C_n$mim refers to the 1-methyl,n-alkylimidazolium cation) on atomically flat mica surfaces [14]. Unlike water which forms an ice-like phase on mica but which is fragile [15], the solid structures of the RTILs were found to be undisturbed by the force applied in AFM measurements. Using similar techniques, Atkin and coworkers have demonstrated the existence of nearly five to six solvation layers in a variety of aprotic RTILs deposited on mica [16]. The solid-like ordering of $[C_4mim][NTf_2]$ has also been studied on mica, amorphous silica and oxidized Si(110) surfaces by Bovio *et al* [17] and on graphite and mica by Yokota *et al* [18]. Perkin and coworkers examined the layering and shear profiles of 1-ethyl-3-methylimidazolium ethylsulfate confined between two mica surfaces using the surface force apparatus [19]. Molecular dynamics simulations of the RTIL-graphite (or graphene) systems have affirmed the pronounced layering [20–22]. A recent work by Saramago and coworkers has looked at an ethanolic solution of $[C_8mim][BF_4]$ deposited on aluminum substrate [23]. Using both AFM imaging and advanced simulation methods, they conclude that the structure of the adsorbed layers is dependent on concentration and strongly on time. The summary of all these studies is the solid-like ordering of ions at the interface. In many cases, the lattice too has been imaged. However, details of molecular level arrangement have not been fully explored.

The literature on fluids adsorbed on a mica surface is rather vast; hence, the focus here is on a few selected simulation studies. Heinz and coworkers have extensively

examined the organization (self-assembly) of alkylammonium chains grafted on a negatively charged mica surface [24, 25]. In particular, they have developed the consistent valence force field (CVFF) for mica and have taken into account the exchange of surface potassium ions of mica with the cations of the adsorbate [24]. They have also studied the phase transitions of the adsorbed layers as a function of temperature [26]. Kirkpatrick and coworkers have studied the nature of hydrogen bonding between liquid water and the surface oxygen atoms of mica using molecular dynamics simulations [27].

Recently, Perkin and coworkers have observed an interesting phenomenon [28]. They carried out measurements of the surface force of RTILs confined between two mica surfaces. The anion was bis(trifluoromethylsulfonyl)-imide (NTf_2), while the cation was [$C_n$mim]. The solid substrates induce layering of the ions which was observed as oscillations in the profile of the surface force as a function of the distance between the two surfaces. For the [C_4mim] based RTILs, the periodicity in the profile was between 0.9 to 1.4 nm. This corresponds to the thickness of a cation and an anion monolayer, in which the alkyl group of the cation lies parallel to either of the two mica surfaces. Interestingly, for the [C_6mim] based RTILs, the periodicity increased to about 2.7 nm, indicating the arrangement of cations whose alkyl tails are oriented perpendicular to the surface. Since the RTIL was confined between two mica surfaces, such an orientational ordering led to the formation of a bilayer. This result is novel and unlike that seen in the bulk form of these liquids. For instance, a liquid crystalline phase in [$C_n$mim][PF_6] appears only for values of n greater than 14 [29]. The interplay between the Coulombic interactions preferred between the charged imidazolium ring of the cation with the mica surface and the propensity for the alkyl groups to aggregate, seems to lower the threshold of the alkyl chain length at which the orientational ordering is observed.

Molecular simulations are ideally placed to offer a microscopic window to this

problem. These simulations have been able to quantitatively reproduce experimental data on nanostructuring and bulk physical properties such as viscosity, electrical conductivity and heat of vaporization [30–32]. It is thus crucial that the RTIL-mica interface be studied using such methods. This work is aimed in that direction. Atomistic molecular dynamics (MD) simulations were done for four RTILs of the kind, $[C_n mim][NTf_2]$ near a negatively charged mica surface and compare these results to the experiments of Perkin *et al* [28]. Although the experiments have been conducted for a liquid confined between two surfaces, these simulations consider the RTIL adsorbed near a single surface. As can be seen from the results, the phenomenon of orientational change with increase in tail length is independent of whether the liquid is confined or not. Anticipating the results, it was found that the layering of ions at the interface and a clear change in the orientation of the hydrocarbon tail of the cation between the C_4 and the C_6 based RTILs. Details of the simulations are present in the next section. This is followed by the presentation and discussion of results.

5.2 Computational details

In the present work, the self assembly of $[C_n mim][NTf_2]$ (where n=2, 4, 6, and 8) on the surface of muscovite mica (see Figure 5.1 for a schematic of the ions employed) have been investigated. Two different set of simulations were carried out. In Set A, the CLAYFF force field was employed for describing the interaction of the mica surface, while in Set B, the CVFF force field was employed. Other crucial differences are: (i) in Set A, atoms of the mica were held rigid (thus were at absolute zero temperature), while in Set B, they were free to move and (ii) full exchange of the surface potassium ions of the mica were considered to be exchanged with the imidazolium cations of the RTIL.

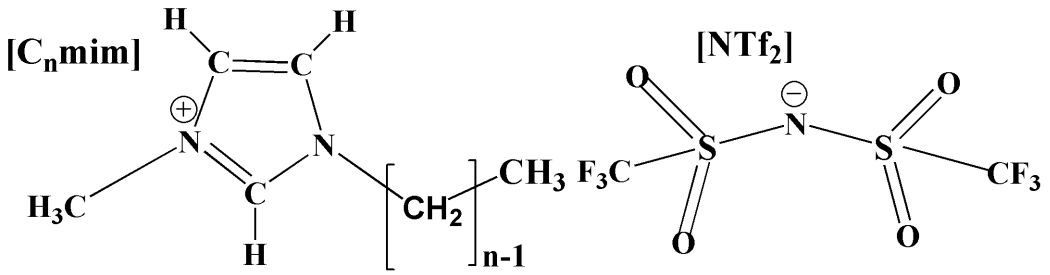

Figure 5.1: Schematic of the cation, [C$_n$mim] (where n=2, 4, 6 or 8) and the anion, [NTf$_2$].

Clay force field : CLAYFF is a general, all-atom force field for natural hydrated materials, e.g. hydroxides,orthohydroxides and clays. Potential energy in CLAYFF is calculated as a combination of electrostatic and Lennard-Jones 12-6 interaction. Bond and angles are modelled using the harmonic approximation. It is not only suited for the multi-mineral components, but their interfaces with fluids too. The ability to distinguish between tetrahedral and octahedral aluminum is a special feature of CLAYFF.

Consistent valance force field: CVFF force field for interfaces was developed by Prof. Heinz's group [24]. This is an all-atom force field used to describe minerals, oxides and metals. The potential form for CVFF is similar to that of CLAYFF. These force fields were especially developed to reproduce surface energetics of minerals or oxides interface with water, organic molecules or biomolecules.

First, the protocols for the simulations of Set A is described. Firstly, the liquids were equilibrated in bulk and were later placed on the mica surface. The initial configuration of RTILs were generated using the Packmol software package and the dimensions of the simulation box were L$_x$= 46.86 Å, L$_y$ = 54.1 Å and L$_z$ = 80.0 Å [33]. The number of ion pairs for [C$_2$mim][NTf$_2$], [C$_4$mim] [NTf$_2$], [C$_6$mim][NTf$_2$], and [C$_8$mim][NTf$_2$] were 475, 418, 372, and 332 respectively. Each system was equilibrated under constant NVT conditions at 300 K for 2 ns. Periodic boundary conditions were applied in all the three directions. The RTILs were modeled with the force field developed by Ludwig *et al* [34]. The potential of interaction was cutoff at

13 Å and a timestep of 0.5 fs was used to integrate the equations of motion. The long range part of the electrostatic interactions were treated using the particle-particle particle mesh (PPPM) method. The equilibrated liquid was then placed over the mica surface with the condition that the no atom should be closer than 3 Å from the surface. The mica surface consisted of 9 x 6 unit cells of linear dimensions L_x= 46.86 Å and L_y= 54.1 Å and the z-axis was chosen as the surface normal. In the z-direction, the mica slab had a thickness of 18.13 Å. The interfacial simulations too were carried out in the canonical ensemble with three dimensional periodic boundary conditions. The box length in the z-direction was set to 280 Å. It ensured that there were no image interactions and thus a clean liquid-vapor interface too was obtained. The system thus consists of a liquid-solid and a liquid-vapour interface. Atoms of the mica were treated as rigid. In mica, each unit cell contains two K^+ ions. On the surface of the sheet, every other K^+ ion was removed and was subsequently placed on the bottom part of the mica sheet. This procedure creates site disorder mimicking the real system, and has been employed earlier by Malani and Ayappa to study the adsorption of water on mica [35]. The interaction parameters of atoms belonging to mica were from the CLAYFF force field and the Lorentz-Berthelot combining rule has been employed to obtain interaction parameters between atoms of mica and those of the RTIL [36]. The length of the simulations on the surface were: 6 ns (C_2), 6 ns (C_4), and 12 ns each for the C_6 and C_8 based RTILs.

In the simulations of Set B, atoms of the mica were treated using the CVFF force field. Unlike CLAYFF, the atoms belonging to mica carry partial charges under CVFF. The use of large atomic charges in CLAYFF have been shown to lead to inaccurate prediction of surface energies when compared to experiments [24]. Apart from bond stretching and angle bending interactions, this force field contains non-bonded electrostatic and 9-6 terms as well. An equivalent Lennard-Jones (12-6) parametrization of CVFF has also been developed by Heinz *et al* [24], which was used

in the current work, as it was amenable to the use of Lorentz-Berthelot combination rules for the mica-RTIL interaction. The parameters of the force field were taken from Heinz *et al* [24]. Since the layering of the RTIL was found not to exceed beyond 25 Å in the simulations of Set A, the system size in Set B was reduced. As before, simulations of the bulk liquids were carried out for 2 ns at 300 K containing the following number of ion pairs: 294, 270, 240 and 215 for the [$C_n$mim] cation based (n=2,4,6, and 8) family. The x,y dimensions of the simulation box in Set B were 51.918 Å and 54.0918 Å respectively, commensurate with the lattice dimensions of the mica sheet that was to be used later. Coordinates of mica sheet were obtained from Prof Heinz's website [37] (Four replicas of mica15_single_sheet.car was used).

The exchange of potassium ions present on the mica surface with the cations of the RTIL was mimicked by removing those K^+ ions. Simultaneously, an equal number of anions selected arbitrarily from the liquid were also removed for reasons of charge neutrality. Thus, for instance in the simulations of [C_2mim][NTf_2] on mica, 294 [C_8mim] and 234 [NTf_2] ions were present. Again, three dimensional periodic boundary conditions were employed and the box length in the z-direction (direction of the surface normal) was set to 200 Å. In simulations of Set B, the coordinates of the atoms of the mica were treated as additional degrees of freedom. Atoms of the RTIL and that of mica were connected to two independent Nosé-Hoover thermostats, both maintained at a temperature of 300 K. The adsorbed RTILs were equilibrated on the surface for 2 ns. Later, a trajectory of 12 ns (16 ns for the C8 system) was generated in which the last 6 ns was used for analysis. In the calculation of the density profiles in Set B, the time-averaged position of the surface oxygen atoms belonging to mica was taken to be at z=0. The simulations were carried out using the LAMMPS package [38]. Simulation trajectories were visualized and snapshots were taken using the VMD [39].

5.3 Results and discussion

The heterogeneity exhibited by the RTIL at the interface can be captured using density profiles of the geometric centre of the cation, of the center of mass of the anion and of the terminal methyl group of the longer alkyl group [C_n] of the cation. Significant changes are observed in the behavior of these profiles for various RTILs.

5.3.1 Density profiles

Set A simulations (CLAYFF): Figure 2 shows the density profiles of various liquid films obtained from simulations of Set A. All of them exhibit pronounced oscillations near the surface implying the layering of molecules. The profile for the ring center of the cation (Figure 5.2(a)) exhibits a sharp peak at a distance of 3.9 Å away from the mica surface (or, at 3.69 Å from the oxygen atoms of the surface). A subtle feature to be noted in the cation density profile is the decrease in the minimum intensity beyond the second peak (around 14 Å) for the C_6 and C_8 based RTILs, relative to the values for cations with shorter alkyl substitutions. It signifies the possible ordering of cations which is more evident in the profile of density of the terminal methyl group. Further, the intensities of the second, third and the fourth peaks are nearly identical in the profiles of C_6 and C_8 based RTILs compared to the progressive decay in C_4 and C_2 based RTILs.

The density profile of the central nitrogen atom of the anion from Set A is shown in Figure 5.2 (b). It exhibits two rather sharp features (it was considered they together constitute the first peak) near the surface, independent of the chain length. However, the relative intensities of these two features changes as a function of the tail length. For the C_2 system, the first of these features is shorter than the second, while for RTILs with cations possessing longer tails, the opposite behavior is observed. The position of the formal second peak shows much variation with alkyl chain length. While for the C_2 and C_4 liquids it is present between 11 and 12 Å, the

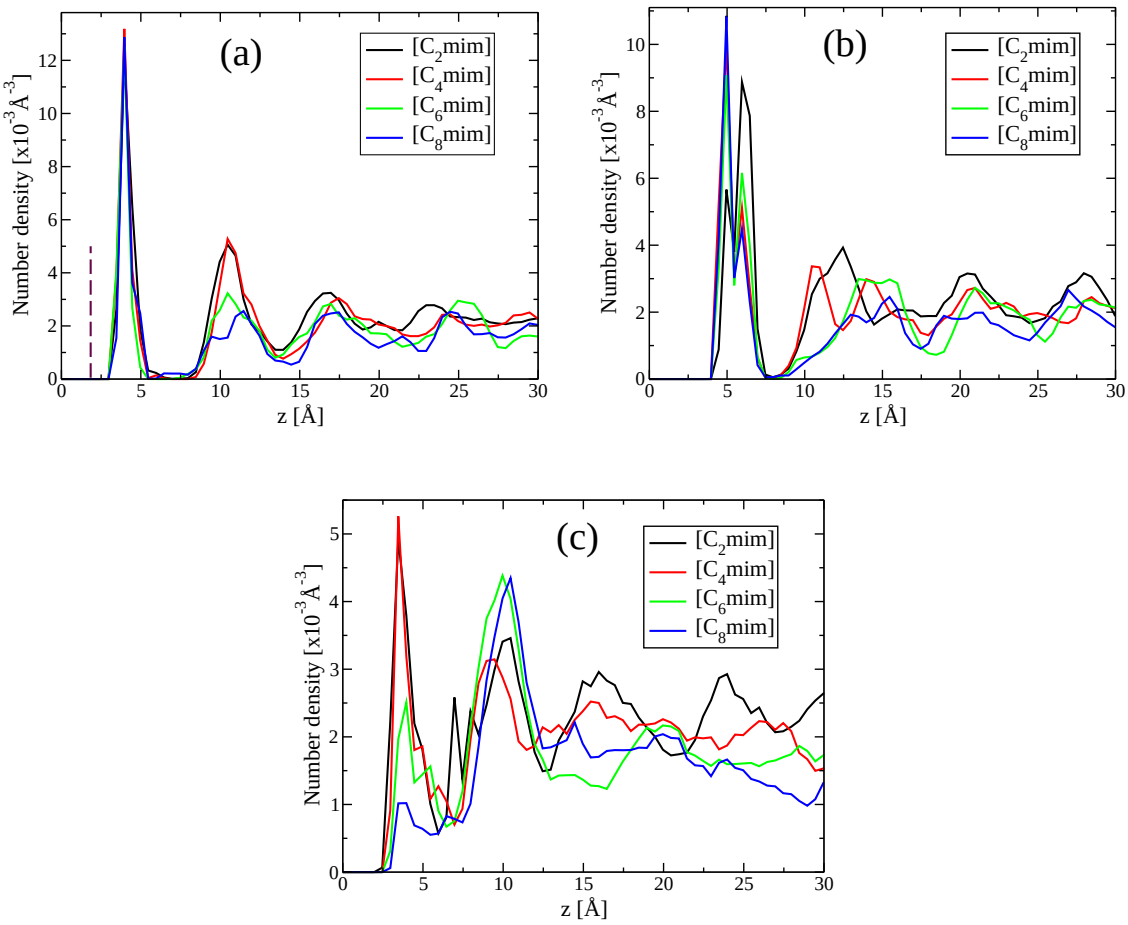

Figure 5.2: (a) Density profile of the geometric ring center of the cations of various RTILs adsorbed on mica. The dashed vertical line is the position of the top layer of K^+ ions of the mica. (b) Density profile of the nitrogen atom of the anion of various RTILs adsorbed on mica. (c) Density profile of the terminal methyl group of the cations of various RTILs adsorbed on mica. The results are from simulations of Set A.

peak is shifted by nearly 6 Å (to larger distances) in the case of C_6 and C_8 based RTILs. Within the anion, the nitrogen atom is located closer to the surface and the less polar character of the CF_3 group keeps it away from the surface (Figure 5.3). The changes seen in the anion density profile are likely related to the ordering seen in the cation density profiles and effectively signals the establishment of a charge depletion layer where anions (as well as the cation ring) are forbidden; this region is likely to be occupied by the non-polar alkyl tail of the cation.

A direct evidence of this effect is obtained through an analysis of the density

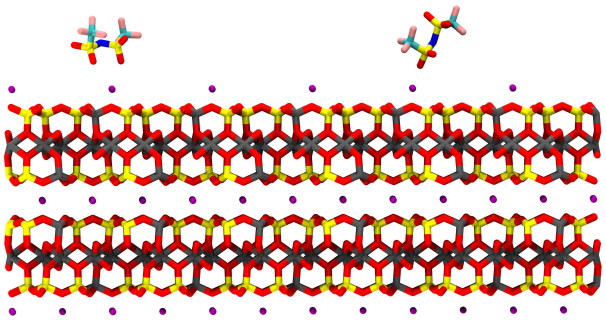

Figure 5.3: CF_3 group in anion tends away from the surface. The results are from simulations of Set A. Color scheme. Sulfur: Yellow, Nitrogen: Blue, Oxygen: Red, Fluorine: Pink, Potassium: Purple, Aluminium: Grey and Carbon: Cyan.

profile of the terminal methyl group which is shown in Figure 5.2(c) (again, from simulations of Set A). The intensity of the first peak in the density profile of the terminal methyl group decreases dramatically for the C_6 and C_8 systems, in contrast to its high value in the C_2 and C_4 based RTILs. Simultaneously, the second peak in the former liquids grows in intensity. The contrasting behavior of the organization of the cations in these two categories of RTILs is brought out well in Figure 5.4. It compares the density profiles of the cation ring center and of the terminal methyl group between the C_2 and C_8 systems. With respect to mica, the ring center is located at the same position in both the RTILs. However, while the terminal methyl group in the C_2 system is located at nearly the same z-value as the ring center, that in the C_8 liquid shows much less intensity at this location. Instead, its density profile for $[C_8mim][NTf_2]$ exhibits larger intensities around the second peak. This is a clear indication of the depletion of the non-polar terminal methyl group close to the surface and its preponderance at a distance much farther away from the charged mica surface.

Set B simulations (CVFF): Similar density profiles as those obtained using Set A simulations were obtained with those from Set B. These are presented in Figure 5.5. Figure 5.5(a) presents the density profile of the ring center of the cation. With increasing length of the alkyl tail, the position of the first peak decreases by

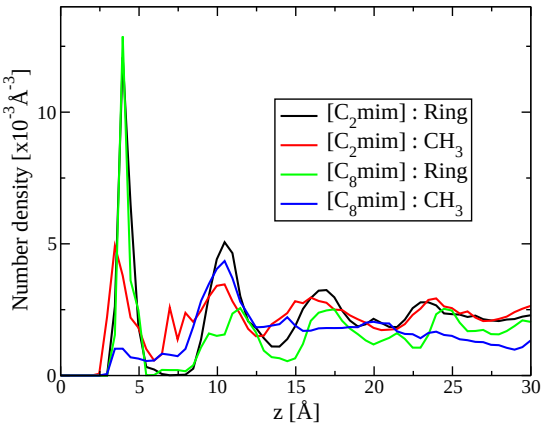

Figure 5.4: Comparison of the cation ring centre and the terminal methyl group density profiles of $[C_2mim][NTf_2]$ and $[C_8mim][NTf_2]$ RTILs. The results are from simulations of Set A.

about 1 Å between the C_2 and the C_8 systems. In fact, for cations with intermediate tail lengths, the first peak is split into two; the position of each of these features coinciding with either that of C_2 or of C_8. The relative intensities of these two features too exhibit a clear trend with increasing tail length. These differences arise from changes in the orientation of the imidazolium ring plane with respect to the surface. This aspect will be explored further later. The orientation of the alkyl tails with respect to the surface can be surmised from the ring density profiles themselves. While the second peak in the C_2 system is present at around 11.3 Å, that in the C_8 system is present at 12.8 Å (a broad one), indicating the larger ring-ring separation (in the z-direction) for the C_8 system.

A remarkable difference in the two sets of simulations is in the anion density profiles. Since the mica surface is devoid of potassium ions in simulations of Set B, the first adsorbed layer is purely made of imidazolium cations in this set. Thus, the anions lie much farther away from the surface in the simulations of Set B than in Set A. This can be observed from Figure 5.5(b) which shows the anion density profiles of all the systems. The intensity of the first peak decreases with increasing tail length and there is a slight shift to higher distances as well. In the C_2 system, the layer of anions closest to mica is found beyond the first cation layer. However, in the C_6

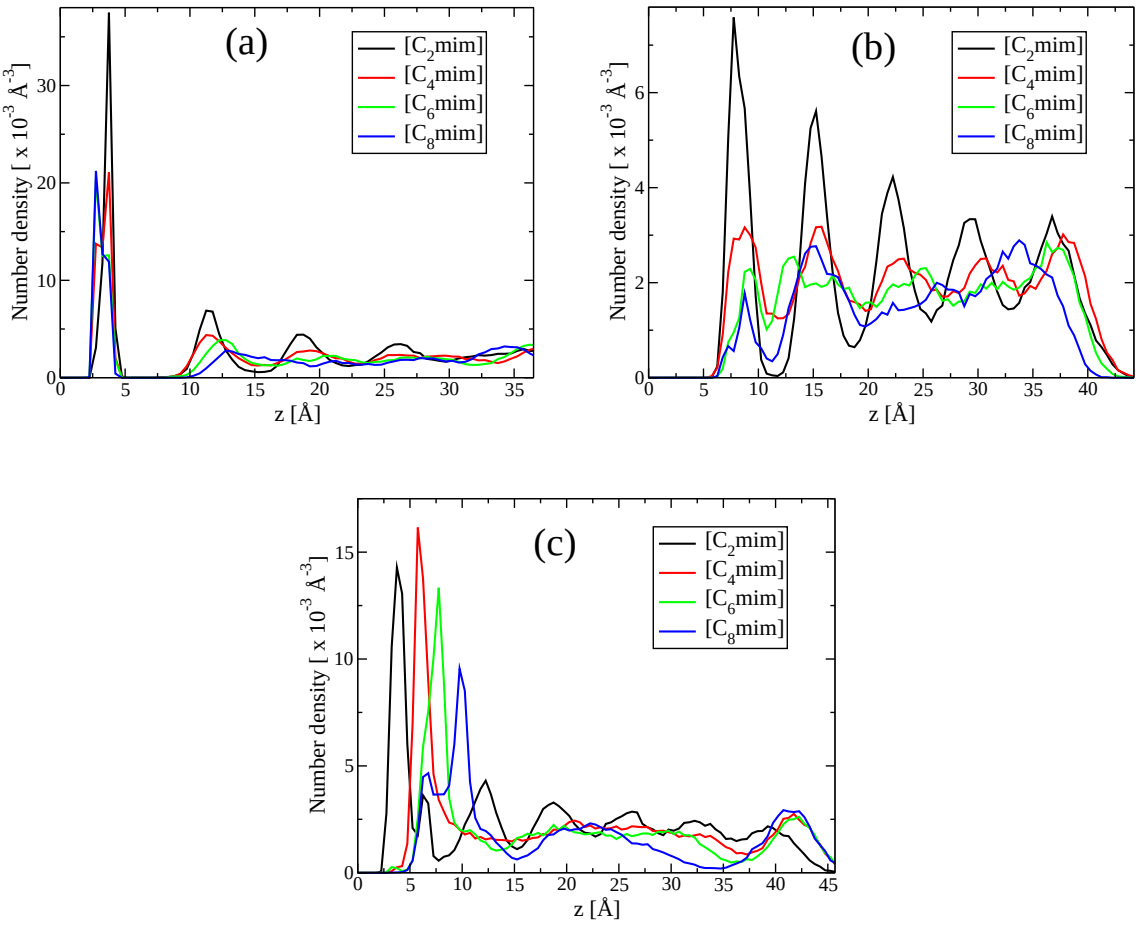

Figure 5.5: (a) Density profile of the geometric ring center of the cations of various RTILs adsorbed on mica. (b) Density profile of the nitrogen atom of the anion of various RTILs adsorbed on mica. (c) Density profile of the terminal methyl group of the cations of various RTILs adsorbed on mica. The results are from simulations of Set B.

(or C_8) systems, such anions are more or less at the same position as the terminal methyl group of the cation. Effectively, the anions share (though to a minor extent) the first adsorbed layer in the C_6 (or C_8) system than in the C_2 system. Absence of potassium ion increases the ordering of the cation near mica surface, which in turn leads to an increase in anion ordering. This change is significant for C_2 and C_4 systems. In the case of C_6 and C_8, due to their large alkyl tails, the net positive charge experienced by the anion is lesser, resulting in less ordered distributions of anions.

The density profiles of the terminal methyl groups shown in Figure 5.5(c) has many similarities with those seen for Set A; however, there are distinct differences as well. The position of the first peak shifts to larger values as the length of the alkyl tail increases, indicating the reorientation of the alkyl group with respect to the surface normal. This fact can be understood better through a comparison of the density profiles of the ring center and the terminal methyl for the C_2 and C_8 systems. Figure 5.6 shows the same. The position of the first peak in the terminal methyl profile coincides with that of the ring center for the C_2 system. However, in the case of the C_8 system, the terminal methyl group of the cations in the first adsorbed layer is far away from the surface (or from the ring center), clearly indicating the changed orientation of the alkyl group for the C_8 cation. The profile for the terminal methyl in the C_8 system shows a split first peak; this is likely due to the presence of gauche defects in the octyl tail of cations present in the first adsorbed layer.

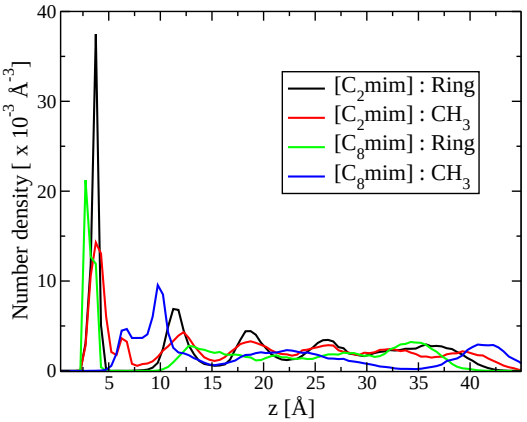

Figure 5.6: Density profile of the cation ring center and the terminal methyl group of the cations of [C_2mim][[NTf_2] and [C_8mim][NTf_2] RTILs adsorbed on mica. The results are from simulations of Set B.

5.3.2 Orientational distributions

Set A simulations (CLAYFF): The increase in the probability to find a terminal methyl group at a farther distance from mica is likely to be related to a change in the orientation of the cation with respect to the mica surface. Figure 5.7 shows the

distribution of the angle that the N-C vector (the nitrogen to the terminal carbon of the C_n alkyl group) of a cation makes with the surface normal. The distributions are calculated from those cations which are present in the first adsorbed layer, as defined using a distance cutoff based on the density profile of the ring center of the cation. In the C_2 cation based RTIL, the distribution shows three peaks at values of -0.5, +0.1 and +0.95. These correspond to angles of 120°, 85° and around 5°. Thus, a few of the C_2mim cations lie with the long axis of the ethyl group parallel to the surface while the rest could be found nearly parallel to the surface normal. A gradual change in this distribution is observed with increasing length of the alkyl tail. For the C_6 and C_8 systems, barely any intensity is found in the negative region of the abscissa. This is due to the fact that in these liquids, the terminal methyl groups of cations in the first adsorbed layer are much farther away from the surface than the nitrogen atom (which is part of the ring and thus is near the center of the positive charge). A concomitant increase in the population of cations with their alkyl tails oriented nearly parallel to the surface normal is observed ($\cos(\theta)$ values larger than +0.7). The significant change in the orientation of the alkyl group for cations with longer alkyl chains is consistent with recent observations from surface force measurements by Perkin *et al* [28].

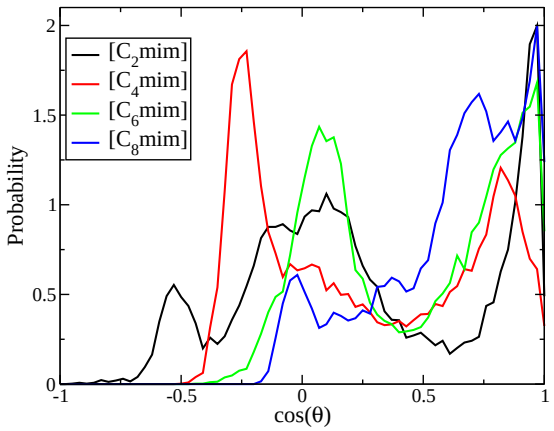

Figure 5.7: Probability distribution of the orientation angle of the hydrocarbon tail of cations present in the first adsorbed layer with respect to the surface normal. The results are from simulations of Set A.

Set B simulations (CVFF): The orientational distribution of the alkyl tail of the cation with respect to the surface normal for these simulations are shown in Figure 5.8(a). The distribution for the ethyl cation exhibits a peak at a cos(θ) value of around 0.2 and thus the N-C vector of the imidazolium cation is nearly perpendicular to the surface normal. However, as the length of the alkyl tail increases, the distribution changes dramatically. For instance, in the C_8 system, it exhibits a sharp peak around a value of 0.97 indicating that the N-C vector of the octyl group is parallel to the surface normal. This is quite consistent with the experimental observations of Perkin *et al* [28]. Another noteworthy feature is the progressive change in the orientational distribution as a functional of alkyl tail length. The distribution of the orientation of the imidazolium ring normal is shown in Figure 5.8(b). In the case of the C_2 cation, the plane of the ring is more or less perpendicular to the surface. However, in the C_8 case, the ring plane is parallel to the surface, primarily to aid the N-C vector of the longer chain to be oriented parallel to the surface normal.

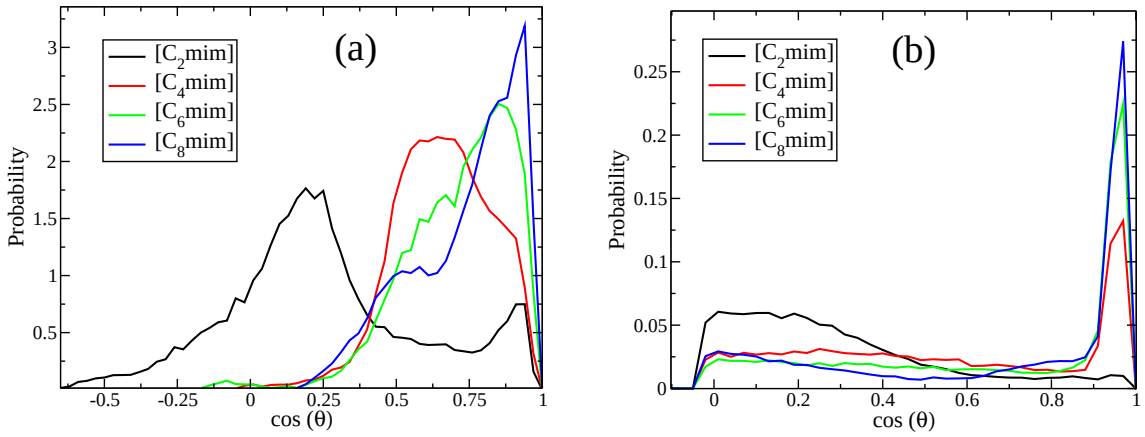

Figure 5.8: (a) Probability distribution of the orientation angle of the hydrocarbon tail of cations present in the first adsorbed layer with respect to the surface normal. (b) Probability distribution of the angle between the ring plane of cations present in the first adsorbed layer with the surface normal. The results are from simulations of Set B.

Snapshots of configurations of ions present in the first adsorbed layer in the C_2 and C_8 RTILs obtained from Set A simulations are shown in Figure 5.10. In the latter, the arrangement of cations with their long axes oriented parallel to the normal to mica surface is clearly seen and the lateral arrangement of ions is ordered. The charged mica surface clearly templates this ordering, which can also be seen in the top view. Similar snapshots obtained from simulations of Set B are shown in Figure 5.11. The similarity in the side views obtained from these two sets (A and B) of simulations is striking and the conclusion is unambiguous. The cation with the longer alkyl tail orients its tail parallel to the surface normal, while that with the shorter tail is perpendicular to it. The change in the orientation of the ring plane between the C_2 and the C_8 systems (obtained from Set B simulations) can also be seen in the top views. Another difference seen between Figures 5.10 and 5.11 is that in the latter, the first adsorbed layer is devoid of anions; however in simulations of Set A, few anions are present in that layer due to the presence of the potassium ions of the mica on the surface. In Set A, mica was treated as rigid. Hence, molecules of the first layer of the RTIL are nearly in an ordered arrangement, as can be seen from the top view shown in Figure 5.10 . However, the thermalization of the mica atoms in simulations of Set B seems to melt the first adsorbed layer of the RTIL. Shown in the Figure 5.11(c) is an enlarged version of a small region of the first adsorbed layer obtained from Set B simulations. In the C_2 system, the imidazolium ring plane is oriented perpendicular to the surface and the acidic proton points toward the surface. In the C_8 system, the orientation of the alkyl group along the surface normal and the consequent parallel orientation of the ring plane and the mica surface is unambiguously seen.

The mean squared displacement (MSD) of ions present in the first adsorbed layer in C_2 systems reported here (Figure 5.9), show sluggish dynamics over the time scales of the simulations. The displacement values over a few nanoseconds is

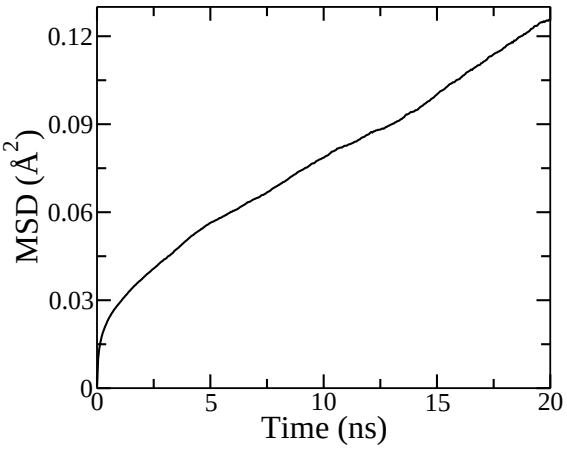

Figure 5.9: Mean square dispalcement of cation center for $[C_2mim][NTf_2]$ adsorbed on mica (first layer). The results are from simulations of Set B.

less an Angstrom. Hence, although one cannot obtain values of diffusion coefficients from such data, it is likely that they will behave in a glassy manner.

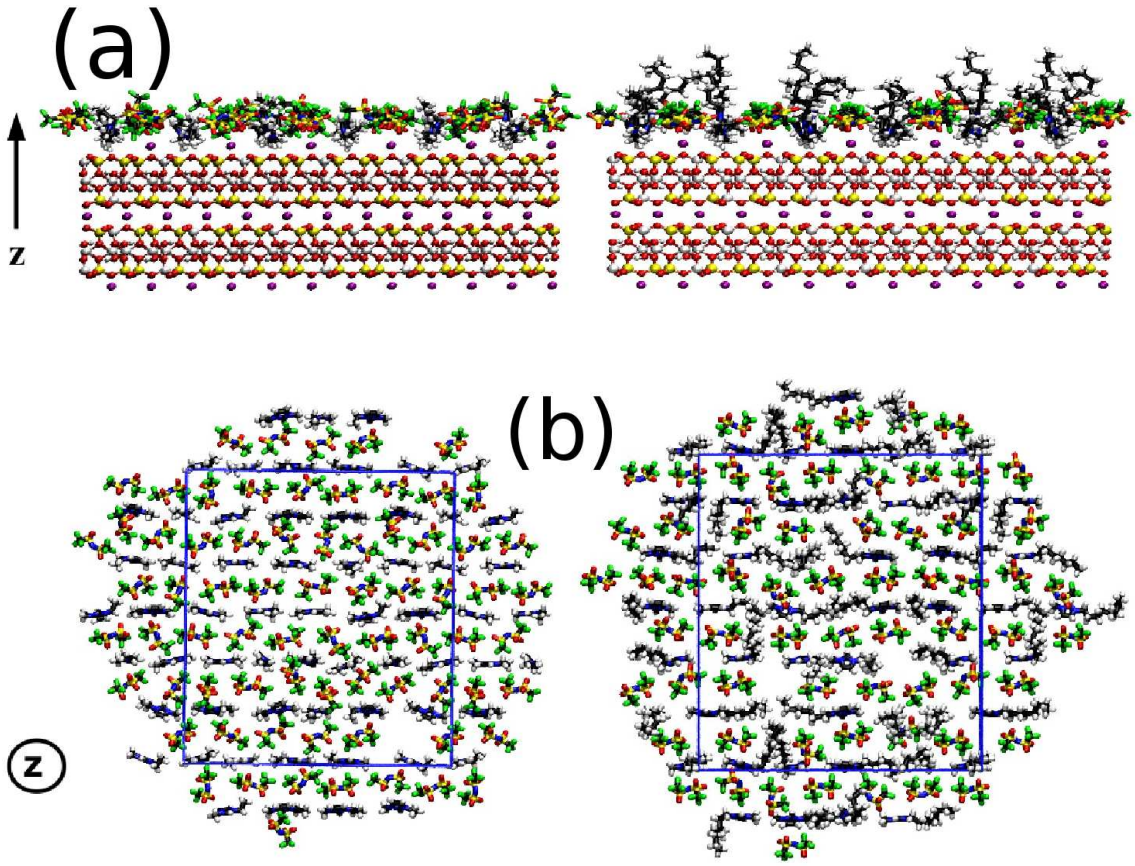

Figure 5.10: Side (Panel a) and top (Panel b) views of the first adsorbed layer of RTILs, $[C_2mim][NTf_2]$ (left) and $[C_8mim][NTf_2]$ (right) on mica. In panel (b), some of the periodic images of ions are also shown to enable the identification of near neighbor molecular arrangements. The rectangle in panel (b) is the box used in simulations whose linear dimensions are 46.86 Å and 54.1 Å. Atoms of the cation are largely in gray or black in color, while atoms of the anion are largely red and green in color. The atoms of the mica substrate are in red, yellow and purple colors. The results are from simulations of Set A.

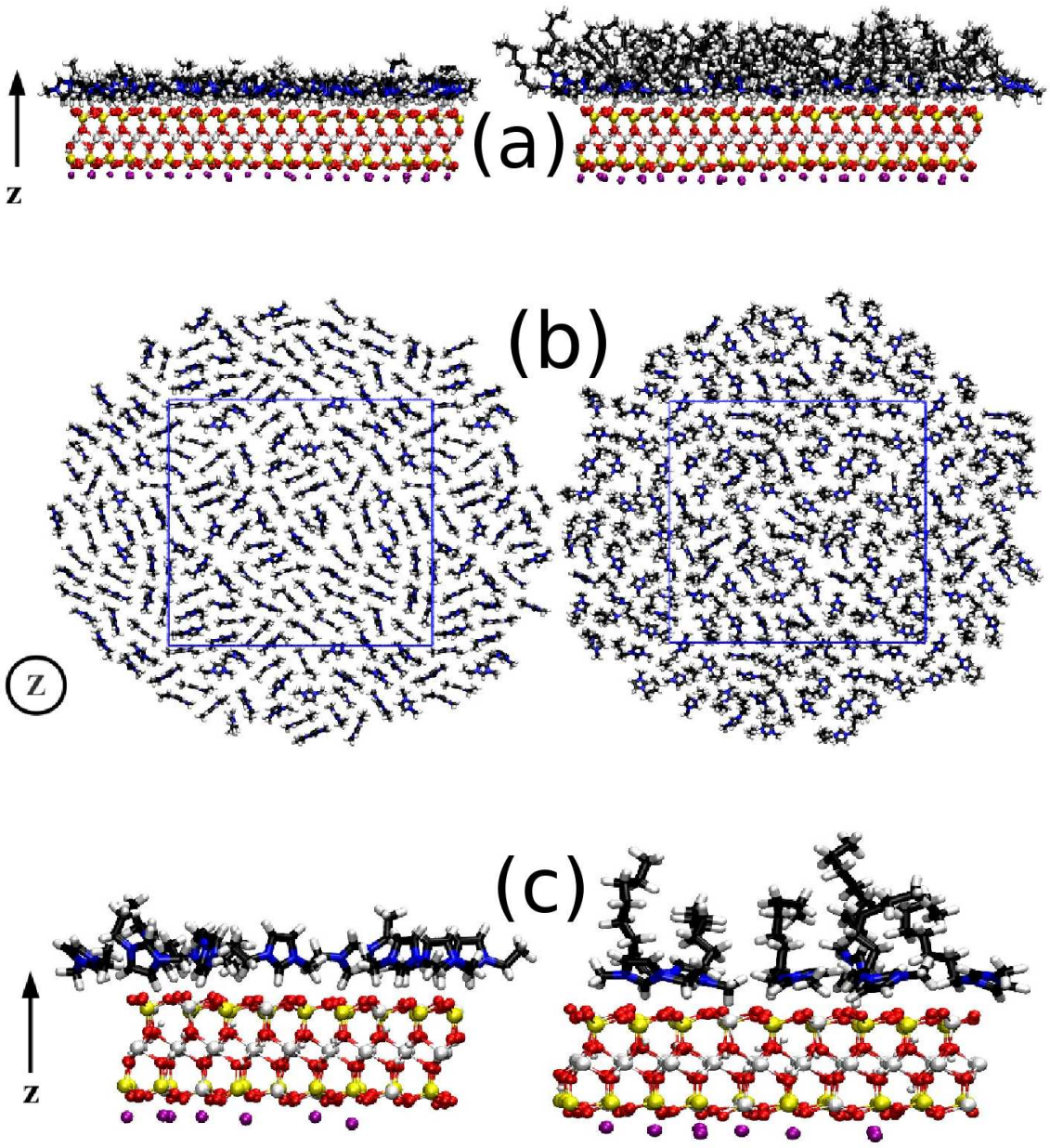

Figure 5.11: Side (Panel a) and top (Panel b) views of the first adsorbed layer of RTILs, $[C_2mim][NTf_2]$ (left) and $[C_8mim][NTf_2]$ (right) on mica. In panel (b), some of the periodic images of ions are also shown to enable the identification of near neighbor molecular arrangements. The rectangle in panel (b) is the box used in simulations whose linear dimensions are 54.918 Å and 54.0918 Å. Atoms of the cation are largely in blue or black in color. The atoms of the mica substrate are in red, yellow and purple colors. A narrow region of the RTIL on mica is shown in Panel (c) (side view) to exemplify the molecular level arrangement. The results are from simulations of Set B.

5.4 Conclusions

Following the recent surface force experiments of RTILs confined between two mica surfaces [28], atomistic MD simulations of the same liquids present on a mica surface have been carried out. The experimental observations of the confined liquid have been reproduced by the simulations. In particular, the negatively charged mica surface induces the layering of ions at the interface. In $[C_n mim][NTf_2]$ RTILs, cations of the n=2 or 4 members (ethyl and butyl) lie with their alkyl tail parallel to the surface, while in the hexyl and octyl based RTILs, the alkyl group is perpendicular to the surface. Thus, in a situation where two mica surfaces confine the RTIL, the latter would correspond to the formation of a bilayer. It is noteworthy that even a single mica surface is able to reproduce reasonably well the experimental observation. In particular, the simulations reported here are able to reproduce the experimental data for the change in the thickness of the solvation layers in the C_4 and the C_6 based RTILs, quantitatively.

Results were obtained from two sets of simulations with two independent force fields, CLAYFF and CVFF for mica. The latter, in particular, has been demonstrated to be superior in many interfacial problems earlier [24, 25]. Further, in the second set of simulations (using CVFF, denoted here as Set B) the atoms of the mica were treated as degrees of freedom and were thermalized. Cation exchange between mica and the RTIL was also considered in this set. It is believed that the simulations of Set B are closer to the experimental conditions. In both the simulations, cations with longer alkyl tails were oriented in such a manner that the long axis of the alkyl group was parallel to the surface normal. Thus, the conclusions reported here are robust and indicate the inherent feature of the organization of RTILs near a negatively charged mica surface.

In the bulk liquid, the strong Coulombic interactions between the imidazolium ring and the anion is usually balanced by the van der Waals interaction between

the alkyl groups manifesting in nanostructural ordering of polar and non-polar domains [40, 41]. At the mica surface, the additional electrostatic interaction from the surface enhances this segregation leading to the self-assembly of cations in $[C_6mim][NTf_2]$ and $[C_8mim][NTf_2]$, which are oriented with their long axes perpendicular to the surface. In the C_8 based system, the ions in the first adsorbed layer are seen to be nearly arranged on a two dimensional lattice. Both the C_2 and C_8 systems show sluggish dynamics and even the current simulations are relatively short to decide unambiguously if the first adsorbed layer is liquid or solid-like. However, structural data indicate that they possess more solid-like character.

Bibliography

[1] Maginn, E. J. *J. Phys. Condens. Matt.* **2009**, *21*, 373101.

[2] Bhargava, B. L.; Balasubramanian, S. *J. Am. Chem. Soc.* **2006**, *128*, 10073–10078.

[3] Aliaga, C.; Santos, C. S.; Baldelli, S. *Phys. Chem. Chem. Phys.* **2007**, *9*, 3683–3700.

[4] Pinilla, C.; Del Popolo, M. S.; Lynden-Bell, R. M.; Kohanoff, J. *J. Phys. Chem. B* **2005**, *109*, 17922–17927.

[5] Baldelli, S. *J. Chem. Phys. Lett.* **2013**, *4*, 244–252.

[6] Peñalber, C. Y.; Baldelli, S. *J. Phys. Chem. Lett.* **2012**, *3*, 844–847.

[7] Lynden-Bell, R. M.; Del Popolo, M. G.; Youngs, T. G. A.; Kohanoff, J.; Hanke, C. G.; Harper, J. B.; Pinilla, C. C. *Acc. Chem. Res.* **2007**, *40*, 1138–1145.

[8] Fedorov, M. V.; Lynden-Bell, R. *Phys. Chem. Chem. Phys.* **2012**, *14*, 2552–2556.

[9] Lynden-Bell, R. M.; Frolov, A. I.; Fedorov, M. V. *Phys. Chem. Chem. Phys.* **2012**, *14*, 2693–2701.

[10] Frackowiak, E.; Lota, G.; Pernak, J. *J. Appl. Phys. Lett.* **2005**, *86*, 164104.

[11] Kuang, D.; Wang, P.; Ito, S.; Zakeeruddin, S. M.; Grätzel, M. *J. Am. Chem. Soc.* **2006**, *128*, 7732–7733.

[12] Armand, M.; Endres, F.; MacFarlane, D. R.; Ohno, H.; Scrosati, B. *Nat. Mater.* **2009**, *8*, 621–629.

[13] Simon, P.; Gogotsi, Y. *Nat. Mater.* **2008**, *7*, 845–854.

[14] Liu, Y.; Zhang, Y.; Wu, G.; Hu, J. *J. Am. Chem. Soc.* **2006**, *128*, 7456–7457.

[15] Hu, J.; Xiao, X.-D.; Ogletree, D.; Salmeron, M. *Science* **1995**, *268*, 267–269.

[16] Hayes, R.; El-Abedin, S. Z.; Atkin, R. *J. Phys. Chem. B* **2009**, *113*, 7049–7052.

[17] Bovio, S.; Podesta, A.; Lenardi, C.; Milani, P. *J. Phys. Chem. B* **2009**, *113*, 6600–6603.

[18] Yokota, Y.; Harada, T.; Fukui, K. *Chem. Commun.* **2010**, *46*, 8627–8629.

[19] Perkin, S.; Albrecht, T.; Klein, J. *Phys. Chem. Chem. Phys.* **2010**, *12*, 1243–1247.

[20] Maolin, S.; Fuchun, Z.; Guozhong, W.; Haiping, F.; Chunlei, W.; Shimou, C.; Yi, Z.; Jun, H. *J. Chem. Phys.* **2008**, *128*, 134504.

[21] Ghatee, M. H.; Moosavi, F. *J. Phys. Chem. C* **2011**, *115*, 5626–5636.

[22] Merlet, C.; Salanne, M.; Rotenberg, B.; Madden, P. A. *J. Phys. Chem. C* **2011**, *115*, 16613–16618.

[23] Köhler, R.; Restolho, J.; Krastev, R.; Shimizu, K.; Lopes, J. N. C.; Saramago, B. *J. Phys. Chem. Lett.* **2011**, *2*, 1551–1555.

[24] Heinz, H.; Koerner, H.; Anderson, K. L.; Vaia, R. A.; Farmer, B. L. *Chem. Mater.* **2005**, *17*, 5658–5669.

[25] H. Heinz, U. W. S., W. Paul; Binder, K. *J. Chem. Phys.* **2004**, *120*, 3847–3854.

[26] Heinz, H.; Castelijns, H. J.; Suter, U. W. *J. Am. Chem. Soc.* **2003**, *125*, 9500–9510.

[27] Wang, J.; Kalinichev, A. G.; Kirkpatrick, R. J. *J. Phys. Chem. C* **2009**, *113*, 11077–11085.

[28] Perkin, S.; Crowhurst, L.; Niedermeyer, H.; Welton, T.; Smith, A. M.; Gosvami, N. N. *Chem. Commun.* **2011**, *47*, 6572–6574.

[29] Gordon, C. M.; Holbrey, J. D.; Kennedy, A. R.; Seddon, K. R. *J. Mater. Chem.* **1998**, *8*, 2627.

[30] Bhargava, B. L.; Balasubramanian, S.; Klein, M. L. *Chem. Commun.* **2008**, 3339–3351.

[31] Zhao, W.; Leroy, F. S. B.; Müller-Plathe, F. *J. Phys. Chem. B* **2008**, *112*, 8129–8133.

[32] Zhao, W.; Leroy, F.; Heggen, B.; Zahn, S.; Kirchner, B.; Balasubramanian, S.; Müller-Plathe, F. *J. Am. Chem. Soc.* **2009**, *131*, 15825–15833.

[33] Martinez, L.; Andrade, R.; Birgin, E. G.; Martinez, J. M. *J. Comput. Chem.* **2009**, *30*, 2157–2164.

[34] Köddermann, T.; Paschek, D.; Ludwig, R. *ChemPhysChem.* **2007**, *8*, 2464–2470.

[35] Malani, A.; Ayappa, K. G. *J. Phys. Chem. B.* **2009**, *113*, 1058–1067.

[36] Cygan, R. T.; Liang, J. J.; Kalinichev, A. G. *J. Phys. Chem. B* **2004**, *108*, 1255–1266.

[37] Website of Prof. H. Heinz http://www.polymeng.uakron.edu/nsl/FF_PHYLLOSILICATES.zip.

[38] Plimpton, S. *J. Comp. Phys.* **1995**, *117*, 1–19.

[39] Humphery, W.; Dalke, A.; Schulten, K. *J. Mol. Graph.* **1996**, *14*, 33–38.

[40] Lopes, J. N. C.; Padua, A. A. H. *J. Phys. Chem. B* **2006**, *110*, 3330–3335.

[41] Triolo, A.; Russina, O.; Bleif, H. J.; Di Cola, E. *J. Phys. Chem. B* **2007**, *111*, 4641–4644.

Chapter 6

Effect of cation symmetry on the organization of room temperature ionic liquids near a charged mica surface*

6.1 Introduction

The last decade witnessed an unprecedented growth in research on room temperature ionic liquids(RTILs). While Coulombic fluids are inherently interesting, the spurt in interest on liquids composed purely of ions has been catalyzed by the fact that most of the neoteric ones are liquids at or near ambient conditions. Apart from electrostatic interactions, many properties of these RTILs arise also from interionic hydrogen bonding, van der Waals interactions, and π stacking. Synthetic chemists have played a crucial role in synthesizing hundreds of such liquids constituted by a variety of cations and anions in each of which one or more of these interaction motifs

*Work reported in this chapter is published in: R. S. Payal and S. Balasubramanian, J. Phys. Condens. Matter **26**, 284101 (2014). Reproduced by permission of IOP publishing.

are dominant or dormant. The field is thus enriched.

Among the large number of applications that RTILs have been studied for, the one that is relevant to the current work is its use as an electrolyte. Their wide electrochemical window, high thermal and chemical stability and reasonable ionic conductivity make them as alternatives to traditional electrolytes [1]. RTILs are widely accepted as electrolytic media for dye-sensitized solar cells [2], Li-ion batteries [3] and super-capacitors [4]. A crucial factor in the use of RTILs as electrolytic media is the electrode-RTIL interface. The solid-liquid interface not only accentuates the nanoscale heterogeneity intrinsic to RTILs, but also induces charge ordering against the solid surface [5, 6].

Many experimental investigations have been carried out to study the RTIL-solid interface. Liu *et al* [7] employed atomic force microscopy to investigate the behavior of RTILs near mica surface. Unlike water which forms a fragile solid layer over mica [8], RTILs were seen to form a more rigid structure. Atkin and coworkers [9, 10] used atomic force (AFM) and scanning tunneling microscopies (STM) to analyze the organization of RTILs near a solid-RTIL interface. Force profiles obtained using AFM and STM show pronounced structuring of RTIL near solid surfaces. They also demonstrated that the strength of the interfacial layer depended on the structure of the cation. Mezger *et al* [11] used high energy X-ray reflectivity to understand the interfacial behavior of sapphire (0001) surface with fluorinated RTILs. High energy X-ray study revealed strong interfacial layering and the existence of cations closer to the sapphire surface. Further, with increasing temperature, the distance between the first cation layer and the sapphire surface decreased. Bureau *et al* [12] described the influence of surface charges on the molecular layering behavior of nanoconfined RTILs. RTILs showed strong layering near mica surfaces, but none was observed near methyl terminated surfaces.

Perkin *et al* [13] used surface force balance to study layering and shear properties

of nanofilms of an RTIL confined between mica surfaces. They observed that nano RTIL films possess friction coefficients which are about one to two orders of magnitude lower than their non-polar counterparts. Baldelli and coworkers used sum frequency generation spectroscopy to study this solid liquid interface [14, 15]. They observed a Helmholtz like layer formation of RTILs near solid surfaces. Recently, Perkin *et al* used the surface force apparatus to study the layering of imidazolium and pyridinium RTILs confined between negatively charged mica surfaces [16, 17]. They observed a monolayer to bilayer crossover. For RTILs containing cations with small tail lengths (say, less than eight carbon atoms), monolayers were observed near the surface while cations with longer alkyl tails led to the formation of bilayers. Atomistic molecular dynamics simulations by our group were able to reproduce these experimental results and provided a microscopic perspective of this crossover [18, 19].

Theoretical studies on RTIL-solid interfaces have also been carried out [20]. Lynden-Bell and coworkers examined the behavior of RTILs near charged electrodes as well as near neutral graphene surfaces [5, 6]. In their simulations, they observed the formation of monolayers even for the neutral graphene surface which arose from the higher affinity of cation for graphene. Further, they observed the cation ($[C_1C_1im]$) ring planes to orient themselves parallel to the graphene surface, while the ring was perpendicular to the electrode surface for charged surfaces. Xing *et al* [21] employed MD simulations to understand the impact of nano-patterning of electrodes on the energy density and capacitance of electrostatic double layer capacitors (EDLCs) using RTILs. Vatamanu *et al* [22] used MD simulation to study the effect of shape and size of carbon nano-electrodes on energy storage of supercapacitors with RTILs. They found that when the curvature and length scale of roughness of nanoparticles used as electrode are comparable to ions dimensions, there is a noticeable rise in the capacitance value. Salanne and coworkers have extensively

studied the behavior of RTILs near carbon electrodes [23–29] to examine the effect of electrode characteristics on the interfacial behavior and capacitance. Also they have studied the impact of solvation of RTILs in acetonitrile on the interfacial behavior of RTILs and electrode.

RTILs in bulk exhibit a nanostructure (nanoscale heterogeneity) which arises from the local "segregation" of moieties which interact either via polar or non-polar forces. The anions are located proximal to the imidazolium ring of the cations where a large fraction of the positive charge is concentrated [30]. Cations with longer alkyl tails tend to organize in a manner such that the alkyl groups lie adjacent to each other. Naturally, this results in a pseudo bilayer-like arrangement which is reminiscent of the structure in a bicontinuous microemulsion [31–36]. Over the last few years, various researchers have examined the role of the symmetry of the cation on the nanostructural organization of RTILs. While traditional imidazolium based cations possess asymmetric alkyl groups in the form of C_nC_m (where n and m are the lengths of the alkyl group attached to the two nitrogen atoms of imidazolium ring), "symmetric" cations of the form C_lC_l exhibit rather interesting structural and dynamical properties [32, 37, 38, 41, 43]. In general, RTILs with symmetric alkyl groups are more structured and more viscous than their asymmetric counterparts, where $2l = n + m$. There can be many different combinations of n and m to achieve a symmetric or asymmetric RTIL. In case when one of the n or m is alkyl group while other is a methyl group, it corresponds to the *most* asymmetric cation.

In this chapter, the organization of such symmetric and asymmetric RTILs at the mica-RTIL interface was examined using atomistic MD simulations. A neat change in the behavior of these compounds was demonstrated as a function of the length of the alkyl group as captured by various structure functions. In the first adsorbed layer, the alkyl groups in symmetric RTILs were found to be highly ordered relative to those in asymmetric ones.

6.2 Details of simulation

In the present work, the effect of symmetry of the cation on the organizational behavior of RTILs near a charged surface have been investigated. In contrast to many experiments, our system consists of only one surface and thus the RTIL is not confined. Muscovite mica was chosen to be the model charged surface, and the family of $[C_nC_m\text{im}][NTf_2]$ (see Figure 6.1) was used as the model RTIL. Mica was modeled using the CVFF [44] force field developed by Heinz and coworkers, while RTILs were modeled using the all-atom force field developed by Ludwig and coworkers [45]. Cross interactions were obtained through Lorentz-Berthlot combination rules. Atomic coordinates for mica were taken from Prof. Heinz's website (four replicas of mica15_single_sheet were used) [46]. Prior to simulating the RTILs over mica, they were equilibrated in bulk conditions. For these simulations, the initial configurations for the RTILs were generated using the software package Packmol [47]. For all the systems, the lateral box dimensions were 51.918 Å and 54.0918 Å, consistent with the periodicity of the mica lattice. Details about the number of ion pairs used in each simulation are provided in Table 6.1. The number of ions chosen produced RTIL films whose thicknesses were in the order of 60Å, large enough for bulk-like properties to be present far from the solid surface. Furthermore, the effect of the solid surface is so strong that the presence of a liquid-vapor interface would not alter our conclusions (see later) on the RTIL structure near the solid. The mica sheet consisted of 2460 atoms and these atoms were also thermalized during the MD runs.

The configurations were first energy minimized, followed by a short MD run in the constant-NVT ensemble at a temperature of 300K for a duration of 500 ps towards equilibration. Subsequently, MD runs in the constant NPT ensemble, wherein the box length along the z-axis alone was allowed to vary, were carried out. This was followed by a short constant-NVT run for a duration of 500 ps.

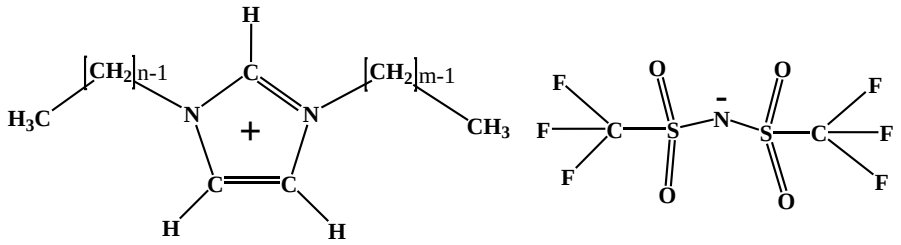

Figure 6.1: Schematic of $[C_nC_m\text{im}][NTf_2]$. RTILs with the following (n,m) combinations have been studied: (2,2), (3,1), (4,4), (7,1), (6,6), (11,1), (8,8) and (15,1).

Table 6.1: Number of ion pairs of used in simulations of the RTIL in bulk and on the mica surface. For RTILs on mica, 60 anions were removed from the bulk RTIL prior to placing the droplet on mica.

RTIL	Number of ion pairs in bulk liquid
$[C_2C_2\text{im}][NTf_2]$	294
$[C_3C_1\text{im}][NTf_2]$	294
$[C_4C_4\text{im}][NTf_2]$	270
$[C_6C_6\text{im}][NTf_2]$	240
$[C_7C_1\text{im}][NTf_2]$	270
$[C_8C_8\text{im}][NTF_2]$	215
$[C_{11}C_1\text{im}][NTf_2]$	240
$[C_{15}C_1\text{im}][NTf_2]$	215

Temperature and pressure controls were achieved through Nosé-Hoover thermostat and barostats. When mica comes into contact with the RTIL, the exchange of potassium ions present on its surface with the imidazolium cations of the RTIL is highly likely. To mimic this process, K^+ ions present on the top layer of the mica surface were removed. Correspondingly, the same number of anions were removed from the RTILs (sixty anions were removed from each RTIL). Subsequently, the RTILs were placed over the mica surface. The surface charge density of the mica is thus calculated to be 2.13×10^{-2} Å^{-2}. MD simulations in the canonical ensemble were carried out for this RTIL-mica system with a box length in the z-direction of 200 Å. NVT production run was carried out for 16 ns for each system. Trajectory run length was chosen such that for last few nanoseconds no change was observes in the density profiles and other properties of the systems. For short alkyl tails

convergence was obtained with in 10 ns. Three dimensional periodic boundary conditions were applied. The equations of motion were integrated using velocity Verlet algorithm with a time step of 0.5 fs. A spherical cutoff of 13 Å was employed for the non-bonded interactions. Long range electrostatic interaction were treated using particle particle particle mesh (PPPM) method [48]. All the simulations were carried out using LAMMPS [49]. MD trajectories were visualized and snapshot of simulations were studied using VMD [50]. All the analysis were carried out with home-grown codes. $z = 0$ in the density profiles corresponds to the location of the oxygen atoms on the top layer of mica.

6.3 Results and discussion

6.3.1 Cation ring:

A characteristic feature of liquids present near a solid surface is the layering of molecules which can be probed through a variety of methods. In computer simulations, the layering can be examined through density profiles. The density profile of the cation ring center are presented in Figure 6.2. For cations with tail length greater than three carbon atoms, the ring center positions in the first absorbed layer coincide, suggesting that all the cations have a similar orientation with respect to the surface, irrespective of the symmetry in their alkyl groups. However, in the case of C_2C_2 and C_3C_1 RTILs, one can observe two distinct peaks within 4.5 Å, suggesting two different orientations of cations in the first adsorbed layer. The intensity of the two peaks are different in these two RTILs. For C_2C_2, the feature at 3.75 Å is taller than that at 2.75 Å. For C_3C_1, the two peaks are of almost the same intensity. Thus, as the length of one of the alkyl group increases, the ring center of the cation approaches the mica surface.

Differences in the intensities of the two peaks in the cation ring density profile

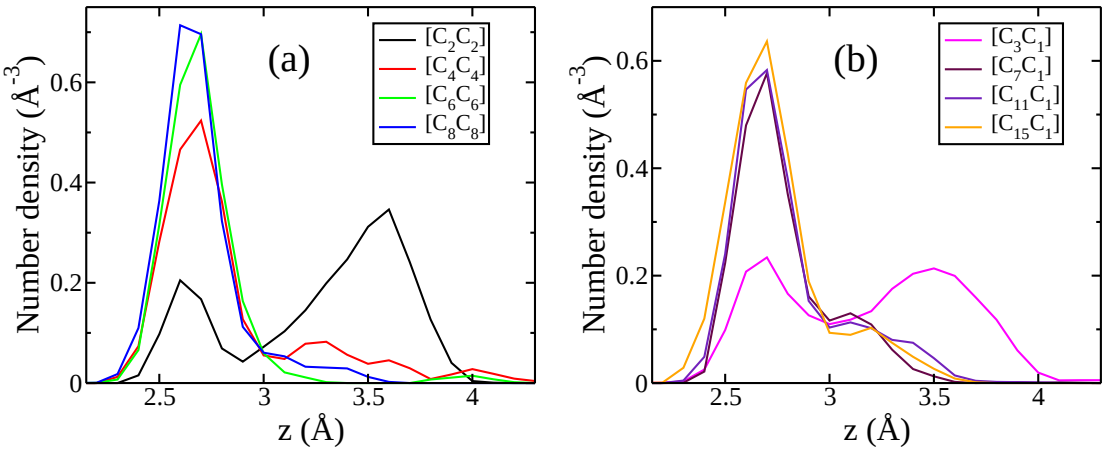

Figure 6.2: Density profile of geometric center of cation ring for (a) cations with symmetric alkyl groups and (b) cations with asymmetric alkyl groups. Region of the profiles near the first adsorbed layer are shown.

could point to differences in the orientation of the ring plane or the positions of the ring planes themselves. Analysis done below demonstrate that it is due to the former. Figure 6.3 displays the top view of the first adsorbed layer for the C_2C_2 and C_3C_1 systems. The cation rings are seen to be oriented in two different manner. In C_2C_2, most of the ring planes are perpendicular to the mica surface, while in C_3C_1, nearly equal number of cation rings are parallel or perpendicular to the mica surface. Radial distribution functions between the ring centers present in the first adsorbed layer are shown in Figure 6.4. Since the exact width of the first adsorbed layer cannot be quantified, the normalization of this function is not objective. However, the positions of the features in this function will not be affected by the value of the normalization. In the case of C_2C_2 and C_3C_1 systems, the peak at 4 Å arises from adjacent cation rings whose ring planes are oriented perpendicular to the mica surface. Relatively minor features present at the same distance in other RTILs, arise due to the small concentration of cations which too are oriented perpendicular to surface. Peaks at 6 Å and beyond arise due to cation ring planes which are parallel to the mica surface. In particular, the sharp first peak for the $[C_6C_6]$ system indicates a high degree of ordering of the cation rings in symmetric RTILs with longer alkyl

groups.

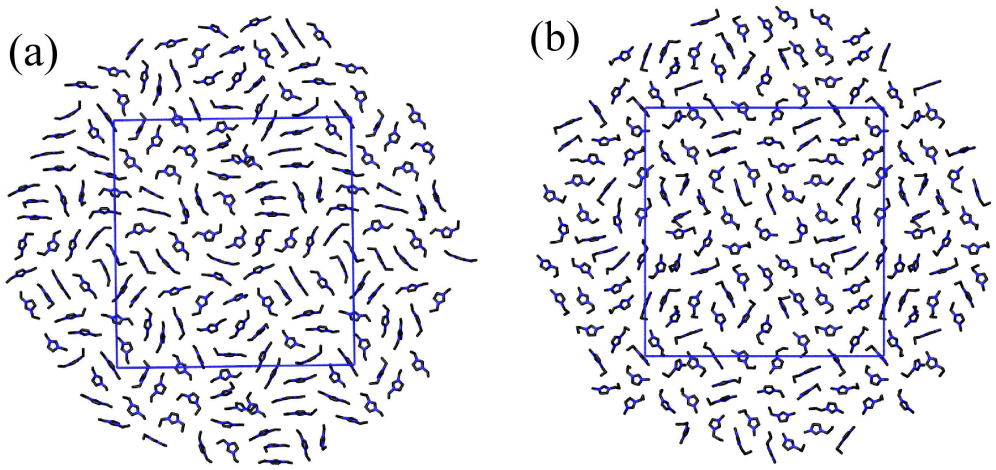

Figure 6.3: Top view (view along z-axis) of the first adsorbed layer of RTILs on the mica surface. (a) $[C_2C_2im]$ and (b) $[C_3C_1im]$ cation. Atoms of the cation are shown in black and blue. Hydrogens are not shown for the sake of clarity. The rectangular box is the simulation cell.

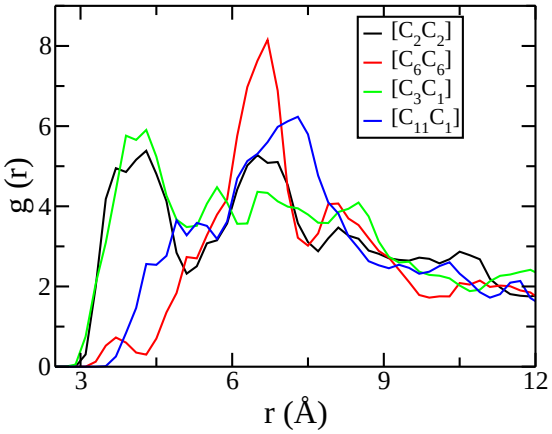

Figure 6.4: Radial distribution function between cation ring centers present in the first adsorbed layer over mica.

As seen from Figure 6.5, almost all the ring planes of cations of both C_4C_4 and $C_{15}C_1$ present in the first adsorbed layer are parallel to the mica surface. However, as discussed earlier (Figure 6.3), a significant number of cations were perpendicular to the mica surface for ions with short alkyl groups, such as C_2C_2 and C_3C_1. In the previous chapter, the C_4C_1 cation were found to approach the mica surface closer

as compared to C_2C_1. These observations suggest that a tail length of four carbon atoms is critical for a majority of cations to orient their ring planes parallel to the mica surface.

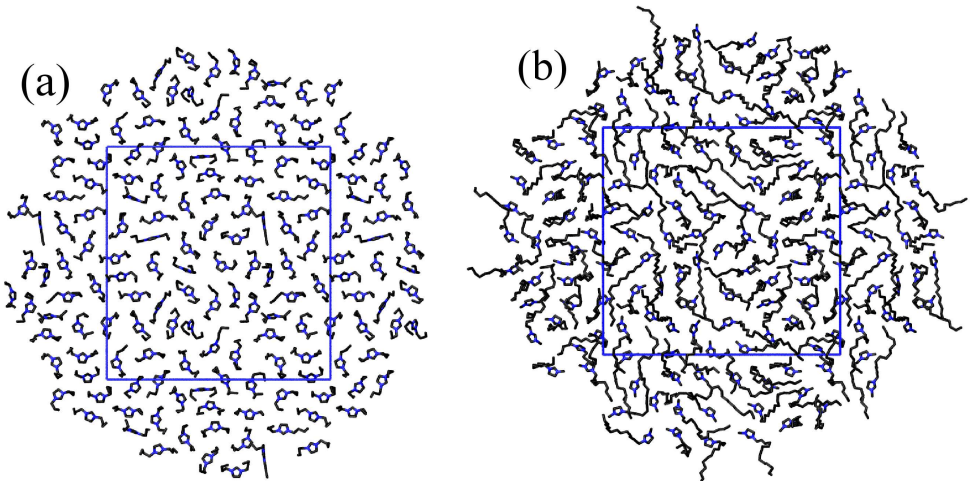

Figure 6.5: Top view (view along z-axis) of the first adsorbed layer of RTILs on the mica surface. (a) [C_4C_4im] and (b) [$C_{15}C_1$im] cation. Cation atoms are shown in black and blue. Hydrogens are not shown for the sake of clarity. The rectangular box is the simulation cell.

6.3.2 Anion:

In the anion density profile (Figure 6.6), a split in the first peak for the C_2C_2 and C_3C_1 systems was observed. This split can be attributed to two different orientations of the anion in its first layer (see Figure 6.7), distinguished by the location of the nitrogen atom of the anion. In the case when nitrogen is closer to mica, all the sulfonyl oxygen atoms of the same anion too are closer to the mica surface. However, in the other orientation of the anion, one of the sulfonyl or the trifluoroalkyl group is closer to mica. The split first peak in the anion density profile is visible only for cations with short alkyl tails i.e., for C_2C_2 and C_3C_1 systems. It can be attributed to the fact that in these systems, the cation in the first adsorbed layer itself has two different orientations. In the case of C_4C_4, C_7C_1 and $C_{11}C_1$ based RTILs, one

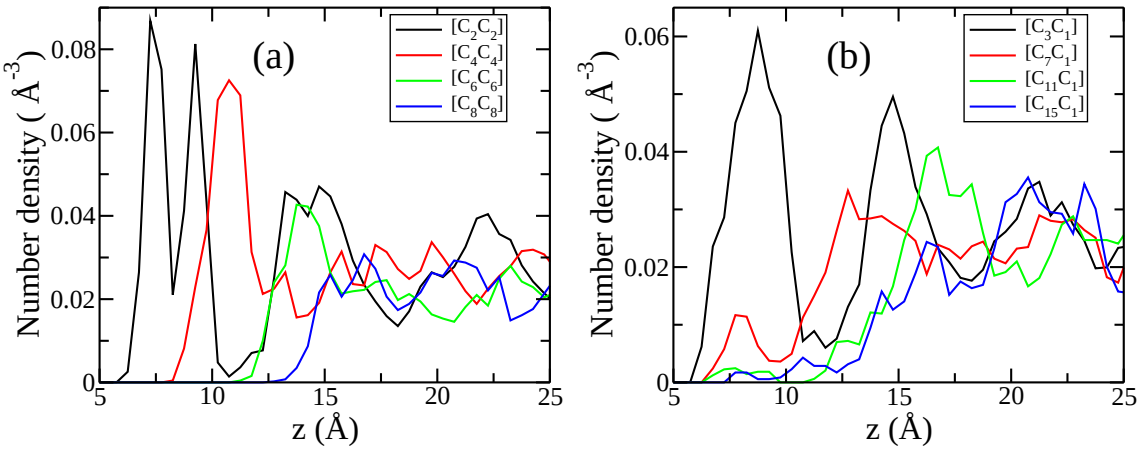

Figure 6.6: Density profile of nitrogen atom of anion for (a) cations with symmetric alkyl groups and (b) asymmetric ones.

can observe a small peak below 10 Å in the anion density profile. This peak arises due to a few anions trapped within the first adsorbed layer of cations. Further, a monotonic shift in the first peak position of the anion density profile with increasing tail length is observed. It is to be noted that the first adsorbed layer of all the RTILs on the mica surface is fully constituted by cations and is devoid of anions. Thus, the anion density profiles closely reflect the cation location. For C_2C_2 and C_3C_1 systems, one can observe multiple strong oscillations in the anion density profile while within the same distance range, fewer peaks are observed in systems with with longer alkyl tails. Since cations with longer alkyl tails occupy more space in the first adsorbed layer (relative to ones with shorter tails), peaks in the anion density profiles too are located farther from mica.

6.3.3 Alkyl group:

Further evidence for this conclusion is obtained from an examination of the density profile of the terminal methyl group (see Figure 6.8). The position of its first peak for short and intermediate tail length varies almost linearly with tail length. Also, in RTILs with longer alkyl groups, a few minor features are seen below 12 Å,

which implies that they (tails) could be orientationally disordered. This disordered orientation of tails is also visible in Figure 6.5(b). Further, it can be seen that the first peak for C_7C_1 is at a lower z value as compared to that for C_6C_6, which implies that symmetric tails align (and pack) themselves more efficiently as compared to asymmetric tails. This finding matches previous simulations studies carried out for alkylammonium salt confined between two mica surfaces [39]. In their work, Heinz *et al* also observed that symmetric alkyl tails are more ordered as compared to asymmetric tails. Tambach *et al* [40] studied the organization of alkylammonium surfactants within clay surfaces. Unlike mica, these can swell with increasing length of the alkyl group. The order-disorder transition in this system depends upon the spacing between two clay layers.

In fact, an examination of the profiles of the terminal methyl group at the liquid-vapor interface demonstrates the $C_{11}C_1$ liquid to form a marginally thicker liquid film on mica than the C_6C_6 film. Features in the profiles shown in Figure 6.8(b) (for C_nC_1 RTILs) are, in general, broader than those for the corresponding symmetric cation based RTILs, suggesting orientational disorder in the former. Figure 6.9 shows a systematic comparison between density profiles of cation ring and the terminal

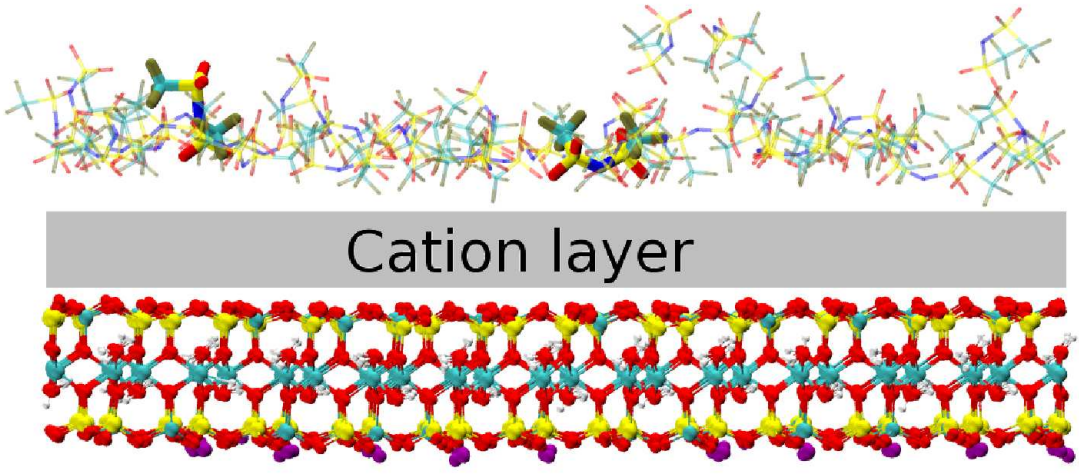

Figure 6.7: Snapshot from simulations demonstrating the existence of two possible orientations of the anion in the RTIL, $[C_2C_2im][NTf_2]$.

methyl group of cation for the symmetric and asymmetric cation based RTILs on mica. A systematic increase in the first peak height for the ring density profile with increasing tail length is seen; however, concurrently the features in the tail profile broadens, indicating considerable disorder in the position of the terminal methyl group, particularly for asymmetric RTILs.

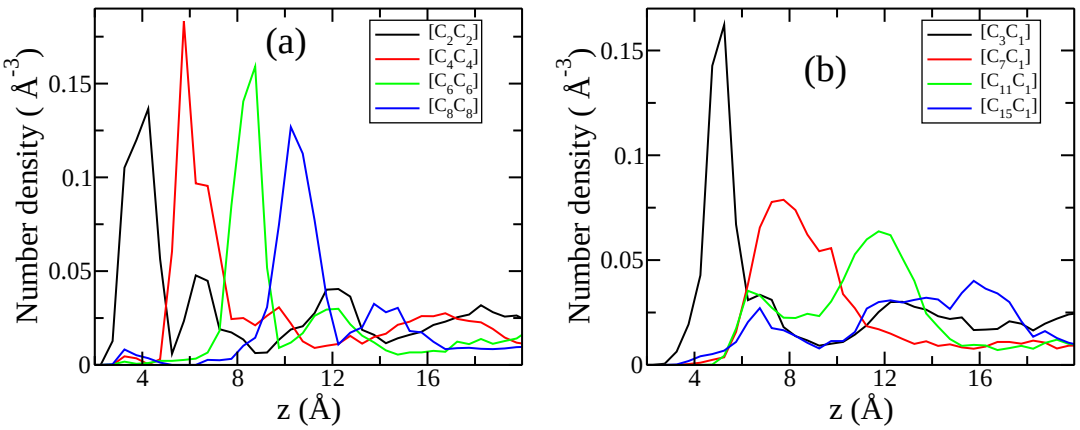

Figure 6.8: Density profile of terminal carbon atom of alkyl tail for (a) cations with symmetric alkyl groups and (b) asymmetric ones.

6.3.4 Orientations:

A quantitative estimate of the orientation of cation rings and the alkyl tail can be obtained from appropriate orientational probability distributions. Only those ions present within the first adsorbed layer were considered for these calculations. The angle that the ring normal and the tail vector (vector between the nitrogen atom and the terminal carbon atom of the cation) make with respect to the surface normal were calculated. Figure 6.10 shows the probability distributions of these quantities. Features at low values of $\cos(\theta)$ in the ring orientational distribution for the C_2C_2 and C_3C_1 RTILs imply that a non-negligible fraction of cations rings are oriented perpendicular to the surface. Further, increasing the tail length leads to more cation ring planes to be oriented parallel to the surface. For tail lengths of four

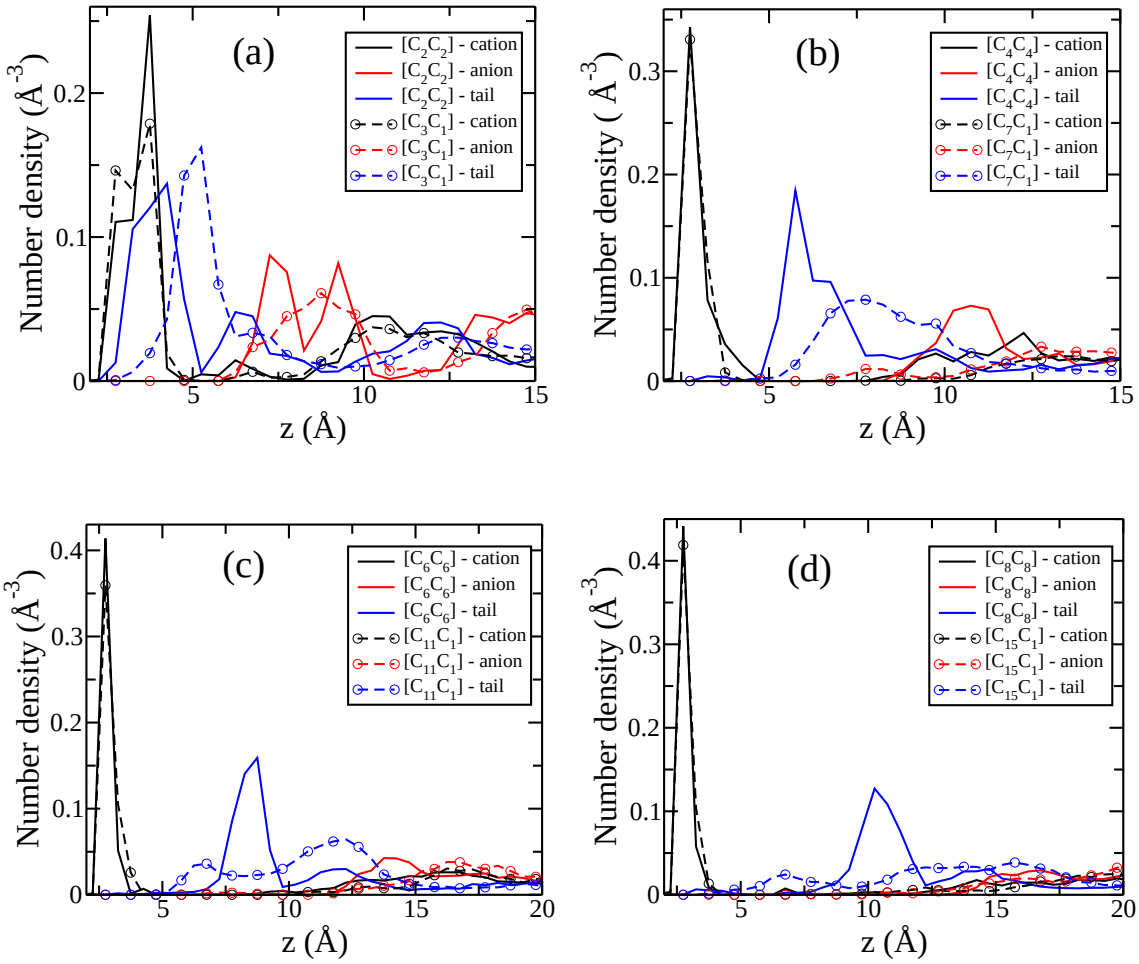

Figure 6.9: Comparison of cation ring centre (ring), anion, and terminal methyl group (tail) density profiles between (a) $[C_2C_2im][NTf_2]$ & $[C_3C_1im][NTf_2]$ (b) $[C_4C_4im][NTf_2]$ & $[C_7C_1im][NTf_2]$ (c) $[C_6C_6im][NTf_2]$ & $[C_{11}C_1im][NTf_2]$ and (d) $[C_8C_8im][NTf_2]$ & $[C_{15}C_1im][NTf_2]$.

or more carbon atoms, the distribution is largely centerd at a $\cos(\theta)$ value of unity, demonstrating that the ring planes are lying flat on the mica surface. Concurrently, the alkyl tail orientational profile too exhibits an interesting behavior with increasing tail length. For the C_2C_2 RTIL, most of the alkyl groups lie parallel to the mica surface, as the distribution possesses a sharp peak at low $\cos(\theta)$ values. A gradual shift in the peak position to larger values is seen with increasing tail length. For the C_3C_3 system, this distribution shifts to intermediate $\cos(\theta)$ values signifying that as the tail length grows, the alkyl groups tend to orient away from the mica surface. For

C_4C_4, C_6C_6 and C_8C_8, a large fraction of the tails are nearly perpendicular to the mica surface. However, for C_7C_1, the distribution again peaks at intermediate range of $\cos(\theta)$ values, signifying that symmetric tails align themselves more efficiently as compared to their asymmetric counterparts. For $C_{11}C_1$ and $C_{15}C_1$, the distribution of tail orientations is significantly broader. This can clearly be seen from a snapshot of the simulations shown in Figure 6.11, where for the C_8C_8 system, all the tails are tending perpendicular to the surface, whereas for the $C_{15}C_1$ system, the tails exhibit considerable disorder, although oriented largely perpendicular to the mica surface.

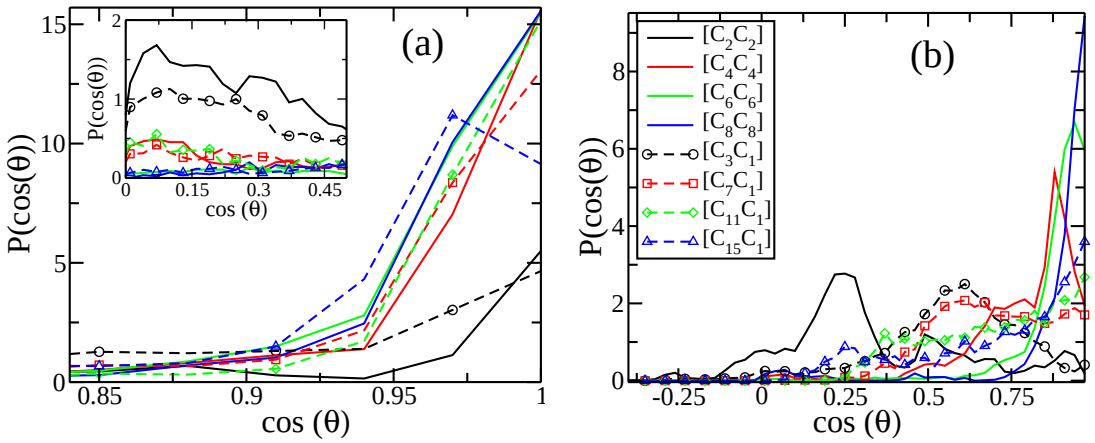

Figure 6.10: Normalized probability distribution of the orientation angle with respect to the surface normal of (a) cation ring normal and (b) alkyl tail, for cations present in the first adsorbed layer. Inset in (a) exhibits the same quantity for small values of $\cos(\theta)$.

The orientational characteristics of alkyl tails can be further quantified through gauche defects. Figure 6.12(a) shows the probability distribution of gauche defects of bonds belonging to the alkyl group of cations present in the first adsorbed layer. The data is averaged over all the bonds in the alkyl group whose rotation produces a conformational change. Figure 6.12(b) is the percentage of bonds in the gauche conformation plotted as a function of the number of carbon atoms in the alkyl groups of the cation. The C_4C_4 system exhibits a large number of gauche defects, whereas the corresponding asymmetric cation (C_7C_1) exhibits far less. Thus, in this tail length regime, increasing the length of the longer alkyl group decreases the gauche

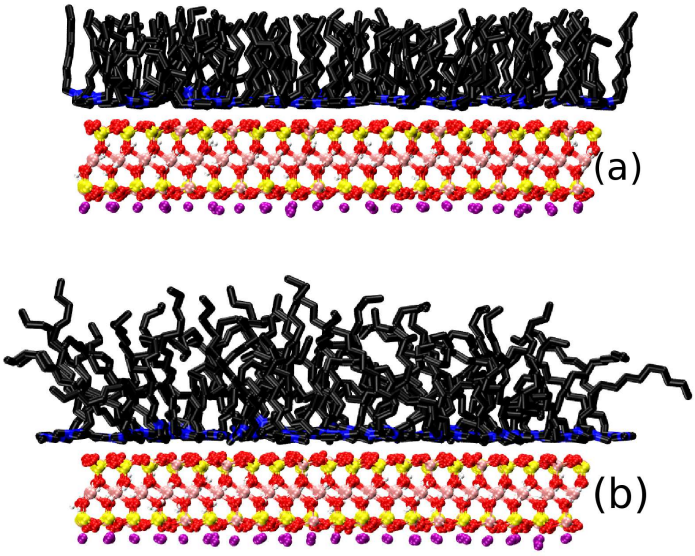

Figure 6.11: Side view of first adsorbed layer of RTILs on mica surface (a) $[C_8C_8][NTf_2]$ and (b) $[C_{15}C_1][NTf_2]$. Mica atoms are shown in pink, yellow, purple, white and red. Cation atoms are shown in black and blue. Hydrogens of cation are not shown for the sake of clarity.

fraction. However, for $n + m = 12$, there is a change in this behavior. The C_6C_6 system possesses fewer gauche defects than the corresponding $C_{11}C_1$ system. Thus, the symmetry of the cation determines the concentration of gauche defects in this size regime. This behavior is more or less maintained for larger $n+m$ values as well.

The dihedral angle distributions for cations in the first adsorbed layer can be benchmarked against those obtained for RTILs in bulk state (i.e., without mica). Figure 6.13 provides this comparison, near the gauche region of the dihedral angle. In case of the C_4C_4 system, the number of gauche defects is reduced for cations in the first layer relative to that in bulk. The distributions for cations with longer alkyl groups are unaffected, as the concentration of gauche defects were lesser in bulk, to start with.

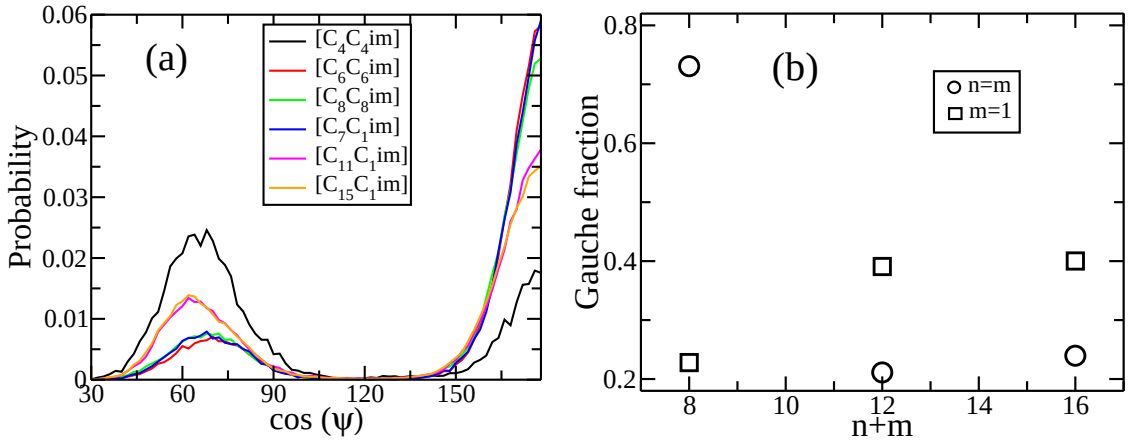

Figure 6.12: (a) Probability distribution of dihedral angle magnitude for bonds belonging to the alkyl group of cations present in the first adsorbed layer. (b) Fraction of gauche defects in alkyl groups plotted against $n + m$ for RTILs of the form $[C_nC_m][NTf_2]$.

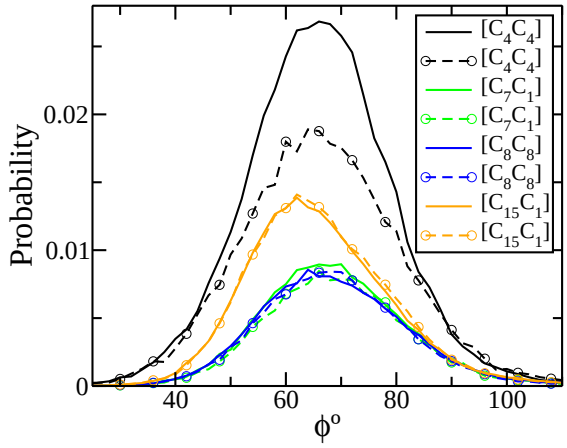

Figure 6.13: Probability distributions of dihedral angle magnitude for bonds belonging to the alkyl group of cations present in the first adsorbed layer (dashed line), compared against the same quantity for cations in bulk RTIL (continuous line) at 300K. Data near the gauche region is shown.

6.4 Conclusions

The effect of cation symmetry on the organization of RTILs near a charged mica surface was investigated using atomistic MD simulations. The simulations employed model RTILs of the form, $[C_nC_m][NTf_2]$ for many combinations of n and m. $n = m$ constituted cations with symmetric alkyl groups, whereas $m = 1$ with different values of n constituted asymmetric cations. A charge ordered solid-liquid interface was observed. While cations exclusively constitute the first adsorbed layer, a thin layer of anions coats it. Oscillations in the density profiles weaken beyond three ion pair layers.

The orientation of the imidazolium ring plane for cations present in the first adsorbed layer exhibits a dependence on the length of the alkyl group attached to it. For alkyl tail lengths shorter than four carbons, the ring plane can either be parallel or perpendicular to the surface. However for longer tails, the cation ring plane is predominantly parallel to the mica surface. Alkyl groups of symmetric cations whose tail length is larger than four carbon atoms orient themselves completely perpendicular to the mica surface. The alkyl tail orientation for asymmetric cations exhibits a broader distribution, whose width increases with increasing tail length. The disordered orientations of C_n alkyl groups in the first adsorbed layer of $[C_nC_1][NTf_2]$ RTILs is correlated to the large number of gauche defects present in its tail.

Imidazolium cation based RTILs with asymmetric distribution of alkyl group lengths on the cation exhibit interesting nanoscale heterogeneity in bulk that has been discussed earlier. The atomistic MD simulations on their symmetric counterparts demonstrated them to be more structured [41–43], in agreement with experiments [32, 38]. It is belived that the current work which has examined the organization of symmetric cation based RTILs near a charged mica surface will spur similar experimental efforts.

Appendix A

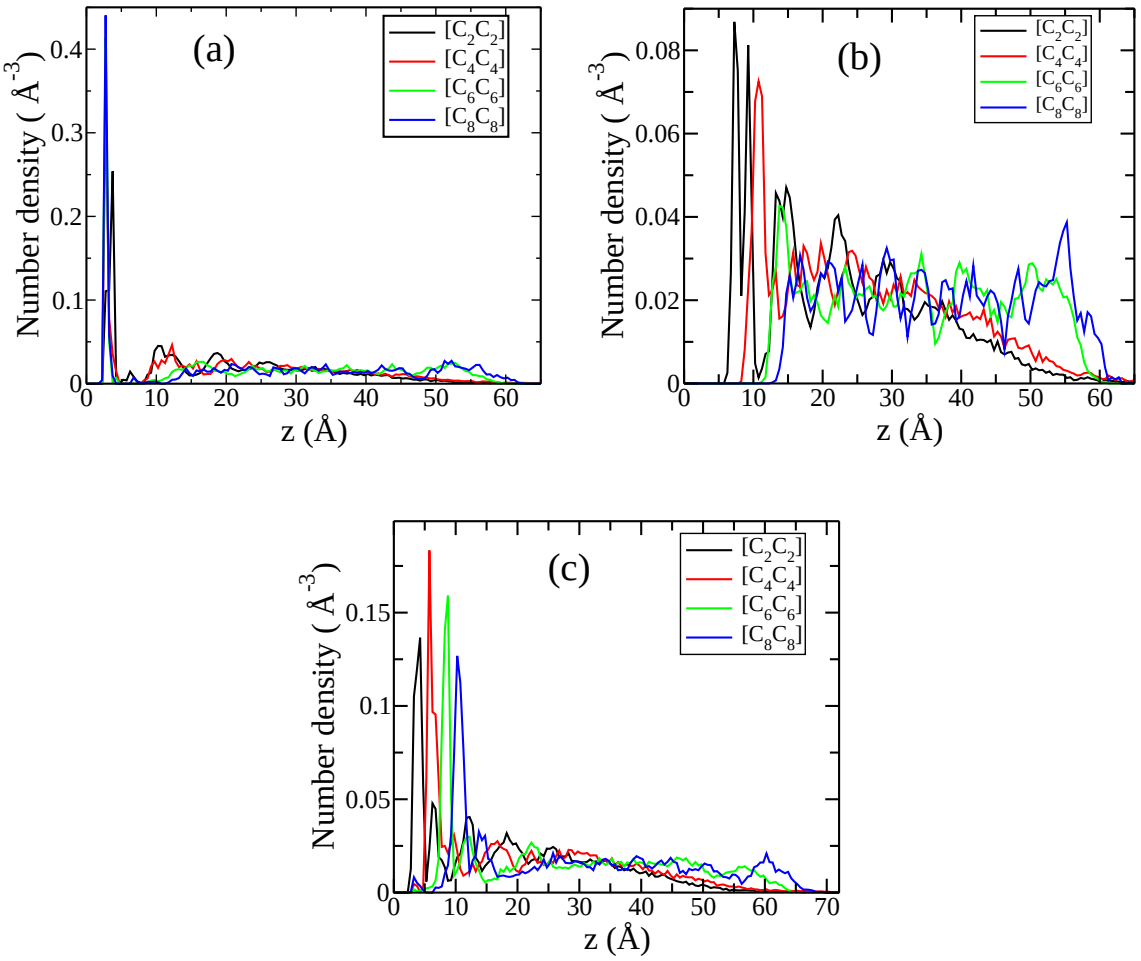

Figure A.1: Complete density profiles for symmetric cation (a) cation ring center, (b) nitrogen atom of anion and (c) cation terminal carbon.

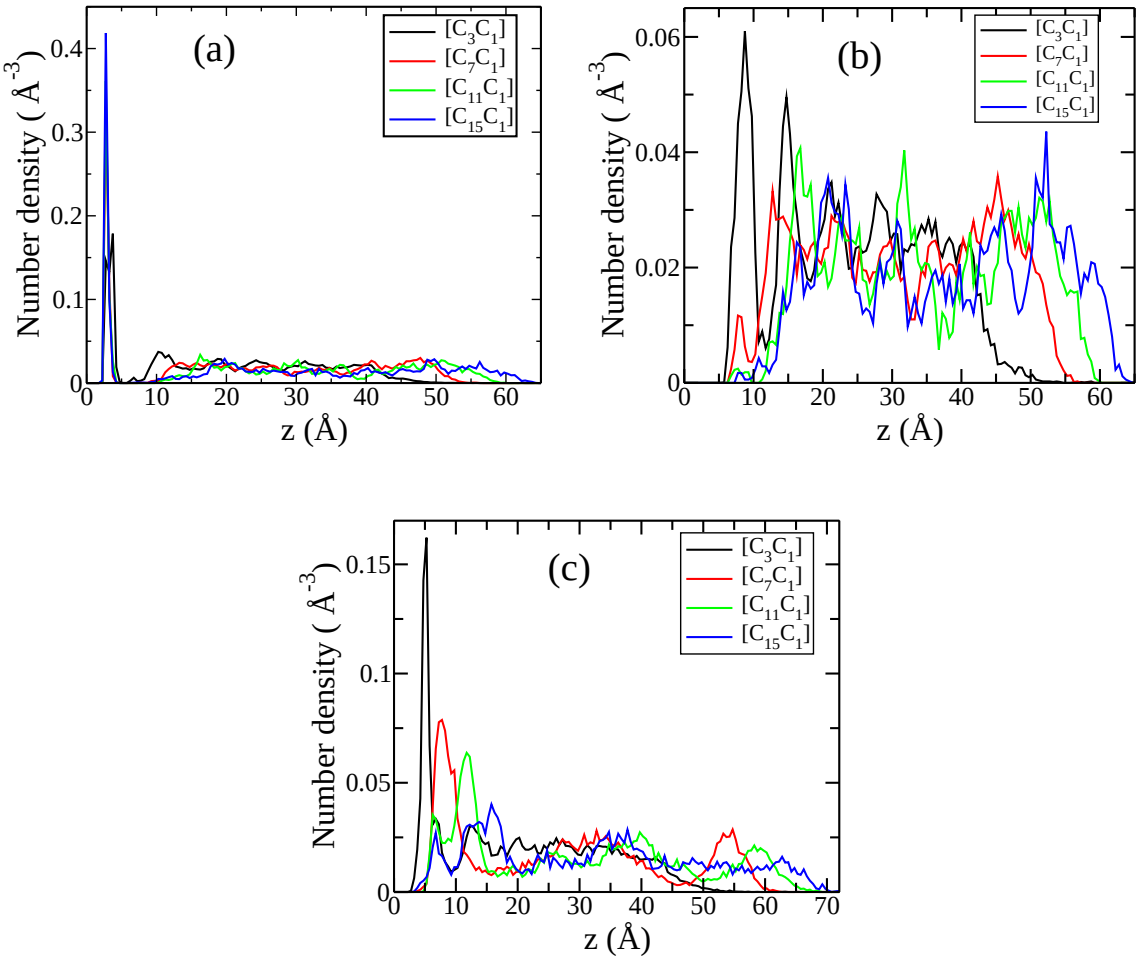

Figure A.2: Complete density profiles for asymmetric cation (a) cation ring center, (b) nitrogen atom of anion and (c) cation terminal carbon.

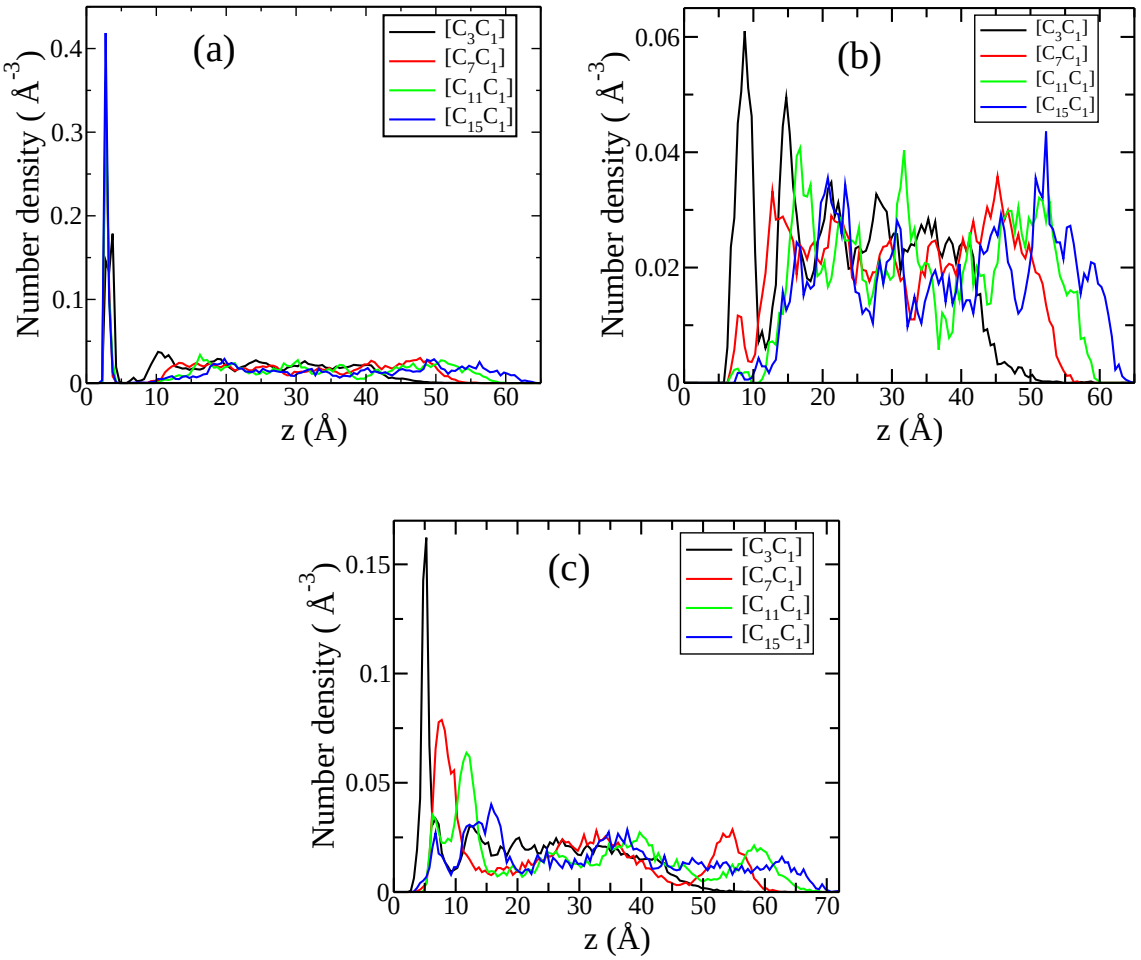

Figure A.3: Complete density profiles for asymmetric cation (a) cation ring center, (b) nitrogen atom of anion and (c) cation terminal carbon.

Bibliography

[1] Galiński M, Lewandowski A and Stępniak I *Electrochim. Acta*, **2006**, 51, 6657-5580.

[2] Grätzel M *Nature*, **2001**, 414, 338-344.

[3] Lewandowski A and Świderska-Mocek A *J . Power Sour.*, **2009**, 191, 601-609.

[4] Seki S, Kobayashi Y, Miyashiro H, Ohno Y, Usami A, Mita Y, Watanabe M and Terada N *Chem. Comm.*, **2006**, 5, 544-545.

[5] Fedorov M V and Lynden-Bell R M *Phys. Chem. Chem. Phys.*, **2012**, 14, 2552-2556.

[6] Lynden-Bell R M, Frolov A I and Fedorov M V *Phys. Chem. Chem. Phys.*, **2012**, 14, 2693-2701.

[7] Liu Y, Zhang Y, Wu G and Hu J *J. Am. Chem. Soc.*, **2006**, 128, 7456-7457.

[8] Hu Jun, Xiao X D, Ogletree D F and Salmeron M *Science*, **1995**, 268, 267-269.

[9] Hayes R, El Abedin S Z and Atkin R *J. Phys. Chem. B*, **2009**, 113, 7049-7052.

[10] Atkin R, El Abedin S Z, Hayes R, Gasparotto L H S, Borisenko N and Endres F *J. Phys. Chem. C*, **2009**, 113, 13266-13272.

[11] Mezger M, Schröder H, Reichert H, Schramm S, Okasinski J S, Schöder S, Honkimäki V, Deutsch M, Ocko B M, Ralston J, Rohwerder M, Stratmann M and Dosch H *Science*, **2008**, 322, 424-428.

[12] Bou-Malham I and Bureau L *Soft Matter*, **2010**, 6, 4062-4065.

[13] Perkin S, Albrecht T and Klein J *Phys. Chem. Chem. Phys.*, **2010**, 11, 1243-1247.

[14] Baldelli S *J. Chem. Phys. Lett.*, **2013**, 4, 244-252.

[15] Peñalber C Y and Baldelli S *J. Chem. Phys. Lett.*, **2012**, 3, 844-847.

[16] Perkin S, Crowhurst L, Niedermeyer H, Welton T, Smith A M and Gosvami N N *Chem. Comm.*, **2011**, 23, 65726574.

[17] Smith A M, Lovelock K R J, Gosvami N N, Licence P, Dolan A, Welton T and Perkin S *J. Phys. Chem. Lett.*, **2013**, 4, 378-382.

[18] Payal R S and Balasubramanian S *ChemPhysChem*, **2012**, 13, 1764-1771.

[19] Payal R S and Balasubramanian S *ChemPhysChem*, **2012**, 13, 3085-3086.

[20] Lynden-Bell R M, Del Popolo M G, Youngs T G A, Kohanoff J, Hanke C G, Harper J B and Pinilla C C *Acc. Chem. Res.*, **2007**, 40, 1138-1145.

[21] Xing L, Vatamanu J, Smith G D and Bedrov D *J. Phys. Chem. Lett.*, **2012**, 3, 1124-1129.

[22] Vatamanu J, Hu Z, Bedrov D, Perez C and Gogotsi Y *J. Phys. Chem. Lett.*, **2013**, 4, 2829-2837.

[23] Pounds M, Tazi S, Salanne M and Madden P A *J. Phys. Condens. Matter*, **2009**, 21, 424109.

[24] Tazi S, Salanne M, Simon C, Turq P, Pounds M and Madden P A *J. Phys. Chem. B*, **2010**, 114, 8453-8459.

[25] Merlet C, Salanne M, Rotenberg B and Madden P A *J. Phys. Chem. C*, **2010**, 114, 16613-16618.

[26] Merlet C, Rotenberg B, Madden P A, Taberna P L, Simon P, Gogotsi Y and Salanne M *Nat. Mater.*, **2012**, 11, 306-310.

[27] Merlet C, Péan C, Rotenberg B, Madden P A, Simon P and Salanne M *J. Phys. Chem. Lett.*, **2013**, 4, 264-268.

[28] Merlet C, Salanne M, Rotenberg B and Madden P A *Electrochim. Acta*, **2013**, 87, 262-271.

[29] Merlet C, Rotenberg B, Madden P A and Salanne M *Phys. Chem. Chem. Phys.*, **2013**, 15, 15781-15792.

[30] Lynden-Bell R M and Youngs T G A *J. Phys. Condens. Matt.*, **2009**, 21, 424120.

[31] Bhargava B L, Balasubramanian S and Klein M L *Chem. Comm.*, **2008**, 29, 3339-3351.

[32] Rocha M A A, Neves C M S S, Freire M G, Russina O, Triolo A. Countinho J A P and Santos L M N B F *J. Phys. Chem. B*, **2013**, 117, 10889-10897.

[33] Bhargava B L, Klein M L and Balasubramanian S *ChemPhysChem*, **2008**, 9, 67-70.

[34] Bhargava B L, Devane R, Klein M L and Balasubramanian S *Soft Matter*, **2007**, 3, 1395-1400.

[35] Lopes J N A C and Pádua A A H *J. Phys. Chem. B*, **2006**, 110, 3330-3335.

[36] Wang Y and Voth G A *J. Am. Chem. Soc.*, **2005**, 127, 12192-12193.

[37] Dzyuba S V and Bartsch R A *Chem. Comm.*, **2001**, 1466-1467.

[38] Xiao D, Hines L G Jr, Li S, Bartsch R A, Quitevis E L, Russina O and Triolo A J *J. Phys. Chem. B*, **2009**, 113, 6426-6433.

[39] Heinz H, Castelijns J and Suter U W *J. Am. Chem. Soc.*, **2003**, 125, 9500-9510.

[40] Tambach T J, Boek E S and Smit B *Phys. Chem. Chem. Phys.*, **2006**, 8, 2700-2702.

[41] Raju S G and Balasubramanian S *J. Mater. Chem.*, **2009**, 19, 4343-4347.

[42] Raju S G and Balasubramanian S *J. Phys. Chem. B*, **2010**, 114, 6455-6463.

[43] Sarangi S S, Raju S G and Balasubramanian S *Phys. Chem. Chem. Phys.*, **2011**, 13, 2714-2722.

[44] Heinz H, Koerner H, Anderson K L, Vaia R A and Farmer B L *Chem. Mater.*, **2005**, 17, 5658-5669.

[45] Köddermann T, Paschek D and Ludwig R *ChemPhysChem*, **2007**, 8, 2464-2470.

[46] Website of Prof. Heinz, http://www.poly-eng.uarkron.edu/nsl/FF_PHYLLOSILICATES.zip.

[47] Martínez L, Andrade R, Birgin E G and Martínez J M *J. Comput. Chem.*, **2009**, 30, 2157-2164.

[48] Hockney R W and Eastwood J W Computer Simulation Using Particles 1988 *Adam Hilger, NY.*

[49] Plimpton S *J. Comput. Phys.*, **1995**, 123, 1-19.

[50] Humphrey W, Dalke A and Schulten K *J. Mol. Graphics*, **1996**, 14, 33-38.

Chapter 7

Homogeneous mixing of room temperature ionic liquids: molecular dynamics simulations*

7.1 Introduction

Room temperature ionic liquids (RTILs) have attracted a lot of attention during the last decade. Low vapor pressure, high thermal and chemical stability enable them as possible chemical reaction media [1]. The fact that their properties can be tailored make them even more interesting. RTILs have been shown to be a suitable choice for biomass and biomolecular dissolution [2, 3]. Various researchers have studied using computational [4–6] as well as experimental techniques [2, 3] the use of RTILs as solvents. Their use in electrolysis [7], catalysis [8] and gas adsorption [9] are of major interest for both academia as well as industry.

Although, there have been many studies on pure, i.e., single component RTILs, binary or ternary RTILs have been much less studied. A binary RTIL consists of

*Work reported in this chapter is published in: R. S. Payal and S. Balasubramanian, Phys. Chem. Chem. Phys. **15**, 21077-21083 (2013). Reproduced by permission of The Royal Society of Chemistry (RSC).

either one common cation and two different anions or vice versa [10]. Among many interesting characteristics, they can exhibit the interesting phenomenon of selective solubilities of gases. The solubilities of gases in RTILs depend on the mole fraction of the non-common ion. Earlier experimental studies carried out by Finotello *et al* [11] showed that the addition of 5 mol% of $[C_2mim][NTf_2]$ to $[C_2mim][BF_4]$ enhances the solubility selectivity of CO_2 with N_2 or CH_4 as compared to neat RTILs. In the same study, they have reported that regular solution theory can be used to explain the solubilities and selectivity of gases in RTILs. Weber *et al* [12] used the binary mixture of RTILs to control the rates of hydrolysis reactions.

Bayley *et al* [13] investigated the transport properties and phase behavior of binary and ternary RTILs as electrolytes for their use in lithium batteries. They studied the binary RTIL system composed of N-methyl-N-propylpyrrolidinium ($[C_3mpyr^+]$) cation, bis(trifluoromethanesulfonylimide) ($[NTf_2^-]$) and bis(flurosulfonylimide) ($[FSI^-]$) anions. They observed the conductivity and the diffusivity of lithium ion to increase rapidly as a function of $[FSI^-]$ and expected that using binary and ternary RTILs as electrolytes in Li-batteries could improve its thermal stability. Baiker and coworkers [14] investigated the binary mixture of $[C_4mim][PF_6]$ and $[C_4mim][BF_4]$ with water and supercritical CO_2 ($scCO_2$) by means of *in situ* attenuated total reflection infrared spectroscopy. They observed that the presence of water neither affects significantly the solubility of $scCO_2$ in binary RTILs nor does it alter the interaction between $scCO_2$ and anion of binary RTILs. Xiao *et al* [15, 16] studied the nanostructural organization of binary RTIL mixtures of 1-pentyl-3-methylimidazolium bis(trifluoromethylsulfonylimide) ($[C_5mim][NTf_2]$) and 1-pentyl-3-methylimidazolium bromide ($[C_5mim][Br]$) using optical heterodyne-detected Raman-induced Kerr effect spectroscopy (OHD-RIKES). They found that the nanostructural order intrinsic to the neat RTILs was preserved even upon mixing. Ghatee and Zolghadr investigated the mixing of $[C_4mim][PF_6]$ and of $[C_4mim][BF_4]$ with water

using ab initio MD simulations [17]. They studied the differences in hydrophilicity of the anions from an electronic viewpoint.

Stoppa *et al* [18] reported ideal mixing behavior with respect to viscosity, molar volume and effective dipole moments for a binary mixture of RTILs. However, the electrical conductivity and dielectric relaxation time of RTILs were found to deviate from ideality. Lopes and coworkers [19] employed atomistic molecular dynamics (MD) simulations to study an equimolar mixture of $[C_2mim][NTf_2]$ and $[C_6mim][NTf_2]$. They observed microphase separation between polar and non-polar domains of the RTIL mixture whose range was intermediate to those of the pure RTIL components. Kirchner and coworkers [20, 21] employed *ab initio* molecular dynamics (AIMD) simulations to understand the behavior of a binary mixture of RTILs with a common cation. They studied the mixture of $[C_2mim][SCN]$ and $[C_2mim][Cl]$ and have also examined the influence of temperature on the mixing behavior. An important result from their work that has bearing on ours is that the Cl ion was able to displace the thiocyanate anion from its preferred coordination site.

In a recent study, Baiker and coworkers [22] examined the nanoscopic ordering in liquid mixtures of $[C_4mim][PF_6]$ and $[C_4mim][BF_4]$ using infrared spectroscopy. They did not observe any nanostructural ordering in the binary RTIL mixture, but instead found good molecular level mixing.

Atomistic and coarse grained MD simulations are apt tools to study such RTIL mixtures. Force fields have matured to an extent so as to capture the diverse interactions present in RTILs, including electrostatics, hydrogen bonding, dispersion, π-stacking etc.. Here, extensive MD simulations were carried out to probe the intermolecular structure in two binary RTIL mixtures, that of $[C_4mim][PF_6]$ and $[C_4mim][Cl]$ and of $[C_4mim][PF_6]$ and $[C_4mim][BF_4]$. Crucial differences were observed in the manner of organization of anions around the cation which depends on

their sizes. The homogeneous nature of these RTIL mixtures through calculations of structure factors is demonstrate here.

7.2 Details of simulation

All-atom (AA) molecular dynamics (MD) simulations were done for two different systems: (i) $[C_4mim][PF_6]$-$[C_4mim][BF_4]$ (ii) $[C_4mim][PF_6]$-$[C_4mim][Cl]$. The anions PF_6-BF_4 or PF_6-Cl were taken in five different molar ratios of 10:90, 25:75, 50:50, 75:25 and 90:10 respectively. The three neat RTILs viz., $[C_4mim][PF_6]$, $[C_4mim][BF_4]$ and $[C_4mim][Cl]$ were also studied. The simulations were carried out at conditions of 300K and 1atm. The melting point of pure $[C_4mim][Cl]$ is 339K [23]; thus it is in a supercooled liquid state during the simulations, while all other mixtures are in the liquid state. For $[C_4mim][PF_6]$ and $[C_4mim][Cl]$, the CLAP [24] force field was used. $[C_4mim][BF_4]$ was modeled with the force field developed by Wang *et al* [25]. Initial configurations for all the systems containing 800 ion pairs each were generated through Packmol software package [26] (Details about the system sizes, i.e. number of ion pairs and box lengths are given in Table B.2 of Appendix). After an energy minimization procedure, a short NVT run of 500 ps duration was carried out to equilibrate the system. MD simulations were carried out in the constant NPT ensemble for a further duration of 12 ns. It was followed by a constant NVT run for 2 ns performed using the mean volume determined from the preceding NPT run. An analysis trajectory of 25 ns duration was carried out subsequently. Three dimensional periodic boundary conditions were applied. A potential interaction cutoff of 13 Å and time step of 0.5 fs to integrate the equations of motion were used. Long range electrostatic interactions were treated using the particle-particle particle mesh (PPPM) method [27]. Pair correlation functions were calculated with a bin width of 0.2 Å. Smaller bin widths produced some noise for pairs of ions at low concentrations and hence, this width was chosen. In the figures, symbols are

shown infrequently for the sake of clarity.

A lack of statistics was noticed in the anion-anion pair correlation functions for the system in which a specific anion is in 10% mole fraction, we developed a coarse grained (CG) model to carry out simulations of very large system sizes. This CG model was developed for [C_4mim][Cl] on the same lines as our earlier efforts for [C_4mim][PF_6] (see Appendix for the details of CG modelling) [28]. Large scale coarse grained MD simulations of the [C_4mim][PF_6]-[C_4mim][Cl] RTILs were also carried out in order to confirm the results obtained from the all-atom MD simulations. The details of these simulations (including force field) and results are presented in the Appendix. Each CG system consisted of 24000 ion pairs. Binary mixtures of RTILs were taken in the same ratio as above. The procedure described above for carrying out atomistic simulations was followed for the CG systems as well. An MD integration time step of 4 fs was used. Total analysis trajectory of 30 ns was generated for each system. All the simulations were carried out using the software package LAMMPS [29]. Spatial density maps were created using the software package VMD [30].

7.3 Results and discussion

Table 1 displays the densities of the simulated RTILs. The calculated densities for the neat RTILs match experimental data rather well. Any experimental densities for the binary mixture of RTILs studied here were not found in literature .

7.3.1 Radial distribution functions

The primary structural feature in RTILs is charge ordering which is a consequence of the dominant electrostatic interactions. Cation-anion pair correlation functions and spatial distribution functions are the appropriate quantities which capture this

Table 7.1: Density (g/cc) of RTILs with [C_4mim] being the cation.

Anion	Fraction	ρ_{sim}	ρ_{exp}	$\Delta\rho$ (%)
[PF_6]	100	1.39	1.37 [31]	1.45
[BF_4]	100	1.23	1.21 [32]	1.63
[Cl]	100	1.08	1.07 [33]	0.93
[PF_6] : [Cl]	10 : 90	1.10	-	-
	25 : 75	1.16	-	-
	50 : 50	1.25	-	-
	75 : 25	1.31	-	-
	90 : 10	1.35	-	-
[PF_6] : [BF_4]	10 : 90	1.25	-	-
	25 : 75	1.27	-	-
	50 : 50	1.31	-	-
	75 : 25	1.35	-	-
	90 : 10	1.37	-	-

feature. In the following, the geometric centre of the imidazolium ring is referred as the "cation". The cation-Cl and cation-PF_6 g(r)s exhibit their first peaks at 4.4 Å and 4.9 Å respectively (see Figure 7.1). The intensity of the former is more than that of the latter, due to the relatively stronger interaction strength of the cation with the chloride ion. A secondary feature is also seen at 5.9 Å and 6.7 Å in these g(r)s which correspond to anions located adjacent to the methyl group of the cation. Similar features are observed in the cation-anion g(r)s in the PF_6-BF_4 mixture as well (Figure 7.2).

In the PF_6-Cl system, the height of the first peak of the cation-Cl g(r) increases with decreasing chloride content. The peak height of cation-PF_6 g(r) too shows the same trend with decreasing amount of chloride. Further, the value of the first peak minimum too decreases with decreasing Cl content, indicating the increased near-neighbor structuring of the liquid with decreasing amounts of chloride. This may appear counterintuitive as the cation-Cl interaction is stronger and one would thus expect the liquid to be well structured at high concentrations of chloride. However, the result can be rationalized as due to the fact that at large concentrations of chloride, all the chloride ions will compete for the best cation interaction sites; this

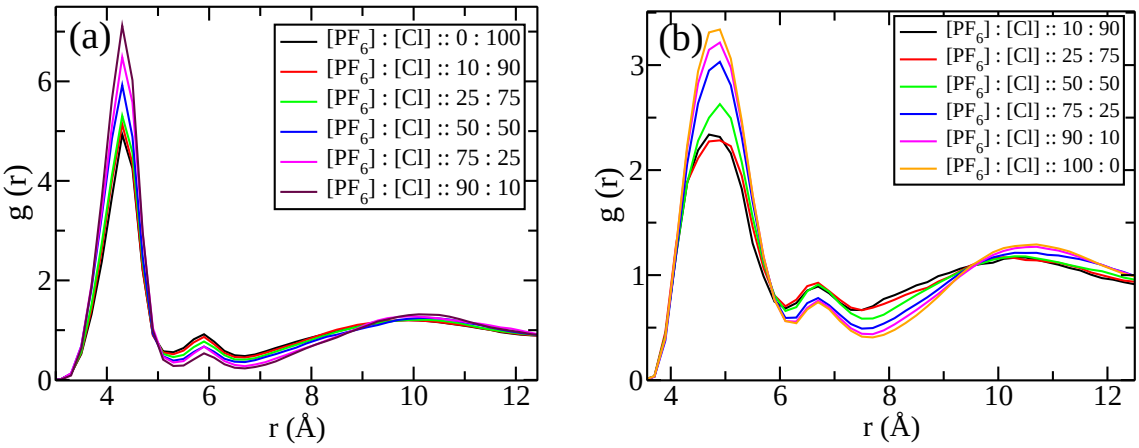

Figure 7.1: Radial distribution functions between (a) Cation-Cl, and (b) Cation-PF_6 in the [C_4mim][PF_6]-[C_4mim][Cl] system.

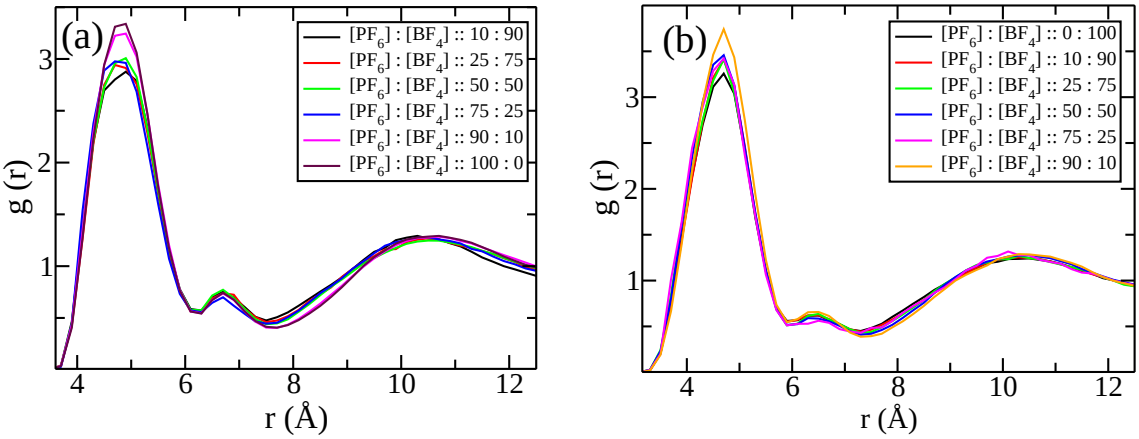

Figure 7.2: Radial distribution function between (a) Cation-PF_6, and (b) Cation-BF_4 in the [C_4mim][PF_6]-[C_4mim][BF_4] system.

is not the case though at low concentrations of chloride. The fewer chloride ions present at such low Cl fraction can easily compete against the weaker PF_6 ions to wrest favorable cation sites. A similar trend can be observed for the second coordination shell as well. But the extent of change is quite less as compared to first coordination shell (see Figure 7.1 and 7.2).

The concentration dependence of the height of the first peak of cation-anion g(r) in the PF_6-BF_4 system is many times weaker than that in the PF_6-Cl system. Compared to the size disparity of PF_6 and Cl ions, the sizes of PF_6 and BF_4 ions are

comparable. Thus, a stronger concentration dependence is observed in the PF_6-Cl mixture than in the PF_6-BF_4 mixture.

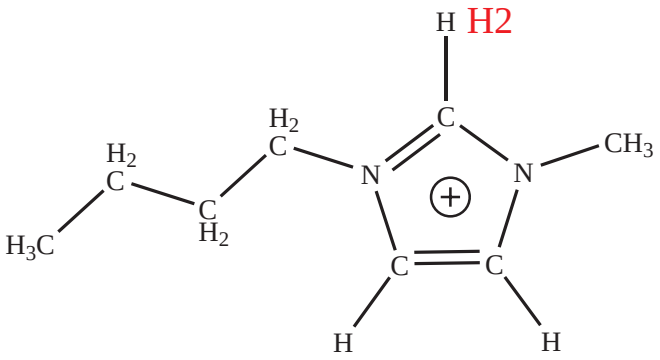

Figure 7.3: Schematic of cation.

The preferred location for the anion around the cation is one where it can form a weak hydrogen bond with the most acidic proton of the imidazolium ring, H2 (Figure 7.3). Shown in Figure 7.4 are the g(r)s of H2-Cl and H2-F in the PF_6-Cl system. As the [PF_6] concentration increases, the peak heights of both the pair correlation functions increase. The H2-Cl peak height is largest when the chloride concentration is the least; this observation is consistent with the behavior discussed in the cation-anion g(r)s. A similar, albeit much weaker dependence on anion concentration is observed in the PF_6-BF_4 system (Figure 7.5). The summary of the cation-anion and the H2-anion pair correlation functions is that the smaller anion prefers to hydrogen bond with the most acidic proton (H2) and the probability density of this event increases with decreasing concentrations of the smaller anion. The dependence of these quantities on anion concentration is stronger for a larger disparity between the anion radii. This result is consistent with AIMD results of Kirchner and coworkers [20, 21], where they found that the chloride ion was able to displace the larger thiocyanate ion from its preferred coordination site. Needless to state, thiocyanate and PF_6 have their own characteristics and herein it only their large size ratios with chloride. It needs to be reiterated though that PF_6 occupies sites above and below the ring plane near H2. Thus, at low concentrations of Cl,

the Cl ions preferentially occupy the site along the C-H2 vector to form a Cl...H2 hydrogen bond.

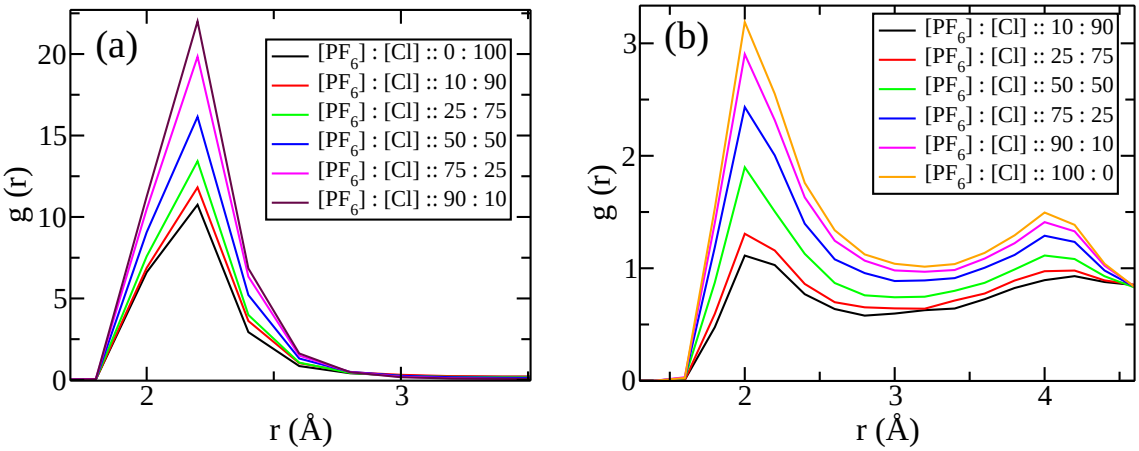

Figure 7.4: Radial distribution function between (a) H2-Cl, and (b) H2-F in $[C_4mim][PF_6]$-$[C_4mim][Cl]$ mixture. Here H2 refers to the most acidic hydrogen on the imidazolium ring of the cation and F refers to the fluorine of PF_6.

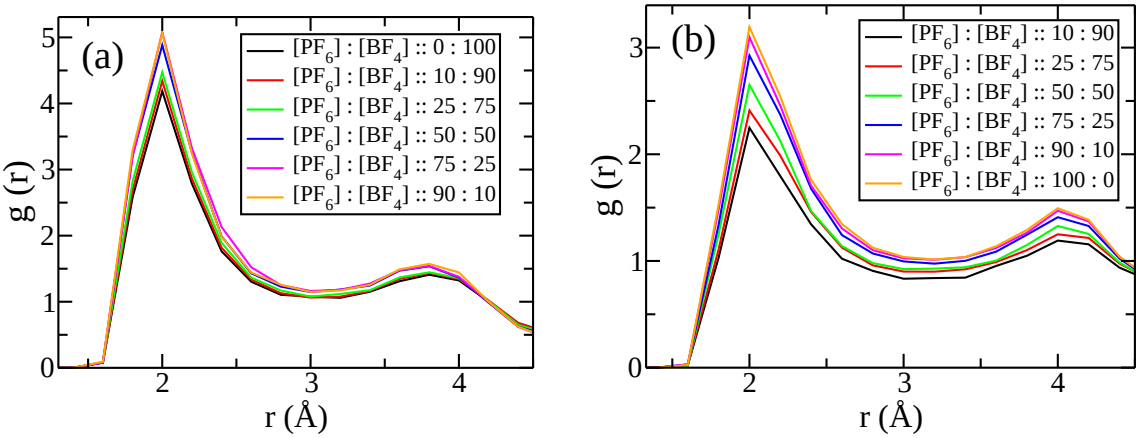

Figure 7.5: Radial distribution function between (a) H2-F (BF_4) and (b) H2-F (PF_6) in the $[C_4mim][PF_6]$-$[C_4mim][BF_4]$ system.

7.3.2 Spatial density maps

The spatial distribution functions of anions around the cation are displayed in Figure 7.6, 7.7 and 7.8. In the PF_6-Cl system, when the chloride is in minority, the

position along the C2-H2 bond vector (in the plane of the imidazolium ring) is occupied purely by it, whereas when it is in majority, this position is occupied by both chloride as well as by PF_6 (of course in different locations of the liquid sample). Similar results have been observed for the iodine position around the cation by Ghatee and coworkers in the pure [C_4mim][I] system using MD simulations [34, 35]. PF_6 occupies positions above and below the ring plane when it (i.e., PF_6) is in minority. A similar behaviour is exhibited in the PF_6-BF_4 system also, although the effect is much weaker due to the smaller radius ratio of the anions.

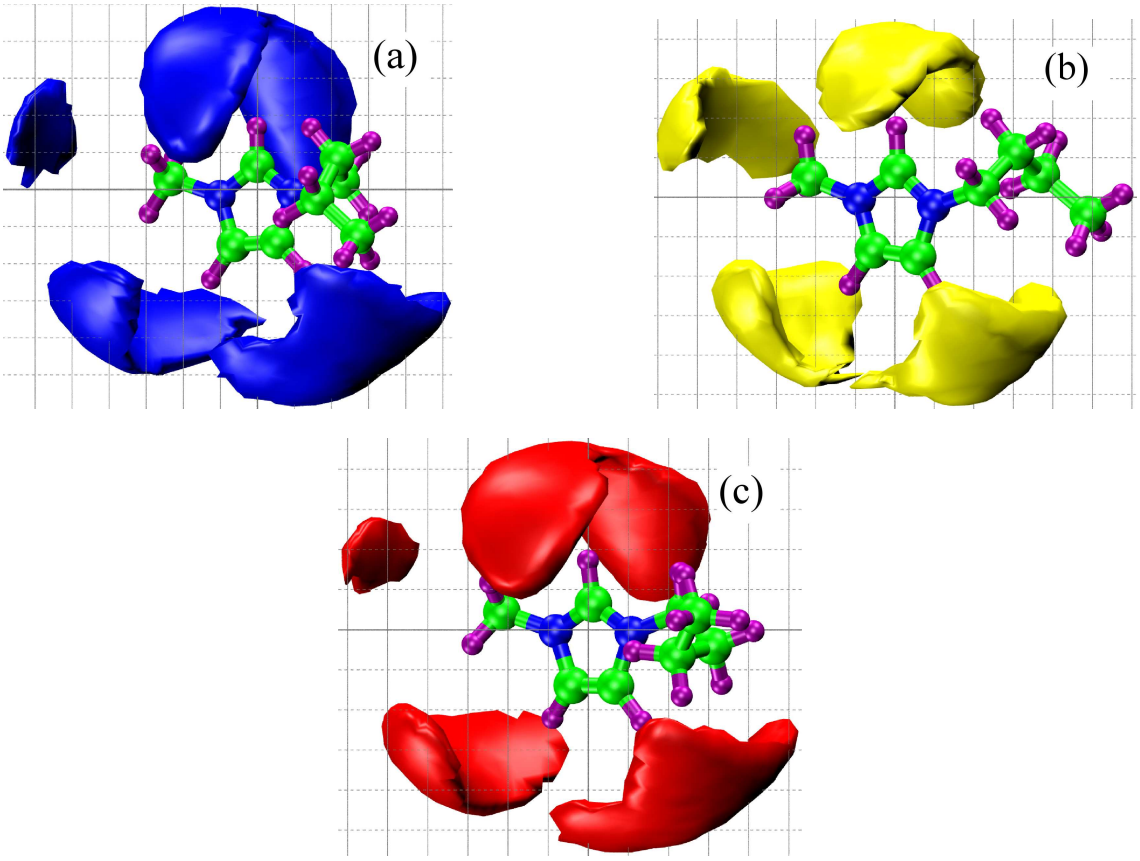

Figure 7.6: Spatial density maps of anion around cation in the three neat RTILs (a) PF_6, (b) Cl and (c) BF_4. Isosurfaces: PF_6 : Blue, Cl : Yellow, BF_4 : Red. Atoms: C in Green, N in Blue, H in Purple. The isosurfaces are at a density of 0.0184 $Å^{-3}$ for all the systems.

The stacking of imidazolium rings (slipped parallel geometry) in room temperature RTILs has been examined by many researchers in the past [36, 37]. The

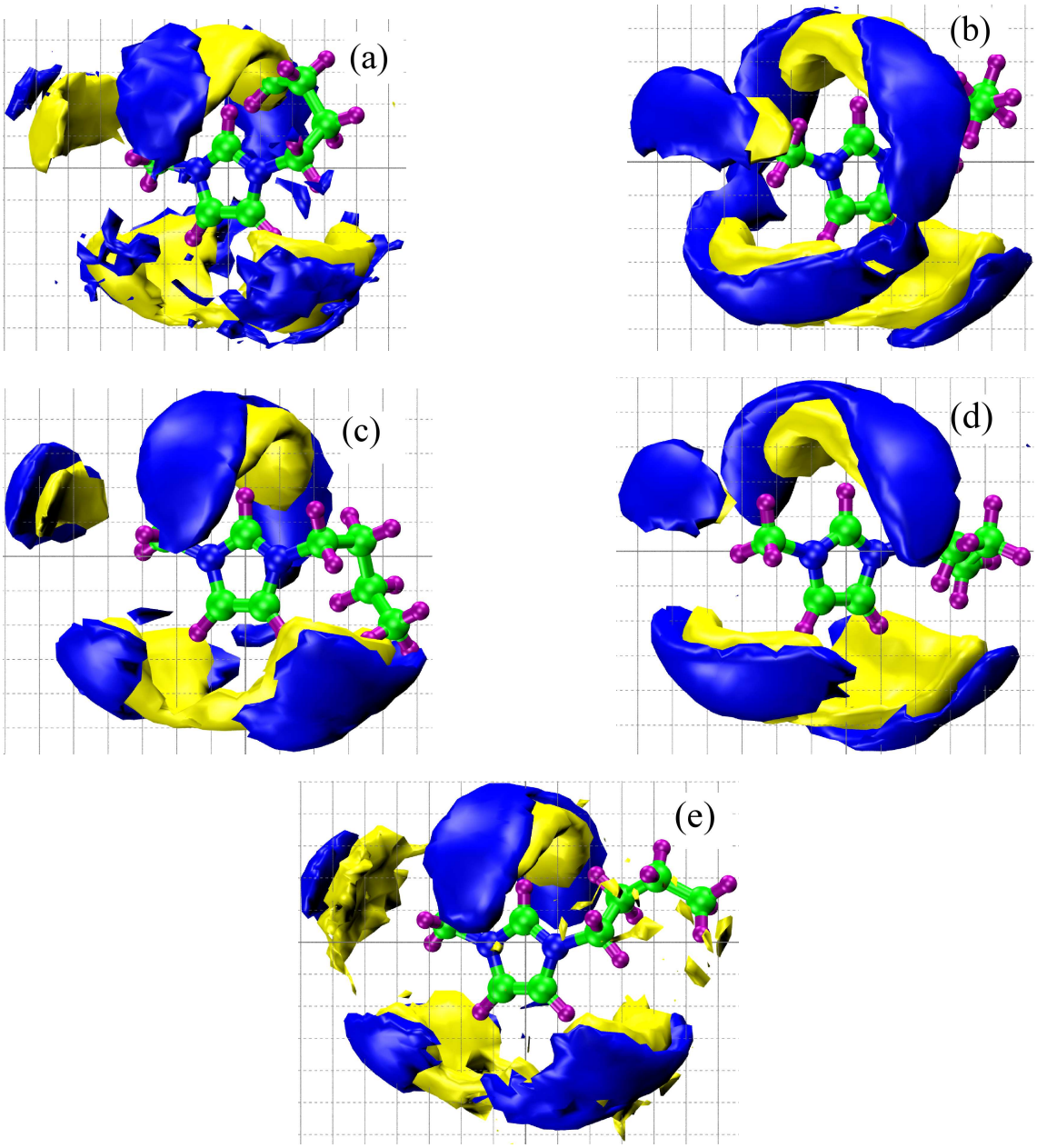

Figure 7.7: Spatial density map of anions around the cation for (a) PF_6:Cl :: 10:90, (b) PF_6:Cl :: 25:75, (c) PF_6:Cl :: 50:50, (d) PF_6:Cl :: 75:25 and (e) PF_6:Cl :: 90:10. Color scheme same as in previous figure. Isosurface values are normalized with respect to neat RTILs.

signature of this geometry is a shoulder (or a pre-peak) in the cation-cation g(r). The same is shown in Figure 7.9 as a function of anion mole fraction for the two systems investigated here. The stacking of cations is strong in pure [C_4mim][Cl] and its propensity decreases with decreasing PF_6 concentration. A similar behavior

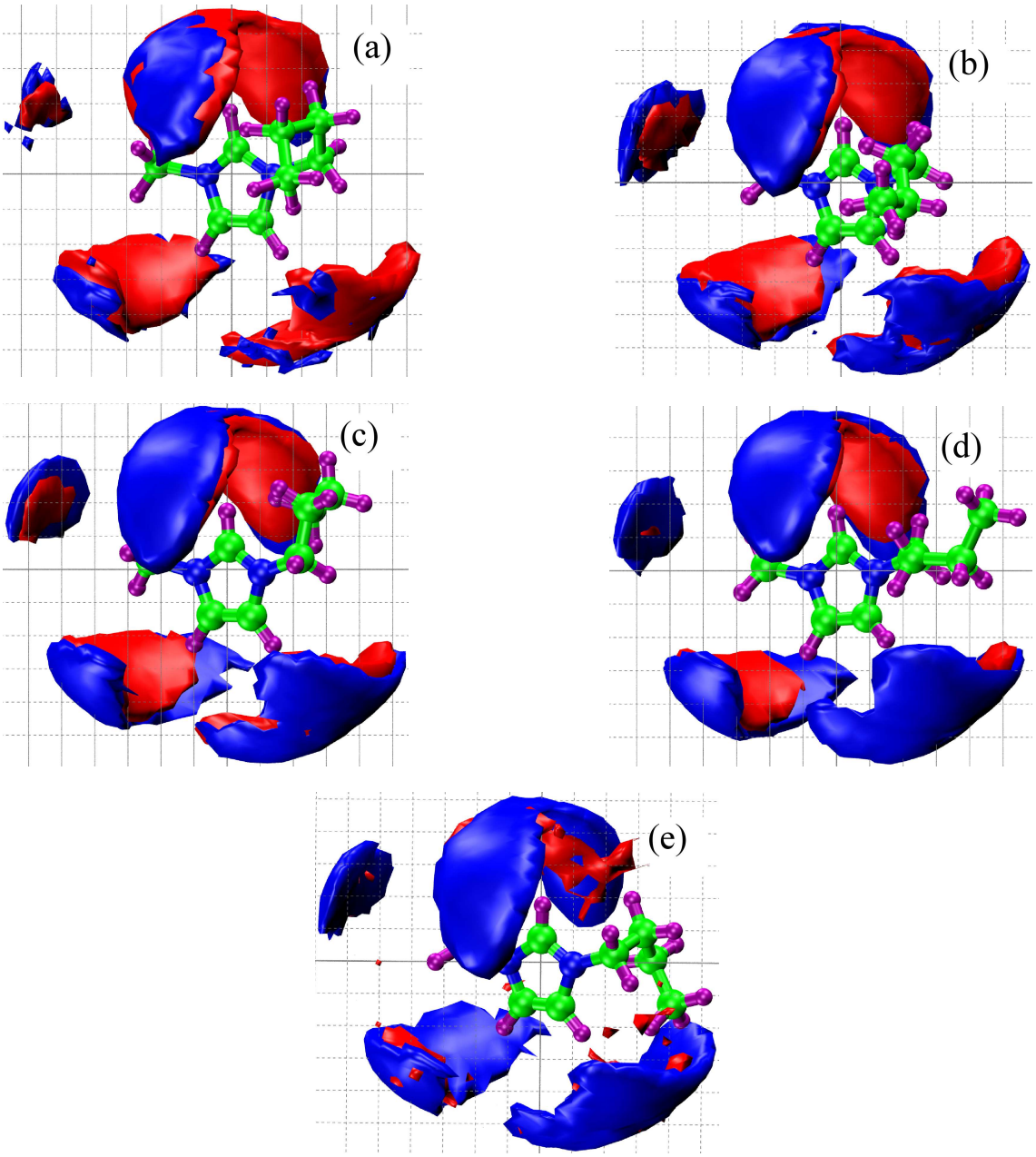

Figure 7.8: Spatial density map of anions around the cation for (a) PF_6:BF_4 :: 10:90, (b) PF_6:BF_4 :: 25:75, (c) PF_6:BF_4 :: 50:50, (d) PF_6:BF_4 :: 75:25 and (e) PF_6:BF_4 :: 90:10. Color scheme same as in previous figure. Isosurface values are normalized with respect to neat RTILs.

is observed in the PF_6-BF_4 system as well. Thus, smaller anions lead to stronger slipped stacking of the cation rings. The arrangement of cations in the mixtures appears to be linearly dependent on the mole fraction of the anion, in agreement with the experimental observations of Xiao *et al* [15, 16].

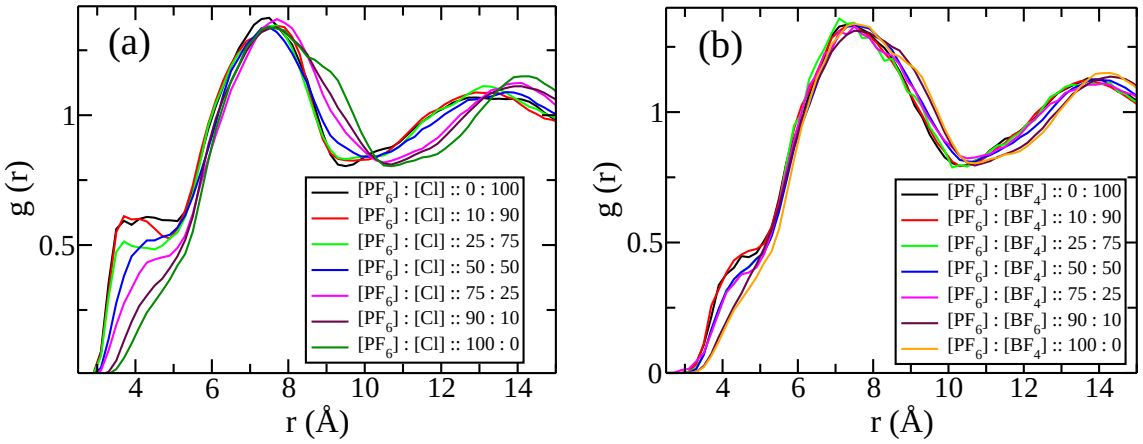

Figure 7.9: Radial distribution functions for cation - cation in (a) PF_6-Cl mixture, and (b) PF_6-BF_4 mixture.

Glimpses of nanostructural ordering inherent to RTILs with longer alkyl tails can be observed in ones with the butyl tail as well. This feature can be studied through the partial structure factor between the terminal carbon atoms of the butyl tail. The same is exhibited in figure 7.10. In both the systems, the function exhibits the characteristic peak at around 0.5 $Å^{-1}$ in all anion mole fractions. It implies that the weak nanostructural ordering inherent to the pure RTIL systems is present in the binary mixtures as well.

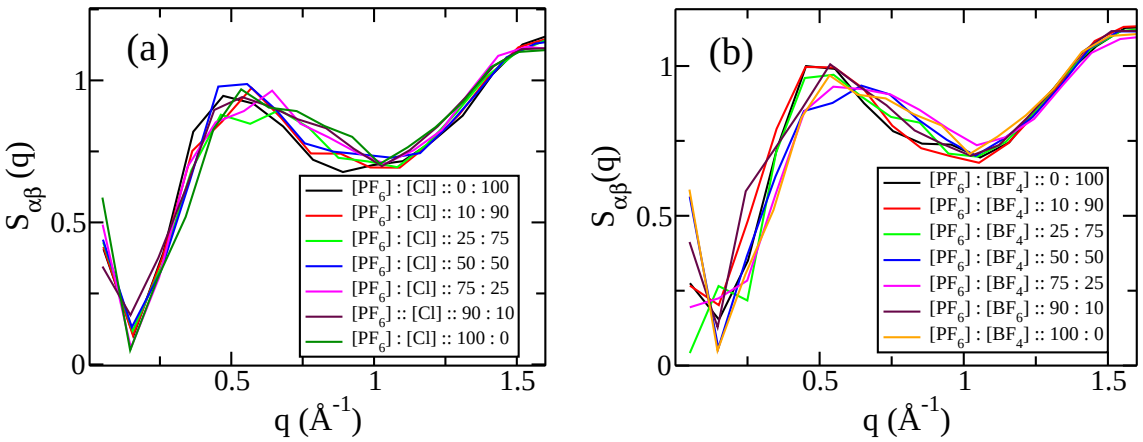

Figure 7.10: Partial structure factor between the terminal carbon atoms in the alkyl group of cations (tail-tail) for (a) $[C_4mim][PF_6]$-$[C_4mim][Cl]$ and (b) $[C_4mim][PF_6]$-$[C_4mim][BF_4]$ systems.

The H2 site prefers to hydrogen bond to a smaller anion when the said anion is

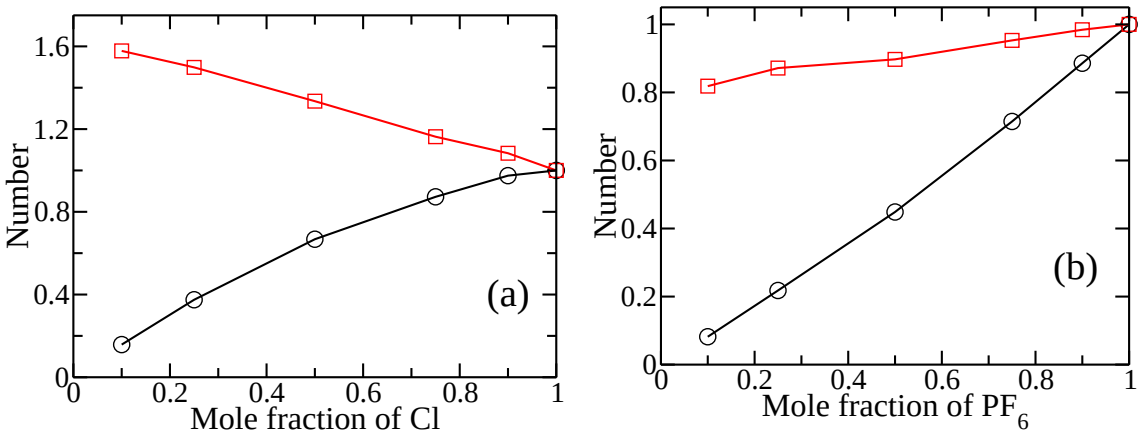

Figure 7.11: Normalized first shell coordination number as a function of mole fraction for (a) H2-Cl, and (b) H2-F in [C_4mim][PF_6]-[C_4mim][Cl] system. The black line with circles is the normalized coordination number while the red curve with squares is the ratio of this quantity to the mole fraction of the anion.

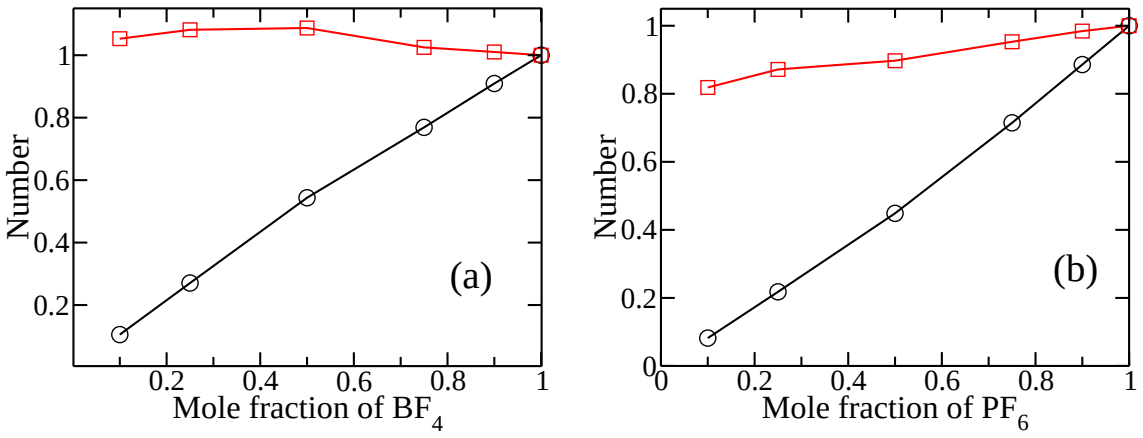

Figure 7.12: Normalized first shell coordination number as a function of mole fraction for (a) H2-F (BF_4) and (b) H2-F (PF_6) in the [C_4mim][PF_6]-[C_4mim][BF_4] system. The black line with circles is the normalized coordination number while the red curve with squares is the ratio of this quantity to the mole fraction of the anion.

in minority, to an extent which is much greater than its mole fraction. Figure 7.11 presents the coordination number of chloride ions around H2 as a function of chloride mole fraction. The data is normalized with the value in pure [C_4mim][Cl]. The coordination number shows an excess over what is expected from a distribution of chloride ions proportional to its concentration. The ratio of the above quantity (i.e., normalized H2-Cl coordination number) to the mole fraction of Cl is also plotted in

the figure. It shows considerable deviation from the value of unity. When chloride is in minority, it coordinates to the H2 site to a degree much above its mole fraction. Naturally, this increased occupancy will have to be compensated by PF_6 ions. The fluorines of PF_6 (also shown in the figure) are under-represented at the H2 site. Not unexpectedly, in the PF_6-BF_4 system, both the anions are coordinated to the H2 site to an extent that is nearly proportional to their mole fractions (Figure 7.12). Thus, the difference in anion size plays a crucial role in their local organization around the cation.

The overwhelming preference of chloride ions (when in minority) to associate themselves with the H2 site of a cation does not lead, however, to their clustering. The anion-anion partial structure factor can be employed to examine any heterogeneous distribution of anions. Shown in Figure 7.16 are these functions for the Cl-Cl and PF_6-PF_6 pairs obtained from all-atom (AA) and coarse grained MD simulations.

7.3.3 Mean square displacement

In order to understand the dynamical behavior of the system, mean square displacement (MSD) of the cation and anions were calculated. Figure 7.13 shows the MSD plots for the pure RTIL systems. It is a well known fact that in the case of RTILs, the cation despite being bulkier diffuses faster than anion [24]. MSD of cation and anion directly varies as their individual strength to bind with each other. Since the chloride ion has higher binding strength to the cation, in [bmim][Cl] system both cation and anions diffuses slowest among the three pure RTILs. $[BF_4]^-$ has the least binding affinity towards the cation and hence [bmim][BF_4] system shows highest MSD.

In case of binary mixture of RTILs, the MSD values are dependent on the concentration of individual anions. MSD plots for [C_4mim][PF_6]-[C_4mim][Cl] and [C_4mim][PF_6]-[C_4mim][BF_4] systems are shown in Figure 7.14 and 7.15 respectively.

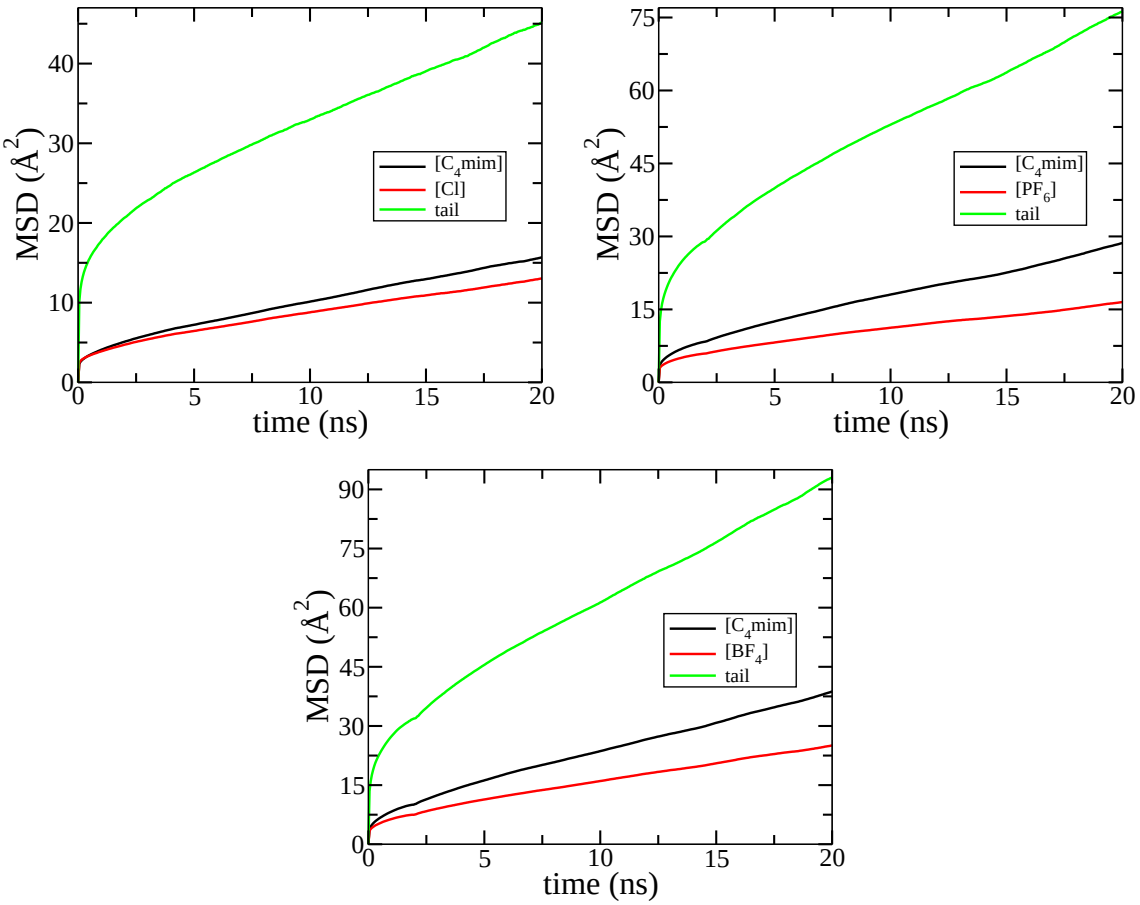

Figure 7.13: Mean square displacement values for (a)[C_4mim][Cl], (b)[C_4mim][PF_6] and (c) [C_4mim][BF_4] obtained using all-atom MD simulations.

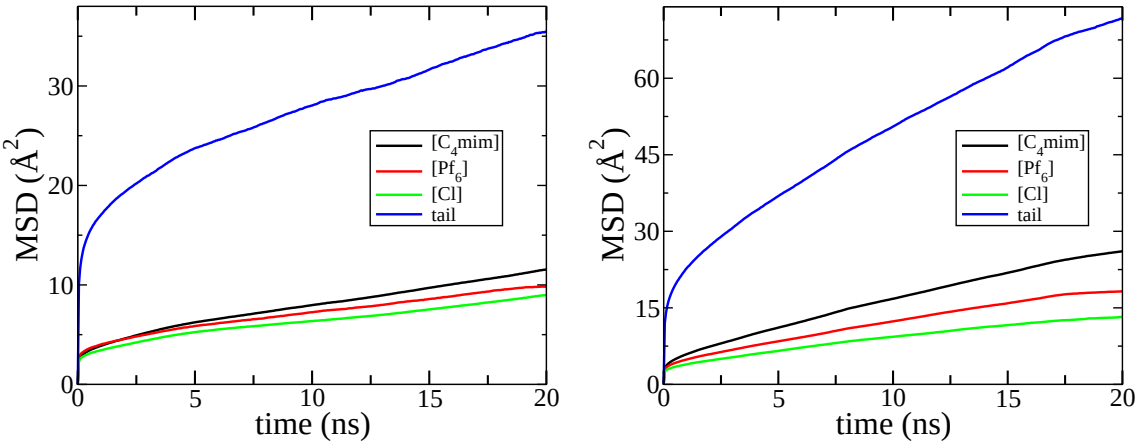

Figure 7.14: Mean square displacement values for (a)[PF_6]:[Cl]::25:75 and (b)[PF_6]:[Cl]::75:25 obtained using all-atom MD simulations.

The diffusion of cation in the system decreases with increasing concentration of that specific anion which has a higher binding affinity. In the case of anions, irrespective of concentration, the anion with higher binding affinity to the cation always moves slower.

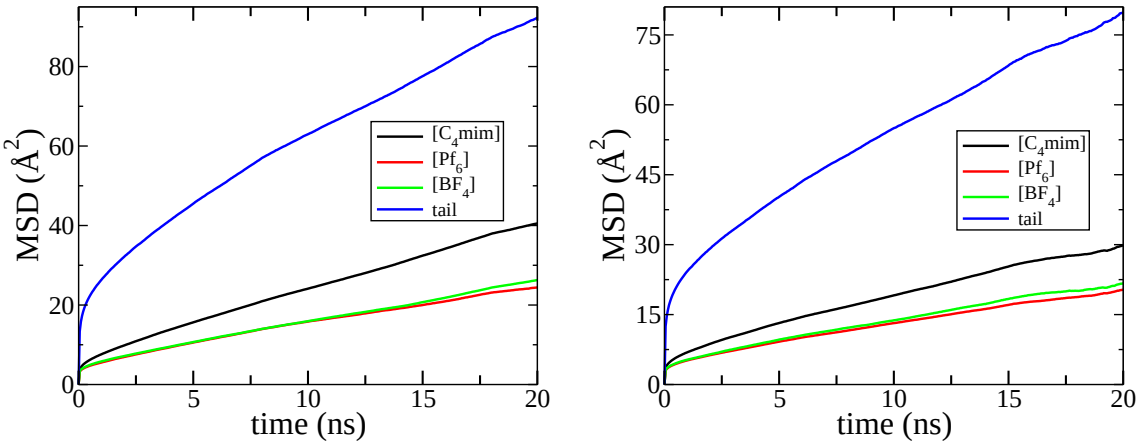

Figure 7.15: Mean square displacement values for (a)[PF_6]:[BF_4]::25:75 and (b)[PF_6]:[BF_4]::75:25 obtained using all-atom MD simulations.

7.3.4 Partial structure factors

Structuring (if any) at low wave vectors can be probed with the CGMD simulations as one can carry out simulations of large system sizes in a facile manner. The partial structure factors shown in Figure 7.16 are featureless below 0.7 $Å^{-1}$ implying the lack of any clustering (or ordering) of like anions beyond this length scale. As a corollary, it implies complete mixing of the two types of anions, both in the PF_6-Cl and in the PF_6-BF_4 systems. The latter is also confirmed through the PF_6-Cl partial structure factor shown in Figure 7.17. The functions, at all mole fractions, are featureless below 1 $Å^{-1}$ suggesting the complete mixing of anions irrespective of the disparity in their sizes. Our results suggest a molecular level mixing of anions, consistent with the infrared spectroscopic study of Baiker and coworkers [22], who found no microscopic phase separation in binary mixtures of RTILs similar to those

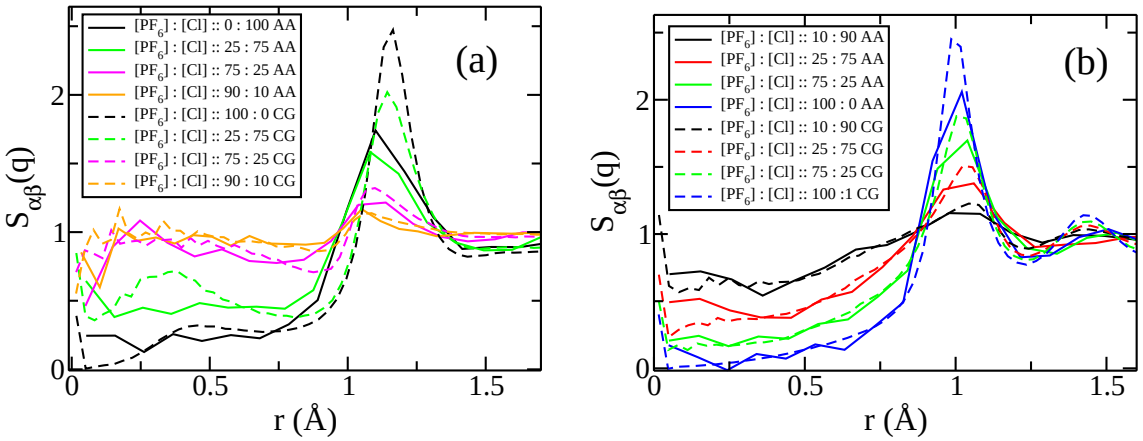

Figure 7.16: Partial structure factors of (a) Cl-Cl, and (b) PF_6-PF_6 obtained using all-atom (AA) and coarse grain (CG) MD simulations. The 10:90 and 50:50 data are not shown for clarity.

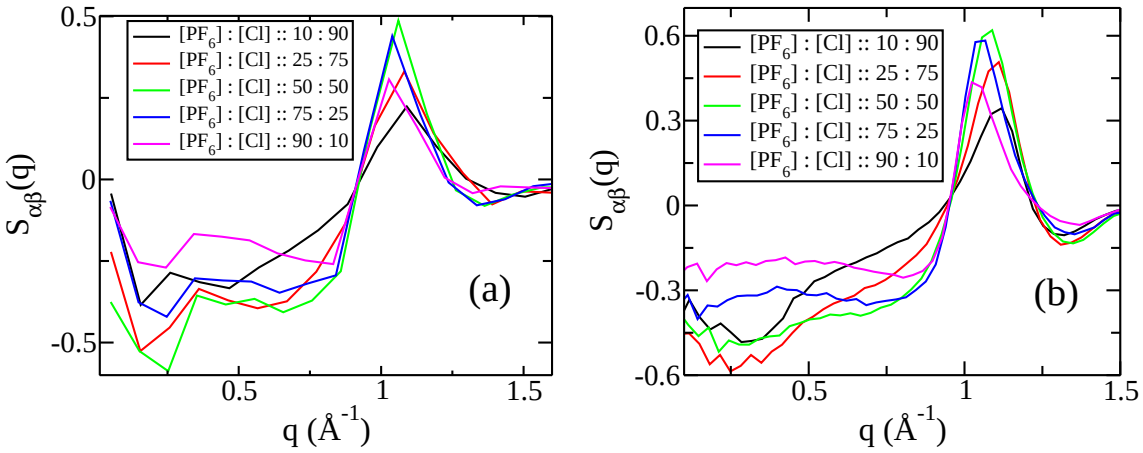

Figure 7.17: Partial structure factors between PF_6-Cl obtained using (a) AA model and (b) CG model.

studied here.

Our simulations point to subtle, but vital differences in the manner in which anions organize themselves around the cation, depending on their radii. However, the regions which exhibit such differences are not correlated in space.

7.4 Conclusions

Binary mixtures of RTILs possessing a common cation were studied using atomistic molecular dynamics simulations in order to identify their microscopic mixing characteristics. Our simulations conclusively point to molecular level mixing of the chosen RTILs. Apart from the neat liquids, two binary mixtures, viz., $[C_4mim][PF_6]$-$[C_4mim][Cl]$ and $[C_4mim][PF_6]$-$[C_4mim][BF_4]$, each at five different concentrations were examined. The anion sizes differed more in the former system than that in the latter.

The chloride anion being much smaller than the hexafluorophosphate prefers to strongly hydrogen bond with the most acidic proton (H2) of the imidazolium ring. This preference increases with decreasing mole fractions of chloride. However, the PF_6 anion is largely located above and below the imidazolium plane and is able to access the H2 site only when it is in majority concentration. The distinction in the anion arrangement around the cation is negligible in the PF_6-BF_4 system as their sizes are not too different. Further, the difference in the coordination behavior of Cl and PF_6 around the cation does not lead to their segregation or clustering. The observations from atomistic MD simulations were confirmed through large scale coarse grained MD simulations of the $[C_4mim][PF_6]$-$[C_4mim][Cl]$ system as well. Analysis of the anion-anion partial structure factors at various mole fractions of the anions are featureless for wave vector values below 1 $Å^{-1}$ implying the absence of like-ion clustering.

Appendix B

Figure B.1 represents the mapping scheme between all-atom (AA) and coarse grained (CG) beads. The bead-bead interaction parameters were chosen from the coarse grained model developed by us earlier [28] for [C_4mim][PF_6]. Correspondingly, the charge of Cl was also scaled to 0.8. Non-bonded interactions of the 9-6 type Lennard-Jones type were determined so that cation-anion pair correlation functions in neat [C_4mim][Cl] obtained from the CG simulations reproduced those from the AA run, as well as the system density. The pair correlations between pairs of different bead types obtained from AA and CG MD simulations are displayed in Figure B.2. These validate the interaction parameters for the CG model adopted here. A real space cutoff of 15 Å was applied for both LJ and Coulombic interactions. Table B.1 displays the parameters employed in our CG simulations for [C_4mim][Cl]. Lorentz-Berthelot mixing rules were employed for cross interactions. Spatial density maps were created using software package VMD [30].

Lennard-Jones 9-6 interactions

$$\mathcal{U}_{ij}(r_{ij}) = 4\varepsilon_{ij}\left[\left(\frac{\sigma_{ij}}{r_{ij}}\right)^9 - \left(\frac{\sigma_{ij}}{r_{ij}}\right)^6\right] \tag{B.1}$$

Table B.1: 9-6 Lennard-Jones interaction parameters for the coarse grain model of [C_4mim][Cl].

Bead pair	ϵ (kcal mol^{-1})	σ (Å)
I1 - I1	0.3757152	4.100
I1 - I2	0.3604245	4.050
I1 - I3	0.2739623	4.050
I1 - CM	0.3914031	4.340
I1 - Cl	0.0457049	4.570
I2 - I2	0.3457295	4.100
I2 - I3	0.2628021	4.050
I2 - CM	0.3754372	4.340
I2 - Cl	0.0557049	4.720
I3 - I3	0.0997725	2.850
I3 - CM	0.2853807	3.800
I3 - Cl	0.2988648	3.810
CM - CM	0.4690000	4.585
CM - Cl	0.2651688	4.243
Cl - Cl	0.0155586	3.150

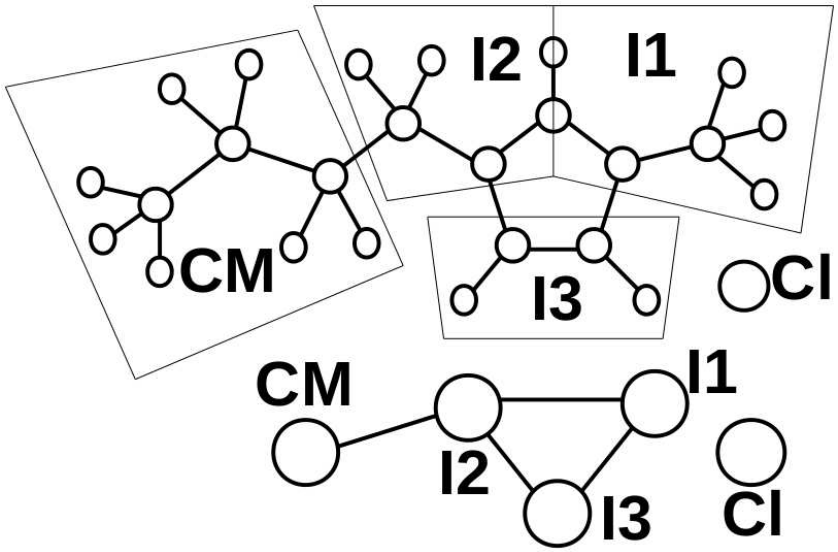

Figure B.1: Schematic showing the mapping from all-atom to the coarse grained model in [C_4mim][Cl].

Table B.2: Box length and fraction of ion pairs for RTILs with [C_4mim] as cation. 800 and 24000 ion pairs were used in the all-atom (AA) and coarse grained (CG) MD simulations respectively.

Anion	Fraction (%)	Box length (Å) (AA)	Box length (Å) (CG)
PF_6	100	64.640	200.8515
Cl	100	59.940	186.0311
BF_4	100	62.344	–
PF_6 : Cl	10 - 90	60.514	188.0311
	25 - 75	61.024	189.6157
	50 - 50	62.220	193.3320
	75 - 25	63.500	197.3093
	90 - 10	64.211	199.5185
PF_6 : BF_4	10 - 90	62.652	–
	25 - 75	63.020	–
	50 - 50	63.400	–
	75 - 25	64.195	–
	90 - 10	64.389	–

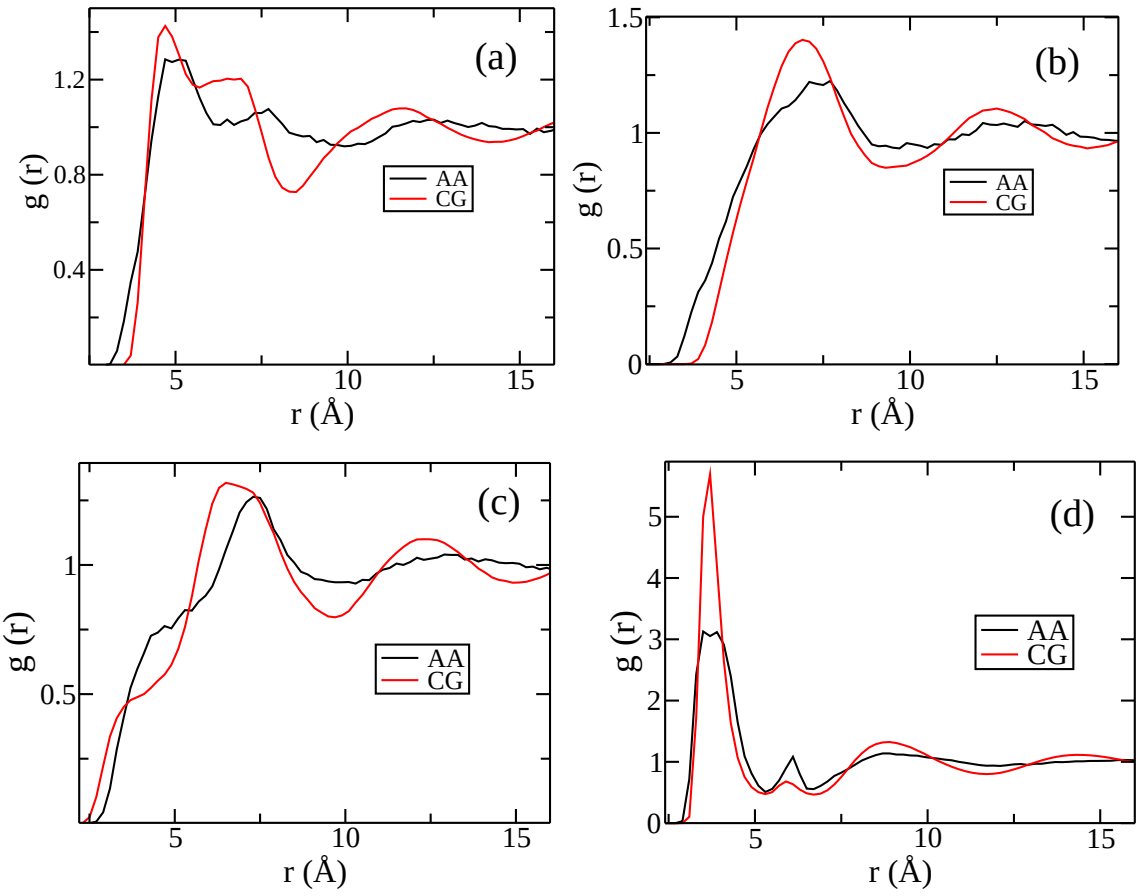

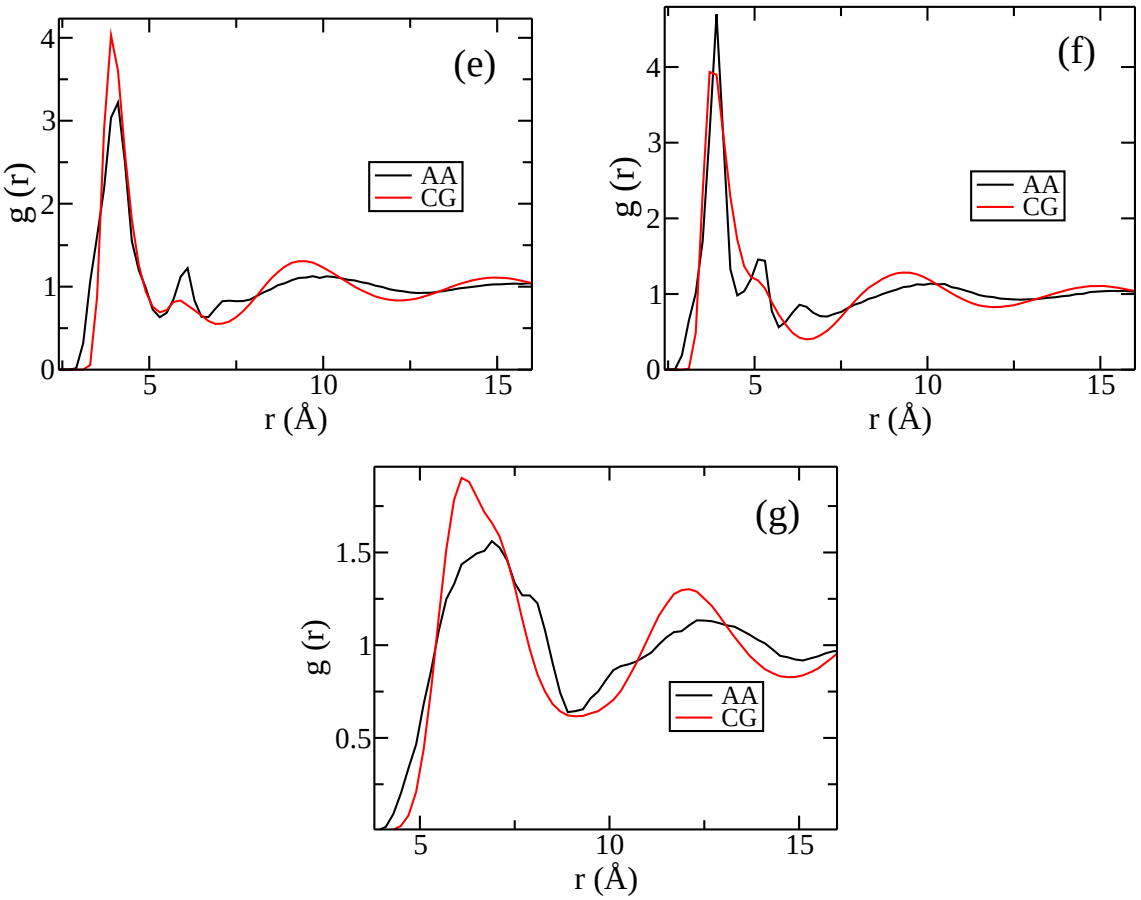

Figure B.2: Radial distribution functions betwen (a) I1-I1, (b) I2-I2, (c) I3-I3, (d) I1-Cl, (e) I2-Cl, (f) I3-Cl and (g) Cl-Cl compared between that from AA and CG MD simulations for pure [C_4mim][Cl].

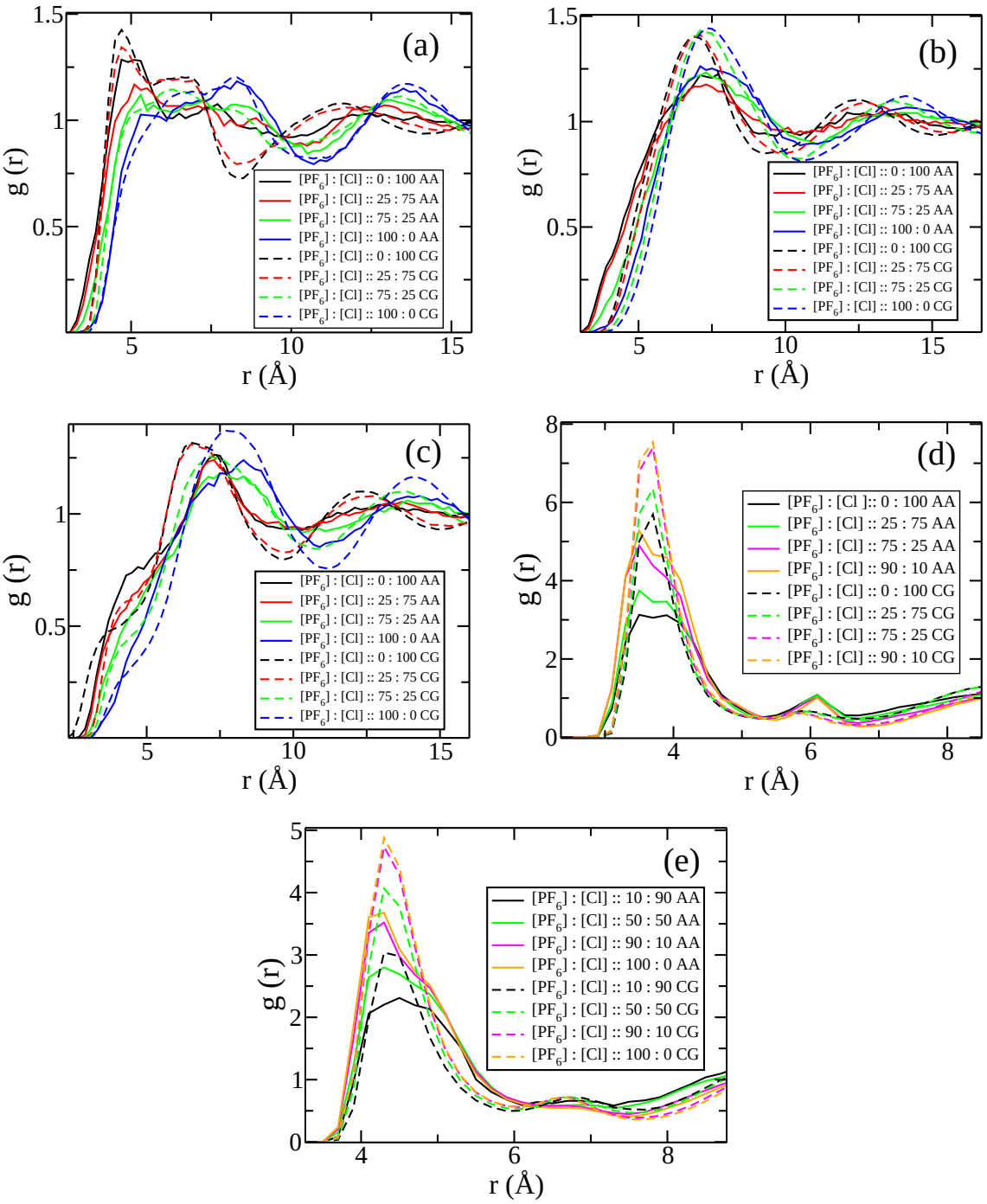

Figure B.3: Radial distribution functions at various concentrations of anions in the [C_4mim][PF_6]- [C_4mim][Cl] system between (a) I1-I1, (b) I2-I2, (c) I3-I3, (d) I1-Cl and (e) I1-PF_6, compared between AA and CG MD simulations.

Bibliography

[1] Earle, M. J.; Seddon, K. R. *Pure Appl. Chem.* **2008**, *72*, 1391 – 1398.

[2] Fort, D. A.; Remsing, R. C.; Swatloski, R. P.; Moyna, P.; Moyna, G.; Rogers, R. D. *Green Chem.* **2007**, *9*, 63–69.

[3] Li, W.; Sun, N.; Stoner, B.; Jiang, X.; Lu, X.; Rogers, R. D. *Green Chem.* **2011**, *13*, 2038–2047.

[4] Liu, H.; Sale, K. L.; Holmes, B. M.; Simmons, B. A.; Singh, S. *J. Phys. Chem. B* **2010**, *114*, 4293–4301.

[5] Cromie, S. R. T.; Del Pópolo, M. G.; Ballone, P. *J. Phys. Chem. B* **2009**, *113*, 11642–11648.

[6] Youngs, T. G. A.; Holbrey, J. D.; Deetlefs, M.; Nieuwenhuyzen, M.; Costa Gomes, M. F.; Hardacre, C. *ChemPhysChem* **2006**, *7*, 2279–2281.

[7] Galiński, M.; Lewandowski, A.; Stępniak, I. *Electrochim. Acta* **2006**, *51*, 5567 – 5580.

[8] Olivier-Bourbigou, H.; Magna, L.; Morvan, D. *Appl. Catal. A* **2010**, *373*, 1 – 56.

[9] Wu, W.; Han, B.; Gao, H.; Liu, Z.; Jiang, T.; Huang, J. *Angew. Chem. Int. Ed.* **2004**, *43*, 2415–2417.

[10] Niedermeyer, H.; Hallett, J. P.; Villar-Garcia, I. J.; Hunt, P. A.; Welton, T. *Chem. Soc. Rev.* **2012**, *41*, 7780–7802.

[11] Finotello, A.; Bara, J. E.; Narayan, S.; Camper, D.; Noble, R. D. *J. Phys. Chem. B* **2008**, *112*, 2335–2339.

[12] Weber, C. C.; Masters, A. F.; Maschmeyer, T. *J. Phys. Chem. B* **2012**, *116*, 1858–1864.

[13] Bayley, P. M.; Best, A. S.; MacFarlane, D. R.; Forsyth, M. *ChemPhysChem* **2011**, *12*, 823–827.

[14] Andanson, J.-M.; Jutz, F.; Baiker, A. *J. Phys. Chem. B* **2010**, *114*, 2111–2117.

[15] Xiao, D.; Rajian, J. R.; Li, S.; Bartsch, R. A.; Quitevis, E. L. *J. Phys. Chem. B* **2006**, *110*, 16174–16178.

[16] Xiao, D.; Rajian, J. R.; Hines, L. G.; Li, S.; Bartsch, R. A.; Quitevis, E. L. *J. Phys. Chem. B* **2008**, *112*, 13316–13325.

[17] Ghatee, M. H.; Zolghadr, A. R. *J. Phys. Chem. C* **2013**, *117*, 2066–2077.

[18] Stoppa, A.; Buchner, R.; Hefter, G. *J. Mol. Liq.* **2010**, *153*, 46 – 51.

[19] Shimizu, K.; Tariq, M.; Rebelo, L. P.; Lopes, J. N. C. *J. Mol. Liq.* **2010**, *153*, 52 – 56.

[20] Brussel, M.; Brehm, M.; Voigt, T.; Kirchner, B. *Phys. Chem. Chem. Phys.* **2011**, *13*, 13617–13620.

[21] Brussel, M.; Brehm, M.; Pensado, A. S.; Malberg, F.; Ramzan, M.; Stark, A.; Kirchner, B. *Phys. Chem. Chem. Phys.* **2012**, *14*, 13204–13215.

[22] Andanson, J.-M.; Beier, M. J.; Baiker, A. *J. Phys. Chem. Lett.* **2011**, *2*, 2959–2964.

[23] Holbrey, J. D.; Reichert, W. M.; Nieuwenhuyzen, M.; Johnson, S.; Seddon, K. R.; Rogers, R. D. *Chem. Commun.* **2003**, 1636–1637.

[24] Canongia Lopes, J. N.; Deschamps, J.; Pádua, A. A. H. *J. Phys. Chem. B* **2004**, *108*, 2038–2047.

[25] Wu, X.; Liu, Z.; Huang, S.; Wang, W. *Phys. Chem. Chem. Phys.* **2005**, *7*, 2771–2779.

[26] Martínez, L.; Andrade, R.; Birgin, E. G.; Martínez, J. M. *J. Comput. Chem.* **2009**, *30*, 2157–2164.

[27] Hockney, R. W.; Eastwood, J. W. *Computer Simulation Using Particles*; Adam Hilger, 1988.

[28] Bhargava, B. L.; Devane, R.; Klein, M. L.; Balasubramanian, S. *Soft Matter* **2007**, *3*, 1395–1400.

[29] Plimpton, S. *J. Comput. Phys.* **1995**, *117*, 1 – 19.

[30] Humphrey, W.; Dalke, A.; Schulten, K. *J. Mol. Graph.* **1996**, *14*, 33–38.

[31] Gu, Z.; Brennecke, J. F. *J. Chem. Eng. Data* **2002**, *47*, 339–345.

[32] Wang, J.; Tian, Y.; Zhao, Y.; Zhuo, K. *Green Chem.* **2003**, *5*, 618–622.

[33] Huddleston, J. G.; Visser, A. E.; Reichert, W. M.; Willauer, H. D.; Broker, G. A.; Rogers, R. D. *Green Chem.* **2001**, *3*, 156–164.

[34] Ghatee, M. H.; Ansari, Y. *J. Chem. Phys.* **2007**, *126*, 154502.

[35] Ghatee, M. H.; Zolghadr, A. R.; Moosavi, F.; Ansari, Y. *J. Chem. Phys.* **2012**, *136*, 124706.

[36] Qiao, B.; Krekeler, C.; Berger, R.; Delle Site, L.; Holm, C. *J. Phys. Chem. B* **2008**, *112*, 1743–1751.

[37] Dommert, F.; Schmidt, J.; Qiao, B.; Zhao, Y.; Krekeler, C.; Site, L. D.; Berger, R.; Holm, C. *J. Chem. Phys.* **2008**, *129*, 224501.

Outlook

The work presented in the thesis can be classified into three major categories: (i) Investigations of dissolution of lignocellulosic biomass (chiefly cellulose) in RTILs (ii) Examination of organization of RTILs near charged mica surfaces and (iii) Understanding intermolecular structure in binary mixtures of RTILs.

(i) Dissolution of lignocellulosic biomass in RTILs

Results: The disruption of inter- and intra-molecular hydrogen bond network present in lignocellulosic biomass is the key to its dissolution. Although the anion plays a dominant role in the process, the cation too is implicated. A good solvent should possess the following attributes (a) strong hydrogen bond acceptor (b) moderate hydrogen bond donor and (c) absence of any electron withdrawing group.

Future prospects: Further efforts need to be made to investigate the role of the cation on cellulose dissolution. In particular, covalent functionalization of the cation so as to create hydrogen bonding sites which can add to the coordination of cellulose can be explored. Also, the dissolution of lignin in RTILs can be studied, and these are expected not to be dominated by hydrogen bonding. Solvation of other biomolecular systems such as lipids in RTILs too can be studied.

(ii) Examination of organization of RTILs near charged mica surfaces

Results: Simulation studies reveal that RTILs self assemble near a charged mica surface. Cations with short alkyl tails have their imidazolium rings perpendicular and alkyl tails parallel to the mica surface which is converse to the behavior exhibited

by cations with longer alkyl tails. Cations with symmetric alkyl substitutions are more ordered as compared to their asymmetric counterparts.

Future prospects: Results presented in the thesis have been obtained for atomically flat surfaces. It is a well known fact that surface roughness can drastically change the organization behavior. Effect of surface roughness and defects on the organization of RTILs can be examined in the future. Also, the organization of RTILs in a confined environment (say, between two plates) can be studied.

(iii) Intermolecular structure of binary mixtures of RTILs

Results: Results presented in the thesis shows a molecular level mixing of two RTILs, irrespective of their ionic radii and strength. Although the cation is seen to exhibit a special preference for an anion with smaller radii and higher ionic strength, the same does not give rise to any phase separation or clustering in the system.

Future prospects: Up to what disparity in anion radii and strength will the homogeneous mixing is sustained needs to be investigated. Furthermore, properties of binary mixtures of two RTILs with differing cation and same anions can be studied.

List of publications

- Density functional theory investigations on the structure and dissolution mechanisms for cellobiose and xylan in an ionic liquid: gas phase and cluster calculations

  R. S. Payal, R. Bharath, G, Periyasamy and S. Balasubramanian, *J. Phys. Chem. B* **116**, 833-840 (2012).

- Dissolution of cellulose in ionic liquids: an ab initio molecular dynamics simulation study

  R. S. Payal and S. Balasubramanian, *Phys. Chem. Chem. Phys.* **16**, 17458-17465 (2014).

- Dissolution of cellulose in ionic liquids: Anion dependence

  R. S. Payal, B. K. Kumar, A. Mondal and S. Balasubramanian (accepted).

- Orientational ordering of ionic liquids near a charged mica surface

  R. S. Payal and S. Balasubramanian, *ChemPhysChem* **13**, 1764-1771 (2012).

- Dynamic Atomic Force Microscopy for Ionic Liquids: Massless Model Shows the Way (Research Highlight)

  RS Payal and S Balasubramanian, *ChemPhysChem* **13**, 3085-3086 (2012).

- Effect of cation symmetry on the organization of ionic liquids near a charged mica surface

  R. S. Payal and S. Balasubramanian, *J. Phys. Condens. Matter* **26**, 284101 (2014).

- Homogenous mixing of ionic liquids: molecular dynamics simulations

  R. S. Payal and S. Balasubramanian, *Phys. Chem. Chem. Phys.* **15**, 21077-21083 (2013).

List of changes

- Figure 1.1 has been changed (Chapter 1, Page 3).
- References have been added (Chapter 1, Page 4).
- Section 1.2 have been added (Chapter 1, Pages 6-7).
- Reference to the correct equation number has been incorporated (Chapter 1, Page 13).
- Symbol labels were changed (Chapter 1, Page 15).
- 'Week' was changed to 'weak' at a few places (Chapter 1).
- Also the limitations of experimental method and importance of simulations have been discussed (Chapter 2, Page 38).
- Discussion regarding the importance of conformational properties of cellobiose have been added (Chapter 2, Pages 38-39).
- Relative sizes of cation, anion, methanol and water have been added (Chapter 2, Page 41).
- Explanation regarding the reversal of stability of cellobiose conformer has been added (Chapter 2, Pages 48-49).
- Difference in binding strength of cation and anion to cellobiose have been added (Chapter 2, Page 51).

- Results from simulations of higher cluster size calculations have been incorporated (Chapter 2, Pages 51-52).
- Dependence of solubility on anion and cation has been added (Chapter 3, Page 65).
- A sentence has been added (Chapter 3, Page 69).
- Details about ABF and COLVAR have been added to the thesis (Chapter 4, Pages 90-91).
- References have been added to the thesis (Chapter 5, Page 110).
- Brief summary about CVFF and CLAYFF were added in the thesis (Chapter 5, Page 113).
- Figure 5.3 (Chapter 5, Page 118) and 5.9 (Chapter 5, Page 125) have been added to the thesis.
- Explanation regarding the increase in the order of anion distribution in Set B has been added to the thesis (Chapter 5, Page 120).
- Inconsistencies in the grammar as well as content have been rectified (Chapter 6, Page 138).
- A sentence regarding CG modeling has been added to the thesis (Chapter 7, Page 165).
- Section 7.3.3 have been added (Chapter 7, Pages 175-177)